Development of bilateral control for pneumatic actuated teleoperation system

Minh-Quyen Le

N° d'ordre 2011ISAL0131 Année 2011

THESE

présentée devant

L'Institut National des Sciences Appliquées de Lyon

Pour obtenir

LE GRADE DE DOCTEUR

par

Minh-Quyen LE

Ingénieur de l'INSA de Lyon

Département Méthodes pour l'Ingénierie des Systèmes – Laboratoire Ampère
Ecole doctorale: Electronique, Electrotechnique et Automatique (EEA)
Spécialité: Automatique Industrielle

DEVELOPMENT OF BILATERAL CONTROL FOR PNEUMATIC ACTUATED TELEOPERATION SYSTEM

Soutenue prévu le 8 Decembre 2011 devant le jury :

C. PRELLE	Maître de conférences, HDR	Roberval – UTC	Rapporteur
J. LOTTIN	Professeur des Universités	SYMME – Université de Savoie	Rapporteur
J. TROCCAZ	Directrice de Recherche CNRS	TIMC-IMAG – Grenoble	Examinatrice
R. MOREAU	Maître de conférences	Ampère – INSA de Lyon	Invité
M.T. PHAM	Maître de conférences	Ampère – INSA de Lyon	Co-directeur
T. REDARCE	Professeur des Universités	Ampère – INSA de Lyon	Directeur

INSA Direction de la Recherche - Ecoles Doctorales – Quadriennal 2011-2015

SIGLE	ECOLE DOCTORALE	NOM ET COORDONNEES DU RESPONSABLE
CHIMIE	**CHIMIE DE LYON** **http://www.edchimie-lyon.fr** Insa : R. GOURDON	M. Jean Marc LANCELIN Université de Lyon – Collège Doctoral Bât ESCPE 43 bd du 11 novembre 1918 69622 VILLEURBANNE Cedex Tél : 04.72.43 13 95 directeur@edchimie-lyon.fr
E.E.A.	**LECTRONIQUE, ELECTROTECHNIQUE, AUTOMATIQUE** **http://edeea.ec-lyon.fr** Secrétariat : M.C. HAVGOUDOUKIAN eea@ec-lyon.fr	M. Gérard SCORLETTI Ecole Centrale de Lyon 36 avenue Guy de Collongue 69134 ECULLY Tél : 04.72.18 60 97 Fax : 04 78 43 37 17 Gerard.scorletti@ec-lyon.fr
E2M2	**EVOLUTION, ECOSYSTEME, MICROBIOLOGIE, MODELISATION** **http://e2m2.universite-lyon.fr** Insa : H. CHARLES	Mme Gudrun BORNETTE CNRS UMR 5023 LEHNA Université Claude Bernard Lyon 1 Bât Forel 43 bd du 11 novembre 1918 69622 VILLEURBANNE Cédex Tél : 04.72.43.12.94 e2m2@biomserv.univ-lyon1.fr
EDISS	**INTERDISCIPLINAIRE SCIENCES-SANTE** **http://ww2.ibcp.fr/ediss** Sec : Safia AIT CHALAL Insa : M. LAGARDE	M. Didier REVEL Hôpital Louis Pradel Bâtiment Central 28 Avenue Doyen Lépine 69677 BRON Tél : 04.72.68 49 09 Fax :04 72 35 49 16 Didier.revel@creatis.uni-lyon1.fr
INFOMATHS	**INFORMATIQUE ET MATHEMATIQUES** **http://infomaths.univ-lyon1.fr**	M. Johannes KELLENDONK Université Claude Bernard Lyon 1 LIRIS - INFOMATHS Bâtiment Nautibus 43 bd du 11 novembre 1918 69622 VILLEURBANNE Cedex Tél : 04.72. 43.19.05 Fax 04 72 43 13 10 infomaths@bat710.univ-lyon1.fr
Matériaux	MATERIAUX DE LYON	M. Jean-Yves BUFFIERE Secrétaire : Mériem LABOUNE INSA de Lyon École Doctorale Matériaux Mériem LABOUNE Bâtiment Antoine de Saint-Exupéry 25bis Avenue Jean Capelle 69621 VILLEURBANNE Tel : 04 72 43 71 70 Fax : 04 72 43 72 37 ed.materiaux@insa-lyon.fr
MEGA	**MECANIQUE, ENERGETIQUE, GENIE CIVIL, ACOUSTIQUE (ED n°162)**	M. Philippe BOISSE Secrétaire : Mériem LABOUNE Adresse : INSA de Lyon École Doctorale MEGA Mériem LABOUNE Bâtiment Antoine de Saint-Exupéry 25bis Avenue Jean Capelle 69621 VILLEURBANNE Tel : 04 72 43 71 70 Fax : 04 72 43 72 37 mega@insa-lyon.fr Site web : http://www.ed-mega.com
ScSo	**ScSo*** M. OBADIA Lionel Sec : Viviane POLSINELLI Insa : J.Y. TOUSSAINT	M. OBADIA Lionel Université Lyon 2 86 rue Pasteur 69365 LYON Cedex 07 Tél : 04.78.69.72.76 Fax : 04.37.28.04.48 Lionel.Obadia@univ-lyon2.fr

*ScSo : Histoire, Geographie, Aménagement, Urbanisme, Archéologie, Science politique, Sociologie, Anthropologie

To those who have encouraged me, believed in me and challenged me to do better.

Abstract

The aim of this thesis is to investigate the development and control of electro-pneumatic actuators in a haptic teleoperation system. For controlling the mass flow rate of such actuators, two types of valve technology are sudied, i.e. solenoid (on/off) valve and proportional servovalve. The servovalves have found widespread applications in which high accuracy of force/position control are needed. They are however typically expensive due to the requirements of high-precision manufacturing. Therefore, the low-cost solenoid valves can be an alternative to the servovalves for achieving acceptable-performance pneumatic control. Generally, the highly nonlinear of the pneumatic actuator is heightened when it uses on/off solenoid valves instead of servovalves. In this case, precise control is challenging due to the discrete-input nature of the system. Our first objective is to demonstrate that it is possible to design an acceptable performance teleoperation system using master-slave robots that have pneumatic actuators equipped with only inexpensive on/off solenoid valves.

To control efficiently the switching on/off valves, several control approaches have been proposed, namely pulse width modulation (PWM), hybrid algorithm, and sliding mode control. PWM is the most popular method utilized for controlling the discrete on/off valves due to its simplicity of implementation and design. A main problem with this method is chattering phenomenon that is caused by the high frequency switching of the valves. A hybrid control theory, which includes more switching control modes, allows to reduce the chattering problem and improve the energy consumption of the valves. Experimental results show that the teleoperation transparency in terms of force and position but also the dynamic behavior of the pressures are better in the case of the hybrid control than the PWM control. It is noteworthy that neither robustness nor stability analysis of overall hybrid system has been investigated in our study due to the complexity of the control approach which is based on the nonlinear model of the pressures and the discrete model of the mass flow rates. Consequently, another strategy (i.e. a sliding mode control), which does not depend on the pneumatic model, is proposed. This control stratgy allows to perform not only the transparent analysis but also the stability analysis. To evaluate the efficiency of the proposed approach, a comparison of transparency has been investigated between three control architectures (position-error-based, force-error-based and direct-force-reflection controls) in a two-channel bilateral teleoperation framework. In order to improve the dynamic performance and reduce the chattering problem in solenoid valve actuated pneumatic teleoperation systems, a five-mode sliding control scheme (consisting of five switching levels) has been used, which can be considered as an extension of the three-mode sliding controller. Our study demonstrates that by increasing the number of possible control actions for the valves, we can reduce the valves' switching activities, hence improving the valve's life times at no cost to teleoperation transparency.

The second objective of the thesis involves in implementing the proportional servovalves on the pneumatic teleoperation system. A comparison related to the teleoperation performance between an on/off valve and a servovalve is carried out. In experiments, it is observed that with the four-channel bilateral teleoperation architecture employing either solenoid valves or servovalves, satisfactory force and position tracking between the master and the slave is obtained under both free-motion and contact-motion conditions. Nonetheless, compared to the on/off valve, the servovalve technology displays less audible noise and smothers signals in terms of force and pressure, which allows to improve the haptic teleoperation performance as well as the human's perception.

In bilateral teleoperation control, force sensors are often omitted to save cost and to lessen weight and volume. Therefore, another aspect of our work consists in using observers for an estimation of operator and environment forces. Experimental results show that acceptable teleoperation transparency based on a simple Nicosia observer and a tangent linear control approach can be achieved. Furthermore, good agreement between force observation and force measurements of the operator and environment at steady state were obtained.

Keywords: Pneumatic actuator, proportional servovalves, on/off valves, PWM control, hybrid algorithm, sliding mode control, observers, teleoperation, stability, transparency.

Résumé

L'objectif des travaux entrepris au cours de cette thèse concerne le développement d'un système haptique de téléopération contrôlé à l'aide d'actionneurs électropneumatiques. Pour réaliser le contrôle du débit de ce type de modulateur, deux solutions technologiques sont possibles : soit des servovalves soit des électrovannes. La première solution est utilisée pour contrôler précisément des systèmes de hautes performances, mais l'apparition d'électrovannes rapides compactes à faible coût offre la possibilité de les utiliser à la place des servovalves (éléments couteux). Même si cela entraîne des défis dans la réalisation de la commande, à cause de l'augmentation des non-linéarités intrinsèques de l'actionneur pneumatique lorsqu'il est piloté par les électrovannes au lieu des servovalves. Le premier objectif a consisté à démontrer la possibilité de réaliser des interfaces maître-esclave à performance acceptable à l'aide d'électrovanne, afin de produire des systèmes à faible coût.

La méthode la plus courante pour commander des électrovannes consiste à utiliser un signal modulé en largeur d'impulsion (PWM). Cependant, les commutations hautes fréquences des électrovannes réduisent dramatiquement leur durée de vie. Afin de contrôler de manière plus optimale les électrovannes, une nouvelle stratégie de la commande basée sur l'algorithme hybride a été développée. Cette commande a été implémentée et testée sur un système de maître-esclave à un degré de liberté développé au cours de ces travaux de recherche. Une comparaison entre la commande hybride et la commande classique de type PWM a été réalisée. L'ensemble des résultats a démontré de meilleures performances dans le cas de la commande hybride en termes de dynamique de pression, des performances de suivi en force/position, ainsi que d'un point de vue énergétique et de durée de vie des composants. L'analyse de la stabilité dans le cadre d'une commande hybride n'a pas été étudiée dans notre cas en raison de la complexité de l'approche qui est basée sur le modèle non linéaire des pressions et le modèle discret des débits. Afin de disposer de l'ensemble des informations (transparence et stabilité) la commande par mode glissant a été choisie. Dans le but d'évaluer l'efficacité de cette approche, une comparaison de la transparence a été réalisée parmi trois architectures (position-position, force-force et force-position) pour un système de téléopération à deux canaux. L'approche théorique a été mise en parallèle avec des tests pratiques et une bonne cohérence de l'ensemble a été obtenue. Pour améliorer les performances dynamiques du système tout en réduisant les phénomènes de « chattering », une commande à cinq-mode (consistant à 5 modes de commutations) qui est étendu à partir de la comamnde à 3-mode a été utilisée. Les résultats ont démontré qu'en augmentant le nombre de modes de commande d'une électrovanne, l'activité de commutation réduite provoquant ainsi une augmentation de la durée de vie des composants, sans pour autant influencer sur les performances en terme de transparence.

Le second point de recherche entrepris est passé par l'utilisation de servovalves dans un système de téléopération, permettant ainsi de réaliser une comparaison entre les deux technologies (servovalve et électrovanne). Dans le cas d'une architecture de téléopération bilatérale à quatre canaux, les données expérimentales pour les deux types d'organes de commandes, ont donné des résultats satisfaisants en termes de suivi de force et de position pour le maître et l'esclave (en espace libre ou en contact). Au final l'étude a démontré que l'avantage de la technologie des servovalves réside dans une nuisance sonore plus faible et la production de signaux plus lisses en termes de force et de pression, permettant ainsi l'amélioration des propriétés haptiques du système de téléopération. Dans le cas de système de téléopération bilatérale, le capteur de force est souvent supprimé dans le but de réduire les coûts ainsi que le poids et le volume du système global. C'est la raison pour laquelle les travaux se sont intéressés à la possibilité d'utiliser des observateurs, à la place de capteurs de force pour déterminer les forces d'interactions entre l'opérateur et l'interface maître ainsi que l'environnement et l'interface esclave. Les données expérimentales montrent ainsi qu'il est possible d'obtenir des bonnes performances de transparence en utilisant un simple observateur de Nicosia.

Finalement ces différents résultats démontrent le potentiel des actionneurs électropneumatiques pour la réalisation le système de téléopération.

Mots-clés: Actionneur pneumatique, servovalves proportionnelles, électrovannes, commande PWM, algorithme hybride, commande par mode glissante, observateurs, téléopération, stabilité, transparence.

Acknowledgements

My first acknowledge needs to go to my advisors, **Tanneguy REDARCE** and **Minh Tu PHAM**, and my collaborator **Richard MOREAU** who allowed me to explore this interesting research direction and who introduced me to many people in the "automation" community. I have been impressed by the quality of their research and also really enjoyed the pleasant working atmosphere. They have spent a lot of their precious time on reading my thesis, making constructive comments and advancing critical suggestions in my research process, and setting great examples of being a mature and serious researcher for me. The quality of their supervision greatly helped me overcome the hurdles inherent in the completion of a PhD thesis.

I would also like to acknowledge comments and suggestions from anonymous reviewers who have critiqued some of the work presented in this document.

I wish to express my warm thanks to the committee members **Jocelyne TROCCAZ**, **Christine PRELLE** and **Jacques LOTTIN** for their invaluable, insightful comments and suggestions that improved the quality of this work.

Thanks to all of Laboratoire Ampère members. It has been a pleasure working with all of you. I would like to thank **Xufeng LINSHI**, **Xavier BRUN**, **Eric BIDEAUX**, **Sylvie SESMAT, Jean-Pierre SIMON** and **Mohamed SMAOUI** for providing help and advices in completing this research. A special thanks is due to **Pascal BEVILACQUA**, **Abderrahime ZAOUI** and **Christophe DUCAT** for helping me in developing the test-bench as well as giving me excellent technical advices.

In addition, I would like to express my deep and sincere gratitude to my collaborator **Mahdi TAVAKOLI** at University of Alberta, CANADA for his guidance and valuable advice during my Ph.D. I also wish to thank **Sean HODGSON,** for his collaboration and friendly help. Their collaboration has had a remarkable influence on my entire research.

A special acknowledge is also due to **Arnaud SELLIER**, **Hassen FOURATI**, and **Talel MAALEJ**. The quality and quantity of the work they put into thier master's report has been a real asset to my Ph.D. work.

I appreciate all my colleagues in the lab, especially **Hong-Viet**, **Ramon**, **Van-Hoa**, **Gerardo**, **Salam**, **Audrey**, **Lilia**, **Mariem**, **Gregory**, **Sajeh**, **Mingming**, **Mahdi**, etc. and my fellow student **Veronica** for her assistance and friendship in my PhD study.

Special thank to my parents, my sister and my brother for their encouragement and their loving support. A special thanks is also due to *mon chéri* **Pierre-Jean**, who supported me during these three years and especially during the delicate writing period. Since he has already completed his Ph.D., I am one of the few Ph.D. students who can say that her (his) boyfriend/fiancé/husband (girlfriend/fiancée/wife) truly has empathy for the Ph.D. process.

Lastly, I would like to thank all of the friends during my years at INSA de Lyon who supplied for their considerable understanding and strong support. And especially **David** and **Vanina** for helping me to discover a rich culture of dance, music, tattoo, and sculpture of French Polynesia. We will come to see you soon in Nuku Hiva. But also **Masae** for your kindness, humor as well as for the afternoons of origami and Japanese gastronomy. I'm really lucky to have you as friends.

I express my apologies and sincere thanks to who that I might forget. It is not easy to express my gratitude to everyone but it is even more difficult to find the right words to thank all of you as much as you are well deserved.

So thanks for your indulgence!

Notations

Pneumatic system

Parameter	Unit	Description
P_{atm}	Pa	Atmosphere pressure
P_{sa}	Pa	Supply pressure
r	J/kg/K	Perfect gas constant
T_a	K	Supply temperature
C_{val}	$kg.s^{-1}.Pa^{-1}$	Sonic conductance
C_r		Critical pressure ratio
α		Polytropic constant
l	m	Cylinder stroke
$S_\bullet$	m^2	Piston area
$P_\bullet$	m^2	Pressure
$q_\bullet$	m^2	Mass flow rate
M	kg	Load
b	$N.s.m^{-1}$	Viscosity coefficient
F_{ext}	N	External force
F_{st}	N	Stiction force
U	V	Voltage control signal

Teleoperation

Parameter	Unit	Description
$F_\bullet$*	N	Exogenous input force
F_h	N	Operator force exerted on the master
F_e	N	Environment force exerted on the slave
F_m and F_s		Controller forces
$Y_\bullet$	m	Position
$Z_\bullet$	$N.m^{-1}$	Impedance
C_s and C_m		Local position controllers
C_5 and C_6		Local force feedback controllers
C_1 to C_4		Position or force transfer controllers
$M_\bullet$	kg	Mass
$B_\bullet$	$N.s.m^{-1}$	Damping
$K_\bullet$	$N.m^{-1}$	Stiffness
h_{ij}		Hybrid parameters
H		Hybrid matrix

Indices

Parameter	Description
p	Chamber p
n	Chamber n
s	Slave
m	Master
h	Human operator
e	Environment

Exponent

Parameter	Description
e	Equilibrium
*	Exogenous force

Abbreviations

DOF	Degree-of-freedom
CH	Channel
PEB	Position-error-based
FEB	Force-error-based
DFR	Direct-force-reflection
MCS	Mode control scheme
PWM	Pulse width modulation
MIS	Minimally invasive surgery
LTI	Linear time invariant
MRI	Magnetic resonance imaging

Table of contents

Introduction

The growth of virtual reality systems for medical training, human motor control research, entertainment applications, etc. has driven development of haptic interface systems which are able to perform a variety of tactile/kinesthetic experiences. By manipulating the haptic device, the user manipulates through a computer rendered virtual environment, and actuators in the device push against the user to synthesize a mechanical interaction with the virtual environment. Realistic representation of the environment places significant demands on the design of both haptic device and control system. As a result, existing design practice struggles to achieve acceptable feedback properties including performance and stability robustness.

Whereas a virtual reality system connects the user to a virtual environment, a teleoperation system, which involves operating one or several robots remotely, connects the user to a physical environment via master and slave manipulators. Applications of teleoperation include robot-assisted surgery, nuclear waste handling, space and sub-sea explorations, etc. where the environments are hazardous or difficult to attain. It is therefore preferable to have the operator remotely located at a safer and more comfortable site.

When the haptic feedback provides to the human operator is representative of the actual forces between the slave robot and the environment, teleoperation is said to be haptic or bilateral. In this case, the operator enables to experience touch-based interaction with the remote environment without requiring direct physical contact. The basic control requirements on a bilateral teleoperation system are related to its stability and transparency. Transparency corresponds to the quality of reproduction of the remote environment mechanical properties for the operator. Transparency in conjunction with stability can ensure successful completion of tasks in the teleoperation mode.

Not all teleoperation systems provide force-feedback; indeed, commercial surgical robots such as Zeus system (from Computer Motion) and daVinci system (from Institute Surgical) used for Minimally Invasive Surgery (MIS) are not force-reflecting (or bilateral) teleoperators. A lack of force information, which has been often reported by surgeons and robotics researchers, is a major limitation of the current MIS systems. In order to provide a realistic impression of the actual contact during surgery, a measurement of the contact forces at the instrument tip is obviously required. Therefore, the development of a teleoperation with force feedback is certainly a future trend in telerobotic applications, especially for the minimally invasive operations.

In teleoperation systems, electrical direct-current (DC) motors are generally used as they are reasonably safe, simple and capable of providing forces suitable for small haptic devices. In DC motor actuated haptic devices that require reflecting high output forces to the operator, the use of gears becomes necessary. This, however, will result in backlash, high inertia and discontinuity in output forces (cogging), which are undesirable as they distort the reflected forces. In addition, electrical motors are not compatible to applications that have extensive magnetic interference, e.g., applications involving Magnetic Resonance Imaging (MRI) because they produce their own magnetic fields and contain ferromagnetic materials. Concerning the pneumatic actuators, their output force is a function of the compressed air pressure that allows to drive much higher force-to-weight ratios than DC motors. Thus, a pneumatic system is capable of consistently reflecting both low and high forces against the human operator's hand while avoiding the traditional DC motor actuation pitfalls. Also, air is inert to magnetic fields, which is crucial in applications such as robot-assisted surgery under MRI guidance. Besides the above benefits, the pneumatic systems also suffer from common drawbacks including friction and limited bandwidth. Moreover, from a control perspective, controlling a pneumatic actuator is a challenge because the system dynamics are highly nonlinear.

The goal of this research is to investigate the development and control of a certain class of electro-pneumatic actuators in a haptic teleoperation system. To control efficiently the input (air) flow

of the pneumatic actuator, most of pneumatic systems have utilized servovalves which allow for a continuous change of the input mass flow rate. However, servovalves are costly due to the precision machining required in their manufacturing. A low-cost alternative to a servovalve is the on/off solenoid valve, which can be as a result found promising applications. Firstly, we demonstrate that good teleoperation transparency can be achieved with the inexpensive on/off valves. Secondly, a comparison in terms of transparency and pressure dynamic behavior between the two technologies (i.e. solenoid valve and the servovalve) is carried out. Finally, we deal with the problem of bilateral teleoperation in force-sensor-less device setups by using observers for force estimations.

The outline of this thesis is described as following:

Chapter 1 gives an overview of haptics including its challenges, achievements and prospects. It consists of three principal points. The first one is dedicated to the fundamental specifications of haptic interfaces such as haptic-rendering algorithms, human-sensing capabilities, and design requirements. The second one describes a brief survey on actuator technologies as well as some concepts and examples of haptic devices which are commercially available and under current research. Application areas will be discussed in the last point, showing the wide range of technologies involved in haptics.

Chapter 2 provides an introduction of the bilateral teleoperation systems, followed by a linear modeling of different components such as human operator, environment, controllers, and master and slave robots. As a typical example for bilateral control, the four-channel architecture – a generalization of many existing approaches – is first presented. Next, performance of other control schemes, including the two-channel and three-channel architectures, is investigated. Stability and transparency are the major goals in every bilateral control design that are also briefly reviewed at the end of this chapter.

Chapter 3 describes the design of a one-degree-of-freedom (1-DOF) haptic interface used in pneumatic-actuated teleoperation system. After a description of the device performance specifications (i.e., bandwidth, life span, maximum and resolution of force and position), a detailed study on the pneumatic cylinders as well as position, pressure and force sensors is carried out. Performance and characteristics of the valve technologies (i.e., proportional servovalves and on/off solenoid valves) which play a key role in pneumatic control, is mentioned in the final of this chapter.

Chapter 4 is aimed at providing different control approaches for the pneumatic teleoperation systems with low-cost on/off valves. Firstly, the pulse width modulation (PWM) method, which is the most commonly used due to its simplicity of design, is presented for force tracking and teleoperation control problems. Secondly, the hybrid strategy is investigated in order to improve the tracking performance and reduce the chattering problem causing by high switching frequency of the PWM. These two control strategies are then implemented and tested on a four-channel master-slave experimental setup. Thirdly, our study focuses on a development of the sliding mode control that enables to perform both transparent and stability analysis for a two-channel bilateral teleoperation framework. Experimental results of different control architectures (position-error-based, force-error-based and direct-force-reflection systems) are presented and a comparison in terms of performance and stability is carried out. Finally, in order to improve the actuator dynamic performance and reduce the switching activities of the valves, we propose an enhanced control design that consists of extending the three-mode sliding control scheme into a five-mode control scheme. Frequency- and time-domain analyses of the new approach are then experimentally investigated, allowing to validate the proposed control law in a bilateral master-slave system.

Chapter 5 deals with modeling and controlling of pneumatic actuator driven by proportional servovalves. In order to implement linear controllers on a bilateral teleoperation system, a tangent linearization of the nonlinear pneumatic actuator is carried out. Stability and transparency analyses of the four-channel master-slave system are then presented. Next, we provide a performance comparison of the two valve technologies (i.e., servovalves and the solenoid valves) in the bilateral teleoperation system. Another aspect of our work is to investigate the use of observers, in place of force sensors, for

an estimation of the operator and the environment forces exerted on the master and the slave devices. Performance analysis of the observers is carried out and then validated by experiments performed on 1-DOF teleoperation system.

Finally, the results of current work and considerations for future investigation are summarized at the end of the manuscript.

Chapter 1
Haptic Systems

Table of contents

I. Introduction

Generally, the word "haptic" refers to the sense of touch, which is one of the most informative senses that human being possess. Mechanical interaction with a given environment is vital when the sense of presence is desired. The aim of haptic interfaces is to enhance the user's immersion in a virtual environment through a stimulation of the haptic sense, or allow them to interact with remote systems through a master-slave telemanipulator.

Haptic interaction essentially combines both *tactile feedback* and *kinesthetic feedback*, which differ in several aspects such as physiology, control requirements, and functionality. Tactile feedback is sensed by receptors placed close to the skin, with the highest density being found in the hand. These high-bandwidth receptors (50–350Hz) sense the first contact with the environment, its surface geometry, temperature, texture, rugosity, and slippage. Force feedback is sensed by low-bandwidth receptors (10–20Hz) placed deeper in the body, typically on muscle tendon attachments to bones and joints (Burdea & Akay 1996). These receptors provide information on the contact force, as well as grasped object compliance and weight. Concerning the functionality, namely the *ability to opposite actively the user volitional hand movement*, force feedback can stop the user's motion, whereas tactile feedback cannot (Burdea & Coiffet 2003). It therefore cannot prevent virtual or robot hands from possibility destroying remotely grasped objects.

The chapter is organized as follow. Section II gives some specifications of haptic interfaces. Section III is dedicated to the technology of haptic feedback, including different type of actuators and a number of devices which are commercially available and under current development. Some application areas will be discussed in section IV. The aim is to show the application fields where haptic feedback has been used. Concluding remarks will be provided in section V.

II. Specifications of Haptic Interface

This section describes the fundamental specifications of haptic interfaces, including basic *haptic-rendering algorithms*, some *requirements for good haptic feedback design*, and *capabilities of the human sensing system.*

II.1. Haptic rendering algorithms

To be able to feel and manipulate virtual objects through a haptic interface, there must be algorithms and computer programs capable of delivering correctly force feedback to the user. The term *haptic rendering* is used to describe these operations, in analogy with the familiar rendering of graphics on a computer display. Unlike graphical rendering which can satisfy the eye by update rates of 30 frames per second or even less, haptic rendering must be done at rates approaching a kilohertz in order to feel accurately the force feedback to the hand (Mahvash & Hayward 2005). In many cases, haptic rendering can be accompanied by simultaneous graphical rendering in what is more properly referred to a visual/haptic interface.

Typically, a haptic rendering algorithm consists of two main blocks: *collision detection* and *collision response* whose the definitions are given as follow (Salisbury et al. 2004)

- Collision detection enables to detect collisions between the haptic device and the virtual objects in order to yield information about where, when, and ideally to what extent collisions (penetrations, indentations, contact area, and so on) have occurred.
- Collision response enables to compute the interaction force between the haptic device and the virtual objects when a collision is detected. This force approximates as closely as possible the contact forces that would normally arise during contact with real objects.

The principle of the haptic rendering loop is illustrated in Fig. 1.1. When the user manipulates the haptic device, new position and orientation are acquired. The collision detection algorithm uses position information to find collisions with the virtual object and report the resulting degree of

penetration or indentation. The collision response algorithm computes interaction forces between the manipulator and the virtual object involved in collisions. These force feedbacks are then conveyed to the user through the haptic device to provide him/her with the sensation of 3D objects and their surface details.

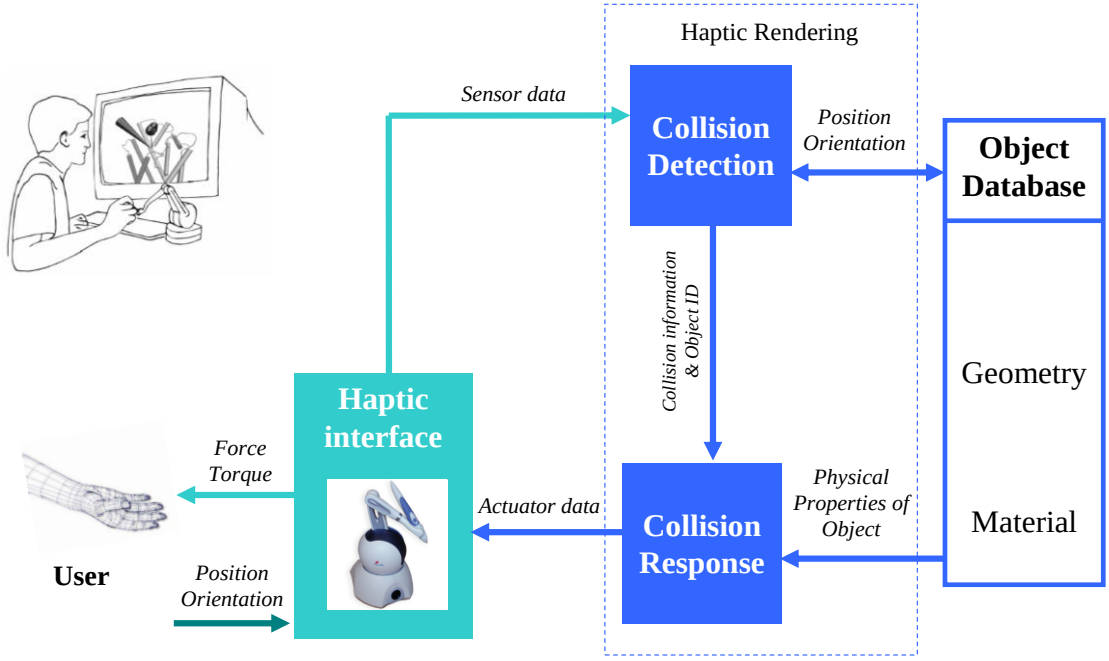

Fig. 1.1. Principle of haptic rendering

In the haptic loop algorithm, there exists a trade-off between rendering accuracy and rendering time that is severely imposed on computer resources. There are also issues of control stability. When we interact haptically with real objects, energy is almost always dissipated, but if the interaction between the haptic device and the virtual object is not correctly modeled, energy can be generated leading to vibration and sudden loss of control. Finding the best haptic rendering algorithms for a given situation continues to be an active area of research.

Another challenge of haptic research is the fidelity of the force feedback in the haptic loop. This fact depends on a number of requirements which are detailed in the following subsection.

II.2. Requirement for a good haptic feedback design

In order to produce a good haptic feedback device, several requirements need to be taken into account. It is difficult to produce a complete set accurate for all devices as the ideal requirements vary for different devices and depend on the application. Some requirements have been compiled from the following source (Massie & Salisbury 1994). A common goal as set out by (Mahvash & Hayward 2005) describes the need to allow unimpeded motion but to be able to exert high fidelity forces and torques. In other words, when the user moves through free space, nothing should be felt, and when a hard virtual surface is contacted, it should feel perfectly rigid. To do this, the device must be able to resolve extremely small changes in position and force. Also, the mechanical constraints for the device should include low inertia, backlash, weight and friction.

When using a device it is important that if the contact point of the device is not colliding with anything in the virtual world then negligible friction should be perceived. A friction level of 5% of the force range was set by (Adelstein & Rosen 1992) during their design phase. Low frictions enable the user to move the device freely when this one is not in contact. Obtaining negligible frictions can be a

problem particularly when high stiffness is required (Hayward & Armstrong 2000). In fact, high stiffness implies a stiff mechanical interface which needs to be constructed from metal. These heavy materials increase the friction as well as increasing the overall weight of the device. This provides a conflict between obtaining high stiffness while keeping low friction. When considering the construction of a force feedback device, two designs are possible, i.e. serial and parallel mechanisms. Serial mechanisms have a larger work space and are easier for control implementation. The downside is that as each section is added to the chain, the total inertia increases and the total stiffness decreases. Parallel mechanisms do not exhibit the above problem and have a much higher stiffness. The disadvantage over serial mechanisms is that the mechanism's elements can physically interfere.

Ensuring the device is statically balanced is another design consideration. This means that the centre of mass of the moving parts remains stationary regardless of movement. If this property can be achieved then there is no need for active gravity compensation and the average torque required from the actuators is zero. The materials used in such devices need to be considered. Some parts of the device will need to be strong enough to take the stress and strain applied by the user and the actuators.

Another consideration, which affects the overall weight of the device, is the type of actuators incorporated. Actuators, as will be discussed in detail in section III.1, provide the forces for the device. In most cases, a good actuator should be compact and light as well as capable of producing the necessary power to deliver the forces. There are tradeoffs between power, volume and weight since actuators capable of producing large forces are generally heavier and are larger in size than those capable of small forces. The power-to-weight ratio of the actuators used is a critical factor when considering portable devices, particularly when multiple degrees of freedom (DOF) are required. For certain devices these constraints can be relaxed. For example, on motion platforms used in flight simulators, the weight and size of the actuators are less critical since low power output is required.

Often haptic devices will be used for long periods of time and so they must be comfortable to use. The weight of a device needs to be taken into consideration. If some components are very heavy then moving them around may cause fatigue in a short space of time, particularly if the device is carried out the user. The position in which the user is expected to operate the device also needs to be considered. For small desktop devices, it is important that the hand and wrist can be positioned comfortably. Many small devices allow the wrist to be supported by the surface on which they sit, similar to operating a mouse. According to (Mahvash & Hayward 2005), a study of wrist motion was undertaken to show that a square region of 150 mm side could be utilized as the workspace area and that 50 g masses were acceptable for applications requiring approximately 30 min to complete. For larger devices, ensuring a comfortable position for operation can be more of a problem. The workspace of such systems should be sufficient and should not restrict the user in natural movement. For the motion of larger devices such as arm exoskeletons, the characteristics of the human arm need to be noted. Moreover, in order for humans to perceive forces smoothly, the device must match or exceed the human sensing resolution.

The following section will examine closely the human sense of touch since it is necessary for the haptic feedback design.

II.2.1. Human haptic perception

Human haptic perception, comprised of tactile and kinesthetic perceptions, is the process of acquiring, interpreting, selecting, and organizing haptic sensory information. *Kinesthetic perception* refers to the sense of force and motion within the muscles and tendons, whereas *tactile perception* specifically concerns the acquisition and interpretation of sensations realized through the mechanoreceptors of the skin.

Many scientists have studied human perception thresholds in order to understand the limits of our abilities. Current studies of the just-noticeable differences (JND) for kinesthetic and tactile senses have focused on discernment of geometries, textures, and volumetric properties of objects held by the human (Allin et al. 2002). The JND (also referred to as the difference limen or the differential threshold) is the smallest change in a specified modality of sensory input that is detectable by a human. The Weber fraction defined as the JND divided by stimulus intensity is a common parameter

used to evaluate the performance of the discrimination. It is usually assimilated to JND (%) in literature.

Early kinesthetic studies by (Clark & Horch 1986) investigated human perception of limb positions. The authors concluded that humans are capable to detect joint rotations of a fraction of a degree performed over a second of time interval. (Jones et al. 1992) also reported the JND for limb movement as 8 % (of stimulus intensity). Further psychophysical experiments conducted by (Tan et al. 1994a) determined the JND for the finger joints as 2.5 %, for the wrist and elbow as 2 %, and for the shoulder as 0.8 %.

II.2.2. Sensory motor control

In addition to tactile and kinesthetic sensory channels, human haptic system also includes a motor subsystem which is based on control body postures, motions as well as forces of contact with objects. In performing manual tasks of real or virtual environments, contact force is perhaps the most important variable that produces an effect both tactual sensory information and motor performance.

The key aspects of human sensory motor control are *maximum force exertion, sustained force exertion, compliance, hand mechanical impedance,* and *sensing and control bandwidth*.

II.2.2.1.Maximum force exertion

Several studies have been conducted to measure the controllable manual maximum force exertion. (An et al. 1986) found a maximum power grasping force of 400 N for males and 228 N for females. Power hand grasping force measurements are illustrated in Tab. 1.1.

	Power grasp	**Tip pinch**	**Pulp pinch**	**Key pinch**
Male	400 N	65 N	61 N	109 N
Female	228 N	45 N	43 N	76 N

TAB. 1.1. FORCE DISTRIBITION AMONG HAND PHALANGES AND GRASPS (AN ET AL. 1986)

Note that the maximum force exertion capability is dependent on the user's posture. It was found that maximum force exertion grows from the most distal joint in the palm to the most proximal one (shoulder). In order to ensure user safety, a haptic interface should never apply forces that the user can not successfully counter.

II.2.2.2.Sustained force exertion

It is important to remember that humans can exert a maximum force only for a short period of time before the onset of fatigue. Muscle fatigue in turn adversely affects both sensing and motor control, and eventually leads to discomfort and pain. Another negative effect of prolonged exertion of high forces is the shift in force perception. It is therefore necessary to determine what force can be sustained comfortably by users for long durations. This information will help to determine the forces that haptic interfaces need to produce during task simulations. Tab. 1.2 shows the sustained forces of human hand, determined by (Tan et al. 1994b).

	Wrist	**Elbow**	**Shoulder**
Male	64.3 N	98.4 N	101.5 N
Female	35.5 N	49.1 N	68.7 N

TAB. 1.2. SUSTAINED FORCES OF HUMAN HAND

Alternatively, (Wiker et al. 1989) performed a study of the relationship between fatigue during grasping as a function of force magnitude, rest duration, and progression of the task. The tests showed a direct correlation between magnitude of discomfort and magnitude of pinch force. The higher the pinch force is, the higher the discomfort is, which also increase linearly as the task progressed.

II.2.2.3.Compliance

Another variable that is important for designing the human-computer interface is the ability to judge compliance of manipulated real or virtual objects. Human perception of compliance (i.e., change in displacement divided by change in force) is presumably based on the perception of both force and displacement, since humans possesses no known special "compliance sensors" in peripheral sensory organs (Tan et al. 1995). Compliance information is critical in certain applications such as training for palpation tasks or telesurgery, since many medical procedures require accurate discrimination of tissue properties (O'Malley et al. 2006). The following discussion presents a short summary of the literature on compliance both with and without the presence of additional visual or auditory clues. If haptic interfaces are involved to be used for exploratory tasks, which require discrimination among objects based on their compliance, designers should ensure that the simulated virtual objects appear sufficiently different to the human operator.

Human perception of compliance involves both the kinesthetic and tactile channels. In fact, spatial pressure distribution within the contact region, which is sensed through the tactile receptors, plays a fundamental role in compliance perception. However, for objects with rigid surfaces, the information available through the tactile sense is limited and in this case, kinesthetic information becomes the dominant information channel. In studies involving such objects, (Jones & Hunter 1990) reported the differential thresholds for stiffness as 23 %. A comparison of compliance discrimination between objects with deformable surfaces and rigid surfaces was found in (Srinivasan & LaMotte 1995). The results showed that subjects can discriminate compliance quite well if the objects have deformable surfaces, but results were much poorer for compliant objects with rigid surfaces.

In further investigations, (Tan et al. 1995) studied compliance discrimination in the context of its dependence on mechanical work (defined as force integrated over displacement) or maximum force applied. When work or terminal force cues were available, subjects exhibited a high sensitivity to compliance (the JND or Weber fraction of 8%). However, when work and force cues were removed, the JND for compliance discrimination was 22%.

Investigating the effect of other cues on compliance perception (DiFranco et al. 1997) observed the importance of auditory cues associated with tapping harder surfaces and concluded that the objects are perceived to be stiffer when such auditory cues are present. In a similar work, (Durfee et al. 1997) investigated the influence of haptic and visual displays on the stiffness perception, while (O'Malley & Goldfarb 2004) studied the implications of surface stiffness for size identification and perceived surface hardness in haptic interfaces.

II.2.2.4.Hand mechanical impedance

The relationship between the applied force and displacement of the hand is given by its impedance. The human *arm impedance* as well as *finger impedance* plays a key role in determining in the sensitivity and stability of human-machine interface. (Yoshikawa & Ichinoo 2003) considered the finger impedance as a mass-damper-spring system. Their study was motivated by the need of better modeling the haptic interfaces which are used to provide force feedback to the fingers. Over all subjects and forces, they estimated the equivalent mass to vary from 3.5 to 8.7 g, the equivalent damping from 4.02 to 7.4 Ns/m, and stiffness from 255 to 1255 N/m. It was noted that the damping and stiffness increased linearly with the applied force.

Concerning the human arm impedance, several general models have been found from literature as shown in Tab. 1.3. As it can be seen, the mass, damping and stiffness parameters differ greatly in magnitude because they depend on the task at hand. For example, when performing a very sensitive microsurgery task, surgeons are accustomed to hold the instrument firmly. Finding a general human

model or even a suitable model for a specific application seems to be difficult. In many cases, only a lower and upper bound, together with a nominal impedance model are considered (see Tab. 1.3).

	Mass (kg)	Damping (Ns/m)	Stiffness (N/m)
(Lawrence 1993)	17.51	175.12	175.12
(Kazerooni et al. 1993)	4.54	6.83	12.5
(Yokokohji & Yoshikawa 1994)	2.0	2.0	10.0
(Daniel & McAree 1998)	1.0	12.6	39.5
(Hogan 1989)	0.8	5.5	568.0
(Lee & Lee 1993)	0.15	0.5	7.0
(Salcudean et al. 2000)	0.5	70	2000
Lower bound	0.12	0.42	4.59
Upper bound	25	501	2500
Nominal	1.44	15.98	68.22

TAB. 1.3. VALUE USED FOR HUMAN ARM IMPEDANCE MODEL (KLOMP 2006)

II.2.2.5.Sensing and control bandwidth

Sensing bandwidth refers to the frequency with which tactile and kinesthetic stimuli are received by human sensors. On the other hand, *control bandwidth* refers to the frequencies at which the human can respond and voluntarily initiate motion of their limbs. In humans, the input (or sensing) bandwidth is much larger than the output (or control) bandwidth. We sense tactile and kinesthetic stimuli much faster than we can respond to them (Burdea & Akay 1996).

In a review paper, (Shimoga 1992) showed that the output loop, which represents the ability of the hand and fingers to exert force, has a 5 to 10 Hz bandwidth. By comparison, the kinesthetic sensing has a bandwidth of 20 to 30 Hz, and tactile sensing has a 0 to 400 Hz bandwidth. Very fine feature recognition, such as surface textures with small rugosities, requires a much higher bandwidth (up to 5000 to 10000 Hz). Tab. 1.4 summarizes the sensing-and-control bandwidth characteristics of the human finger (Shimoga 1993a, Shimoga 1993b).

Bandwidth range	Descriptions
5000–10000 Hz	The bandwidth over which the human finger needs to sense vibration during skilful manipulative tasks
320Hz	The bandwidth beyond which the human fingers cannot discriminate two consecutive force input signals
20–30 Hz	The minimum bandwidth with which the human finger requires the force input signals to be present for meaningful perception
12–16 Hz	The bandwidth beyond which the human finger cannot correct their grasping force if the grasped object slips
8–12 Hz	The bandwidth beyond which the human finger cannot correct for its positional disturbance
5–10 Hz	The maximum bandwidth with which the human finger can apply force and motion commands comfortably
1–2 Hz	The maximum bandwidth with which the human finger can react to unexpected force/position signals

TAB. 1.4. HUMAN SENSING AND CONTROL BANDWIDTH

Finally, it is critical to ensure that the level of haptic feedback is sufficient for task completion while being comfortable for the user. For example, when we design an application that needs repetitive force exerted by the user, the required rate should not be more than 5 to 10 times a second (Brooks 2002).

III. Technology of Haptic System

Haptics research grew rapidly in the 1990's as researchers and corporations discovered more uses for force feedback technology. A number of application areas of haptic feedback are under exploration, some of them have been recently available commercially in a wide range of designs and sizes. The commercialization of haptic devices is due primarily to technological advances that have reduced the cost of necessary components, including *sensing*, *computer control platforms*, and *actuation*.

The key requirement of sensors for haptic applications is high resolution, and many solutions such as optical encoders and non-contact potentiometers are providing increased resolution without compromising the back-drivability of haptic devices due to their non-contact nature.

Another set of technological advances is in the area of computational platforms. First, data acquisition systems, which enable transformation from analog and digital signals to the sensors and actuators for the digital computation carried out by the control computer, are achieving higher and higher resolutions. Second, real-time computation platforms and increasing processor speeds allow haptic displays (typically rendered at a rate of 1000 Hz) to exhibit increasingly greater complexity in terms of computation and model realism. This, in turn, broadens the range of applications for which haptic feedback implementation is now feasible. Finally, embedded processors and embedded computing allows haptic devices to be more portable.

Improved actuator technology is a crucial criterion to increase the availability of high-quality haptic interface hardware. The novel actuators, such as piezoelectric, electro-active polymers, etc., enable the design and fabrication of small size and light-weight kinematic mechanisms that are well suited to the portable force feedback devices. The classical actuators, such as electrical motors, hydraulic and pneumatic cylinders, are used in almost all present haptic interfaces thanks to their well-known characteristics and controlling. Nonetheless, it should be noted that these actuation technologies are still a key limitation in haptic device design (i.e., heavy, cumbersome, etc.).

In order to justify the choice of driven actuation for our further development, this section provides an overview of the different actuator technologies. Concerning the sensors and the computer control platforms, they will be detailed in chapter 3 (section IV) and chapter 4 (section IV.1.4.1), respectively. Some concepts and example of haptic devices that consist of both non-portable and portable feedback systems are reported in the final of this section.

III.1. Actuation

Haptic interfaces incorporate actuators that are used to return force or tactile sensations to the user. Without actuators, the interface can only function as an input device to the computer. In this case, the haptic feedback loop is broken, and the simulation realism is degraded. Therefore, actuator plays an important role in providing good performance to haptic devices.

Ideally, the haptic interface should be transparent, which means that no force should be exerted on the user's hand (or other parts of the body) when no physical interactions exist in the virtual reality simulation. In this case, the actuators could be able to follow the user's hand motion rapidly, and without opposition, a quality called *back-drivability*. Also, the user should not feel any friction forces present in the actuator and gears or transmissions incorporated in the interface. Therefore, back-drivability requires *minimal static friction* and *low actuator inertia*. An additional negative effect of friction is the possible masking of small feedback forces, calculated by the computer but never felt by the user. The ratio of maximum actuator output versus its friction defines its dynamic range. High simulation fidelity requires actuators with *high dynamics range* and *high bandwidth*.

Finally, haptic feedback actuators are placed in close proximity to the user, therefore their *intrinsic safety* becomes a concern. High pressure fluids, high voltages, or high currents could be dangerous for the user during the operation. Additional harm to the user can come from excessive noise, thus noisy actuators should also be avoided.

In this subsection, we provide the various classical actuators technologies used today (e.g., electrical motors, hydraulic, and pneumatic cylinders) as well as several novel actuators which show interesting properties for use in tomorrow's haptic interfaces (e.g., shape memory alloys, electro/magneto-rheological fluids, piezoelectric actuators, and electro-active polymers). Depending on the characteristics and application requirements, some actuators can be employed in a master device, the other can be integrated into a slave one. Furthermore, certain of them may be suitable for a development of both master and slave interfaces. In the following, actuator technologies will be presented for the applications of master and/or slave systems. A comparison between the different haptic actuation technologies will be conducted at the end of the subsection.

III.1.1. Classical actuators

III.1.1.1. Electrical actuators

By far, the haptic actuators most used today are electrical direct-current (DC) motors (see Fig. 1.2). They are easy to install (no complex piping, wiring, or pump room needed), clean (no leaks), quiet (no noise generating oscillations), and easy to control. It has been known that all the DC motors are active elements that apply power to the user. There is, however, a second class of passive electrical actuators that can absorb, or dissipate the power generated by the user during the operation. These are magnetic particle brakes (MPB) actuators which have been recently used in some haptic devices for the development of a safe and passive system (Conti et al. 2007).

(a) 3DOF Phantom Omni (SensAble[1])

(b) 6DOF Delta (ForceDimension[2])

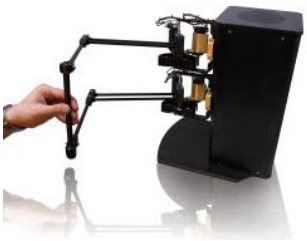

(c) 5DOF haptic Wand (Quanser[3])

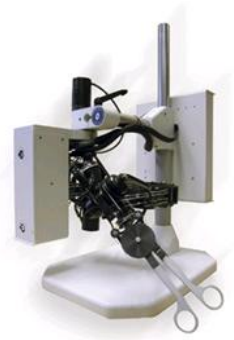

(d) 7DOF Freedom 7S (MPB[4])

(e) 6DOF Cyberforce (Immersion[5])

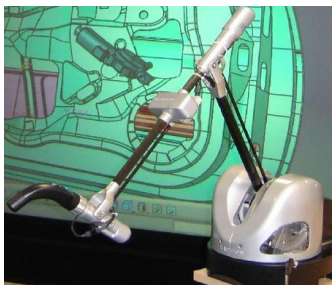

(f) 6DOF Virtuose (Haption[6])

Fig. 1.2. Commercialized haptic devices based on electrical motors

[1] http://www.sensable.com/products-haptic-devices.htm (last visit on 16 June 2011)
[2] www.sensable.com (last visit on 16 June 2011)
[3] http://www.quanser.com/net/industrial/Systems_and_Products/Sys_5Dof_Haptic.aspx (last visit on 16 June 2011)
[4] http://www.mpb-technologies.ca/mpbt/mpbt_web_2009/_en/7dof/index.html (last visit on 16 June 2011)
[5] http://www.immersion.com/ (last visit on 16 June 2011)
[6] http://www.haption.com/site/eng/index.html (last visit on 16 June 2011)

III.1.1.2. Pneumatic actuators

The second class of actuators discussed in this section is pneumatic actuators. Their force output is a function of the compressed air pressure used to transfer energy from the power source (i.e., compressor) to the haptic interface. Typically, air is compressed at low pressure (maximum of 700 kPa), resulting in a smaller force/torque exertion capability than with hydraulic actuators (addressed in subsection III.1.1.3). The advantages of pneumatic actuator can be cited as follow:

- Since their supply pressures are significantly lower, the pneumatic actuators have a lighter construction with respect to the hydraulic ones.
- The manufacturing process of pneumatics is simpler and much cheaper than hydraulics.
- Air is inflammable, cheap, and clean.
- In pneumatics, unlike hydraulics, there is no return piping to the compressor, because air is exhausted at the control valve.
- Compared to the electrical motors, pneumatic actuators have higher mass-to-force ratio and can generate larger force without any reduction mechanism. This leads to high power-to-weigh ratios that are superior to those of electrical motors.

Despite of all the above advantages, pneumatic actuators have their drawbacks. Air is compressible, therefore, the bandwidth is lower than those of hydraulic actuators. Static friction is important since air is not self-lubrication. Large friction forces can mask small feedback forces produced during interaction with soft virtual objects.

There exist two main types of pneumatic actuator, i.e. cylinders and pneumatic artificial muscles.

Air cylinders are available in a variety of sizes and can typically range from 2.5 mm diameter, which might be used for picking up a small object (e.g., transistor or other electronic components), to 400 mm diameter, which would impart enough force to lift a car, for example. However, some pneumatic cylinders reach 1000 mm of diameter, and may be used in place of hydraulic cylinders for special circumstances where leaking hydraulic oil could impose an extreme hazard.

Pneumatic artificial muscles (PAMs) are extremely lightweight actuators and have much higher power-to-weight ratios (1000–1500 W/kg) than the cylinders (100–300 W/kg). Among different types of PAMs, braided muscles (or McKibben muscles), introduced by McKibben as an orthotic actuator in the late 1950's, are the most commonly used today because of their simple design and assembly. In spite of their widespread use, the braided muscles present several drawbacks. Firstly, due to dry friction between the braid and the tube, substantial hysteresis of the tension-length relationship occurs, as determined by (Tondu et al. 1995). This leads to a complex actuator models of the controlled system. Secondly, the dynamic behavior of the McKibben muscles is extremely slow (about 0.3Hz against 1–15Hz in the cylinder case) due to a compression time of more than 20s and a return-relaxation time of about 10s. Thirdly, deformation of the rubber tube requires additional energy consumption and therefore, applied pressure has to exceed a threshold value to start the expansion of the tube. This value depends on the toughness of the rubber (e.g., 100 kPa for typical McKibben muscles). A fourth weak point is related to the failure of "membrane material" (or rubber) that can reduce the actuators lifetime. In addition to the above drawbacks, the displacement capability of braided muscles is rather limited. Total displacement, which is usually expressed as a percentage with regard to a reference length (at rest), ranges between 20% to 30% (Chou & Hannaford 2002).

Recently, a variant of the McKibben muscles was designed and commercialized by Festo[1]. They are mainly used by several research groups for anthropomorphic design, prostheses and orthotics. Fig. 1.3 shows a Blackfingers[2] and a Softech[3] humanoid robot, actuated by the McKibben muscles.

[1] http://www.festo.com/net/startpage/ (last visit on 16 June 2011)
[2] http://home.dei.polimi.it/gini/Humanoid.htm (last visit on 16 June 2011)
[3] http://www.softmech.net/index-eng.html (last visit on 16 June 2011)

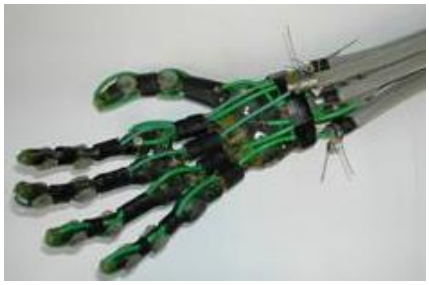

(a) Blackfingers actuated by McKibben muscles

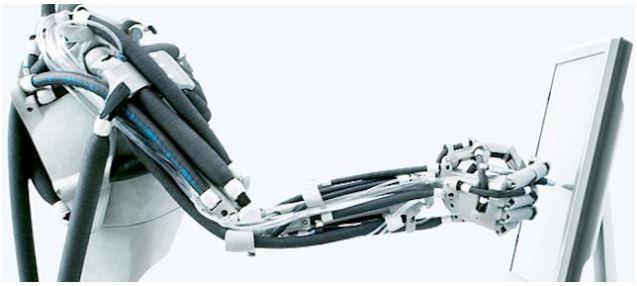

(b) Softech humanoid robot with Festo muscles

Fig. 1.3. Example of PAM prototypes

To resume, Tab. 1.5 shows a comparison between pneumatic cylinders and pneumatic artificial muscles.

Technologies	Advantages	Disadvantages
Cylinders	Large range of displacement No fatigue of material → long lifetime	High static friction More cumbersome and heavier than PAMs → limit design and architecture
Artificial Muscles	High power-to-mass ratio Light weight Flexible → similar to human muscle	Very slow dynamics Non-negligible hysteresis Limited displacement Rubber's fatigue failure Complex actuator models and control

TAB. 1.5. COMPARISON OF TWO PNEUMATIC ACTUATORS

III.1.1.3. Hydraulic actuators

Hydraulic actuators exhibit a superior bandwidth over pneumatic actuators. This is due to the incompressibility of the hydraulic fluid (oil) transmitting energy from the pump to the feedback interface. Additionally, the large oil pressure (10 to 20 MPa) involves in a very large force/torque exertion capability. The actuators designed to withstand such pressures are necessarily heavier, but their resulting power-to-weigh ratio is very high (300–700 W/kg). Another advantage of hydraulic systems is their high stiffness because of incompressible oil. Furthermore, oil is self-lubrication (unlike pneumatic systems), so that friction does not pose a problem.

The drawbacks of hydraulic actuation come at a price. First, using high-pressure oil requires a complex hydraulic system to pressurize, transmit, and regulate oil flow. Secondly, large valve pressure losses involve low energy efficient and systems that are costly to produce and operate. Finally, despite of careful fitting and piping design, oil leaks do occur. In the best case, the leaks result only in the contamination of the simulation site. This possibility makes hydraulic haptic interfaces unusable in clean environment (such as hospital operating room). In the worst case, high-pressure oil leaks are a safety hazard. Indeed, according to (Stadler 1995), oil can quickly soil a large area, and the nearly invisible high-pressure stream can damage equipment and injure the human operators. Also, oil is flammable, which requires extreme caution to maintain proper operating temperatures, whereas pneumatic systems are relatively indifferent to temperature changes.

One of the first applications of hydraulic force feedback systems in the hazardous/hostile environments are proposed by (Ostoja-Starzewski & Skibniewski 1989). These authors have shown that thanks to force feedback, enhancements in tracking performance and operator's perception could be achieved by such an interface.

Recently, Computational Neuroscience Laboratory[1] develops a SARCOS teleoperation system, which is designed to emulate the human arm (see Fig. 1.4). The system consists of 10-DOF for each robotic manipulator (i.e., master and slave) where 7-DOF in the arm, and three additional DOF in the finger. The system is used for manipulation experiments and real-time learning of motor skills.

(a) Hydraulic slave arm (b) Hydraulic master arm

Fig. 1.4. SARCOS telemanipulator (ATR Computational Neuroscience Labs, Japan)

Another example of the telemanipulation using hydraulic actuators is a MAESTRO robot (Modular Arm and Efficient System for Telerobotics), developed by CEA[2] (Commissariat à l'énergie atomique et aux énergies alternatives), in collaboration with CYBERNETIX[3] company (specialized in robotics and automation for interventions in hostile environments) and IFREMER[4] (French Research Institute for Exploitation of the Sea). As it can be seen in Fig. 1.5, this manipulator is a serial robot composed of six links and six hydraulic rotational joints (rotary jack fed by flow control servovalve). The MAESTRO is used when human intervention is not possible such as operation in nuclear or offshore hostile environments. Thanks to the dexterity, accuracy and strength of the hydraulic technology, this powerful remote handling robot can be dedicated to many tasks like inspection, maintenance, dismantling, and cleaning, etc.

Fig. 1.5. MAESTRO robot (CEA, France)

[1] http://www.cns.atr.jp/(last visit on 16 June 2011)
[2] http://www.cea.fr/(last visit on 16 June 2011)
[3] http://www.cybernetix.fr/(last visit on 16 June 2011)
[4] http://wwz.ifremer.fr/(last visit on 16 June 2011)

III.1.2. Novel actuators for haptic devices

The design of dextrous force-reflecting hand master, in particular the portable haptic devices (will be introduced in section III.2.2), presents daunting challenges. Power densities require from the actuators in such systems are not attainable with the classical technology, and may be impossible without significant innovations. Therefore, researches are currently investigating a number of novel technologies including piezoelectric actuators, shape memory alloys, electro- and magneto rheological fluids, electro-active polymer, etc. These actuators are developed based on *smart materials* which can be significantly changed in a controlled fashion by external stimuli, such as stress, strain, temperature, moisture, pH, electric or magnetic fields (Smith 2005). However, most of the developments on such actuators still stay within laboratory and only few of them are commercially available.

In the following subsections, some of the novel actuators as well as their potential use in the field of haptic feedback will shortly be introduced.

III.1.2.1. Piezoelectric actuators

Piezoelectric actuators have some properties that can be very interesting for feedback of tactile information. By applying a high voltage, the crystals change their shape. Accompanied by huge forces, translation can be achieved this way. Their disadvantages for haptic feedback applications are the tiny translations of a few μm. On the other hand, vibration around 1kHz (beyond the sensible frequency of the human) can be achieved without any problems. Tactile feedback is feasible (Caldwell & Gosney 2002), thus simulations of different textures are possible.

III.1.2.2. Shape Memory Alloys

Shape memory alloys (SMAs) belong to the group of metallic materials that demonstrate the ability to return to some previously defined shape when subjected to the appropriated thermal constraint. When SMAs encounter resistances during this transformation, they can generate large forces, which would be of great advantage for force feedback devices. The most two common SMAs available on the market are the NiTi or the copper-based alloys. A wide variety of applications can be found in free or constrained recovery, proportional control, super elastic applications (Auricchio et al. 1997). SMA actuators can produce much more useful work per unit volume than most actuating mechanisms. However, we must take into account the forces, displacements, temperature conditions, and circle rates required by a particular actuator. Unfortunately their long relaxation time (from seconds to minutes) makes them useless for most haptic feedback tasks.

III.1.2.3. Electro-rheological fluids

Electro-rheological fluids (ERFs) are materials that respond to an applied electric field with a change in viscosity behavior (Tao & Roy 1994). Typically, this change is manifested by the development of a yield stress that increases with applied field. Just as quickly, the fluid can be returned to its liquid state by the removal of the field. It was demonstrated in (Han & Choi 2006) that the electro-rheological actuators could be used for haptic feedback devices. Also, they can achieve high frequencies around 1kHz and high shear stress around 2-4kPa. However, high voltage is needed (around 2-4kV per millimeter gap between the electrodes) with the consequence that safety aspects have seriously to be taken into consideration. There exist other disadvantages, such as sedimentation (i.e., inhomogeneity) for instance, which can change properties of fluid and therefore resulting in degraded electric-mechanic power converter of the actuators.

III.1.2.4. Magneto-rheological fluids

Magneto-rheological fluids (MRFs) show the same effect in a magnetic field, as the ERF do in the electric field. A change of viscosity is observed while the field is on. MRFs have much higher

shear stress (around 60-120kPa) than ERFs. The possibility of using MRF actuators in haptic interfaces is exploited by (Winter & Bouzit 2007). Although these actuators have been studied and developed in the laboratories, they are limited in commercial feasibility due to their disadvantages of being costly (high-quality fluids), cumbersome, and heavy (presence of iron particles).

III.1.2.5. Electro-active polymers

Electro-active polymers (EAPs) exhibit a significant shape or size change in response to an electrical stimulation. In the last decades, they have received more and more attention by haptic designers due to their flexibility, light weight, highly dynamics, damage tolerant, and low power consumption. These attractive characteristics present great potentials for micro electromechanical systems (Liu & Bar-Cohen 1999), bionic robots (Staab et al. 2007) and biologically inspired technology (Bar-Cohen & Breazeal 2003). However, the disadvantages of the EAPs cannot be ignored, such as the required high voltages or the non-ideal polymers for instance. The important characteristics of latter have still to be completely understood. In addition, the manufacturing process is still very complicated and far away to be suited for mass production. Consequently, these polymers themselves are difficult to find and just a few of them are available on the market.

III.1.3. Comparison of the different technologies

In order to justify the choice of the actuator for our further development, Tab. 1.6 summarizes some advantages as well as drawbacks of the classical and the novel technologies.

The novel actuators have a potential in terms of superior bandwidth, compactness, mass, and power consumption over the conventional actuators. Applications of these actuators include tactile/force feedback in virtual reality, artificial muscles, synthetic limbs and prostheses in medicine, miniature robotic arms, miniature insect-like robots, and ink-jet printers in process techniques. Although the novel technologies are rightly seen as having many potential applications, most of their developments stay within laboratory and only few of them are commercially available. Promising applications do exist, as mentioned, but will grow slowly until several problems such as poor knowledge of material characteristics, complicated manufacturing process, and cost are overcome. Due to these reasons, the novel actuator will not be chosen for the development of our device.

Concerning the classical actuators, electrical DC motors are currently the choice of most applications as they are simple and capable of providing high bandwidth at relatively low cost and maintenance. The drawbacks are that they exhibit some level of torque ripple and tend to be heavy. Transmission mechanisms are often used to overcome the weigh problem but they always introduce some friction and backlash that degrade performance. In addition, electrical motors are not compatible to applications involving Magnetic Resonance Imaging (MRI). Indeed, any ferromagnetic materials in electric motors will generate noises that make difficult to scan highly-precise MR images. Moreover, no ferromagnetic material is allowed inside the scanner (Oura et al. 2006). This represents a severe design limitation for surgical robots that have to work under MRI guidance.

On the other hand, hydraulic/ pneumatic actuators lead to higher force-to-weigh ratios than DC motors. Moreover, they are inert to magnetic fields and thus completely MRI-compatible (Yu et al. 2008). Finally, these actuators can give an easier way to deal with the design and control of the mechanical compliance, that allow to ensure human safety when interacting with robots.

Although the pneumatic actuators are limited by low bandwidth and high friction, they lead to a smaller, cleaner, safer and cheaper haptic device than the hydraulic ones. Thus, this kind of actuators are considered to be the best suited for our future development, where the dynamics required by the system is slow enough.

In this section, we reviewed various actuator technologies could be used in present haptic interfaces. These actuators based on specific performance criteria (such as power-to-weight ratio, bandwidth, cost, etc…) which are crucial for haptic interface design. This discussion allows to justify the choice of actuator technology (i.e., pneumatic) for our device and also to provide the necessary foundation for the next section describing actuator integration in various haptic feedback systems.

Technologies	Advantages	Disadvantages
Electric	Simple energy transmission from power supply to device (flexible wires) Easy to control and high bandwidth Clean and quiet Low cost	Low force-to-weight ratio High inertia Backlash → distortion force/torque Over-heating with heavy load Not compatible in MRI environment
Pneumatic	Lightweight, small size, high mass-to-weight ratio Compliance No return lines required for exhausted fluid Clean system, non-flammable fluid, inert to magnetic fields → MRI application	Low bandwidth High stiction friction Highly nonlinear properties (compressibility of air, friction effect, dynamics of valve) Leakage
Hydraulic	Very high power-to-weigh ratio Compliance High bandwidth Self-lubricating → low friction	Viscosity of oil changes with temperature High-pressure oil leaks are unsafe Flammable oil Costly to produce and maintain Leakage
Piezoelectric	Small size High bandwidth, high frequencies Low actuation power Wide range of operating temperature	Limited strains and low tensile strength Fragile materials High driving voltage
SMAs	Large active stresses High energy density High material strength and high elasticity	Low bandwidth Low efficiency High hysteresis (long relaxation time) Problem in fatigue failure
ERFs	High dynamics Wide range of operating temperature	Limited shear stress Sedimentation problem
MRFs	High shear stress Low voltage power	Costly (high-quality fluids) Heavy (high loading of dense iron)
EAPs	Large active strains High energy density Small size and intrinsic softness → MEMs and nanostructure applications High bandwidth	Moderate active stresses Limited temperature range Complicated manufacturing process High driving voltage

TAB. 1.6. ACTUATOR COMPARISON

III.2. Concepts and examples of haptic devices

After having reviewed the underlying actuator technology, in the following subsections, we take a closer look at two main categories of haptic force feedback, i.e. non-portable and portable interfaces. Some examples presented have been chosen to show essential features of their respective categories. Also, they demonstrate the wide range of technologies involved in haptics.

III.2.1. Non-portable force feedback

III.2.1.1. Joystick

Joysticks are widely used as simple input devices for computer graphics, industrial control, and entertainment. Most general-purpose joysticks have two DOF with a handle that the user can operate.

As illustrated in Fig. 1.6, the handle is supported at one end by a spherical joint and at the other by two sliding contacts (Adelstein & Rosen 1992).

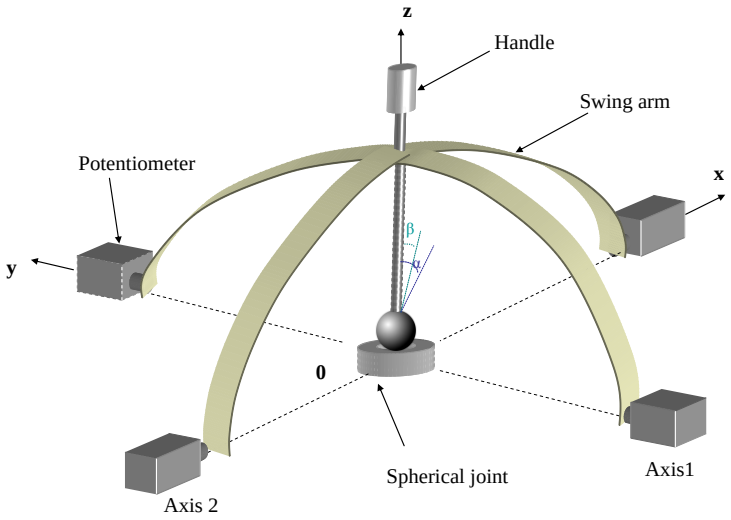

Fig. 1.6. Two-DOF slotted swing arm joystick.

Haptic joysticks vary both in mechanical design and actuation mechanisms. *Spherical joysticks*, as the name implies, have a sphere-shaped workspace. They present the particularity of having a fixed center point that can be chosen at the center of the user hand, thus, eliminating the need for arm motion. Such a device has been successfully tested at Laval University, Canada (Birglen et al. 2002) (Fig. 1.7).

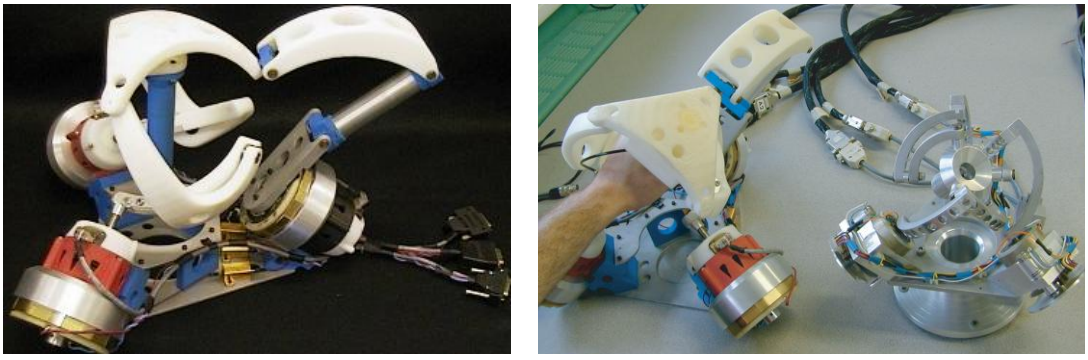

Fig. 1.7. Spherical 3-DOF haptic device (SHaDe)

The Cartesian joysticks differ from spherical ones in that they have two or three orthogonal axes that allow the entire base of the handle to translate. This leads to a larger work volume and increase mobility for the user. An example is the six-DOF Cartesian joystick comprised of a moving platform sliding using guiding blocks and rails developed by Afma Robotics[1], France (Fig. 1.8). This device has a square-shaped planar workspace, and is equipped with a pneumatic prehensor mounted on the end-effector.

While the spherical joysticks can be used with just wrist movements, the Cartesian joysticks require the user to employ other joints of the arm, like the elbow or the shoulder. Consequently, the workspace and force output of Cartesian joysticks can be greater than that of similarly sized spherical models.

[1] http://www.masterseek.fr/afma-robotics_profile_54039.htm (last visit on 16 June 2011)

Fig. 1.8. Cartesian 6-DOF haptic device[1] (Afma Robotics Company, France)

Another possible design involves *Stewart platform joysticks*. This prototype, developed by (Stewart 1965), was used as a motion platform for flight simulations. It consists of a fixed base and a mobile platform interconnected by six actuators that are kinematically in parallel. The high force output and great rigidity of Stewart platforms has attracted the attention of numerous designers in haptics. Fig. 1.9 (a) shows an example of such a device using pneumatic actuators for palpation test (Takaiwa & Noritsugu 2003). Another Steward platform type with electrical motor is the 6-DOF Haptic Master illustrates in Fig. 1.9 (b). This device, produced recently by Nissho Electronics Co. of Japan[2], is based on the earlier prototype developed by (Iwata 1990) at the university of Tsukuba.

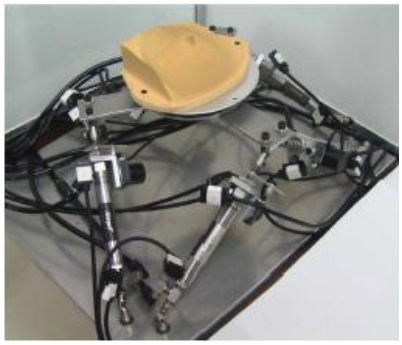

(a) Pneumatic actuator technology

(b) Electrical actuator technology

Fig. 1.9. Examples of Steward platform joysticks

The last type of force feedback joystick to be discussed here is the magnetically levitated device developed by (Salcudean & Vlaar 1997). Whereas all previously mentioned joysticks had some static friction, the magnetically levitated prototype has no friction at all and is particularly suited for display of small force and stiff contact. A drawback of this technique is that the range of motion is limited by the distance between the joystick handle (or flotor) and stator. Indeed, a small distance permits to capture the magnetic fields effectively. Fig. 1.10 shows the magnetically levitated device developed by Mellon University, USA.

[1] http://www.irisa.fr/lagadic/material/material-eng.html (last visit on 16 June 2011)

[2] http://www.nissho-ele.co.jp/ (last visit on 16 June 2011)

Fig. 1.10. Magnetically levitated device (Carnegie Mellon University)

III.2.1.2. Pen-based master

Pen-based haptic devices allow interaction with the virtual environment through tools such as a pen (or pointer) or scalpel (in surgical simulations). These devices are compact with a workspace larger than that of spherical and magnetically levitated joysticks and have three to six DOF. The best-known example of a pen-based haptic interface is the Phatom commercialized by SenAble (Fig. 1.11).

Originally developed by (Massie & Salisbury 1994), the Phantom is an electrically actuated serial-feedback robotic arm that ends with a finger gimbal support and thus can be replaced with a stylus. The gimbal orientation is passive and the serial arm applies translational forces to the operator's fingertip. A six-DOF interface in (Iwata 1993) allows to apply both forces and torques to the operator's hand. The system replaces the single serial arm of the Phantom with two 3- DOF arms connected to a stylus. This results in more complex interactions between the human operator and the remote/virtual environment.

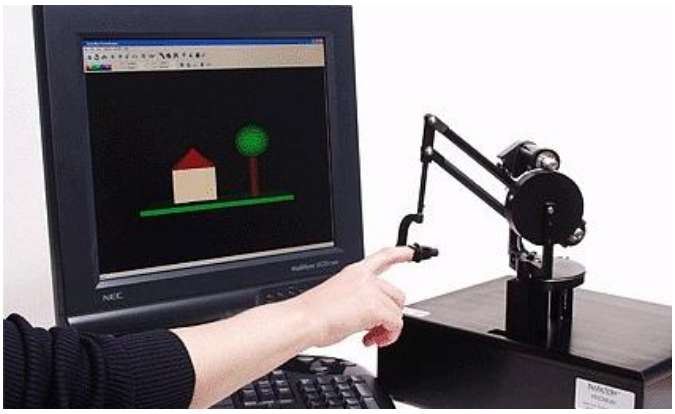

Fig. 1.11. The Phantom Premium device (SensAble)

III.2.1.3. Stringed haptic interface

Most haptic interfaces are composed of rigid links which are simply too heavy (requirement of gravity compensation), strong, expensive, and not dexterous enough to achieve widespread application. Due to these limitations, researchers have looked to other methods of providing force feedback to the user. A solution that has gained prominence involves using *stringed haptic interfaces* (Williams II 1998). In such a device, actuators are placed remotely from the hand, being attached to a cube supporting structure. The system has therefore very low weight, small inertia and substantially

larger work space than the joysticks. However a major drawback of stringed haptic interfaces is their unidirectional (tensile) force exertion capability. To be able to exert three-dimensional forces/torques, it is necessary to use a large number of strings and actuators.

One of the early stringed haptic interfaces is the Texas 9-string developed by (Lindemann & Tesar 1989). It is originally designed as a generalized master for space telerobotics applications. As shown in Fig. 1.12, this six-DOF device has nine strings and three pneumatic cylinders supporting a T-shaped handle in the middle of a cubic enclosure. The large dimension of air cylinders results in large spherical workspace and large haptic forces to the user. However, it was reported that due to the design's numerous strings and low bandwidth, performance is seriously hindered by string interference and delayed response.

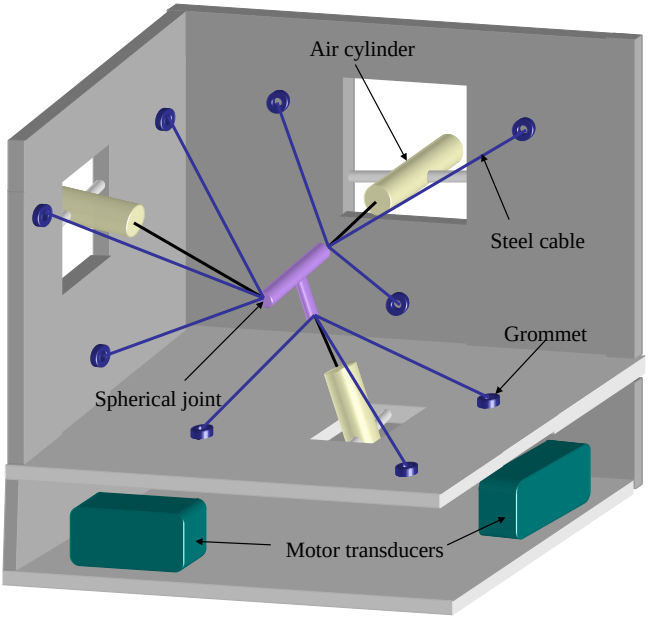

Fig. 1.12. The Texas 9-string force display

Another stringed haptic interface is the SPIDAR (Space Interface Device for Artifitial Reality) developed by (Ishii & Sato 1994) at Tokyo Institute of Technology, Japan. Compared to the Texas 9-string interface, the SPIDAR system has a simpler and more compact to design. The initial prototype shown in Fig. 1.13 (a) has four strings attached to a cap worn on the user's finger. Subsequently, the SPIDAR systems was modified to allow feedback to both thumb and pointer fingers as shown in Fig. 1.13 (b). With both fingers requiring four strings, the system now has eight strings. Occasional kinematic interference is reported by the researchers for extreme abduction/adduction angles. The SPIDAR II system makes possible the simulation of grasping forces and of the virtual object weight. The workspace is now a sphere of 30 cm diameter and virtual object such as 5 cm cubes are comfortable grasped.

The last version of SPIDAR system is two-handed with multi-fingers, namely SPIDAR-8 (Walairacht et al. 2002). This new system allows a user to use thumb, index, middle, and ring fingers on both left and right hands to manipulate virtual objects in the simulated virtual world (Fig. 1.14 (a)). The user can perform the cooperative work using both hands and perceive force feedback at eight fingertips while manipulating the virtual objects. As application illustrated in Fig. 1.14 (b), the simulation of the Virtual Rubik's Cube game was implemented and obviously showed the abilities of the system.

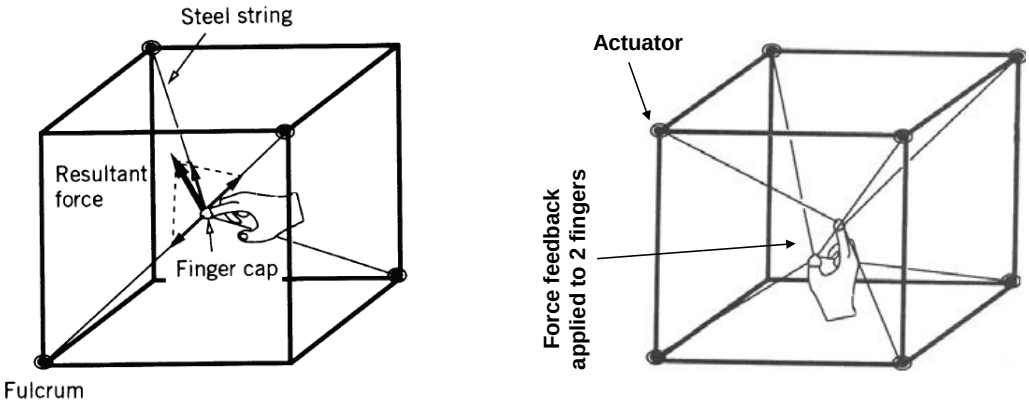

(a) SPIDAR I (b) SPIDAR II

Fig. 1.13. The two earliest versions of SPIDAR system

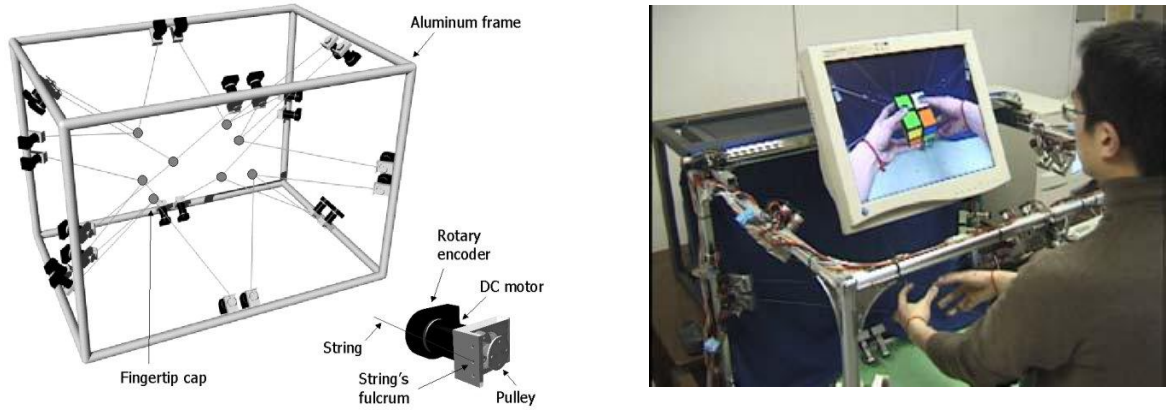

(a) SPIDAR-8 (b) Virtual Rubik's cube

Fig. 1.14. The last version of SPIDAR system

III.2.1.4. Floor- and ceiling-grounded interfaces

Generally, floor- and ceiling-grounded interfaces are larger, more complex and more expensive than desktop devices. Owing to their large force output, and as a result, user safety becomes critical. This is especially true for exoskeletons where the operator is inside the device workspace at all times. High cost and increased user safety concerns account for use of such systems outside research laboratories.

Fig. 1.15 (a) shows one of the first generalized master arms that is developed by Jet Propulsion Laboratory (JPL[1]) of National Aeronautical and Space Administration (NASA[2]), USA. It is a six-DOF interface with a three-axis hand grip that slides and rotates about a fixed support attached to the floor. The JPL device is another example of a point contact haptic interface where the forces are applied at the user's hands. As compared to joysticks or desktop devices though, it provides a much larger work volume with greater force output capabilities, coupled with greater freedom of arm movement. These larger devices are useful for remotely manipulating large robotic manipulators like those used in space (Bejczy & Salisbury 1980).

An example of a grounded exoskeleton haptic interface is the MAHI arm exoskeleton (Fig. 1.15 (b)) built at Rice University, USA (Sledd & O'Malley 2006). This five-DOF exoskeleton is designed

[1] http://www.jpl.nasa.gov/ (last visit on 16 June 2011)

[2] http://www.nasa.gov/ (last visit on 16 June 2011)

primarily for rehabilitation and training in virtual environments. The device encompasses most of the human arm workspace and can independently apply forces to the elbow, forearm, or wrist joints. This feature makes it extremely suitable as a rehabilitation interface that allows the therapist to focus treatment on isolated joints.

(a) Six-DOF JPL arm master.

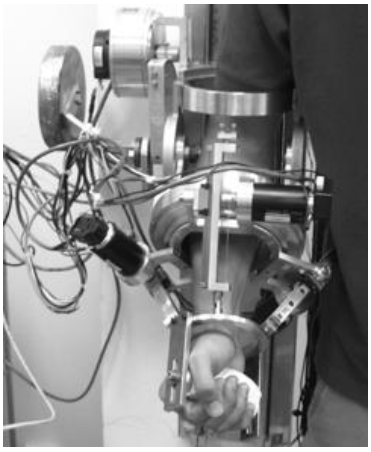

(b) MAHI haptic arm exoskeleton

Fig. 1.15. Examples of the floor- and ceiling-grounded interfaces

III.2.2. Portable force feedback

The previous section described non-portable force-feedback interfaces that are mechanically grounded to a desk, ceiling, or floor. The advantage of such devices lies in their ability off-load the actuator from the user. The drawback is a reduction in the user's freedom of motion, and thus in the simulation naturalness. Therefore, it is necessary to use portable force-feedback interfaces where their actuating or sensing is grounded on the user's body (either on the back, chest, arm or palm). Such portable masters are more difficult to design due to the limitations in overall weight and volume to avoid user fatigue during prolonged simulation. Indeed, this implies high power-to-weight and power-to-volume ratios for the actuating system. Although several non-portable force-feedback interfaces are commercially available, most portable systems are under active research, reflecting the state of transition in haptic feedback hardware.

III.2.2.1. Arm exoskeletons

One of the earliest modern haptic arm exoskeletons is developed by (Bergamasco et al. 1994). The five-DOF arm provides feedback to the shoulder, elbow, and forearm joints using DC motors and a complex cable transmission. The user controls the exoskeleton through a handle attached to the last rigid link. The user controls the exoskeleton through a handle attached to the last rigid link. The device can apply torque up to 20 N/m at the shoulder, 10 N/m at the elbow, and 2 N/m at the wrist joint.

The arm exoskeleton described above uses DC motors that have low power-to-weight ratios. This results in a heavy interface structure that weighs in excess of 10 kg. Researchers at the University of Salford, United Kingdom are currently working on a lightweight arm master (Caldwell et al. 1995). The significant reduction weight in exoskeleton is due to the use of very light pneumatic muscle actuators described in III.1.1.2. These compact actuators are 15 cm long and weigh only 15 grams, however their contractile force cannot exceed 150 N (at 700 kPa). Subsequently, (Tsagarakis et al. 1999) has reported very large forces of 1000 N (at 800 kPa). As shown in Fig. 1.16, the design uses actuators acting in opposition for each exoskeleton joint. The overall structure has 7-DOF (three at the shoulder, two at the elbow, and two at the wrist) and it is attached to the user through a body brace. The exoskeleton is constructed of a combination of steel and aluminium and weighs only 2 kg. Its geometry allows the user to reach over 90 % of his work volume. This device does limit shoulder

extension (behind back), but this is considered unimportant for the intended use in a virtual reality simulation.

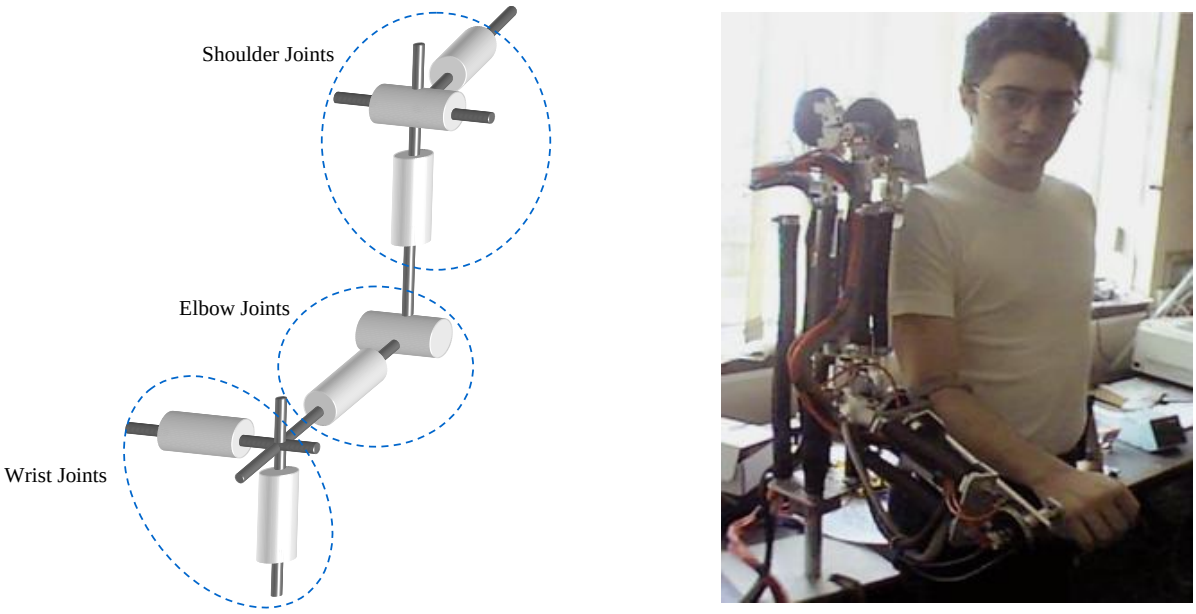

(a) Arm kinematics (b) overall system attached to person's arm

Fig. 1.16. Exoskeleton using pneumatic muscle actuators

Recently, CEA has developed a motorized exoskeleton that is shaped like a human arm and designed to guide or assist movements. One of its major innovations is the jackscrew-cable actuation system that allows to achieve a compact, quiet, and reversible system. To optimize movement assistance, the actuator has a very low level of friction and low inertia, comparable to a human arm.

Fig. 1.17. Orthotic prototype of CEA-LIST[1]

III.2.2.2. Hand masters

One of the first string-based hand master is the Dextrous Hand Master (DHM) developed at Laboratoire de Robotique de Paris, France (Bouzit et al. 1993). The DHM uses tendons to apply forces on each phalanx of the hand. Each of the 14 joints is actuated through a tendon-sheath transmission by DC disk motors, placed remotely from the hand. Miniature force sensors are placed on each phalanx in order to measure string strain and permit the implementation of force/impedance control techniques.

[1] http://www-list.cea.fr/gb/actualites/news_2008/news_27_10_4.htm (last visit on 16 June 2011)

As illustrated in Fig. 1.18 (a), this haptic device provides force feedback to all fingers at 14 hand locations.

The only commercially available haptic glove is the CyberGrasp (McLaughlin et al. 2005), which is a retrofit of the CyberGlove[1] manufactured by Immersion Technologies[2]. As illustrated in Fig. 1.18 (b), the CyberGrasp consists of a cable-driven exoskeleton structure on the back of the hand. The interface is powered by electrical actuators capable of applying 12 N resistive forces to each finger. The exoskeleton attachment to the back of the palm allows full fist closure, but requires the remote placement of actuators in a control box. This results in high backlash and friction, and reduces the dynamic range of the device. Even with the remote placement of its actuators, the weight of the glove is quite high (450 grams), which may lead to user fatigue during prolonged use.

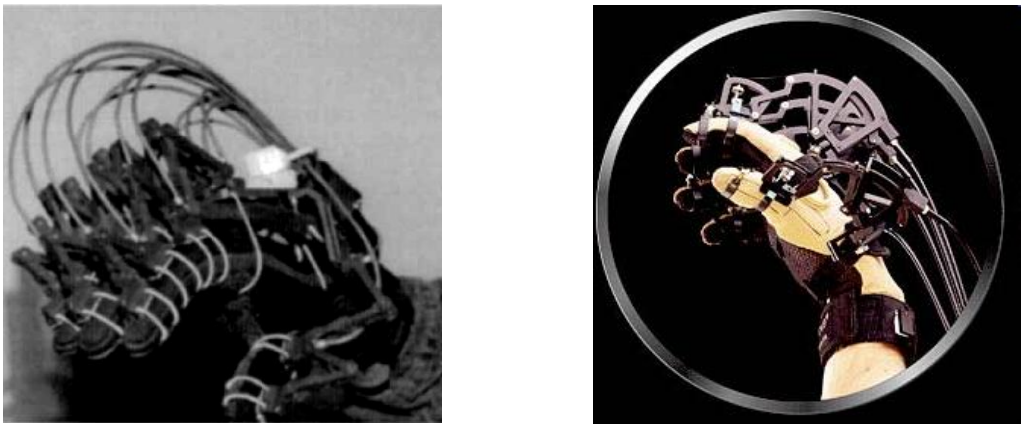

(a) The "Dextrous Hand Master" (b) The CyberGrasp glove

Fig. 1.18. Hand Master with electrical technology

The Rutgers Master II illustrated in Fig. 1.19 (a) is a research prototype developed at Rutgers University, USA. It has a smaller weight than the CyberGlove (130 grams versus 450 grams), due to the use of pneumatic actuators with high power/weight ratio. The low friction of the actuators and their placement in the hand provide for high interface dynamics. The device uses a direct-drive configuration and compressed air, such that each fingertip is resisted in flexion with up to 16 N. This force is higher than the peak force of the CyberGrasp (i.e., 12N). With the Rutgers Master II, positions of each of the four fingers can be separately mapped in the virtual or remote environment, and respective forces displayed back to the user. This makes it an ideal interface for tasks where grasp or manipulation of objects is desirable. Examples of such application include palpation, virtual tours of homes and museums, and remote manipulation of robotic grippers.

Another example of a portable hand master using pneumatic technology is the orthotic exoskeleton built at Carnegie Mellon University, USA (Fig. 1.19 (b)). The goal of this research involves developing an exoskeleton that could help people who were unable to pinch object between their index finger and thumb. The user would indicate their intent through activation of another set of muscles (e.g., their biceps) and the device would supply a grasping force to the two fingers. In order to obtain the intent of the user, Electromyography (EMG) signals from the biceps are used in two different manners. Firstly, they are used as binary signals. If the EMG signal is above a certain threshold then the grasping force can be applied. Otherwise, there is no grasping force. Secondly, they use a variable grasping force, where the force applied is proportional to the EMG signal. Advantage of pneumatic actuators in such a system is the possibility to provide smooth motions and high force feedback values.

[1] http://www.cyberglovesystems.com/ (last visit on 16 June 2011)

[2] http://www.immersion.com/ (last visit on 16 June 2011)

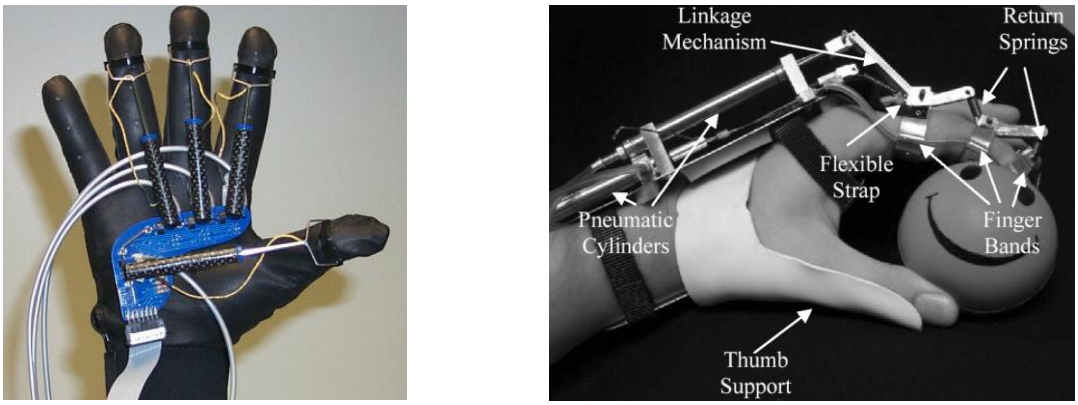

(a) The "Rutgers Master II" (b) The orthotic exoskeleton

Fig. 1.19. Hand Master with pneumatic technology

Finally, portable force feedback interfaces allow a significant increase in the user's freedom of motion during the simulation. Arm exoskeletons provide force feedback at the wrist and forearm. On the other hand, portable hand masters provide feedback to independent fingers and thus, are suited for the simulation of dexterous manipulations tasks. The vast majority of the devices described in this section use DC motors which are placed remotely from the desired force application point. This is because of the poor power-to-weight and power-to-volume ratios of electrical actuator technology. On the other hand, the pneumatic technology offers a possibility to place direct-drive actuators in the palm of hand master, resulting in a simple and extremely light design.

IV. Haptic Feedback Applications

The application of haptic interfaces in areas such as computer-aided design and manufacturing (CAD/CAM) enables users to manipulate virtual objects before fabrication, thus enhances production evaluation. Along the same lines, the users of simulators for training in surgical procedures, control panel operations, and hostile work environments benefit from such a capability. Haptic interfaces can also be employed to provide force feedback during execution of remote tasks (known as teleoperation) such as telesurgery or hazardous waste removal. With such a wide range of applications, the benefits of haptic feedback are obviously recognizable.

In the following subsections, applications are surveyed in terms of activity areas (Hayward et al. 2004). The research is now so intense that only a few references will be included.

- *Learning and training*

Research indicates that a considerable portion of people are kinesthetic or tactile learners—they understand better and remember more when education involves movement and touch. Because formal education has traditionally focused on visual (reading) and auditory (hearing) learning, these learners have been at a disadvantage. Thus, haptics opens the door to an entirely different learning method and style, one that for many students provides the best opportunity to learn. Moreover, even for visual and auditory learners, haptics can improve learning. For a broad range of subject matter, incorporating sensory data and feedback allows for a richer understanding of the concepts at hand.

Also, another opportunity is arising to incorporate haptic technology into training efforts. Dangerous systems (e.g., real weapons for combats) or systems with very limited availability (e.g., surgery patients) can be simulated using haptics for training purposes. Surgical training, in particular, is the subject of intense research (Schmidt et al. 2005). Other opportunities including the training of sensory motor skills is also investigated (Feygin et al. 2002).

- *Rehabilitation*

Applications include the improvement of working conditions for visually impaired people, and better interfaces to alleviate motor system impairment (Gupta & O'Malley 2006).

- *Scientific discovery*

Data display was in fact one of the earliest applications of haptics, with the molecule docking project (Brooks et al. 1990). Other display applications include: multi-dimensional maps, data mining in geology (or in related, applied fields such as oil and gas prospecting), remote sensing, and the display of fields and flows. An attractive property of haptics is the ability to convey the existence of small details, which typically clutter the graphical presentation of data, while minimizing the need to zoom in and out. Projects exist to use haptics to enhance the human interface of imaging instruments such as scanning, tunneling, and atomic force microscopes (Falvo et al. 1995).

- *Engineering industry*

Researchers in major automotive and aerospace companies are already looking for practical ways to adapt haptics technology to improve quality and reduce costs in product development. Boeing, for example, has demonstrated how force feedback can be used in computer-aide design analysis and factory-floor training. The demonstration system will include a handle, attached to the end of a haptic device, that engineers can grasp and move along a particular pathway in the product simulation. Also, Boeing has developed software called VoxMap Pointshell[1] that generates forces over all six directions of motion for the system's rigid body manipulator (McNeely et al. 1999).

- *Manufacturing*

In manufacturing, many opportunities exist. For example, haptics can assist design for assembly, in terms of reducing the need for prototyping, and as well as for rapid prototyping. It is also possible to assess human maintainability of complex systems before they are built (Ren et al. 2006). Programming of complex manufacturing devices such as multi-axis, numerically-controlled machines or robots can be facilitated.

- *Game*

Modes of interaction and the sense of user immersion are greatly enhanced by applying force feedback to the player. Dexterity games available earlier in fixed form can be made infinitely programmable: placing, balancing, hitting and bouncing. As well, many opportunities exist for educational games (Corradini et al. 2005). It is possible to illustrate concepts in dynamics, kinematics, magnetism, waves, flows and many other physical phenomena, and anatomy. Other kinds of games include combinatorial mind games, puzzles, and guess games that include visual and mechanical constraints, as well as most situation games. In the latter case, force feedback is already at the commercial stage (e.g., the Falcon haptic device of Novint[2]), to assist in driving, piloting, exploring, and so on.

- *Arts and creation*

Musicians and visual artists are increasingly using computers. However, creators often prefer to use their hands as directly as possible (as in sketching). Haptic communication with computers opens completely new opportunities.

(Ehmann et al. 2001) have resulted in haptic sculpting environments, where the operator sculpts virtual clay using a haptic stylus, and haptic painting systems which allows users to feel the texture and response of a virtual canvas and brush. In music, advances in real-time synthesis tools increase the demand for interactive controllers which are presently mostly confined to the existing MIDI (Musical

[1] http://www.haption.com/site/eng/images/pdf_download/lv2006/BOEING-lv2006.pdf (last visit on 16 June 2011)

[2] http://home.novint.com/products/novint_falcon.php (last visit on 16 June 2011)

Instrument Digital Interface) fixed interfaces (Rovan & Hayward 2000). Lastly, in graphic arts and design, especially the creation of animation, much activity is under way (Yoshida et al. 2004).

- *Multi-media publishing*

Current multi-media and hypertext applications include text, sound, images, and video. For lack of appropriate devices so far, haptics has been ignored as a medium of communication. One could envision "mechanical documents". For example, a new form of document would include movement which can be experienced visually (video), auditively (spatialization), and also haptically. This raises the question of authoring tools (such as Immersion Studio[1]) and their necessity for the design of haptic sensations. Material properties can also be conveyed. A frequently mentioned application of this capability is the creation of online catalogues with haptic feedback. These would however benefit greatly from the development of practical, distributed tactile displays, which are not yet available (Hayward et al. 2004).

- *Telerobotics and teleoperation*

According to (Hayward et al. 2004), teleoperation is considered to be one of principal disciplines in robotics. Haptic devices are used in supervisor control modes such as teleprogramming, telesurgery, telemanipulation, etc. Teleoperation systems still have a need for high quality manual controllers. This issue will be discussed further in the chapter 2 regarding the control and design of haptic feedback in teleoperation applications.

V. Conclusions

In this chapter, we have provided an overview of haptic interface such as operating principle, haptic design requirements and actuator technologies. A study based on different actuators allowed to choose the most appropriate solution to our future development, i.e., pneumatic actuators with their interesting properties such as high power-to-weigh ratio, clean, cheap, compliance, etc.

A concept of several devices was then described as part of more general problem for creating haptic interfaces including portable and non-portable force feedbacks. High performance haptic designs have to take into account all characteristics of the human perception as well as sensory motor skills in order to assure an efficient, comfortable, and realistic communication between the humans and machines.

The final section is dedicated to a number of potential applications where haptic feedback is well suited to provide value. Meanwhile, some future applications of haptics are still under consideration due to the complex design on both concept and control, e.g. teleoperation. Indeed, the master-slave teleoperation system has been investigated since the 50's but most of current commercial devices do not provide any solution of measuring or resituating the contact force to the user (e.g., the daVinci[2] surgical robot for minimally invasive surgery). In consequence, one of our objectives is to develop the master-slave controllers for force feedback devices. The next chapter provides a closer look about analysis and control in haptic teleoperation.

[1] http://gamingdeveloper.immersion.com/downloads/IStudio/HTML/ISTUDIO/Overview_of_Immersion_Studio.html (last visit on 16 June 2011)

[2] http://www.intuitivesurgical.com/products/ (last visit on 16 June 2011)

Chapter 2
Teleoperation Systems

Table of contents

I. Introduction

Teleoperation is the manipulation of an object using a robotic tool. We can often use our bare hands to manipulate object, but sometimes tools are compulsory. These tools can be purely mechanical or equipped with various electromechanical features (Christiansson 2007). When the operational side of the tool is a robot, we call it teleoperation (see Fig. 2.1).

The operator holds on an interface, called the *master device*, and gives force/movement commands to the system. The remote robot, called the *slave device*, follows the motion of the operator and collects information from the remote site. The master device and the slave device are connected via a *controller* and a *transmission line*, sometimes with significant time delays.

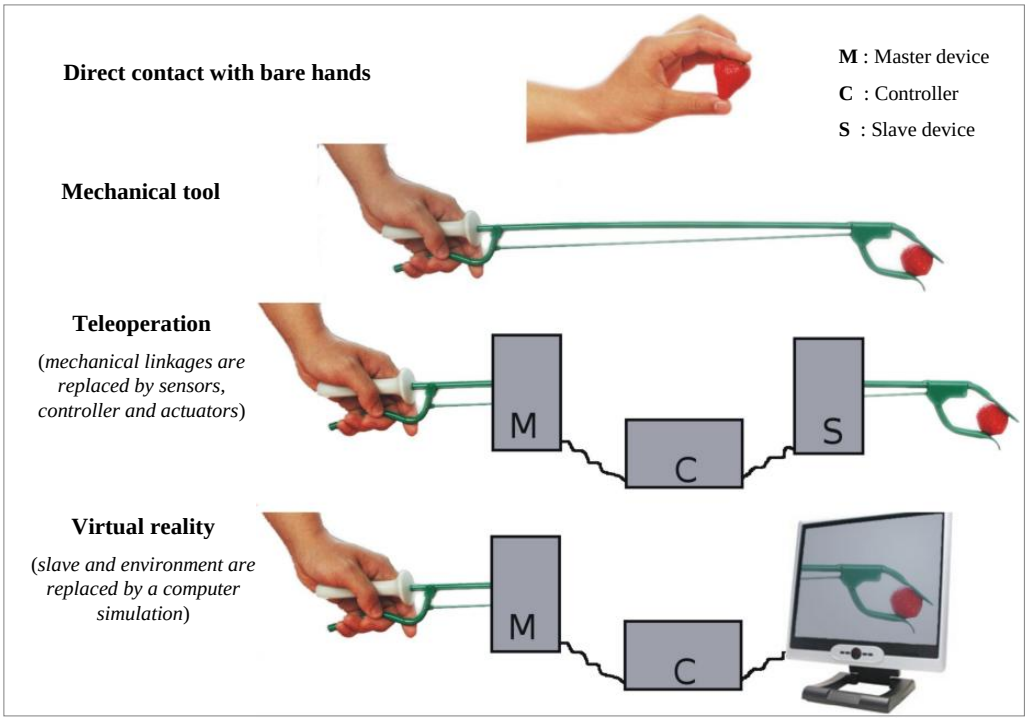

Fig. 2.1. Different forms of interaction (Christiansson 2007).

In a teleoperation system, the slave manipulator tracks the motion of the master manipulator, which is driven by a human operator, in an environment. To improve task performance, information about the environment should be provided to the human operator. Such feedback can be provided in various forms such as audio, visual, and/or force information. Force feedback to the human operator, representing the slave/environment interaction, provides a highly intuitive and natural sensory input for the human operator. Indeed, force feedback is shown to improve the three main metrics of a motor task (precision, speed and force) during teleoperation (Shimoga 1993), meaning that it helps the operator in probing a possibly unknown environment with higher precision, in shorter time, and with less damage to the manipulated object. When the contact force is reflected by the master manipulator to the operator's hand, the teleoperation system is said to be *haptic* or *bilateral*.

In a bilateral teleoperation system, apart from the basic requirement of *stability*, there are primarily two control design goals for ensuring a close coupling between the human operator and the environment. The first goal is that the slave manipulator tracks the position of the master manipulator, and the second goal is that the environment force acting on the slave displayed to the master. These goals result in *transparency* of the teleoperation system, meaning that through the master manipulator, the operator feels as if he/she is directly operating on the remote environment.

The content of this chapter is categorized into five sections. Sections II and III provide some basic concepts of the haptic teleoperation such as linear modeling and control architectures. Section IV

and V go deeper into the analysis of the teleoperation systems - how to quantify performance and stability. Section VI provides an overview of various applications in teleoperation system. Finally, conclusion is given in Section VII.

II. Teleoperation System Building Blocks

A teleoperator is an interface (master-controller-slave) that communicates force and movement between the human operator and the remote environment. As it can be seen in Fig. 2.2, the operator and the environment are not part of the teleoperator itself but mechanically connected to the teleoperator. Due to this mechanical coupling, they influence the dynamics of the teleoperation system, mainly regarding stability (see section V.1).

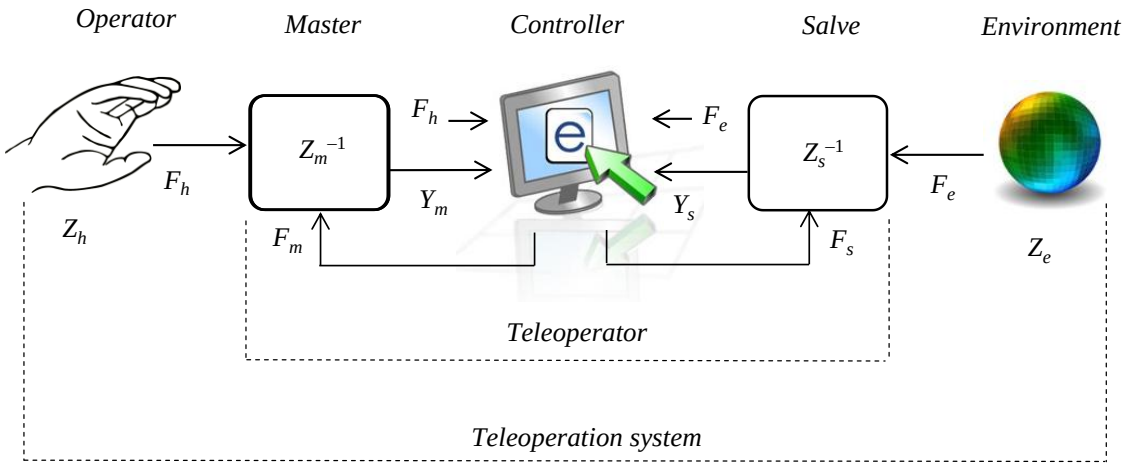

Fig. 2.2. Master-Controller-Slave is in contact with operator and remote environment.

In Fig. 2.2, Z_m and Z_s denote the master and slave manipulators' linearized dynamics, which are generally approximated by simple mass-spring-damper systems; Z_h and Z_e denote the dynamic characteristics of the human operator's hand and the environment; Y_m and Y_s are the master and slave positions; F_m and F_s are the (force) control signals for the master and slave manipulators; F_h and F_e are the operator force exerted on the master and the environment force exerted on the slave.

In this section, all the operation components and the controllers are modeled as *linear-time-invariant* (LTI) systems. This is the dominating modeling framework in the literature, and the linearized analysis gives usually sufficiently good results, even though many aspects of the system cannot be expressed accurately (Lawrence 1993; Zhu & Salcudean 2000; Tavakoli et al. 2008).

The signals used in the teleoperation are also called "power variables" effort (force) and flow (velocity), conform to the major part of the literature. This heritage comes from the linear network theory that allows to simplify energy-based-analysis. This leads to a definition of impedance as force divided by velocity. Some researchers instead define the impedance as force over position (Aliaga et al. 2004). It seems more natural to use position, as most real teleoperation systems do measure position. Furthermore, ensuring velocity tracking between the master and the slave might cause small offsets between the master and slave positions (*i.e.*, steady-state errors in position tracking). Generally, when the delay in the communication channel is negligible, the use of position controllers or velocity controllers does not affect the stability of the teleoperation system, thus we opt to use position controllers.

Also, only teleoperators with one DOF movement of the end-effector are considered. It means that the methods and formulae presented are useful for the teleoperation system where the end-effector degrees of freedom are decoupled, *e.g.* the 3-DOF setup by (Sirouspour et al. 2000).

To sum up, the modeling is based on the following assumptions (Christiansson & Helm 2007):

- Decoupled degrees-of-freedom: this reduces the analysis to single-DOF models, which can be analyzed separately;
- Linear-time-invariant (LTI) models: the component models are modeled as Laplace models.
- All linear component models are invertible: Impedance ($Z(s) = F(s)/Y(s)$) and admittance ($Z^{-1}(s) = Y(s)/F(s)$) are used interchangedly, depending on the purpose of the model.

Firstly, each component of the teleoperation system is modeled separately (section II.1–II.5), and then the complete model will be composed by using the H-matrix notation (section II.6).

II.1. Human operator model

The human operator is usually modeled as impedance. This choice has a rather large impact on the teleoperation system, since it implies that the human can be assumed passive. For stability, this makes passivity analysis possible.

However, a human is not passive at all, since he/she can apply an active force to the master. In aerospace this leads to a well known problem called "Pilot Induced Oscillations". Still, in haptic literature it is assumed that human is more likely to be a stabilizing component than to cause instability. Two classes of models can be identified as following (Ben-Dov & Salcudean 1995):

- Passive operator: the human operator can not increase total energy in the system, that means he/she does not perform actions that will make the teleoperation system unstable.
- Active operator: the human operator provides input signals based on his goal and perceives information about the state of the system.

The first class can be a simple impedance model. For more details about the complex dynamic model, the reader can referred to (Zhu & Salcudean 2000). The input signals provided by the second class, can be considered as disturbances, with lower and upper bounds. With a nonlinear generalization of the *Adaptive model theory*, (Neilson & Neilson 2005) try to achieve a model that can predict the input signal. This model uses a modeling framework that is compatible with the control and the teleoperation system.

To some extent, each operator holds with different strengths, and has different masses. Furthermore, one person can change the grip forces and modulate his dynamics in a wide range during operation, in general to stabilize the complete system. The operator can also adjust his/her capacity of force and movement based on the current task in order to improve the performance.

Much can be said about the operator component in the global teleoperation system, but here, the discussion kept short by observing that the operator model is mainly used in the stability analysis. Therefore, in our case, the operator is assumed to be passive and its impedance can be approximated by a low-order model with parameters in certain range. For linear analysis, we choose the mass-spring-damper model for the operator impedance as

$$Z_h = M_h s^2 + B_h s + K_h \tag{2.1}$$

where M_h, B_h, and K_h are assumed to be positive corresponding to the mass, damping and stiffness of the operator.

II.2. Environment model

The environment is generally the most uncertain component in the teleoperation system. The variation in environment impedance can be large (*i.e.*, from zero to infinity), especially when the slave moves in free space and suddenly comes in contact with a stiff object. Often, the environment can be approximated as a LTI mass-spring-damper system

$$Z_e = M_e s^2 + B_e s + K_e \tag{2.2}$$

where M_e, B_e, and K_e are assumed to be positive corresponding to the mass, damping and stiffness of the environment.

In practice, it is useful to look at the extreme values (*i.e.*, the maximum and the minimum impedances) of the environment, and test these for stability. For certain control architectures, such as *position error based* (called PEB, explained in section III.2.1), the free-motion stability is the most critical. For other scheme including force sensor measurements, like the Lawrence's four-channel control (see section III.1), the highest environment impedance limits the stability (Christiansson 2007).

Furthermore, an environment model is often used to quantify the performance of the teleoperation system. The transparency expresses how well the system can reproduce a certain remote environment to the operator. The performance of the teleoperation system will be elaborated in section IV.

II.3. Controller model

By definition, the controller is a model of all the components (sensors, amplifiers, transmission line, controller hardware) between the master and slave devices.

Assuming that the four signals of forces and positions (F_h, Y_m, F_e, Y_s) are measured, the aim is to choose the controller transfer functions K_{ij} to optimize the performance (i.e., transparency and stability) of the teleoperation system

$$\begin{aligned} F_m &= K_{11}F_h + K_{12}Y_m + K_{13}F_e + K_{14}Y_s \\ F_s &= K_{21}F_h + K_{22}Y_m + K_{23}F_e + K_{24}Y_s \end{aligned} \tag{2.3}$$

In the literature, there are several teleoperation control architectures, which present certain choices of the controller parameters, and will be deeply explained in section III.

II.4. Master/Slave model

Most of literature describes the master and slave manipulators as linear models. This implicates that all nonlinearities and disturbances (e.g. Coulomb friction) are cancelled by using compensation techniques. For more details about nonlinear model identification compensation of n-DOF systems, the reader can refer to (Pawluk & Ellis 1991).

Generally, the master/ slave manipulators can be categorized as admittance or impedance type, depending on whether they behave like velocity or force sources, respectively. This behavior is determined by the structural design and actuation employed by the manipulator. By definition, an impedance device receives a force input and applies force to the environment in response to the measured position. For example, magnetically levitated wrists (Hollis et al. 1991) and SensAble's Phantom[1] (Massie & Salisbury 1994) are among the devices that possess high back-drivability and low impedance. On the other hand, an admittance device receives a velocity/position input and applies a velocity/position to the environment in response to the measured contact force. As an example, a heavily geared Puma robot (Clover et al. 1997) or hydraulic robots such as excavators (Salcudean et al. 1999) are devices with low back-drivability and low admittance.

Most of the proposed control architectures are adapted to haptic teleoperation systems with impedance types of master and slave manipulators. Therefore, in our study, the impedance-type teleoperation that are driven by "force source" actuators, is chosen.

The impedance of the master and slave device can be expressed as either a simple mass system (Lawrence 1993; Yokokohji & Yoshikawa 1994) or a mass-damper system (Hannaford 1989) as given by

$$Z_m = M_m s^2 + b_m s = \frac{F_h + F_m}{Y_m}, \qquad Z_s = M_s s^2 + b_s s = \frac{F_s - F_e}{Y_s} \tag{2.4}$$

[1] http://www.sensable.com/ (last visit on 16 June 2011)

In the illustration of Fig. 2.3, the environment force F_e is defined as the contact force pushing on the slave device – opposite the direction of the controller force F_s. It is in contrast to the definition of the human force F_h in the model of the master device where F_h and F_m are the same direction.

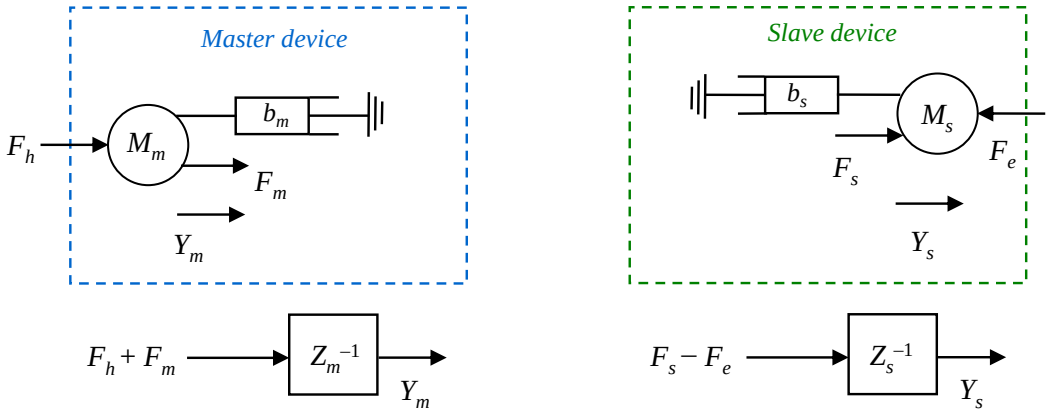

Fig. 2.3. Example of master and slave device models.

II.5. Transmission line

In the bilateral teleoperation, the force and position signals are transmitted from the master to the slave and vice-versa. These signals pass through the communication line that, in general, cause time delays in the transmission. It has been recognized that the presence of time delay is one of the most important barriers in teleoperation systems. This problem is mainly due to the distance separating the master from the slave site. To overcome this problem, many concepts, such as network theory, passivity and scattering theory have been used (Aziminejad et al. 2008). The idea is to analyse mechanisms responsible for the loss of stability and derive a time delay compensation scheme to guarantee stability

In this study we do not deal with the presence of time delay in the teleoperation system's communication channel. Such delay is commonly presented in remote teleoperation systems, but is generally not significant in local teleoperation systems, such as scaled teleoperation systems for dexterity enhancement or glove-box teleoperation systems for purposes of biological or radiological isolation.

II.6. Formulation using a two-port presentation

Let us consider the equivalent electrical circuit of a 1-DOF teleoperation system model as shown in Fig. 2.4, where the master, the transmission line and the slave are lumped into a two-port network (Lawrence 1993). It is assumed that the operator and the environment are in contact with the master and the slave, respectively. The dynamics of the operator and the environment can be modeled by linear-time-invariant impedances Z_h and Z_e according to

$$F_h = F_h^* - Z_h Y_m \ , \quad F_e = F_e^* + Z_e Y_s \tag{2.5}$$

where F_h* and F_e* are the operator's and the environment's exogenous input forces, respectively, and independent of teleoperation system behavior. In most of cases, the operator as well as the environment are supposed to be passive (F_e* = 0).

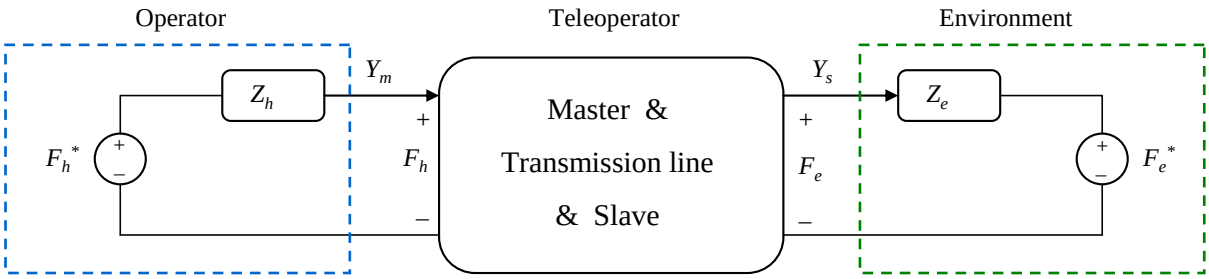

Fig. 2.4. Network block diagram of teleoperation system.

To evaluate the transparency of teleoperation, the hybrid representation of the two-port network model of a master-slave system is most suitable (Hannaford 1989). In this representation, master position Y_m and slave force F_e are chosen as input

$$\begin{bmatrix} F_h \\ -Y_s \end{bmatrix} = \begin{bmatrix} h_{11} & h_{12} \\ h_{21} & h_{22} \end{bmatrix} \begin{bmatrix} Y_m \\ F_e \end{bmatrix} \tag{2.6}$$

The H-matrix parameters h_{ij} are rational transfer functions, containing all the information about the device models and the controller. By combining (2.3) and (2.4), h_{ij} can be calculated. Note that the tradition of choosing $-Y_s$ as the output signal comes from the electrical linear representation, where positive currents are going into the network.

In an ideally transparent teleoperation system, the master and the slave positions and forces will match regardless of the operator and environment dynamics:

$$Y_m = Y_s \quad , \quad F_h = F_e \tag{2.7}$$

From (2.6) and (2.7), perfect transparency is achieved if and only if the H-matrix has the following form:

$$H_{\text{ideal}} = \begin{bmatrix} 0 & 1 \\ -1 & 0 \end{bmatrix} \tag{2.8}$$

Each element of the H-matrix has a physical meaning (Tavakoli et al. 2007a). The parameter $h_{11} = F_h / Y_m \big|_{F_e=0}$ is the input impedance in free-motion condition. Nonzero values for h_{11} mean that even when the slave is in free space, the user will receive some force feedback, thus providing a sticky feel of free-motion movements. The parameter $h_{12} = F_h / F_e \big|_{Y_m=0}$ is a measure of force tracking when the master is locked in motion (perfect force tracking when $h_{12} = 1$). The parameter $h_{21} = -Y_s / Y_m \big|_{F_e=0}$ is a measure of position tracking performance when the slave is in free space (perfect position/velocity tracking when $h_{21} = -1$). The parameter $h_{22} = -Y_s / F_e \big|_{Y_m=0}$ is the output admittance when the master is locked in motion. Nonzero values for h_{22} indicate that even when the master is locked in place, the slave will move in response to slave/environment contacts.

Note that the H-parameters contain all the characteristics of the teleoperation system. Furthermore, they are very easy to obtain through two simple experiments where $F_e = 0$ (in free space) and $Y_m = 0$ (in hard contact).

III. Basic Control Architectures

The teleoperator system under consideration is primarily an impedance–impedance teleoperator system where the master and slave are impedance devices. In a generic bilateral teleopeartor system, both force and position are communicated bilaterally between the master and slave devices.

For achieving the ideal response (2.8), various teleoperation control architectures are proposed in the literature. A general classification is based on the number of communication channels (two, three or four channels) that are required for transmitting position and force signals from the master to the slave and vice versa. The aim of this section is to provide some basic concepts of the different teleoperation architectures as well as an initial choice of their controller parameters.

III.1. Four-channel (4CH) diagram

Fig. 2.5 depicts the general 4CH bilateral teleoperation architecture proposed by (Lawrence 1993). Here, C_m and C_s denote the local position controllers of the master and the slave sides; C_5 and C_6 are local force feedback terms for the master and the slave; and C_1 to C_4 are position or force controllers embedded in the communication channel.

This architecture involves four types of data transmission between the master and the slave: force and position (or velocity) from the master to the slave and vice versa. It is shown in (Lawrence 1993) that having the 4CH of data transmission is of critical importance in achieving high-performance telepresence (*i.e.*, full transparency) in terms of accurate transmission of task-related information such as the environment impedance to operator. Nonetheless, by proper adjustment of the local feedback parameters (C_5 and C_6), it is possible to obtain two classes of three-channel architectures, which can perform as well as the 4CH system (Hashtrudi-Zaad & Salcudean 2001).

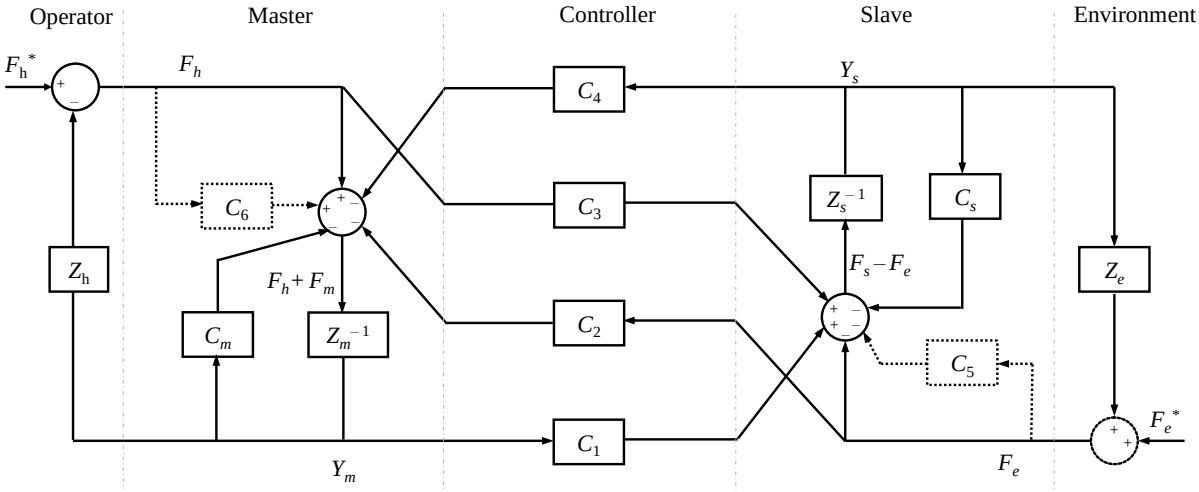

Fig. 2.5. 4CH bilateral controller (Lawrence 1993).

The controller forces F_m and F_s of the master and slave manipulations in Fig. 2.5 are given by

$$\begin{aligned} F_m &= C_6F_h - C_mY_m - C_2F_e - C_4Y_s \\ F_s &= C_5F_h - C_sY_m - C_3F_e + C_1Y_s \end{aligned} \tag{2.9}$$

The H-parameters can be derived in terms of the system and control parameters from (2.4) and (2.9) as

$$\begin{aligned} h_{11} &= \left(Z_{ts}Z_{tm} + C_1C_4\right)/D & h_{12} &= \left(Z_{ts}C_2 - (1+C_5)C_4\right)/D \\ h_{21} &= -\left(Z_{tm}C_3 + (1+C_6)C_1\right)/D & h_{22} &= -\left(C_2C_3 - (1+C_5)(1+C_6)\right)/D \end{aligned} \tag{2.10}$$

where $Z_{ts} = Z_s + C_s$, $Z_{tm} = Z_m + C_m$ and $D = -C_3C_4 + Z_{ts}(1 + C_6)$ with $D \neq 0$. Note that the elements h_{ij} depend both on the device hardware and the controller parameters chosen. As mentioned in (Lawrence 1993), a sufficient number of control parameters in the 4CH architecture allows to achieve ideal transparency. In fact, from (2.10), by selecting C_1 through C_6 according to

$$C_1 = Z_{ts} \qquad C_4 = -Z_{tm} \qquad C_6 + 1 = C_2 \qquad C_5 + 1 = C_3 \tag{2.11}$$

the perfect transparent condition (2.8) is fully met.

III.2. Two-channel (2CH) diagrams

The 2CH diagrams can be represented by the 4CH diagram through the appropriate selection of the controllers C_1 to C_6. This architecture involves two types of data transmission between the master and the slave: position/velocity (or force) from the master to the slave and vice versa. The 2CH architectures are usually classified as position–force (*i.e.*, position control at the master side and force control at the slave side), force–position, position–position, and force–force architectures. Such architectures have been reported in a number of papers because they require fewer sensors and are less complicated to implement. In addition, due to the simplifications provided by eliminating two out of four data transmission channels, the analytical study of the 2CH systems can be easily achieved.

Among these four architectures, the position-force scheme has not yet been implemented, except for haptic simulation applications in (Adams & Hannaford 1999), where it was employed to communicate between an admittance-type haptic device and a virtual environment. It was shown in (Adams & Hannaford 1999) that such architecture does not take advantage in the impedance-type teleoperation, thus it will not be considered in our study.

III.2.1. Position error based (PEB)

A position-error-based, also called position–position, system involves the simplest bilateral controller in which no force sensors are required. As can be seen in Fig. 2.6, the aim of this architecture is to minimize the difference between the master and the slave positions.

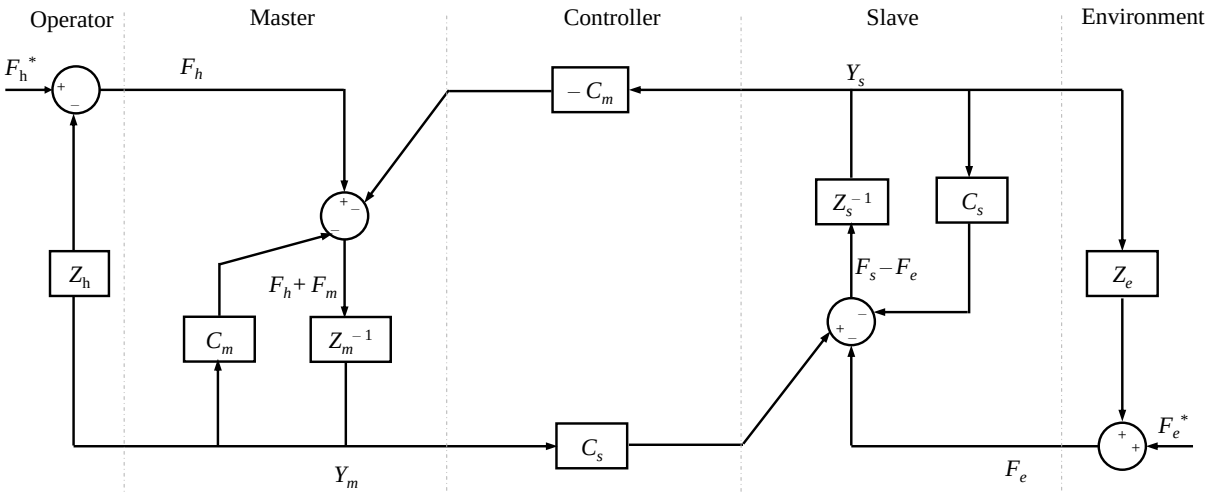

Fig. 2.6. PEB bilateral control architecture.

In the PEB control architecture, which was further developed and analyzed in (Anderson & Spong 1989; Fite et al. 2001; Aliaga et al. 2004), the direct force feed-forward terms are set to zero (*i.e.*, $C_2 = C_3 = 0$). For this controller, the hybrid matrix is given as

$$H_{\text{PEB}} = \begin{bmatrix} Z_m + C_m Z_s / Z_{ts} & C_m / Z_{ts} \\ -C_s / Z_{ts} & 1/Z_{ts} \end{bmatrix} \tag{2.12}$$

As a result, the PEB method suffers from a distorted perception in free-motion condition ($h_{11} \neq 0$). This means that in the absence of a slave-side force sensor, control inaccuracies (*i.e.*, nonzero

position errors) lead to proportional force feedback to the user even when the slave is not in contact with the environment (Tavakoli et al. 2007a). In the contact motion, due to a non-ideal force tracking ($h_{12} \neq 1$), the operator does not have impression to directly manipulate the object and his/her feeling of the contact is deteriorated. Indeed, what he/she really feels does not depend on the environment's impedance but on the position tracking error as well as the controller parameters. For example, a high value of C_m or a high difference between Y_m and Y_s can give the operator the perception of a contact object, even when the slave is completely in free motion.

With regard to the position tracking, its performance can be improved by choosing the controller C_s as large as possible. In this case, when the slave dynamics Z_s is low enough, we have $C_s + Z_s \approx C_s$, thus $h_{21} \approx -1$ and good movement accuracy could be achieved.

III.2.2. Force error based (FEB)

A force-error-based, also called force–force, teleoperation architecture is shown in Fig. 2.7. The difference between this system and the PEB system is that the position sensors are replaced by the force sensors.

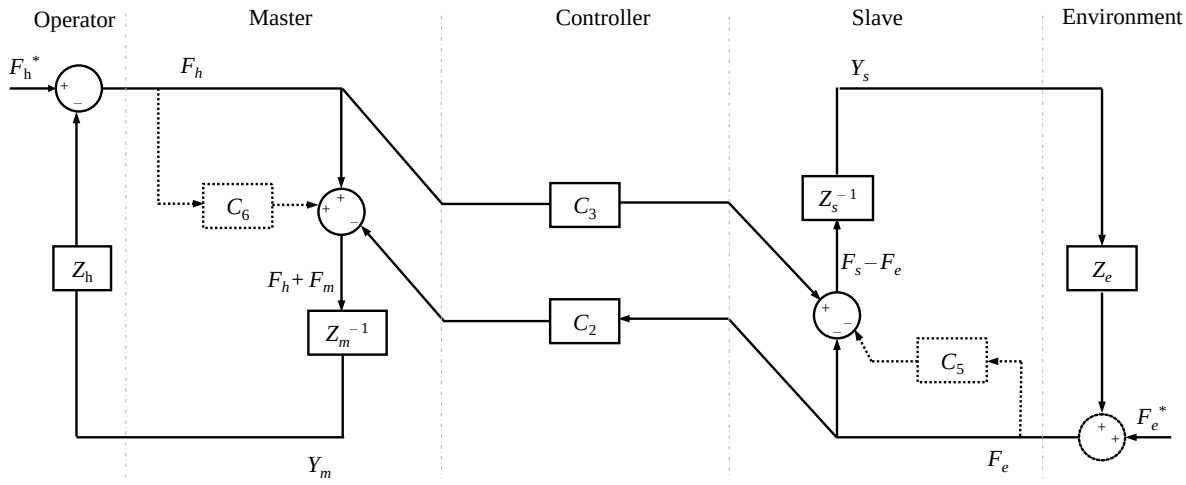

Fig. 2.7. FEB bilateral control architecture.

Besides (Kazerooni et al. 1993), who proposed this architecture, the literature does not show much interest in the FEB controller since two force sensors are required with no significant performance improvement. According to (Hu et al. 1995), it is motivated by robust control idea based on small gain theory. Recently, (Richert et al. 2010) use an adaptive backstepping approach in the FEB architecture with presence of time delay in the master-slave interface.

By setting the controllers as $C_1 = C_4 = C_m = C_s = 0$, $C_2 = C_6 + 1$ and $C_3 = C_5 + 1$, we have

$$H_{\text{FEB}} = \begin{bmatrix} Z_m/C_2 & 1 \\ -Z_m C_3/Z_s C_2 & 0 \end{bmatrix} \tag{2.13}$$

As stated by (Kazerooni et al. 1993), although the FEB controller leads to a wider communication bandwidth between the master and slave manipulators, the entire system may still suffer from a position error buildup. As it can be seen in (2.13), when the master and slave manipulators are identical ($Z_m = Z_s$), a good position accuracy could be theoretically achieved ($h_{21} = -1$) by taking $C_2 = C_3$. However, in practice it is difficult to guarantee the equality of these two impedances because they depend on the dynamics of the system. For instance, in the free-contact motion, the master and the slave are under different constraints ($F_e = 0$, $F_h \neq 0$) which results the difference of Z_m and Z_s. As a result, the FEB system suffers from a non-ideal position tracking. It is contrary to the PEB system whose position tracking can be improved by tuning the controller parameter C_s.

On the other hand, the FEB architecture shows a good force tracking performance ($h_{12} = 1$) in hard-contract motion ($Y_m = 0$). Furthermore, an ideal value of the output admittance ($h_{22} = 0$) in this architectures shows that when the master is locked in motion, the slave's movement in response to external force disturbances quickly converges to zero. Therefore an excellent stiffness is obtained for the slave manipulator.

III.2.3. Direct force reflection (DFR)

A direct-force-reflection, also called force–position, teleoperation architecture is shown in Fig. 2.8. The DFR system has been developed, implemented, and analyzed by many researchers for the past three decades (Handlykken & Turner 1980; Hannaford & Anderson 1988; Chopra et al. 2005). In this architecture, we get the controller as $C_3 = C_4 = 0$, $C_2 = 1$ and $C_1 = C_s$. Thus the hybrid matrix is

$$H_{\mathrm{DFR}} = \begin{bmatrix} Z_m & 1 \\ -C_s/Z_{ts} & 1/Z_{ts} \end{bmatrix} \tag{2.14}$$

Consequently, although the perception of free motion is still less than ideal ($h_{11} \neq 0$), a perfect force tracking is attained ($h_{12} = 1$). Nonetheless, compared to the PEB method, h_{11} is much closer to zero in the DFR method, and the user only feels the dynamics of the master interface (Z_m) when the slave is not in contact. Although the DFR method tends to be better than the PEB method, both methods suffer from the non-ideal h_{22} value with respect to the FEB method, which results in poor slave stiffness. However, concerning the position tracking, the FEB system is not on par with that in the others.

Finally, the DFR architecture takes advantage of both PEB and FEB architectures in terms of position and force tracking. Nonetheless, it is not suitable for applications with very hard contact (Tavakoli et al. 2007a), or requiring high bandwidth where the master and the slave display fast movements (Klomp 2004).

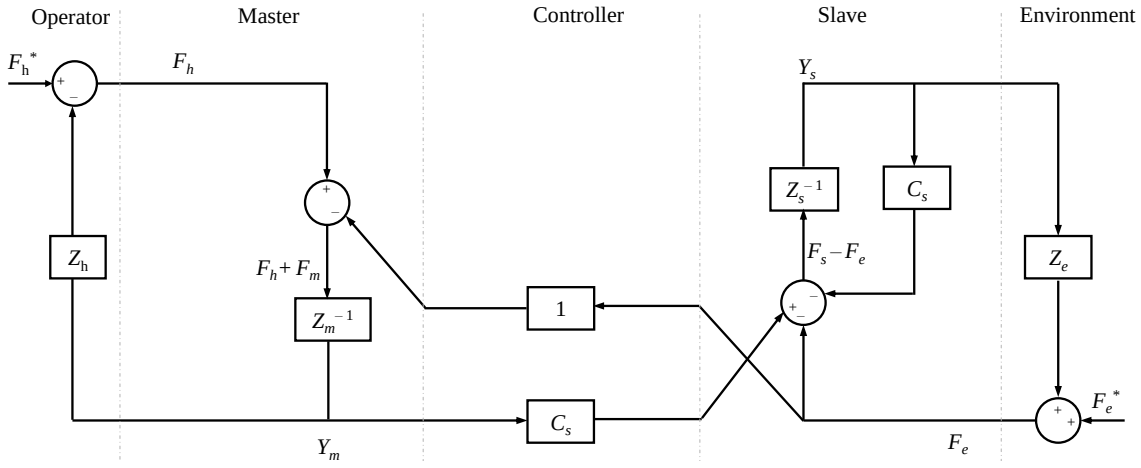

Fig. 2.8. DFR bilateral control architecture.

III.3. Three-channel (3CH) diagrams

Another benefit of the general 4CH architecture of Fig. 2.5 is that by proper adjustments of the control parameters, it is possible to obtain two classes of 3CH control architectures, which can be transparent under ideal conditions. The first class of 3CH architectures is derived by setting $C_2 = 1$ and $C_3 = 0$. As a consequence, $C_5 = -1$ and $C_6 = 0$. In this way, there is no need for master/operator interaction force measurement. The second class of 3CH architectures is obtained by setting $C_2 = 0$ and $C_3 = 1$, in which case force measurement at the slave side is not needed. The need for fewer force sensors without degrading transparency makes the 3CH architectures attractive from the implementation point of view (Tavakoli et al. 2007a).

IV. Performance

During the last decades, a lot of researches have been investigated in haptic teleoperation performance, since it is the key criterion to assess proposed control architectures. In the performance analysis, several characteristics of the master and slave devices are carried out in order to optimize certain conflict goals: light weight, stiff, fast, strong and stable. Nonetheless, some important device characteristics cannot be described by a linear model, most notably friction and saturation (*e.g.* maximum actuation force). These aspects have to be considered separately, and that is outside the scope of this thesis.

In the following, an overview of the most important performance criteria, expressed as function of linear model (H-matrix), is given.

IV.1. Tracking errors

The most straightforward way to see how well a teleoperator works consists in comparing the movements and forces of the master and the slave. The position and force tracking errors were also the first measures used to quantify teleoperator performance (Yokokohji & Yoshikawa 1994). Position tracking is calculated when the slave robot is in free motion ($F_e = 0$), and force tracking when the slave robot is in contact with a hard object ($Y_m = 0$).

The use of the maximum error in (2.15) over the frequency range of the task was introduced by (Pawluk & Ellis 1991). However, by focussing on the gain of the frequency function, the important effects of phase lag is left unquantified. Consequently, this performance measure is not suitable for the teleoperation system with significant time delay.

$$\max\left|\Delta X(s)\right| = \max\left|\frac{X_m - X_s}{X_m}\right| = \max_{\omega}\left|1 + h_{21}\right| \qquad \max\left|\Delta F(s)\right| = \max\left|\frac{F_h - F_e}{F_e}\right| = \max_{\omega}\left|h_{12} - 1\right| \tag{2.15}$$

IV.2. Bandwidths

Bandwidth is related to the information transfer between the operator and the remote environment. The requirements for information transfer in the two directions differs considerably (Lawrence 1993). The human operator gives force and movement commands with a relatively low frequency content, in the range of 0-10 Hz, whereas the contact information at the slave side often contains frequencies up to 1000 Hz for stiff environments.

It is usually stated that the bandwidth should be as high as possible, and often a lower bound is given (Fischer et al. 1990). Each of the four transfer functions h_{ij}(s) between forces and positions has its own bandwidth. This corresponds to position bandwidths from the master to slave ($\omega_{y,m\to s}$), slave to master ($\omega_{y,s\to m}$); and force bandwidths with similar notations ($\omega_{f,m\to s}$ and $\omega_{f,s\to m}$).

The position bandwidth is defined as the frequency where the tracking error is −3 dB below the low frequency gain (Christiansson 2007), and can be calculated by solving

$$\left|1 + h_{21}(j\omega_{y,m\to s})\right| = \frac{1}{\sqrt{2}}\left|1 + h_{21}(0)\right| \qquad \left|1 + g_{21}(j\omega_{y,s\to m})\right| = \frac{1}{\sqrt{2}}\left|1 + g_{21}(0)\right| \tag{2.16}$$

The force bandwidth is similarly calculated in the same way, as the solution to

$$\left|1 - h_{12}(j\omega_{f,m\to s})\right| = \frac{1}{\sqrt{2}}\left|1 - h_{12}(0)\right| \qquad \left|1 + g_{12}(j\omega_{f,s\to m})\right| = \frac{1}{\sqrt{2}}\left|1 - g_{12}(0)\right| \tag{2.17}$$

where $g_{21} = -\dfrac{h_{12}}{h_{11}h_{22} - h_{21}h_{12}}$ and $g_{12} = -\dfrac{h_{21}}{h_{11}h_{22} - h_{21}h_{12}}$

Just as for the tracking error, the bandwidth performance measure has no information about delays or phase lag, which is a reason for caution. Two systems with the same bandwidth and different phase lag can feel significantly different.

IV.3. Scaling product

Scaling defines how forces and positions are magnified between the master and the slave. The force scaling and the position scaling are easily calculated from the H-matrix (2.8), and their product is called the scaling product. As (Lawrence 1993) has pointed out, the scaling product is often assumed to be unity, also for micromanipulation. However, by choosing a scaling product of less than unity, the remote environment is less accurately represented while stability can be improved thanks to artificial energy loss. Therefore, the product of the scaling factors can be seen as a performance measure, with a nominal value of one. Here we choose the low frequency limit value:

$$\text{ScalingProduct} = \lim_{s \to 0} \left| h_{12}(s) h_{21}(s) \right| \tag{2.18}$$

IV.4. Transmitted impedance

Another aspect of teleoperator assessment is related to the perception of the device (how heavy/damped/springy), when the slave manipulator is in free-motion or in contact-motion with different remote environments. In practice, the operator will never feel exactly the same impedance at the master device as the real environment (Lawrence 1993). By taking into account the remote environment impedance Z_e (*i.e.*, $F_e = Z_e Y_s$), the transmitted impedance felt by the operator Z_{to} can be computed (2.19) from the H-matrix model (2.8)

$$Z_{to} = \frac{h_{11} + (h_{11}h_{22} - h_{12}h_{21})Z_e}{1 + h_{22}Z_e} \tag{2.19}$$

Theoretically, the transmitted impedance would be exactly the same as the remote impedance (*i.e.*, $Z_{to} = Z_e$), so that the operator feels exactly the same forces for the same movement as if he touched the object with his bare hands (Yokokohji & Yoshikawa 1994).

Not that in free-space motion (*i.e.*, $Z_e = 0$), the transmitted impedance Z_{to} is simplified to the H-parameter h_{11}. As mentioned in section II.6, the 4CH and 3CH architectures allow to obtain an ideal h_{11} value (*i.e.*, $h_{11} = 0$). On the other hand, in hard-contact (*i.e.*, $Z_e \to \infty$), (2.19) becomes

$$Z_{to} = \begin{cases} h_{11} - h_{12}h_{21}h_{22}^{-1} & \text{if} \quad h_{22} \neq 0 \\ h_{12}h_{21}Z_e & \text{if} \quad h_{22} = 0 \end{cases} \tag{2.20}$$

We see that when $h_{22} \neq 0$, Z_{to} is insensitive to Z_e, which results in degraded perception of the operator.

Generally, the transmitted impedance is a rational polynomial frequency function, which might be difficult to estimate. Therefore it is usually modeled as a mass-spring-damper linear function

$$Z_{to} \approx M_{to}s^2 + B_{to}s + K_{to} \tag{2.21}$$

The values M_{to}, B_{to} and K_{to} can be calculated for any given remote impedance, but usually for two extremes where $Z_e = 0$ and $Z_e \to \infty$. This allows to determine the minimum and maximum impedance that can be presented by the master device. These values should be done over a frequency range relevant to the application. For example, most tasks require a range of $0.1 - 10$ Hz.

To some extent, the extreme $Z_e \to \infty$ will not likely occur in most of application, especially in the medical area. Usually this requirement is hard to acquire with a controller. Thus a more realistic upper extreme should be chosen. Also, the lower extreme (*i.e.*, $Z_e = 0$) should be less strict, since there exists a minimum levels of mass, damping and stiffness that below that one, a human being can hardly distinguish (Shimoga 1993b).

IV.5. Transparency

Transparency is the most common performance criterion used in literature. As mentioned in section II.6, perfect transparency means that the master and the slave positions and forces will match

regardless of the operator and environment dynamics (2.7) and (2.8). In order to further investigate the influence of the environment to the operator's perception, (Lawrence 1992b) defined transparency as the quotient between the transmitted impedance and the remote impedance.

$$T_z = \frac{Z_{to}}{Z_e} = \frac{h_{11}Z_e^{-1} + (h_{11}h_{22} - h_{12}h_{21})Z_e}{1 + h_{22}Z_e} \tag{2.22}$$

The transparency would ideally be unity for all frequencies. As we see in (2.22), transparency depends both on the teleoperator properties (H-parameters) and the remote impedance (Z_e). In our case where the environment impedance is unknown, the use of the transparent conditions in (2.7) for time domain and in (2.8) for frequency domain seems more appropriate (see chapter 4).

Finally, performance is always achieved with a trade-off on stability. In the subsequent section, some popular stability criteria will be investigated.

V. Stability

Stability is a prerequisite for performance. In essence, stability means that energy does not increase in any part of the system. Typically, instability looks like oscillations with increasing amplitude or that one part moves away uncontrollably in a certain direction. A teleoperation system can be often stable in some configurations (in contact with a certain environment and a certain operator, in a certain point of the workspace) while it is unstable for some other configurations.

To analyse the stability of the teleoperation systems, different definitions of stability have been proposed. The first concept is *bounded input-bounded output* (BIBO) stability. A system is said to be BIBO if every bounded input results in bounded outputs regardless of the system state (Franklin et al. 1994). Another concept of stability, from *Lyapunov*, is that the output and all the internal variables never become unbounded when time tends to infinity for sufficiently small initial conditions. This is called *asymptotic internal stability*.

A first set of stability analysis (section V.1) can be used when the impedances Z_h and Z_e are known. A second set (section V.2) can be used when these impedances are not exactly known, but they fulfil some conditions, *e.g.* passivity. The second set is a stricter requirement for the teleoperation system, because it guarantees that the system is stable in contact with a larger range of human and environment impedances.

V.1. Stability analysis with known operator and environment models

This section investigates the stability analysis of the teleoperation system that depends on the operator and environment impedances. For this, several criterion are possible such as *root locus* (Love & Book 2004), *Nyquist* (Lawrence 1993), and *Lyapunov* (Strassberg et al. 1992).

In this section, only Lyapunov method is presented. Indeed, compared to other methods, the Lyapunov offers a possibility to deal with a nonlinear system such as pneumatic system used in our work.

Lyapunov stability is based on a state space model (2.23), where x is a state vector

$$\dot{x} = f(x) \tag{2.23}$$

It is assumed that the equations have been rewritten in such a way that $x = 0$ is an equilibrium point, *i.e.* $f(0) = 0$. The Lyapunov function $V(x)$ has to satisfy these following properties:

1. $V(0) = 0$;
2. $V(x) > 0$, $\|x\| \neq 0$;
3. V and its derivative are continuous with respect to all components of x;
4. $\dot{V}(x) \leq 0$.

The theorem affirms that if there exists a Lyapunov function for the state equations and if, in addition, $\dot{V}(x) < 0$, then the stability is asymptotic. In the case of a linear system, the last condition mentioned can only hold if all the poles of the system are in the left half-plane.

The Lyapunov stability criterion has the following advantages:

- The criterion is applicable to nonlinear systems;
- The stability conditions are not conservative.

Concerning the disadvantages:

- The criterion cannot address the infinite-dimensional models generated by communication delays;
- Stability margins are not available;
- It is necessary to use the human operator and environment models.

V.2. Stability analysis with unknown operator and environment models

Generally, for the stability analysis of the teleoperation system, the knowledge of the human operator and the environment dynamics are needed in addition to the teleoperator model (2.6). However, assuming that Z_h and Z_e are passive, we might be able to draw stability conditions that are independent of the human operator and the environment. In such conditions, *absolute stability* based on passivity theory is used. For more details about the passivity theory, the readers can refer to (Haykin 1970).

Absolute or unconditional stability means that the system is stable for all possible passive operators and environments. The necessary and sufficient conditions for absolute stability can be expressed in terms of the H-parameters (Haykin 1970). These conditions are known as Llewellyn's criterion for absolute stability:

1. $h_{11}(s)$ and $h_{22}(s)$ have no poles in the right half plane;
2. Any poles of $h_{11}(s)$ and $h_{22}(s)$ on the imaginary axis are simple with real and positive residues;
3. For $s = j\omega$ and all real values of ω

$$\begin{aligned} &\Re(h_{11}) \geq 0 \\ &\Re(h_{22}) \geq 0 \\ &2\Re(h_{11})\Re(h_{22}) - \Re(h_{12}h_{21}) - |h_{12}h_{21}| \geq 0 \end{aligned} \tag{2.24}$$

where $\Re(.)$ and $|\,.\,|$ denote the real and the absolute values, respectively.

If any of the above conditions is not satisfied, the network is potentially unstable, *i.e.* there exists a combination of operator and environment for which the system is unstable. However, it does not mean that a potentially unstable system is necessarily unstable.

The last equation of condition 3 can also be rewritten (Hashtrudi-Zaad & Salcudean 2001) as:

$$\eta \geq 1 \tag{2.25}$$

where η is called the *network stability parameter* and defined as

$$\eta = -\cos\left(\arg(h_{12}h_{21})\right) + 2\frac{\Re(h_{11})\Re(h_{22})}{|h_{12}h_{21}|} \tag{2.26}$$

It is interesting to notice that with identical forces and velocities at master and slave side (2.8), $\eta = 1$. This means that the perfectly transparent system is marginally absolutely stable. As a result, to have a higher stability robustness, perfect transparency has to be compromised. This is another illustration of the classical trade-off between stability and performance.

The advantages of absolute stability is

- Models of the human operator and environment are not needed.

Disadvantages are

- The stability conditions can be conservative;

- The criterion is not applicable to nonlinear systems.

VI. Applications

From its early use in the remote handling of radioactive materials, the application of teleoperation has expanded to include manipulation at different scales and in virtual worlds. Teleoperation systems are useful in remote or hazardous operations such as space and underwater explorations, as well as in delicate operations such as micro-surgery and micro-assembly.

VI.1. Handling hazardous material

Haptic teleoperation technology is said to have had its origins in the work of (Goertz 1952), who developed the first master/slave remote manipulator for the CEA at Argonne National Laboratory[1]. This electromechanical teleoperation device allowed humans to handle radioactive materials more safely by connecting them to the mechanical arms that moved the dangerous substances solely by electrical connections (Fig. 2.9).

However, until the development of modern computing components such as microprocessors, the joints of the master and slave were directly coupled, where the motion of each joint of the master device directly replicated in those of the slave unit. With widespread availability of microprocessors in the 1980s, research in haptic teleoperation has begun to flourish. In that era, it was (Bejczy 1980) who recognized the importance of force reflection/feedback in the man-machine interface. Another works involve handling nuclear materials with visual and force feedbacks are mentioned by (Vertut & Coiffet 1986). Also, a recent application appears in (Wang & Yuan 2004) for detecting leaks of sealed radioactive materials.

Fig. 2.9. The first teleoperation system developed by (Goertz 1952)

VI.2. Underwater vehicle

During the 1980 and 1990 years, one of the main applications of teleoperation was in unmanned underwater vehicles for scientific exploration or military applications. The use of the tethers to control such vehicles is not practical as they get caught and tangled (Fig. 2.10). On the other hand transmitting control and feedback signals through aquatic media introduce significant delays which affect the performance and even stability.

[1] http://www.anl.gov/ (last visit on 16 June 2011)

The method for dealing with teleoperated systems is the supervisory control, thus the time delay problem was tackled from this angle (Funda & Paul 1991).

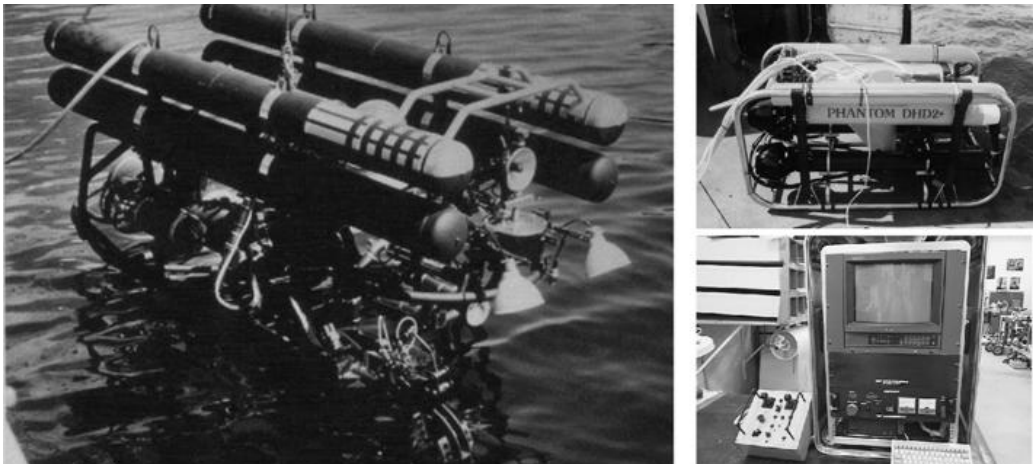

Fig. 2.10. Cable-controlled Underwater Recovery Vehicle (left) and its control console (right) (SPAWAR Systems Center, San Diego).

VI.3. Space robots

Space exploration and operation in geosynchronous orbits require teleoperated robots in order to reduce cost of assembly, maintenance and repair tasks in space as well as risk reduction for the astronauts. More recently, experiments were conducted by (Imaida et al. 2004) that allowed teleoperation of a 6DOF robotic arm on board of the Engineering Test Satellite VII in orbit with over a 7s delay, using a virtual environment scheme and predictive display.

Germany's ROKVISS[1] (RObotic Components Verification on the International Space Station) is one of the more recent projects towards these objectives, which is aimed at conducting experiments in outer space of lightweight robotic manipulators (Fig. 2.11)

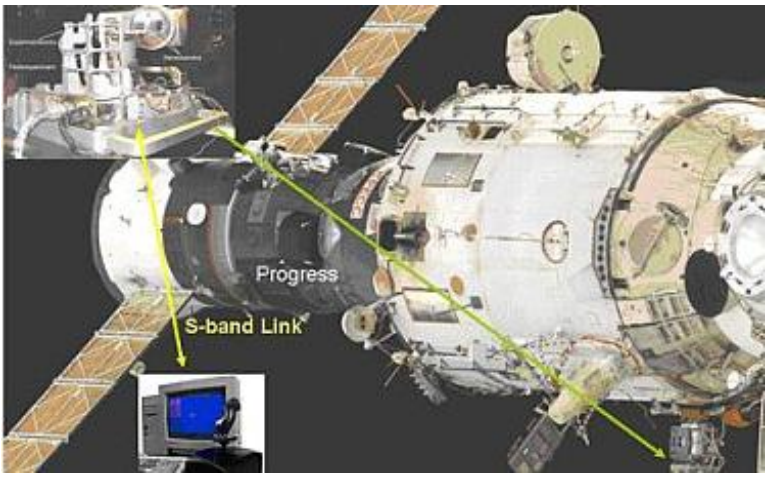

Fig. 2.11. ROKVISS robot (ISS-photo by courtesy of NASA).

[1] www.robotic.dlr.de/ (last visit on 16 June 2011)

VI.4. Micro-surgery

Microsurgical procedures involve tool positioning and force sensing capabilities bordering on the normal range of human abilities. The motions required are typically as small as a few microns and the forces encounters may be as delicate as a few milli-newtons (mN). Generally, microsurgery constitutes a few hours of operation that can result in a fatigue or a physiological tremor for the surgeons. Despite the increasing demand for microsurgery operations, only a few physicians are opting for this specialty because of excessive physical and psychological stress involved. Micro-surgery requires an advanced level of training and employs highly specialized equipment (Riviere et al. 2003). Thus, microsurgery is an ideal field to take advantage on the teleoperation technology (see Fig. 2.12).

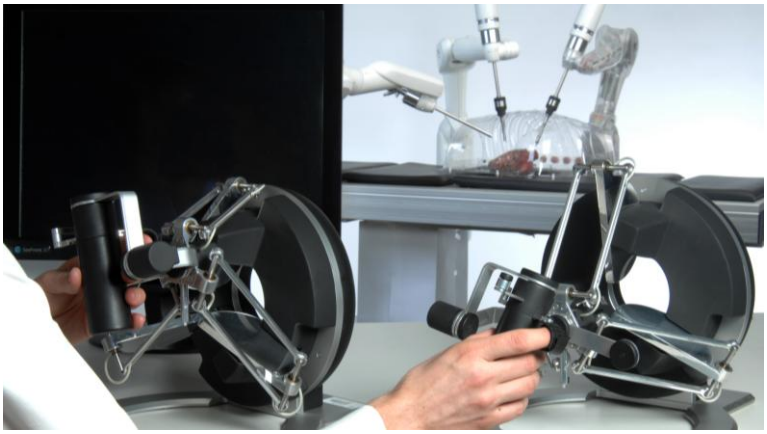

Fig. 2.12. Example of microsurgery using haptic teleoperation system.

As it can be seen in Fig. 2.12, the use of teleoperation technology with force feedback allows to enhance the skills of surgeons, improve the success rates of microsurgical procedures, and reduce surgical costs by increasing the precision and speed of operations. Furthermore, it offers a possibility to exchange the medical expertise around the world without requiring the physician to travel. Design issues in microsurgery can be found in (Son & Lee 2008); and remote telesurgery experiments have been reported with a distance of approximately 700 km (Mitsuishi et al. 1995), where time delays are a major concern.

VI.5. Mobile robots

Mobile robots have recently emerged as a new application of bilateral teleoperation. Although mobile robots do not fall into the traditional teleoperation setting, since kinematic similarity between the master and slave is eliminated, it is still possible to place them under force feedback through the use of a haptic device as in (Diolaiti & Melchiorri 2002). Recently, (Dongjun Lee et al. 2006) also incorporate time delays into the communication loop.

Once operating in a remote location, mobile robots send visual feedback to the human operator that allows her/him to assess the surroundings. However, this requires a high bandwidth to transmit real-time visual data to the operator, besides the fact that the camera has a limited viewing angle. Therefore, it is necessary to send an extra force feedback signal to the operator allowing him to sense the surrounding of the mobile robot and alleviating the need for high quality visual feedback (see Fig. 2.13).

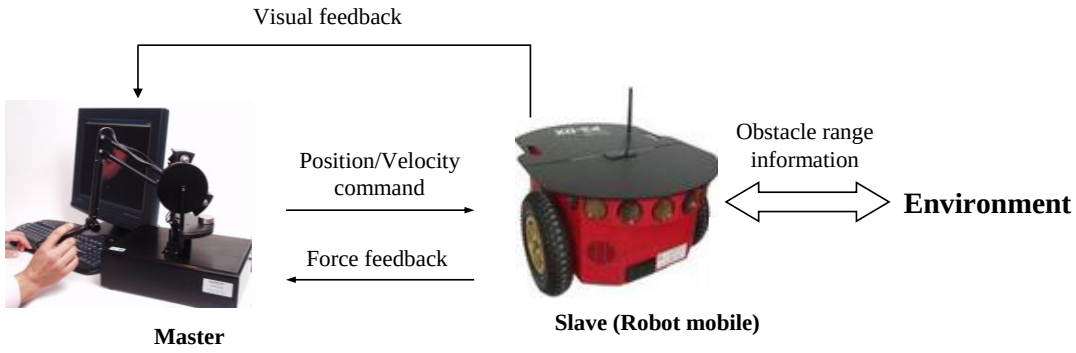

Fig. 2.13. Control scheme of the mobile robot.

VI.6. Future trends

Telemedicine is an area that requires great care in teleoperation since mistakes are life threatening. Moreover, delays and loss of information could be dramatic. The basic results in this area can be further expanded along the lines of remote surgery and possibly remote examination. First responders at an accident scene, fire, or other disaster would benefit from having robotic devices that can communicate wirelessly, carry video, audio, and tactile sensors, and have manipulation capability to rescue, examine, or administer first aid to victims. Multiple such devices could be used within large buildings and would have to communicate among themselves and with a human operator (Hokayem & Spong 2006).

In a mobile robotic context, the recent problem of coordinating multiple mobile agents to achieve a common heading or perform a certain task is a natural extension since the one-to-one teleoperation can be scaled into one-to-many setting. These applications suggest that the next step in bilateral teleoperation is to take a leap from one-to-one master slave system onto one-to-many, as in Fig. 2.14, or even n-to-m master slave systems. However, adopting centralized versus decentralized control for this problem is still a research topic (Hokayem & Spong 2006).

In the area of nanotechnology, nanomanipulation using teleoperation offers many challenging problems for future research. These problems are only just beginning to be addressed (Jian Wang & Shuxiang Guo 2007; Onal & Sitti 2009).

Finally, haptic teleoperation is an exciting field, and it contains numerous interesting challenges to be investigated.

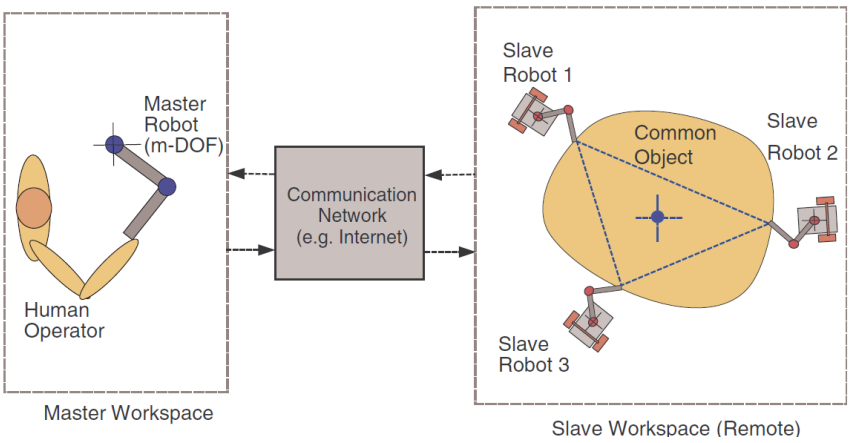

Fig. 2.14. Single master operator commanding multiple slaves.

VII. Conclusion

This chapter has provided a brief overview of the bilateral teleoperation system, in which some relevant points have been raised.

The first point described a general linear model of the different blocks (i.e., operator, environment, controller, transmission line, master, and slave) in a teleoperation system, allowing to explain how forces and movements are bilaterally transmitted from the operator to the environment and vice versa. For an easier performance analysis and controller design of the teleoperator, a representation of the two-port network was investigated so that the force and position relationship of the master and slave could be expressed through the H-matrix parameters (h_{11}, h_{12}, h_{21}, h_{22}). According to (Aliaga et al. 2004), the most appropriate selection of experimental tests to fully characterize any teleoperation system is free motion and hard contact tests. In other words, these test's data allow us to fully identify the teleoperator's H-matrix elements, by using system identification methods.

The second point presented a transparent analysis and comparison of the most commonly used LTI teleoperation architectures (i.e. 2CH, 3CH or 4CH) whose classification is given by the number of communication channels. It has been established in the literature that the 4-CH control architecture is the most successful in terms of ensuring full transparency (Lawrence 1993; Yokokohji & Yoshikawa 1994). On the other hand, none of other methods (2CH) such as position error based, force error based, and direct force reflection can achieve ideal transparency. From (Tavakoli et al. 2008), the 3-CH control architectures can be theoretically considered transparent under ideal conditions. However, in practice, due to the lack of master/operator or slave/environment interaction force measurement, the force tracking performance in the 3CH architecture may be somewhat degraded. This aspect will be experimentally justified in chapter 4.

In the last point, performance measurements and stability formulae that based on the linear model of hybrid matrix notation were investigated. It has been seen that there exist several performance criteria such as tracking error, bandwidths, scaling product, transmitted impedance, transparency, etc. that allow to assess the above control architectures. In our case, only transparent condition will be considered since it is assumed to be sufficient to evaluate our control approach (cf. chapter 4 and chapter 5). It is noteworthy that stability in bilateral teleoperation commonly depends on the characteristics of both operator and environment. However, when the operator and environment are passive, stability analysis can be used when these characteristics are not exactly known. This method based on the passivity theory is frequently presented in literature because it ensures that the system is stable in contact with a larger range of human and environment impedances.

To resume, one can notice that most of literature on bilateral teleoperation discusses only the linear case, neglecting in some sense the fact that in reality nonlinear dynamics are involved. Moreover, a decoupling assumption is often made, i.e. generally only a one-dimensional case is considered. Very few authors have faced the full geometric (3D) problem of teleoperation systems, considering the couplings that may arise for example between linear and rotational motions/forces (Stramigioli et al. 2002). In conclusion, although the relevant and impressive quantity of research developed in teleoperation field, there are questions and aspects that still wait to be solved in a satisfactory manner. For these reasons, teleoperation will constitute in the next years a very challenging area for the control community.

During the first two chapters, several research perspectives on haptic devices and teleoperation systems have been addressed. Most of existing force-feedback teleoperations uses direct-current motors as actuators thanks to their simplicity in implement and control. Pneumatic actuators, which offer further advantages such as high force-to-mass ratio, MRI compatibility and adaptable compliance, are considered to be an alternative to the electrical ones. However, due to the challenging control problem caused by their highly nonlinear model, pneumatic actuators are less used in haptic teleoperation systems. Ampere laboratory, with its domain expertise in fluid power as well as in robotic control (Kella 1987; Det 1991; Prelle 1997; Thomann 2003; Smaoui 2005; Olaby 2006), offers a possibility to realise such systems that controlled by pneumatic technology. Therefore, our work will firstly focus on a design of the pneumatic actuated haptic teleoperation system. For controlling the mass flow rate of the pneumatic actuators, two valve technologies are employed, i.e. on/off solenoid

valves and proportional servovalves. Next, several bilateral control laws with different teleoperation control architectures (i.e., 2CH, 3CH, and 4CH) will be studied and testified on the experimental setup. Finally, a comparison among different control strategies in terms of transparency and haptic sensation is investigated in order to justify the efficacy of each method. It is noteworthy that for an easier validation of the control law, only 1-DOF master-slave system is elaborated in our study. A design of a more complex mechanical architecture – a multi-DOF system remains as future work.

Chapter 3
Description of a single DOF Pneumatic Haptic Interface

Table of content

I. Introduction

In this chapter, we describe the design of a one-DOF haptic interface used in pneumatic-actuated teleoperation system. Most of applications required multi-DOF system. However, as a first prototype and for the sake of simplicity, the mechanical design of our system is relatively simple where the master and the slave are identical and are one-DOF pneumatic manipulators. In the following, we will justify the choice of this architecture for our development.

There are important differences between the single-DOF case and the multi-DOF case. First, the tasks are different, and the force feedback information is clearly less complex in one-DOF. Secondly, multi-DOF robots have highly non-linear dynamics and kinematics which vary significantly over the workspace of the manipulator (Buttolo et al. 1994). This means that linear analytical tools such as the two-port matrix (cf. chapter 2, section II.6) are only locally valid. Still, it is relatively easy to implement control laws in one-DOF, as well as to measure performance. Finally, significant insights into control law performance can be gained rather quickly as a first step for a future test in multi-DOF systems (Lawn & Hannaford 1993).

Commonly, the teleoperation systems with identical structures for master and slave robots is widely used since the control theory is getting much more complicated when dealing with totally dissimilar kinematics. This is especially the case when slave robots are required to explore wide workspaces and carry out sophisticated tasks. However, most teleoperation systems involve the use of ground-based haptic devices with limited workspaces (e.g., a few cubic centimeters). In order to adjust both workspaces of master and slave robots, several control strategies have been investigated. (Conti & Khatib 2005) developed a computer mouse-like drifted workspace control which significantly increased the workspace area. Among others, the control law proposed in (Chotiprayanakul & Liu 2009) ensured workspace mapping by variable position scaling factors. Moreover, (Formaglio et al. 2008) solved the limited workspace issue by mounting the haptic interface on a mobile platform. Since our study is focused on the implementation of the bilateral controller for a simple haptic teleoperation system, the master and slave actuators are designed to be identical.

This chapter is organized as follows. Section II introduces the specifications of the haptic teleoperation device. Sections III describes a low-friction technology of the pneumatic actuator, followed by section IV which provides some features and principles of sensors used in our prototype. Section V is dedicated to the performance and characteristics of the proportional servovalves and on/off solenoid valves. Section VI presents the experimental prototype. Finally, conclusion is drawn in Section VII.

II. Performance Specifications

As no practical application has been selected for our system, the features of our haptic device are not based on any specific operating task, but rather on existing haptic devices dedicated to surgical procedure.

The master and slave manipulators should be able to apply a maximum force of about 100 N, which is enough to perform numerous tasks in surgery (needle insertion, palpation, MIS technique in orthopedics). Concerning the workspace, an amplitude of 0.1 m along the one DOF is chosen. This value is high enough to allow most of surgical gestures. Position resolution generally depends on the task requirements. In our case, a value of 0.5 mm is chosen is because it is considered the desired precision of the position tracking error.

Furthermore, the interfaces should be designed to reduce friction as much as possible. Indeed, this disturbance force could be felt by the user when moving the master robot, which pollutes haptic rendering and deteriorates human perception. Although compensation of the friction can be done by software, that could be never total. As a result, another appropriate option to minimize the disturbance force involves employing a suitable mechanical design. In our case, a low-friction pneumatic cylinder and a non-contact position sensor are chosen (cf. Sections III and IV.1), that allow to reduce significantly friction in the haptic device.

Lastly, the system is considered to have a small motion bandwidth (i.e., less than 5 Hz), which correspond to the bandwidth of position that human can generate. On the other hand, a high control bandwidth (i.e., greater or equal than 500 Hz) is necessary to achieve a good haptic-loop performance. This condition determines the choice of an appropriate valve technology (cf. section V).

To sum up, the developed haptic interface has to satisfy the following specifications (Tab. 3.1)

Parameters	Value	Unit
Maximum force	100	N
Force resolution	0.1	N
Friction force	< 2	%
Maximum displacement	0.1	m
Position resolution	5.10^{-4}	m
Mechanical bandwidth	< 5	Hz
Control bandwidth	≥ 500	Hz

TAB. 3.1. SPECIFICATIONS OF OUR 1-DOF HAPTIC INTERFACE

Fig. 3.1 shows the mechanic principle of our interface. Each master and slave device equipped by a double acting pneumatic actuator (with two chambers p and n), pressure/force/position sensors, and (solenoid or servo) valves.

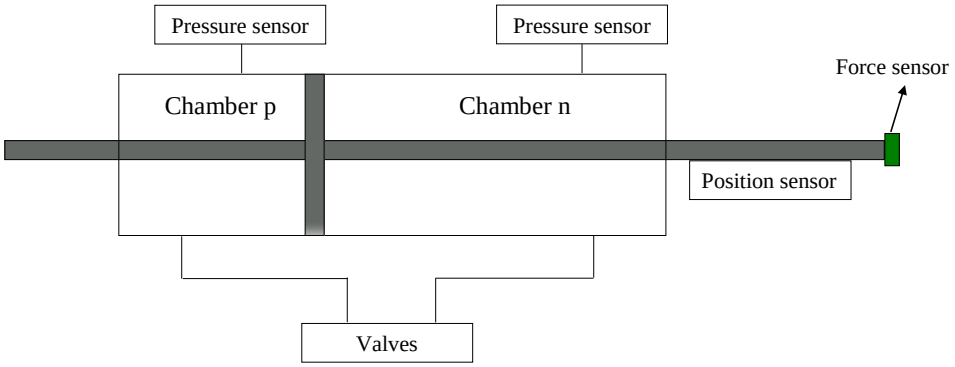

Fig. 3.1. Mechanical principle of a pneumatic system

In the following sections, a description of the different components, i.e. actuator, sensors, and valves used in our system (Fig. 3.1) are respectively introduced.

III. Actuation

As mentioned in chapter 1 (section III.1.1.2), due to the well-known advantages of the pneumatic actuators such as high power-to-mass ratio, low heat generation, and clean source, they are used for various applications of haptic teleoperation in recent years. For instance, Tadano and Kawashima (Tadano & Kawashima 2007) propose a forceps manipulator for a surgical master-slave system, which is able to estimate external forces without using any force sensor. (Durbha & Li 2009) proposed a passive scheme for bilateral teleoperation with human power amplification using pneumatic actuators. The input human force was amplified through the pneumatic teleoperator to provide assistance for the human operator in terms of performing the task (for lifting a heavy object). Pneumatic muscle actuators have been also recently used in the teleoperation system (Tondu et al.

2005). They are compact and have high power/weight density, but they are difficult to control and require an accurate experimental characterization. In addition, as detailed in chapter 1 (section III.1.1.2), other limits of pneumatic muscle actuators are slow dynamics, limited displacement, high hysteresis, etc. Therefore, this kind of technology will not be chosen for our development.

In this study, we investigate the use of pneumatic cylinders in a master-slave teleoperation system. As any actuators, the pneumatic cylinders have some drawbacks, in particular friction effect which may deteriorate the performances of the haptic interface. In order to minimize this disadvantage, a research of low-friction cylinders was undertaken. Among different products existed in the market, Airpel cylinders, i.e. designed and commercialized by Airpot[1], is chosen according to the characteristics defined in Tab. 3.1.

An advanced technology used in Airpel is that it employs a precision graphite piston which can slide freely – without lubrication – inside a Pyrex glass cylinder (see Fig. 3.2). A fire-polished surface of the glass is inherently smooth, allowing to reduce significantly the friction.

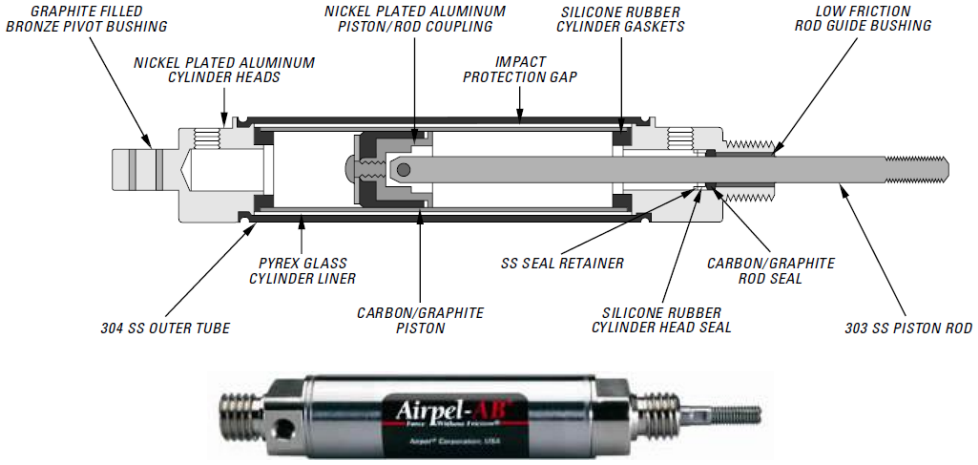

Fig. 3.2. Airpel cylinder construction[2]

As illustrated in Fig. 3.3, the Airpel cylinder presents a superior performance in terms of static friction over conventional cylinders. Due to the benefit of ultra-low friction, the Airpel cylinder is particularly well-suited to applications requiring smooth motion at low pressures – and to move delicate loads at either slow or high speeds.

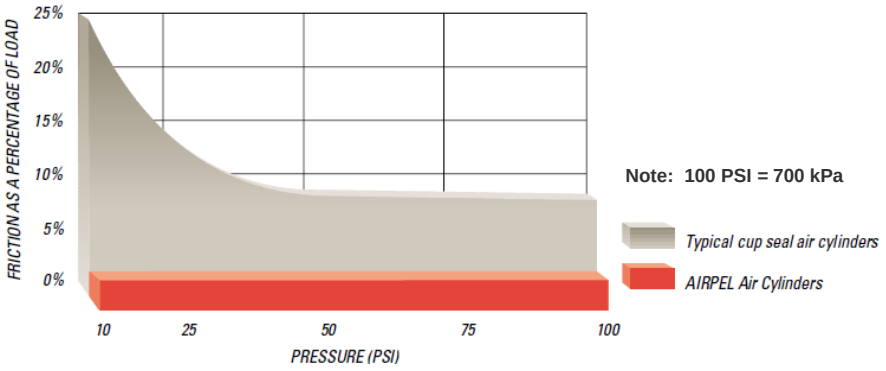

Fig. 3.3. Pressure versus static friction of Airpel and typical air cylinders[1]

[1] http://www.airpot.com/ (last visit on 16 June 2011)

[2] http://pdf.directindustry.com/pdf/airpot/everything-you-need-to-know-about-airpel-anti-stiction-air-cylinders/Show/11558-45874-_5.html (last visit on 16 June 2011)

A main downside of low-friction cylinders is a risk of air leakage. Indeed, there is generally a trade-off between friction and leakage. In conventional air cylinders, no air leakage is in exchange for higher friction. On the other hand, with Airpel cylinder, a little air leakage is in return for ultra-low friction (see Tab. 3.1). Since friction is one of our main concerns in haptic design and since small air loss is not relevant in most of teleoperation applications, Airpel cylinder is chosen.

Between two principal types of cylinders, i.e. the double acting and the simple acting, the first one is selected because it enables to control independently the pressure/mass-flow-rate of each chamber, thus resulting in improved force and motion controls.

The M16D100D cylinder whose features shown in Tab. 3.2 has been chosen to actuate the master and slave manipulators. This choice was done according to the specifications required for our application (Tab. 3.1).

Parameters	Value	Unit
Bore	16	mm
Stroke	100	mm
Diameter of piston rod	5	mm
Max pressure	700	kPa
Min pressure differential required for actuation	< 1.5	kPa
Maximum force	110	N
Piston friction as % of load	1−2	%
Operating temperature range	−55 to 150	°C
Maximum leakage (at 340 kPa)	1.39	Nl/mn
Weight of piston/rod assembly	60	g
Weight of complete unit	166	g

TAB. 3.2. TECHNICAL DATA OF M16D100D PNEUMATIC CYLINDER[1]

Note that the pneumatic actuator used (M16D100D) is a symmetric cylinder whose rod extending from both sides of the piston. This leads to simplicity in guidance and implementation since the surface parameter of two cylinder chambers and the leakage phenomenon may be considered to be identical. Also, it is possible to add external mass or some mechanical joints on both sides of the piston.

IV. Sensing

Besides all kinds of actuation have been developed, sensing is also an essential criterion to design a high-quality haptic control. Sensors in the last few years tend to be more accurate. The aim of this subsection is to provide a little basic knowledge of the operating principle as well as some features of position, force and pressure sensors.

IV.1. Position sensor

The use of the position sensor is necessary since the information about the position of the end-effector is compulsory. Among the different technologies of position sensor, the linear variable

[1] http://www.airpot.com/html/airpels.html (last visit on 16 June 2011)

differential transformer (LVDT) is chosen thanks to its advantages such as low cost, non-friction, high repeatability, fast dynamic response and long lifetime.

The 2000 DC-EC[1] model with the signal conditioning equipment of Measure Specialities[2] (MEAS) is presented in Fig. 3.4. This model is chosen according to the specifications shown in Tab. 3.1.

Fig. 3.4. LVDT sensor – 2000 DC-EC model of MEAS

The features of the 2000 DC-EC position sensor are shown in Tab. 3.3 below.

Parameters	Value	Unit
Nominal linear range	± 0.05	m
Nominal input voltage	± 15	V
Power supply current	± 25	mA
Output voltage	± 10	V
Output impedance	< 1	Ω
Response (-3 dB)	200	Hz
Accuracy[3]	± 0.1	%
Operating temperature range	0 to 70	°C
Survival temperature range	–55 to 95	°C

TAB. 3.3. TECHNICAL DATA OF THE 2000 DC-EC POSITION SENSOR

Fig. 3.5 shows the output voltage responses versus the position of the two sensors used for master and slave manipulators. These data calibrations are provided by standard sensor datasheet of MEAS. As it can be observed, the output voltage is perfectly linear with respect to the position, reflecting an excellent linearity of the LVDT sensors. In consequence, it is easy to determine the relationship between the output voltage and the real position ($y = ax + b$).

[1] http://www.meas-spec.com/product/t_product.aspx?id=2620 (last visit on 16 June 2011)

[2] http://www.meas-spec.com/ (last visit on 16 June 2011)

[3] Combined nonlinearity, hysteresis and repeatability (last visit on 16 June 2011)

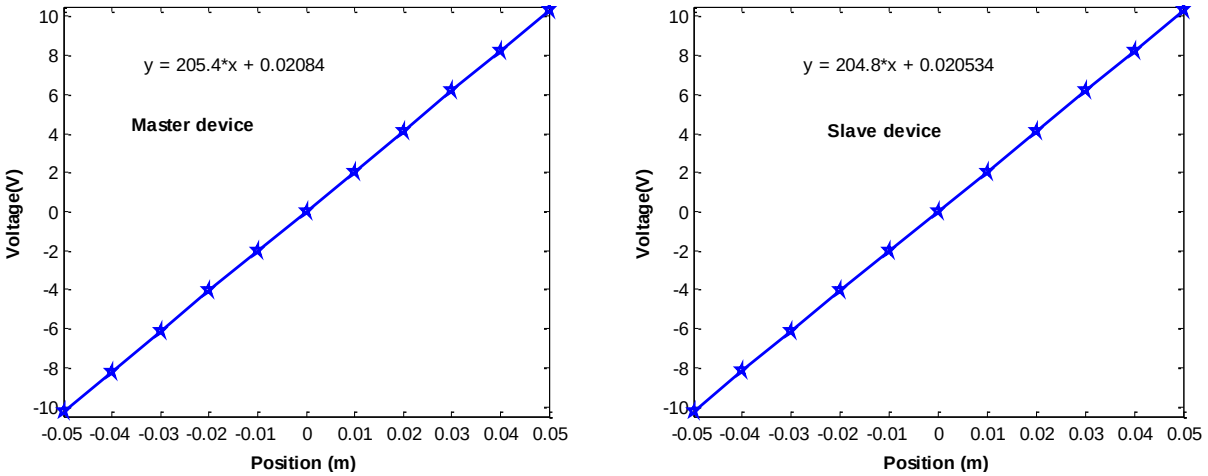

Fig. 3.5. Calibration of two position sensors

IV.2. Force sensor

Force sensors are widely used in robotic applications. There exist two main methods for determining forces, i.e., *load cell* and *force observer*.

Load cell uses strain gage technology to measure force. The strain gages, which compose four (active or fixed) resistors with the same nominal value, are used in a Wheatstone bridge circuit so that a small change in resistance will lead to a change in voltage, i.e., proportional to the applied force. A main advantage of the load cell is a possibility to achieve high force accuracy because the Wheatstone bridge is well suited for measuring the small resistance change in the strain gage. However, major drawbacks of the load cell are extra mass, high cost and implementation complexity. Indeed, special care must be taken to ensure that the force is applied perpendicular to the surface at a predefined position. A default of alignment in the mechanical link can distort the measurements and also damage the instrument.

Force observer, which is based on measurements of position and/or pressure in combination with pneumatic actuator model, can be used as a substitute for force sensors. Nonetheless, proper functioning of the software has to be ensured in order to achieve satisfactory results. Since accuracy is one of the most important criteria in haptic device, load cell is chosen for a first feasibility study (cf. chapter 4). A study of the force observer in the pneumatically-actuated haptic teleoperation systems will be presented in chapter 5, section IV.

Tab. 3.4 resumes the advantages and disadvantages of the force observer and the load cell.

	Advantages	Disadvantages
Load cell	Accurate measurements	Design precaution (alignment problem) Add extra mass to the system → size and weight problem Expensive
Observer	No extra mass added to the device	Performance depends on system model and data quality → model and data errors might result in incorrect measurements

TAB. 3.4. COMPARISON OF FORCE MEASUREMENT OPTIONS

Among the different load cell models of MEAS, ELPF[1] model shown in Fig. 3.6 (a) is selected due to its small size, high performance and acceptable cost. Indeed, it enables to measure both

[1] http://www.meas-spec.com/product/t_product.aspx?id=2430 (last visit on 16 June 2011)

compression and extension forces thanks to the full bridge architecture as illustrated in Fig. 3.6 (b). Moreover, it is possible to integrate a high-amplified-output module, leading to increase resolution of the sensor (see values of output voltage in Tab. 3.5).

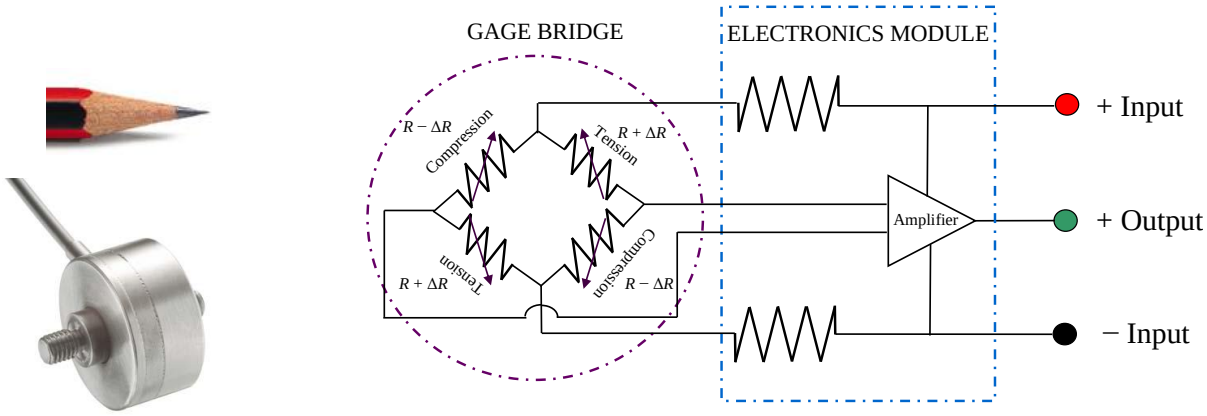

(a) Mechanical part (b) Electrical scheme

Fig. 3.6. ELPF model of MEAS force sensor

The features of the ELPF model are shown in Tab. 3.5.

Parameters	Value	Unit
Force range	± 100	N
Maximum overload	250	%
Nominal input voltage	5	VDC
Power supply current	40	mA
Output voltage (amplified module)	0.5 – 4.5	V
Output voltage (bridge output)	20	mV/V
Output at no load (zero force)	± 5	%
Input impedance	3	kΩ
Output impedance	2.2	kΩ
Accuracy	± 0.1	%
Operating temperature range	–14 to 120	°C
Deflection at rate load	< 0.05	mm
Weight	40	g
Cycle life expectancy	unlimited	cycles

TAB. 3.5. TECHNICAL DATA OF THE FORCE SENSOR – ELPF MODEL

A calibration of the two load cells were carried out in the laboratory (see Fig. 3.7). As it can be seen, the voltage output of the force sensors is linear with respect to the applied force.

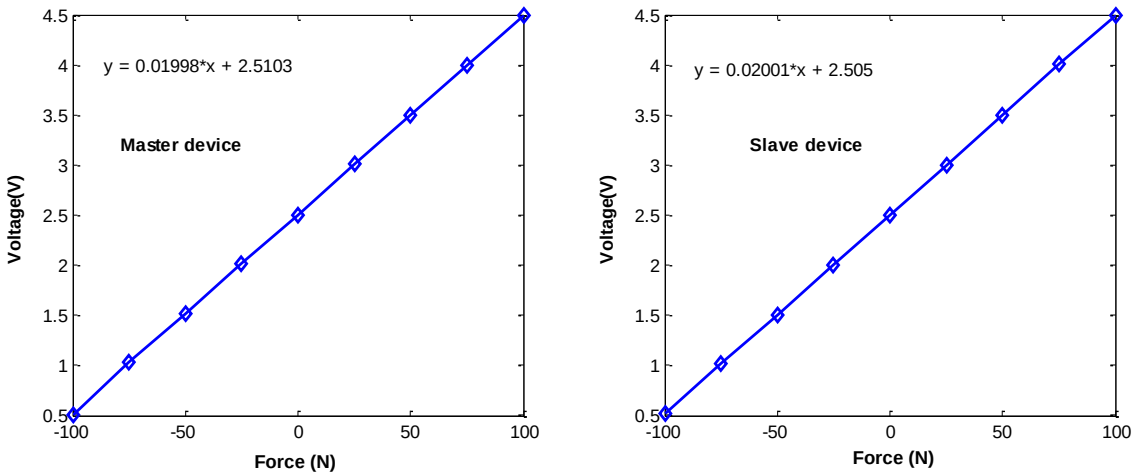

Fig. 3.7. Experimental results of static force sensor calibration

IV.3. Pressure sensor

The last kind of measuring instrument that we present here is pressure sensor. Although there are various types of pressure sensors (e.g., thermal conductivity, resonance frequency, piezoelectric, capacitive, sound velocity, etc.), one of the most common is the strain-gage base transducer. The conversion of pressure into an electrical signal is achieved by the physical deformation of strain gages which are bonded into the diaphragm of the transducer and wired to the Wheatstone bridge configuration. Pressure applied to the sensor produces a deflection of the diaphragm which introduces strain to the gages. The strain will produce an electrical resistance change proportional to the pressure.

Fig. 3.8 shows the U5100 model, commercialized by MEAS.

Fig. 3.8. Pressure sensor – U5100 model[1]

Besides the benefit of high quality-to-price ratio, a main downside of the U5100 model is its cumbersome size. It is therefore impossible to incorporate the sensor into the cylinder chambers and finally, the result of pressure is not exactly equal to what it is desired to measure.

The features of pressure sensor can be found in the following table. As it can be seen, its performance is good enough for our system.

[1] http://www.meas-spec.com/product/t_product.aspx?id=2886 (last visit on 16 June 2011)

Parameters	Value	Unit
Pressure range	0 – 700	kPa
Burst pressure	3000	kPa
Pressure overload	1500	kPa
Nominal input voltage	5	V
Power supply current	40	mA
Output voltage	0.5 – 4.5	V
Accuracy	± 0.2	%
Response time	1	ms
Operating temperature range	– 40 to 125	°C
Weight	82	g
Pressure cycle	10	million

TAB. 3.6. TECHNICAL DATA OF THE U5100 PRESSURE SENSOR

For both master and slave manipulators, four pressure sensors are needed. In fact, each cylinder requires one sensor per chamber (and thus two sensors). The sensor calibrations are presented in Fig. 3.9. The output voltage is linear according to the input pressure for each sensor. Note that all calibration is performed at room ambient temperature and under atmospheric pressure (~ 100 kPa).

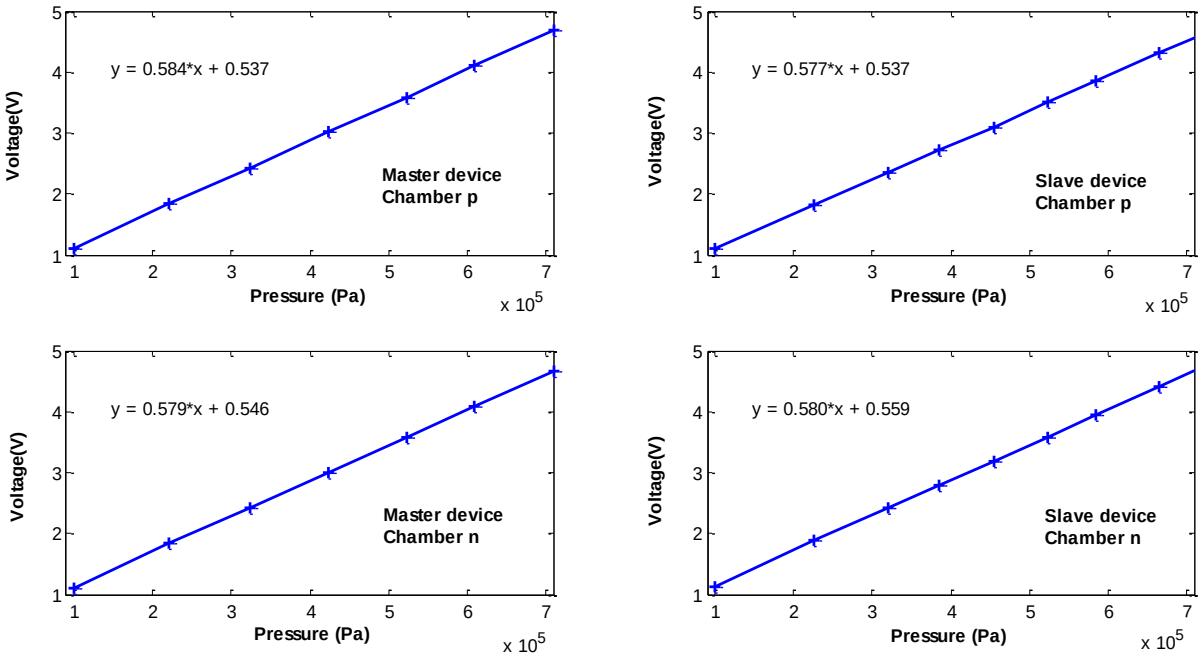

Fig. 3.9. Experimental result of the static calibration of four pressure sensors

V. Pneumatic Valves Technologies

The control of pneumatic actuators is typically implemented using proportional servovalves to control the air flow into and out of the cylinder. The continuous behavior of the mass flow rate delivered by these valves has made them a suitable choice for closed-loop servo applications. Several researchers have studied the design and control of such systems, including (Shearer 1956; Mannetje

1981; Bobrow & McDonell 1998) whose studies involve servo control via spool-type servo-valve, (Jacobsen et al. 1986; Ben-Dov & Salcudean 1995; Sesmat 1996; Henri et al. 2002) whose studies involved control via *flapper* or *jet-pipe* type servovalves. In such systems, due to the requirements of high-precision manufacturing, the cost of the servovalves in nearly all cases dominates the cost of the actuator.

In the pneumatic actuation control system, an alternative to the proportional servovalves is to utilize fast-switching on/off valves. Owing to their low cost, lightweight and small size, the on/off valves have received considerable attention over the last years (Gentile et al. 2002; Barth et al. 2003; Ahn & Yokota 2005; Le et al. 2011a). Thanks to the breakthroughs in valve technology such as leak reduction, miniaturized mechanical elements and fast electronic components, the solenoid valves now are faster and more accurate than the former valves. There exist however some drawbacks such as acoustic noise and chattering effect, caused by fast-switching frequency. Furthermore, using on/of valves with inherent discrete behavior can result in complex nonlinearity of the pneumatic system.

This section is dedicated to the principle, performance and characteristics of the proportional servovalves and on/off solenoid valves. Practical implementation of these two technologies in the pneumatically-actuated teleoperation system will be performed in chapters 5 and 4.

V.1. Servovalves

In pneumatic-actuated robotic systems, jet-pipe type servovalves are normally used for obtaining precise control and accurate responses thanks to their simple structure, high sensitivity for control level, and wide frequency range (Shearer 1956). Contrary to the *spool* or *poppet* valves, the jet-pipe servovalves require low supplied current, i.e., typically less than 50 mA, offering a large mechanical benefit such as compact and small size. A main drawback of the jet-pipe technology is low efficiency caused by magnetically deflected for control, at the expense of extra air leakage (Henri et al. 2002).

In the following subsections, we first describe the operation principle of the jet-pipe technology. A characterization of the servovalves is then provided, in which we establish a mathematical model of the mass flow rate as a function of pressure and current. A comparison between the theory model and the experimental measurements will be carried out to validate our model.

V.1.1. Operating principle of jet-pipe pneumatic type servovalve

Fig. 3.10 shows a schematic representation of the jet-pipe servovalve, which can be separated into two stages:

- The first stage includes a torque motor, a projector jet and two receivers.
- The second stage includes a four-way sliding spool (i.e., supply, exhaust, orifices p and n), controlled by a force feedback closed-loop servo system.

Between the first and the second stages, a mechanical feedback connected to the spool and jet-pipe is employed to stabilize the valve operation. The jet-pipe servovalves operates as follows:

- At first step, the jet is equally separated between the two receivers, making the pressures on both sides of the spool equal. The balanced force created by equal pressures in both chambers holds the spool in a stationary position (see Fig. 3.11 (a)).
- When the motor receives an excitation applied as current to the coils, electrical signal is converted into a mechanical torque on the armature and jet pipe assembly. When the jet pipe and armature rotate around their pivot point, the fluid jet is directed to one of the two receivers, creating a higher pressure in the spool chamber connected to that receiver. The differential pressure pushes the spool in opposite direction to the jet pipe displacement (see Fig. 3.11 (b)).
- As the spool starts moving, it pushes the return spring, creating a torque on the jet pipe to bring it back to null position. When the restoring torque due to spool movement equals the applied torque on the armature, the spool will stop in a particular position, until reversing the polarity of the

applied current. The resulting spool position opens a specified flow passage at the ports p and n of the second stage of the valve (see Fig. 3.11 (c)).

Since the torque-motor forces are proportional to the input current and the feedback forces are proportional to spool position, the resulting spool position is proportional to the input current. Increasing the applied current to the torque motor shifts the spool from null position.

When the polarization of the applied current is reversed, the armature is attracted to the opposite magnetic pole and therefore, the jet deflects to the opposite receiver. The spool moves in an opposite direction until a balanced force is achieved by the return spring.

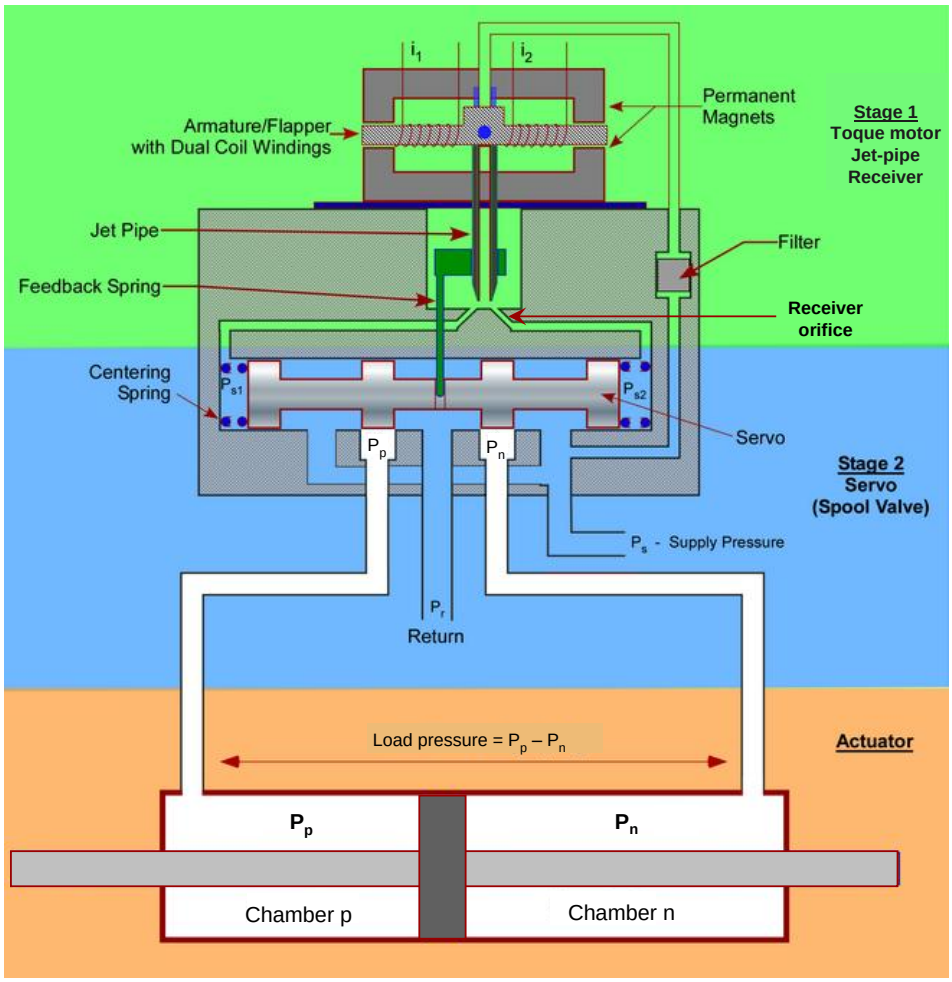

Fig. 3.10. Structure design of the two-stage jet-pipe servovalves[1]

[1] http://www.daerospace.com/HydraulicSystems/ServovalveDesc.php (last visit on 16 June 2011)

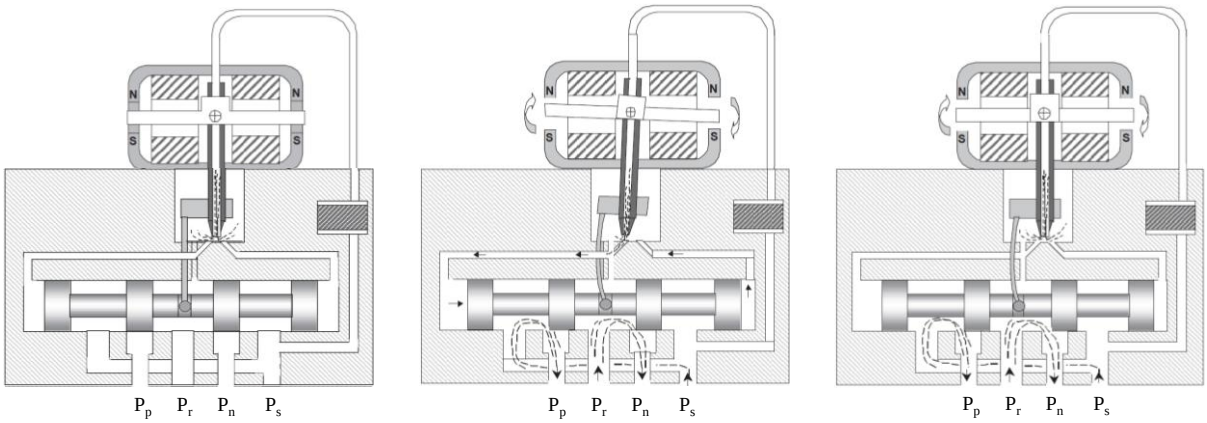

(a) At neutral position (b) With input current (c) Stabilized with current

Fig. 3.11. Three steps of jet-pipe operation[1]

It is noteworthy that the major of jet-pipe servovalves are two-stage design, but there also exist single-stage design whose torque motor directly attached to the spool. Such a design is limited a power capability of the motor's output force. Therefore, they are only used in a few applications of pneumatic actuators with low capability of mass flow rate.

On the contrary, the two-stage servovalves has a preamplifier which substantially multiples the force output of the torque motor to a level sufficient, allowing to overcome considerable stiction forces and force resulting from vibration. This is a reason for the wide use of the two-stage servovalves in both hydraulic and pneumatic systems.

V.1.2. Characterization of the Atchley 200PN-176

Atchley, which is now acquired by Moog[2], proposed the jet-pipe technique with high performance. The Atchley 200PN-176 model (Fig. 3.12), which has been already available in our laboratory, is implemented on our device since its characteristics answer our specifications. This servovalve is a single-stage type that includes four ways, i.e., supply air, exhaust, and two orifices which can connect to both chambers of a cylinder. The single-stage design is suitable for our pneumatic teleoperation system that requires small load force and low mass-flow-rate control.

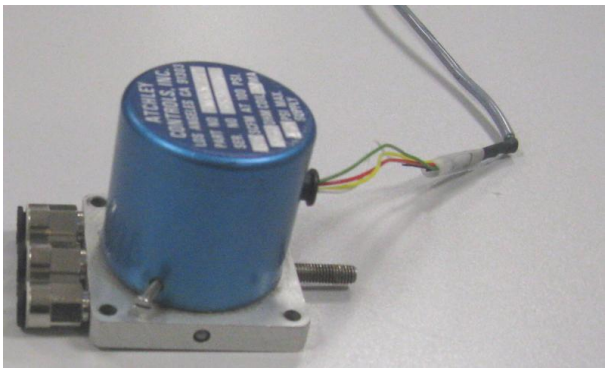

Fig. 3.12. Atchley 200PN-176 servovalve

[1] http://www.moog.com/literature/ICD/jet_pipe_servovalves_overview.pdf (last visit on 16 June 2011)

[2] http://www.moog.com/ (last visit on 16 June 2011)

The general characteristics of the 200PN-176 is shown in the below table.

Parameters	Descriptions
System filtration	25 micron
Fluid	Clean dry gas
Design	Single stage
Pressure range	0 – 1100 kPa
Burst pressure	3000 kPa
Pressure overload	1700 kPa
Power supply current	± 20 mA
Coil resistance	250 Ω
Temperature range	–40 °C to 70 °C
Hysteresis	3 % max of rated current
Threshold	0.02 % max of rated current

TAB. 3.7. PERFORMANCE SPECIFICATIONS OF THE 200PN-176 MODEL

At the moment, there is still no acceptable theoretical model that describes the behavior of the jet-pipe servovalve with sufficient precision to carry out a preliminary study in simulation. Our objective here is to find out the relationship between the voltage/current, pressure and mass flow rate of the Atchley servovalve.

V.1.2.1. Characteristics of the voltage-to-current converter i = f(u)

A supplied current of the servovalve comes from a voltage-to-current converter where the input voltage is provided from the dSPACE card. Note that the development and characterization of the converter are realized during the thesis. The electronic circuit of the converter based on TLE2061 operational amplifier is shown in Fig. 3.13 (a). This component is chosen due to its simple structure and excellent output drive capability.

In a normal operation of the amplifier, a linear relationship between the output current and the input voltage can be obtained as

$$i = \frac{R_2}{R_1 R_5} U \tag{3.1}$$

where $R_1 = R_3$ and $R_2 = R_4 + R_5$. As a result, the current i depends only on the voltage U, for any given load. Nonetheless, in practice, a too high value of load's resistance (e.g., several hundred MΩ) could lead to saturated amplifier. In our case, the coil resistance of the servovalve equals 250 Ω, enabling the converter to operate correctly as in (3.1).

Since the voltage range of the dSPACE card is ± 10 V and the applied current range of ± 20 mA is required to ensure an optimal use of the servovalve, the following condition needs to be satisfied

$$\frac{R_2}{R_1 R_5} = 0.002\,\Omega^{-1} \tag{3.2}$$

In this case, the values of the resistors can be set as $R_1 = R_3 = 10$ kΩ, $R_2 = 2$ kΩ, $R_4 = 1.9$ kΩ, and $R_5 = 100$ Ω.

To check the amplifier linearity, we plotted the data of current as function of the input voltage. A perfect linearity is obtained as illustrated in Fig. 3.13 (b).

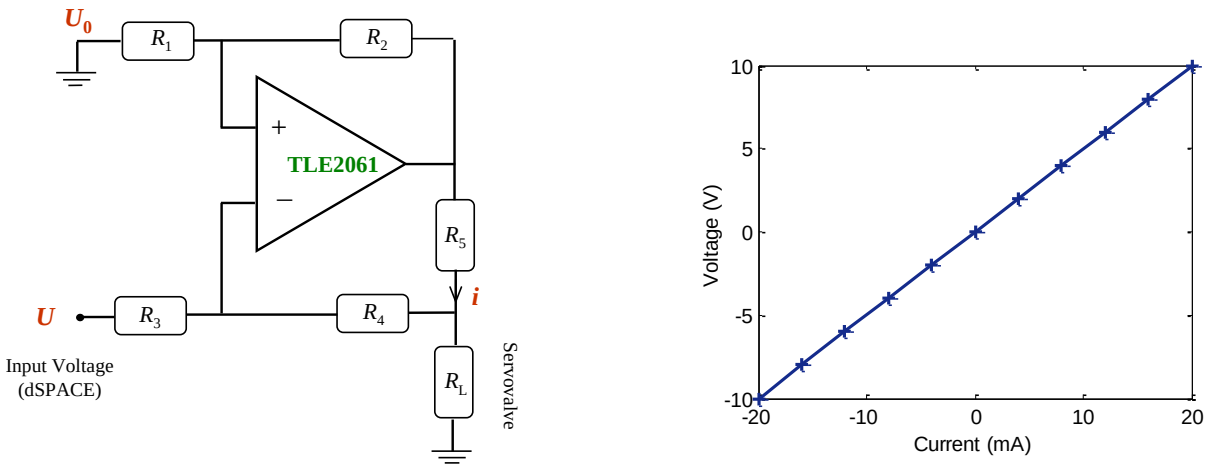

(a) Electrical scheme (b) Characteristics $U = f(i)$

Fig. 3.13. Voltage-to-current converter

In the following subsections, all experimental measurements are provided by (Fourati & Maalej 2006). Note that for an easier manipulation, the input control signal is chosen as the voltage U instead of the current i. This does not affect the characteristics of the servovalve since U and i have a linear relationship as shown in Fig. 3.13 (b).

V.1.2.2. Pressure gain characteristics P = f(U)

The goal of this experiment is to determine the characteristics of the pressure gain in function of the input voltage U when the mass flow rate equals zero. The supply pressure of 520 kPa is used for all the measurements. Note that the air flow of each orifice (p and n) of the servovalve directly charges to a chamber equipped with pressure sensor – this will help to measure the pressures P_p and P_n (at null value of mass flow rate).

Fig. 3.14 shows a static behavior of the pressures in chambers p and n. In order to observe a hysteresis phenomenon, the measurements were carried out by gradually increasing U to the maximum value (i.e., 10 V) and then reducing it to the minimum value (i.e., – 10 V). As it can be seen, P_p and P_n have a linear behavior for low values of pressure, but above 300 kPa, nonlinearity appears in both increasing and decreasing processes.

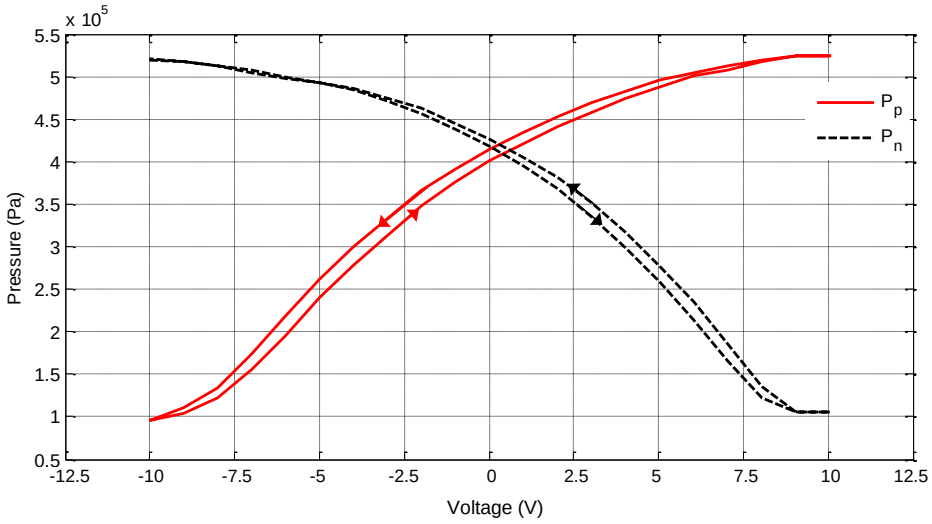

Fig. 3.14. Pressure gain characteristics $P = f(U)$ at null mass flow rate

Since the orifices p and n have identical mechanical structures, the pressure P_p and P_n may be considered to be symmetric with respect to the control voltage, i.e., P_p (U) = P_n (–U). Thus, in the following subsections, only one of them (e.g., orifice p) is shown for the characterization of the mass flow rate.

V.1.2.3. Mass flow rate gain characteristics q = f(U)

In this part, the characterization of the mass-flow-rate gain is carried out when the orifice is connected to exhaust. It is necessary to get a considerable amount of data, particularly at a large variation zone of the mass flow rate. The measurements are taken by exploring a whole scale of the input voltage. In order to obtain a hysteresis curve, we increase U to the maximum point and then decrease it back to the minimum**.**

When U varies from –10 to –9 V, the mass flow rate q is equal to zero because the orifice p of the servovalve is still at the end-stop. Once it opens, the mass flow rate increases rapidly in function of the control voltage. As shown in Fig. 3.15 (b), similar behavior has been observed when the voltage is within the interval [9 V, 10 V].

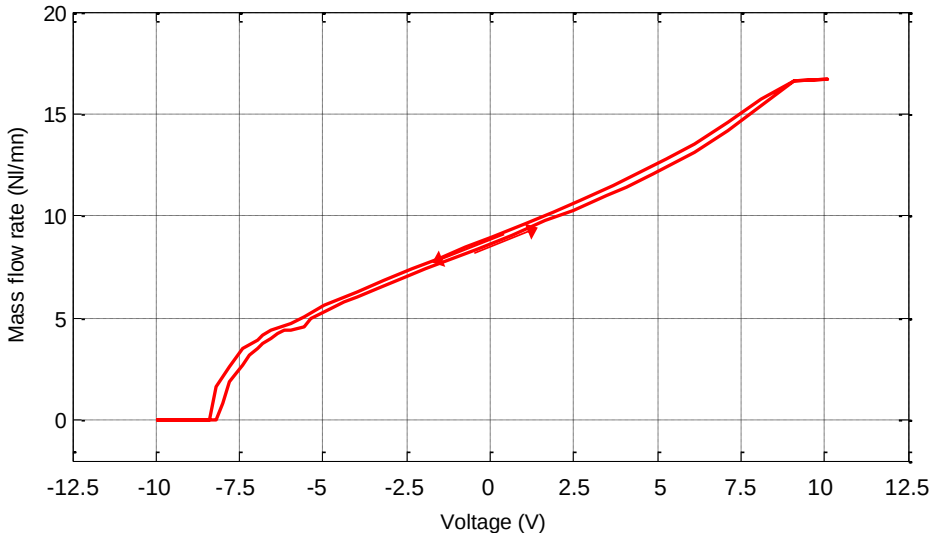

Fig. 3.15. Mass flow rate gain characteristics $q = f(U)$

V.1.2.4. Mass flow rate versus pressure and voltage q = f(P,U)

In this subsection, a static mass-flow-rate mathematical model issued from the global characterization is presented. This corresponds to the measurements of the output mass flow rate q according to the input voltage U and the pressure P_p.

For each series of measurement, a fixed voltage value is applied to the servovalve and the mass flow rate is acquired when varying the pressure which is controlled with a tap. This test is repeated by increasing the voltage signal to the maximum value and then decreasing it back. It can be seen in Fig. 3.16 (a) that the difference of the mass flow rate between the increasing and decreasing processes is relatively low. Non zero values of the subtraction, in particular at local peak points, reflect the hysteresis phenomenon that has been observed in Fig. 3.15 (b).

To reduce the complexity of the static model, we calculate the average value of the mass flow rate obtained from the two processes. This enable to obtain a single (average) model of the servovalve as illustrated in Fig. 3.16 (b).

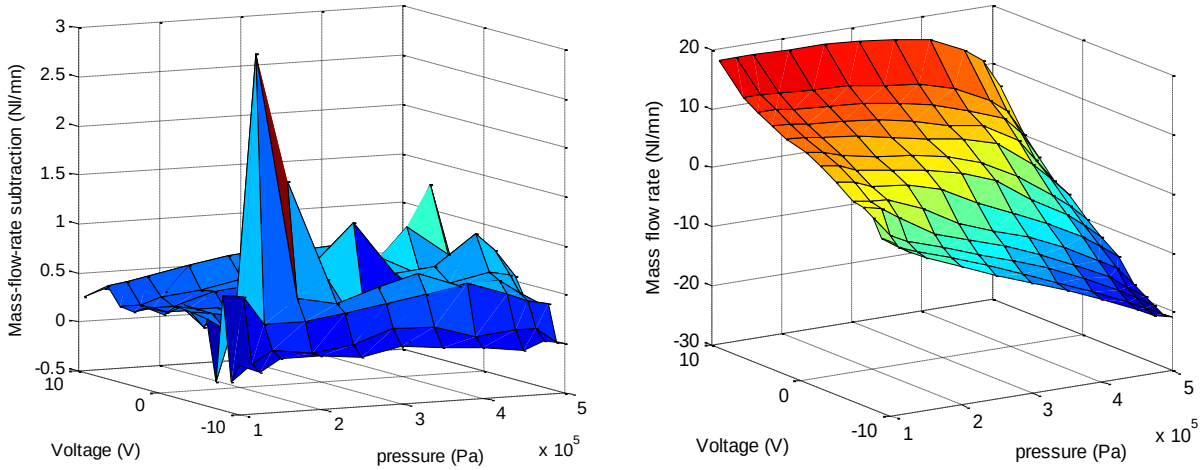

(a) Subtraction of decreasing and increasing processes (b) Average response

Fig. 3.16. Static characteristics $q = f(P, U)$

By projecting the curve of Fig. 3.16 (b) on the different plans, we obtain the mass flow rate in terms of voltage or pressure as shown on Fig. 3.17. It can be observed that the mass flow rate increases in function of the voltage and decreases according to the pressure. As it has been observed in Fig. 3.17 (a), an inevitable drawback of the jet-pipe type is that event when the control signal is null (U = 0V), it can be existed an amount of airflow passing through the orifice (in case the upstream and downstream pressures are different). This can be undesirable in certain applications, especially at the initial condition where the chambers could be under pressure (i.e., superior to the atmosphere pressure).

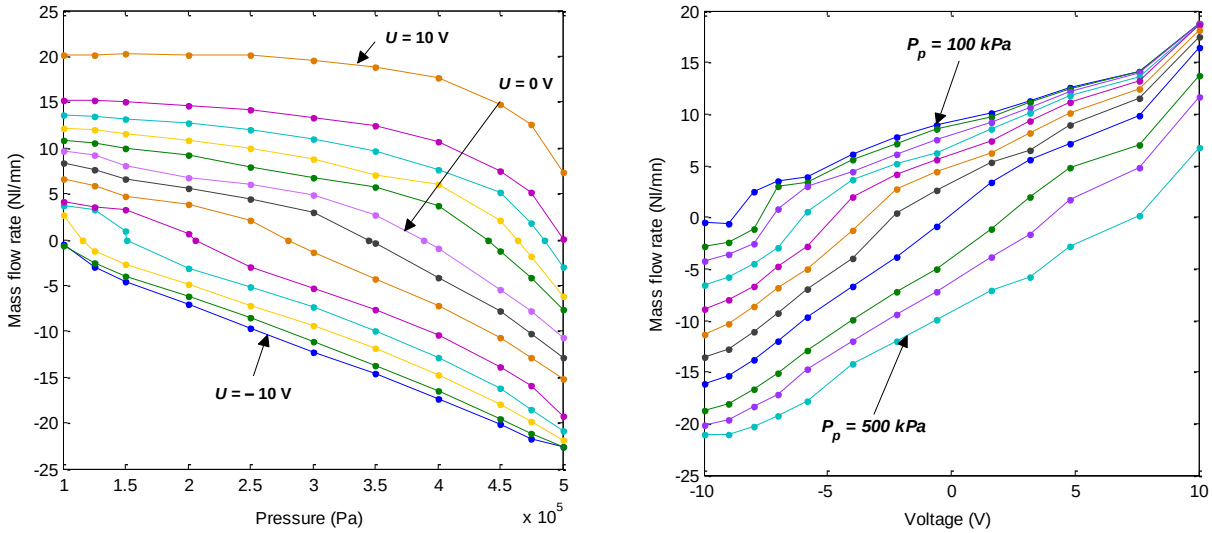

(a) Average mass flow rate versus pressure (b) Average mass flow rate versus voltage

Fig. 3.17. Projection on the different plans

Based on the above results, it is possible to establish a theoretical model of the mass flow rate in term of the pressure and the control voltage. This part is detailed in Appendix 1.

V.2. Solenoid valves

Matrix on/off valve, designed and manufactured by Bibus[1], is one of the fastest switching valves that are now commercially available. In the following, we provide a brief overview and some essential characteristics in terms of response time, current, and mass flow rate of this technology.

V.2.1. Overview of Matrix – high speed valve technology

The traditional technologies employed in solenoid valves suffer in different ways, due to the high inertia of their mechanical components, friction effect, and high temperature caused by electric windings.

A highly innovative principle used in Matrix pneumatic technology is the absence of internal friction during the shutter's opening and closing phases (see Fig. 3.21, subsection V.2.3). The absence of friction combined with the reduction of the moving mass gives the control extremely fast response times. This results in increased precision, repetitiveness and reliability of overall system. Further advantages of Matrix technology are long lifetime components and high insensibility to ranges of temperature.

Besides the mechanical advances discussed above, another solution allows to enhance the response times of Matrix solenoid valves is speed-up control techniques (presented in the following section). Actually, a short response time is essential for dynamic control systems since it enables to obtain rise/fall fronts similar to a logic drive, with very small phase lag.

V.2.2. Speed-up control techniques

The speed-up control is used for applications where the dynamic performance is fundamental. It consists in generating a double option of control, either in current or in voltage. The technique is able to supply a high breakaway energy to open the valve at full speed (called *speed-up phase*) and then to decrease the control level to keep it in open position (called *holding phase*).

XX version is designed for the current control which includes two levels. The first current level, generated by a supply power of V_1 = 24 VDC, must be limited through a suitable device present in *electronic control driver* with a value of I_1 = 0.7 A (namely *speed-up current*). In case of non limit, the current I_1 tends towards the maximum value, which is determined by the voltage V_1 and the resistance of the windings (R = 15 Ω), resulting in damaged components. The second current level occurs during the holding phase where its value is limited to 0.3 A, called *holding current*. This leads to reduced dissipated power where $P_2 = 15.\ 0.3^2 = 1.35$W (cf. Tab. 3.8).

KK version, which does not required any current limitations, is designed for the control system with double voltage levels. The first level with a 24 V power (i.e., equivalent to a current of 0.8A at steady state) is applied during the speed-up time. On the other hand, to keep the valve open, the second level V_2 = 5 VDC is used, resulting in decreased current absorption (i.e., I_2 = 0.17 A) and dissipation power (i.e., $P_2 = 5.\ 0.17 = 0.85$ W) on the resistance (R = 30 Ω) (cf. Tab. 3.8).

Versions	R	I_1	V_1	P_1	V_2	I_2	P_2
Current control (XX)	15 Ω	0.7 A	24 V	16.8 W		0.3 A	1.35 W
Voltage control (KK)	30 Ω	0.8 A	24V	19.2 W	5 V		0.85 W

TAB. 3.8. NUMERICAL VALUES OF SPEED-UP CONTROL (BIBUS DATASHEET)

[1] http://www.bibus.co.uk/products-solutions/pneumatics/valves/high-speed-valves/?show_all=1&pcatid=5245&cHash=bd6fc363d3 (last visit on 16 June 2011)

The speed-up technique is realized through the HDSB900 driver board (see Fig. 3.18), which allows to regulate the current/voltage by converting an input control signal into a pulse width modulation signal. This method is called PWM whose operating principle is detailed in Appendix 2. The driver card, including nine identical channels, enable to control at the same time nine 2/2 valves or four 3/3 valves. It is suitable for driving a wide range of Matrix solenoid valves in both current and voltage controls.

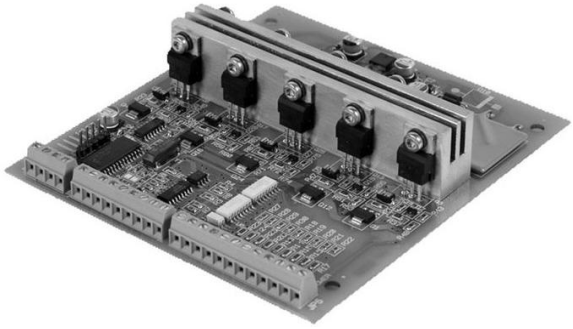

Fig. 3.18. HDSB900 driver board[1] (Bibus datasheet)

Fig. 3.19 illustrates PWM waveforms generated by the speed-up driver for both XX and KK versions. In the KK version, the control voltage (dashed wave) is constant and remains at high level (5V) during the speed-up time. To decrease the current level during the holding time, the voltage control is modulated at a fixed frequency of 20 kHz by using the PWM technique. Commonly, this frequency should be higher enough than that one of the input control (solid signal). Knowing a relationship with the duty cycle of the PWM wave, a desired holding current could be easily achieved. Similar principle is obtained for the XX version. However, after the current rise time, the control voltage (dotted wave) becomes a pulse width modulated signal (instead of a constant signal) whose duty cycle is tuned as function of a desired speed-up current.

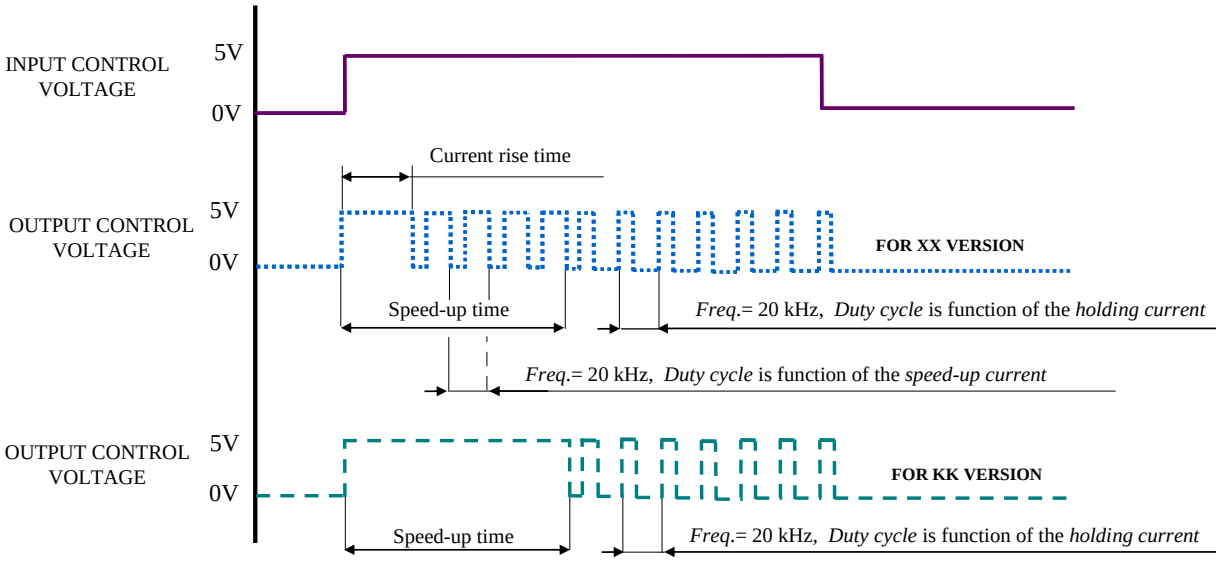

Fig. 3.19. Waveforms generated by speed-up driver for XX and KK versions (Bibus datasheet)

Finally, the use of a speed-up card for driving the solenoid valves allows to decrease the supply voltage during the holding phase, reducing in such a way its consumption and thermal dissipation.

[1] http://www.bibus.co.uk/products-solutions/pneumatics/valves/high-speed-valves/matrix-driver-board/ (last visit on 16 June 2011)

V.2.3. Characterization of the Matrix valves – series 820[1]

In our study, the fast switching on/off valves – series 820, (called 820-Matrix), are chosen since they are available in CC version (closed center – 3/3 way), which enable to control independently charging and discharging phases of the valves (see Fig. 3.20 (b)). Moreover, they include all innovations of Matrix solenoid valves such as low inner friction, small mass of moving element and possibility to be speed-up controlled. In this way, high dynamic performance can be achieved with fast response times (milliseconds) and long operating lifetime (over 500 million cycles).

V.2.3.1. General characteristics

As it can be seen in Fig. 3.20, the solenoid valve 3/3 way consists of two fast switching spring return 2/2-NC valves (normally closed), controlled independently.

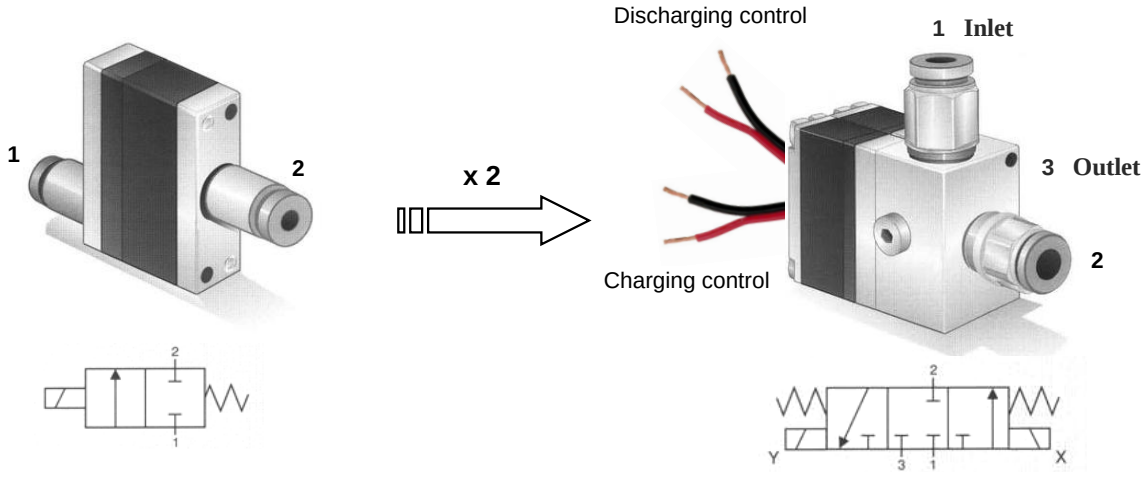

(a) 2/2-NC (Normally closed) (b) 3/3-CC (Closed center)

Fig. 3.20. Two types of Matrix solenoid valves – series 820[2]

The simplified scheme of the 2/2-NC is shown in Fig. 3.21. In the absence of power excitation, the valve is kept at its closed end-position by the return spring, *called normally closed*. When the solenoid is energized by DC voltage, the resulting magnetic force displaces the moving part (i.e., shutter and armature assembly) against the return spring, leading to open the valve and thus letting the air flows through an orifice.

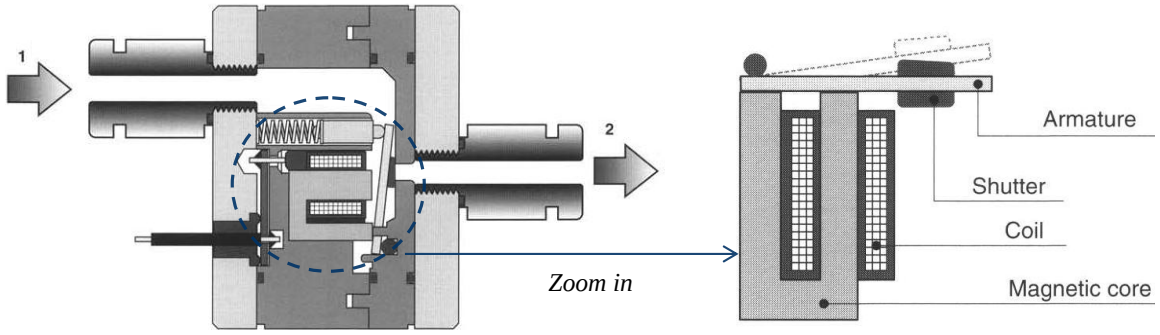

Fig. 3.21. Mechanical structure of the 2/2-NC

[1] http://www.bibus.co.uk/products-solutions/pneumatics/valves/high-speed-valves/matrix-series-820/ (last visit on 16 June 2011)

[2] http://www.bibus.co.uk/fileadmin/product_data/matrix/documents/matrix_datasheet_en_serie820_2-2_3-3.pdf (last visit on 16 June 2011)

Thanks to the possibility to be speed-up controlled, the dynamic characteristics of the 820-Matrix is significantly improved. Indeed, standard solenoid valves with 24 VDC control can only be sampled at a maximum frequency about 200 Hz. On the contrary, solenoid valves driven by speed-up control have response times less than 2 ms in opening and 1ms in closing, leading to maximum switching frequency of 500 Hz.

The general features of the 820-Matrix (model GNK821213C3) is shown in Tab. 3.9. Note that this model is available in both speed-up versions. In our case, the KK version is chosen since the output control driven by our dSPACE card are voltage signals.

Parameters	Value	
Fluid	Non-lubricated dry air, neutral gases	
Filtration rating	Min 40 micron	
Response time in opening	< 5 ms (24V)	< 2 ms (speed-up)
Response time in closing	< 2 ms (24V)	< 1 ms (speed-up)
Maximum frequency	200 Hz	500 Hz
Supply voltage	24 VDC ± 10 %	
Pressure range (relative)	0 – 800 kPa	
Mass flow rate (at 600 kPa)	100 Nl/mn	
Weight	130g	
Operating temperature range	–10 to 50 °C	
Product life expectancy	≥ 500 million cycles	

TAB. 3.9. GENERAL CHARACTERISTICS OF MATRIX SOLENOID VALVES– SERIES 820

In the following subsections, we will take a closer look to specific characteristics of the fast switching solenoid valves (i.e., current characteristics and mass flow rate characteristics), which influence the successful operation of the entire pneumatic system.

V.2.3.2. Current characteristics

In this subsection, an analysis of the current's dynamics is investigated in order to verify the switching time of the solenoid valve. Fig. 3.22 shows the current response when the input signal is at ON level for 5.5 ms. Note that the current is measured from a current probe, which is serially connected to the solenoid valve.

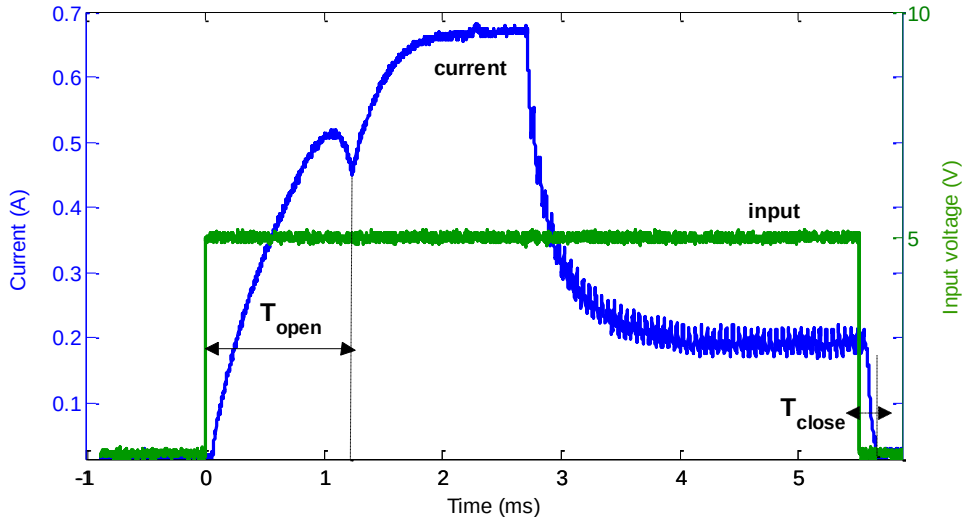

Fig. 3.22. Experimental characteristics of the valves switching time

The time interval of the current in Fig. 3.22 consists of several stages which should be interpreted and justified with the actual behavior of the valve. We can describe these stages as follows:

1. When the input voltage is applied at t = 0, the current starts to rise until the magnetic force overcomes the spring force and the shutter starts to move at approximately t = 1.1ms. As a result of shutter motion, the equivalent length of the total magnetic circuit l_{eq} decreases and the solenoid inductance L increases, as shown by the following equation (Taghizadeh et al. 2009).

$$L(t,x) = \frac{N^2 A_e \mu_c}{l_{eq}(t,x)} \tag{3.3}$$

where A_e is the effective cross sectional area of flux path, μ_c is the permeability of the core, N is the number of coil turns, and x is the displacement of the shutter with respect to the initial position.

2. The increase of the inductance L leads to an increase of the counter electromotive force (CEMF). According to the Lenz's law[1], the CEMF is in the opposite direction to the applied voltage and opposes a change in the current. Consequently, the current experiences a local peak (about 0.52 A) when the shutter starts to open and begins to decrease until the shutter reaches its end stroke and stop at approximately t = 1.3ms, i.e., the complete opening time.

3. When the shutter stops, the inductance of the solenoid is considered to be constant and the current starts increasing again (Taghizadeh et al. 2009). As far as the input voltage is applied, the current continues to increase exponentially (the behavior of the first order R-L circuit as given by the following equation) to reach a steady state value (about 0.7A).

$$\frac{d}{dt} i(t) + \frac{R}{L} i(t) = \frac{V(t)}{L} \tag{3.4}$$

4. Once the valve completely opens, the amount of current needed to keep the shutter at its end position (holding current) is much less than the current required for moving it from its initial position (speed-up current). Therefore after approximately 2.7s, the current is reduced and maintained at a constant holding level. This task is carried out by the driver board as discussed previously. Fig. 3.23 zooms in on the holding current during 0.4 ms in order to get a close-up view of its behavior. The current is regulated to an average value of 0.19 A through the voltage controlled PWM at a rate of 20 kHz (section V.2.2). As a result, the current also oscillates at this frequency and stabilizes within 0.19 ± 0.02 A (see Fig. 3.23).

5. When the input voltage switches to OFF level (Fig. 3.22), the current drops to zero with a very fast response time, T_{close} = 0.2 ms. Such a switching time could be achieved due to the fact that the current at the beginning of the de-energizing process was significantly reduced (from 0.7 A to 0.2 A). When no excitation power is applied to the valve, the shutter returns to the initial position due to the spring force. The current remains at zero level for a duration of the OFF time until the next cycle begins.

[1] http://en.wikipedia.org/wiki/Lenz%27s_law (last visit on 16 June 2011)

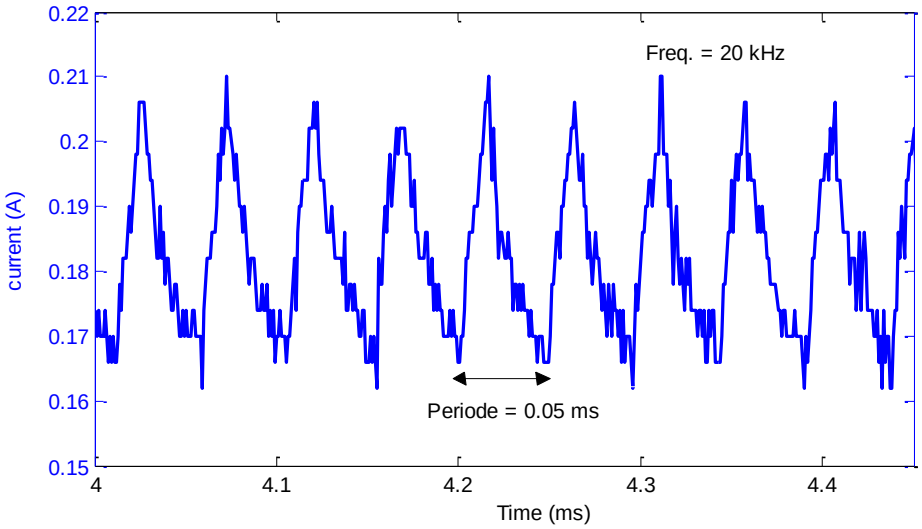

Fig. 3.23. Zoom in of the holding current

V.2.3.3. Mass flow rate characteristics

Fig. 3.24 shows the static mass flow rate q in terms of upstream and downstream pressures (i.e., P_{up} and P_{down}, respectively). These data (i.e., provided by BiBus) present the pressurizing process in which P_{up} corresponds to the supply and P_{down} corresponds to the pressure of the orifice. For each fixed value of the upstream pressure, the mass flow rate is measured by varying the downstream pressure from its minimum (i.e., P_{atm}) to its maximum (i.e., P_{up}).

The generalized model of the static mass flow rate is described by two parameters, i.e., the critical pressure ratio C_r = 0.433 and the sonic conductance C_{val} = 16.10^{-5} Nl.mn^{-1}.Pa^{-1}. Finally, the mass flow rate in Fig. 3.24 can be written as (McCloy 1968):

$$q\left(P_{up},P_{down}\right)=\begin{cases} C_{val}P_{up}\sqrt{\dfrac{T_{atm}}{T_{up}}} & \text{if } \dfrac{P_{down}}{P_{up}}\le C_r \text{ (sonic)} \\ C_{val}P_{up}\sqrt{\dfrac{T_{atm}}{T_{up}}}\sqrt{1-\left(\dfrac{\frac{P_{down}}{P_{up}}-C_r}{1-C_r}\right)^2} & \text{otherwise (subsonic)} \end{cases} \tag{3.5}$$

In the above, P_{up} and P_{down} are respectively the absolute upstream and downstream stagnation pressures of the valve (Pa); T_{atm} is the atmosphere temperature (°K), and T_{up} is the upstream stagnation temperature (°K).

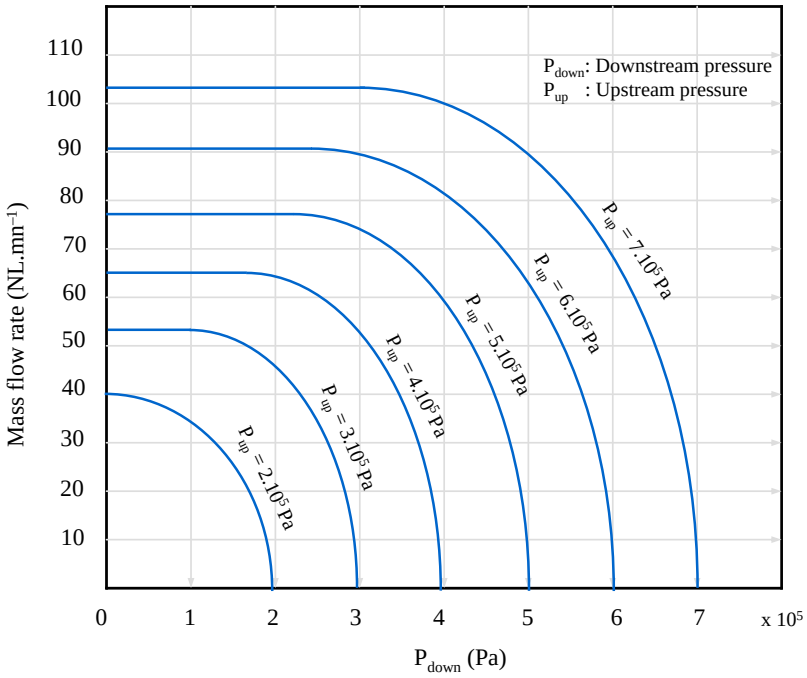

Fig. 3.24. Mass flow rate versus upstream and downstream pressures (Bibus doc)

In order to obtain a single curve, Fig. 3.25 illustrates a normalized mass flow rate q/P_{up} versus a pressure ratio P_{down}/P_{up}. As it can be seen, at sonic regime, the flow remains constant despite any change in pressure ratio. On the contrary, when subsonic regime occurs, the flow drastically decreases with a further increase of the pressure ratio.

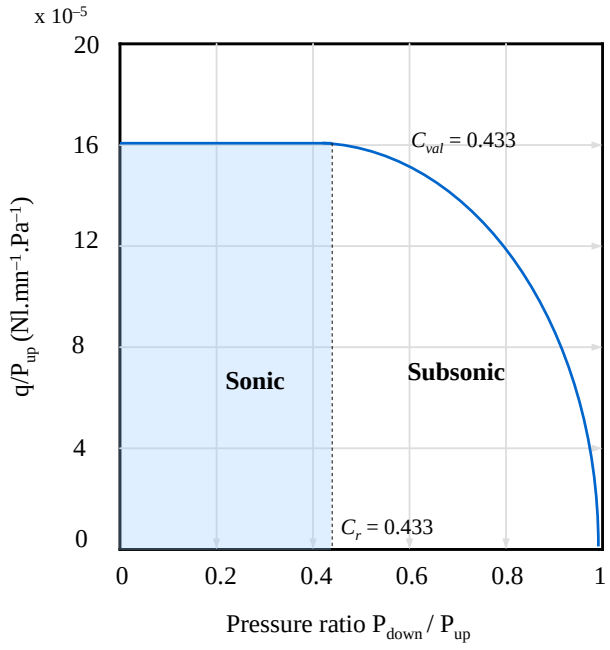

Fig. 3.25. Normalized mass flow rate versus pressure ratio

VI. Presentation of prototype

Fig. 3.26 and Fig. 3.27 present the final prototype, which consists of two identical master and slave interfaces, actuated by proportional servovalves and solenoid valves, respectively.

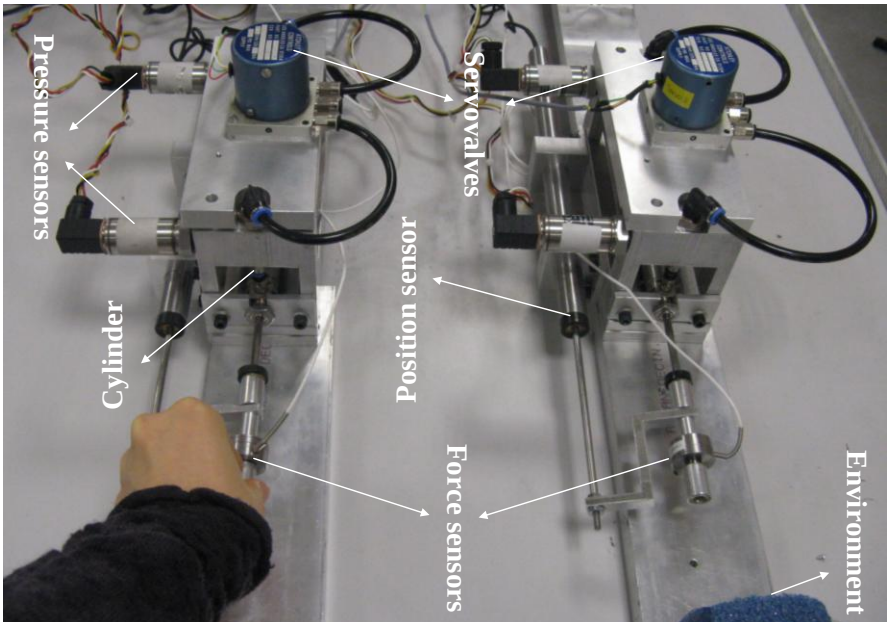

Fig. 3.26. Mechanic principle of a pneumatic actuated teleoperation system with servovalves

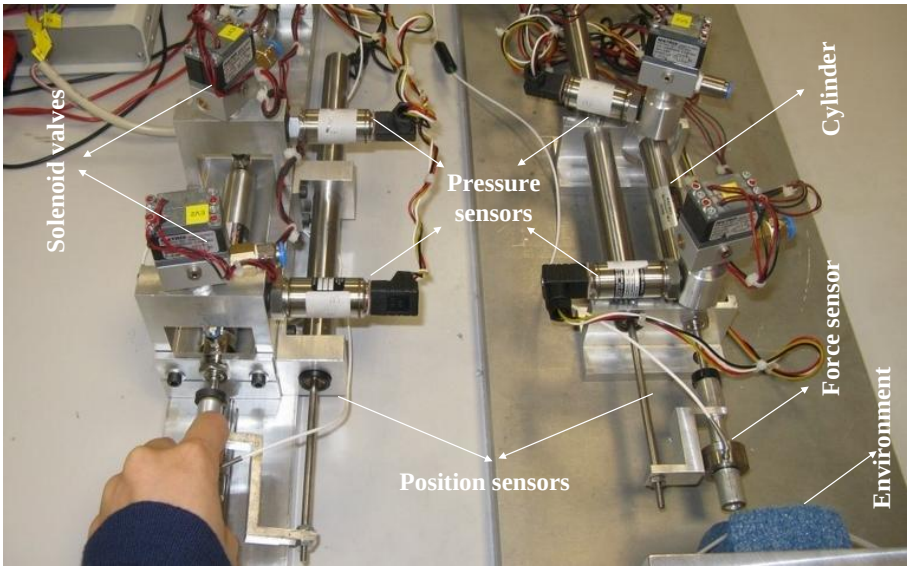

Fig. 3.27. Mechanic principle of a pneumatic actuated teleoperation system with on/off valves

VII. Conclusion

In this chapter, we have presented the mechanical principal of a 1-DOF pneumatic system. The specifications of haptic interfaces give some essential criteria for efficiently selecting the components, i.e., actuators, sensors, fast switching on/off valves and proportional servovalves. Several criteria such

as high control bandwidth, large workspace, low friction, etc. are required to achieve good pneumatic teleoperation performance.

It has been seen that the mechanical design and the choice of materials are important since their quality defines intrinsic limitations in the haptic feedback device. In our case, high resolution sensors are required to provide high accuracy in force and motion measurements. Similarly, high-bandwidth valves are needed to generate a rapid rise in force or a fast movement. Also, frictionless cylinders were selected in order to overcome a major drawback of the classical pneumatic actuators, i.e., its high friction-to-force ratio.

To sum up, the following table resumes all materials required for our prototype.

Material	**Type**	**Model**	**Quantity**
Sensors	Position	MEAS 2000 DC-EC	2
	Force	MEAS ELPF	2
	Pressure	MEAS U5100	4
Actuator	Pneumatic cylinder	Airpel M16D100D	2
Valves	Solenoid valve	Matrix series 820	4 (type 3/3)
	Speed-up driver	Matrix HDSB900	1
	Servovalves	Atchley 200PN-176	2

TAB. 3.10. MATERIALS FOR BOTH MASTER AND SLAVE MANIPULATORS

Finally, the teleoperation performance depends not only on the hardware but also on the software where the controllers are implemented. Therefore, in the subsequent chapters, we focus on the development of different bilateral control designs for the pneumatic master-slave system equipped with either solenoid valves or proportional servovalves.

Chapter 4
Bilateral Control of a Pneumatic-Actuated Teleoperation Systems with Solenoid Valves

Table of contents

I. Introduction

The non-linear nature of a pneumatic actuator is highlighted when it uses on/off solenoid valves, which are widely used due to the high cost of servovalves (Le et al. 2010a). For this reason, accurate control with high performance is a challenge because of the discrete-input nature of the system. Most solenoid valve pneumatic systems utilize a pulse width modulated (PWM) input. Using time averaging, a PWM input with a sufficiently high frequency can approximate the input/output properties of a servo-valve (Shen et al. 2004).

This chapter is aimed at providing, apart the traditional PWM method, different control schemes of pneumatic systems with on/off valves. Another aspect of our study is to show that good transparency in teleoperation can be obtained without using expensive proportional servovalves.

The structure of this chapter is described as follows. First, the modeling of a pneumatic manipulator composed of a cylinder and four solenoid valves is presented in Section II. Sections III–V describe the different control designs, namely pulse width modulation (PWM), hybrid strategy, and sliding mode control for a master-slave telemanipulator. Experimental results are also provided that allow to validate the performance of the proposed control laws. Finally, concluding remarks are drawn in Section VI.

II. Model of Pneumatic System

As mentioned in chapter 3, the master and the slave manipulators are identical, thus only one pneumatic device is presented in this section.

II.1. Model of the actuator

The actuator model can be obtained using two physical laws: the pressure dynamics of the chambers and the fundamental mechanical relation.

The pressure evaluation of the chambers with variable volumes is obtained with the following assumption (Andersen 1967):

- Air is a perfect gas and its kinetic energy is negligible in the chamber,
- the pressure and the temperature are homogeneous in each chamber,
- the evolution of the gas in each chamber is polytropic and is characterized by coefficient α,
- the temperature variation in chambers is negligible with respect to the supply temperature,
- the temperature in each chamber can be considered equal to the supply temperature,
- the mass flow rate leakages are negligible, and
- the supply and exhaust pressures are constant.

A schematic of a 1-DOF pneumatic actuation system is shown in Fig. 4.1. The device consists of a pneumatic cylinder, four identical solenoid valves of type 2/2, a position sensor and two pressure sensors. Each chamber has two solenoid valves. Valves 1 and 4 can be either locked or connected to a compressed air supply (source pressure) while valves 2 and 3 can be either locked or connected to exhaust (atmosphere pressure).

The choice of four valves rather than two valves allows us to increase the number of possibilities in the choice of the control vector and the resulting behavior of the closed-loop system. Indeed, with two solenoid valves, only four configurations are obtained as following:

- both valves are open,
- both valves are closed,
- one valve is open and the other closed,
- and vice versa.

On the other hand, as it will be shown in Section IV.1.2, nine configurations can be achieved with four solenoid valves. Generally, there would be a total of sixteen discrete modes at any given

time. However, since we cannot have a chamber connected to both supply and exhaust at the same time, only nine discrete modes exist.

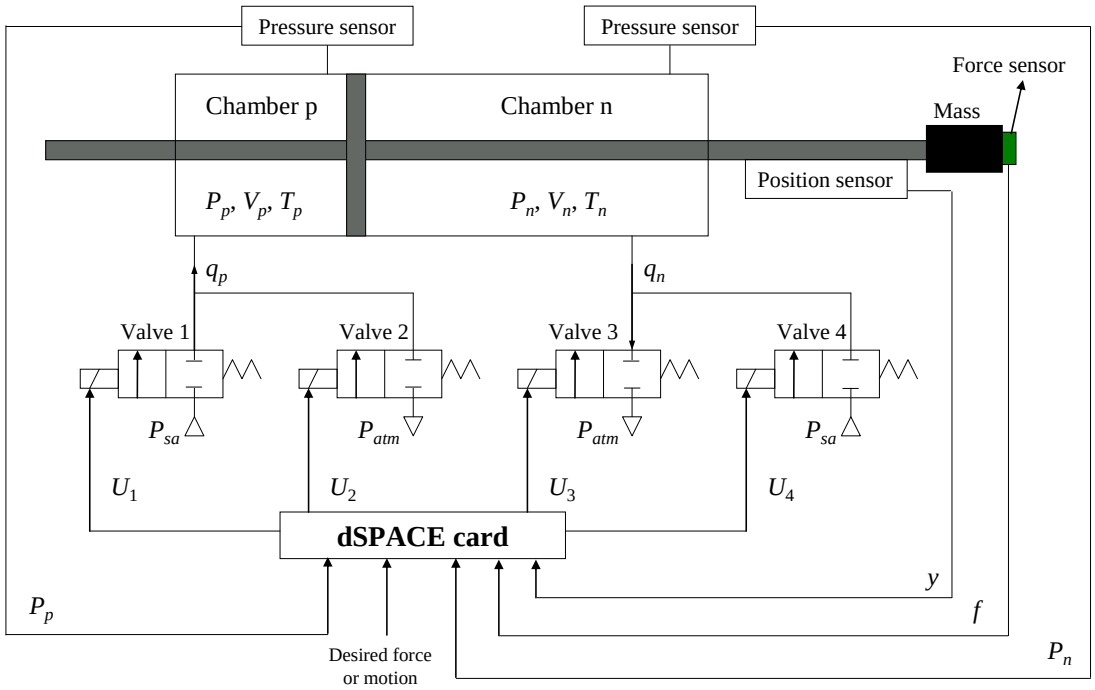

Fig. 4.1. Electro-pneumatic system with four on/off valves

The behavior of the pressure inside each chamber of the cylinder can be expressed as (Blackburn 1960):

$$\begin{aligned}\frac{dP_p}{dt} &= \frac{\alpha r T_a}{V_p(y)}\left(q_p(U_1,U_2,P_p) - \frac{P_p}{rT_a}S_p\dot{y}\right)\\ \frac{dP_n}{dt} &= \frac{\alpha r T_a}{V_n(y)}\left(q_n(U_3,U_4,P_n) + \frac{P_n}{rT_a}S_n\dot{y}\right)\end{aligned} \tag{4.1}$$

where $\begin{matrix}V_p(y)=V_p(0)+S_p y\\ V_n(y)=V_n(0)-S_n y\end{matrix}$ with $\begin{matrix}V_p(0)=V_{dp}+S_p l/2\\ V_n(0)=V_{dn}+S_n l/2\end{matrix}$;

the subscripts p and n indicates the chambers p and n as shown on Fig. 4.1; $V_p(0)$ and $V_n(0)$ are the volumes at the zero position (m^3); V_{dp} and V_{dn} are the dead volumes present at each extremity of the cylinder (m^3); l is the cylinder stroke (m); U_1, U_2, U_3 and U_4 are the discrete control voltages (1 or 0) of the valve 1, valve 2, valve 3, and valve 4; y and $\dot{y}$ are the position (m) and velocity (m/s) of the piston; P_p and P_n are the pressures inside the chambers (Pa); S_p and S_n are the piston cylinder area (m^2); q_p and q_n are the mass flow rates (kg/s); T_a is the temperature of the supply air (K); r is the perfect gas constant (J/kg/K) and α is the polytropic constant.

Finally, the dynamics of the mechanical actuator involving the applied force on the piston and the resulting piston motion is

$$M\ddot{y} = S_p P_p - S_n P_n - b\dot{y} - F_{st} - F_{ext} \tag{4.2}$$

where b is the viscous friction coefficient (N.s/m); M is the moving load (kg); F_{ext} is the external force and F_{st} is the friction force. Because of the difficulties to identify the friction force with a good precision due to hysteresis and non-repetitive phenomena, the friction force was assumed to be negligible in the theoretical model in comparison to the pneumatic drive force. In our experimental setup, the friction force could be neglected because we used ultra-low friction pneumatic cylinders.

II.2. Model of the mass flow rate

The mass flow rates q_p and q_n can be derived in terms of the discrete control voltages U_1, U_2, U_3 and U_4 shown in Fig. 4.1 and the continuous pressures P_p and P_n:

$$q_p(U_1,U_2,P_p)=\begin{cases} q(P_{sa},P_p) & \text{for } U_1=1 \text{ and } U_2=0 \text{ (chamber p fills)} \\ 0 & \text{for } U_1=0 \text{ and } U_2=0 \text{ (chamber p closes)} \\ -q(P_p,P_{atm}) & \text{for } U_1=0 \text{ and } U_2=1 \text{ (chamber p exhauts)} \end{cases} \tag{4.3}$$

$$q_n(U_3,U_4,P_n)=\begin{cases} q(P_{sa},P_n) & \text{for } U_3=0 \text{ and } U_4=1 \text{ (chamber n fills)} \\ 0 & \text{for } U_3=0 \text{ and } U_4=0 \text{ (chamber n closes)} \\ -q(P_n,P_{atm}) & \text{for } U_3=1 \text{ and } U_4=0 \text{ (chamber n exhauts)} \end{cases}$$

where P_{sa} and P_{atm} are the pressures of the supply air and the atmosphere. The '0' state of each input voltage corresponds to a closed valve and the '1' state corresponds to an open valve. In the above, the cases of $U_1 = U_2 = 1$ and $U_3 = U_4 = 1$ have been prohibited to avoid a bypass of the valves. The function q in (4.3) is given by the following standard expression for the mass flow rate (see chapter 3, section V.2.3.3):

$$q(P_{up},P_{down})=\begin{cases} C_{val}P_{up}\sqrt{\dfrac{T_{atm}}{T_{up}}} & \text{if } \dfrac{P_{down}}{P_{up}}\le C_r \text{ (sonic)} \\ C_{val}P_{up}\sqrt{\dfrac{T_{atm}}{T_{up}}}\sqrt{1-\left(\dfrac{\frac{P_{down}}{P_{up}}-C_r}{1-C_r}\right)^2} & \text{otherwise (subsonic)} \end{cases} \tag{4.4}$$

III. PWM Control Design

PWM control offers the ability to ensure servo control of pneumatic actuators at a significantly lower cost by utilizing switching on/off valves instead of proportional servo-valves. In a PWM controlled system, the power delivered to the actuator is discretely estimated by packets of the mass flow rate via a valve that is either "fully on" or "fully off" (Shen et al. 2006). If delivery of these packets occurs on a time scale, which is significantly faster than the system dynamics (i.e., dynamics of the actuator and load), the system will response to the average mass flow rate into or out of the cylinder, in a manner similar to the continuous case.

Several researchers have investigated the use of PWM control of solenoid valves for the servo control of pneumatic actuators. The first application of PWM control in pneumatic systems emerged towards the end of 1960's. (Goldstein & Richardson 1968) investigated the principles of pulse modulated control using free floating flapper disc switching valves. A study was carried out by (Taft & Harned 1980) on the development of a four way electro-pneumatic valves using permanent and ferromagnetic valve switching elements. (Morita et al. 1985) implemented a PWM technique in pneumatic manipulators to control pressure and contact force. It was demonstrated in (Noritsugu 1987; Kirat 1992) that if a linear relationship between the output mass flow rate and the input voltage of a valve could be established, the highly nonlinear pneumatic system is easier to control with a higher level of accuracy. (Ye et al. 1992) investigated a model for determining the maximum operating modulation ratio of pneumatic PWM solenoid valves. (Paul et al. 1994) proposed a switching controller based on a "reduced-order'' nonlinear model of an electro-pneumatic system. The "reduced-order" aspect of their approach allows to guarantee the stability of the system in the Lyapunov sense. However, it requires simplified assumptions, which cannot accommodate the full nonlinear behavior of a pneumatic servo system. In particular, they neglect the nonlinearity in the chamber pressure dynamics, the change in pressure boundary conditions that results when switching the direction of

control effort (i.e., the upstream and downstream pressures switch from supply and chamber, respectively, to chamber and atmosphere), and the distinction between the sonic and subsonic flow regimes through the solenoid valves. These combined effects constitute significant nonlinear behavior in such systems. To deal with the full (i.e., non-reduced-order) nonlinear model of the pneumatic servo systems, (Shen et al. 2006) present an averaging technique which is then utilized as the basic for the development of a PWM-based sliding approach.

For details about the PWM principle, the readers can refer to appendix 2.

III.1. Basics

In the application of PWM technique to electro-pneumatic switching valves, it is necessary to understand that the characteristics of the valves including the *switching time*, *dead band*, and *saturation band* will exist in the actuation of the valves with PWM signal. It is in contrast to the electrical system where the commutation of transistors' state between "fully on" and "fully off" is quite fast (typically less than 100 nanoseconds). In the following, basic concepts of PWM technique are applied to switching valves.

PWM control method is used in pneumatic servo systems with solenoid valves to obtain a linear relationship between the mean value of mass flow rate and the input signal. According to the valve opening and closing times (i.e., T_{open} and T_{close}, respectively), the following conditions must be satisfied to ensure that the on/off switching operation is completely executed (Topçu et al. 2006; Taghizadeh et al. 2009a):

$$\begin{cases} t_{\text{on}} \geq T_{\text{open}} & \text{(Opening condition)} \\ t_{\text{off}} \geq T_{\text{close}} & \text{(Closing condition)} \end{cases} \tag{4.5}$$

As $T_{\text{PWM}} = t_{\text{on}} + t_{\text{off}}$, the above inequalities lead to the following conditions:

$$T_{\text{PWM}} \geq \ T_{\text{open}} + T_{\text{close}} \quad \text{and} \quad f_{\text{PWM}} \leq \ 1/(\ T_{\text{open}} + T_{\text{close}}) \tag{4.6}$$

Since $t_{\text{off}} = T_{\text{PWM}} - t_{\text{on}}$ thus, from (4.5) we have

$$T_{\text{open}} \leq t_{\text{on}} \leq T_{\text{PWM}} - T_{\text{close}} \tag{4.7}$$

Dividing each term of (4.7) by T_{PWM} yields

$$T_{\text{open}} / T_{\text{PWM}} \leq dc \leq 1 - T_{\text{close}} / T_{\text{PWM}} \tag{4.8}$$

Hence we infer the minimum and maximum values of the duty cycle as:

$$dc_{\min} = T_{\text{open}} / T_{\text{PWM}} \quad \text{and} \quad dc_{\max} = 1 - T_{\text{close}} / T_{\text{PWM}} \tag{4.9}$$

To some extend, the minimum duty cycle indicates the dead band in the relationship between the duty cycle and the valve flow. A smaller value than the minimum duty cycle can keep the valve completely closed. On the other hand, the maximum duty cycle indicates the end of the proportional range in the valve input-output relation. Beyond the maximum value of duty cycle, the valve is saturated and remains open (See Fig. 4.2). The effective range of duty cycle (*ERDC*) can be expressed as (Taghizadeh et al. 2009b):

$$\begin{aligned} ERDC &= dc_{\max} - dc_{\min} \\ &= 1 - (T_{\text{open}} + T_{\text{close}}) / T_{\text{PWM}} \\ &= 1 - (T_{\text{open}} + T_{\text{close}})\, f_{\text{PWM}} \end{aligned} \tag{4.10}$$

To have an acceptable control performance with a good resolution of the PWM duty cycle, the *ERDC* must be large enough. Equation (4.10) indicates that a smaller PWM frequency leads to a larger *ERDC*. On the other hand, to have smoother flow behavior through the on/off valves, frequency must be as high as possible. But increasing the frequency decreases the *ERDC*. A trade-off between having enough large *ERDC* and continuity of the flow must be made when selecting the PWM frequency (see

Fig. 4.2). However, by using faster switching valves, higher PWM frequencies could be achieved without much reducing the *ERDC*.

Fig. 4.2. Switching valve operation as function of duty cycle

The above descriptions give a good understanding of the relationship between frequency, valves response times, and ERDC. However, it is not considered as an analytical basis for accurately selecting the PWM frequency. In previous articles (Noritsugu 1985; Barth et al. 2002; Taghizadeh et al. 2009a), different frequencies (mostly between 25 and 60Hz) have been empirically selected and applied to pneumatic switching valves. In our experiment, a PWM frequency of 100Hz was chosen. Indeed, the fast switching valves used that are proposed by Bibus (chapter 3, section V.2) enable us to choose a higher PWM frequency than the other literature's one.

III.2. Force tracking controller design

Since the control signals of the master and slave manipulators in an impedance-type teleoperation system are force signals (chapter 2, section III.1), the PWM strategy presented in this section is applied to a force tracking problem. The bilateral teleoperation scheme based on PWM control will be shown in section III.3.

The method of the PWM control in the pneumatic system can be inspired from the operating principle of the single phase inverter where the four solenoid valves are considered to be similar to four switches (K_1 to K_4) (see Fig. A.5, appendix 2).

As the same way to the electrical case, with four independent on/off valves, the pneumatic system has two possible modes, which corresponds to the following behaviors:

Mode 1: $\underline{U}$ = [1 0 1 0], chamber p fills, chamber n exhausts

Mode 2: $\underline{U}$ = [0 1 0 1], chamber p exhausts, chamber n fills

where $\underline{U} = [U_1\ U_2\ U_3\ U_4]$ is defined as the input control vector of the valves. The force control can be achieved with these two modes. Mode 1 corresponds to a control force in one direction while mode 2 corresponds to a control force in the opposite direction.

A PWM force control can be then realized as shown on the block diagram in Fig. 4.3.

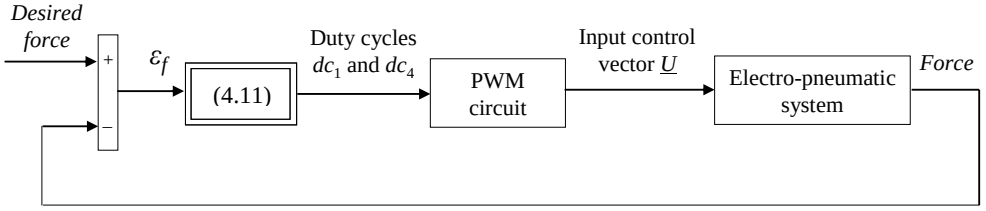

Fig. 4.3. Block diagram of PWM force control

According to (A.13) appendix 2, the force tracking error ε_f can be converted into variable duty cycles of the PWM signals, as given by

$$dc_1 = 0.5 + K_{PWM}\varepsilon_f \quad , \quad dc_4 = 0.5 - K_{PWM}\varepsilon_f \tag{4.11}$$

where dc_1 and dc_4 are the duty cycles of the control signals U_1 and U_4 for valves 1 et 4, respectively; and K_{PWM} denotes the proportional gain of the force control.

Since $U_2 = -U_1$ and $U_3 = -U_4$, the duty cycles of the control signal for valve 2 et 3 can be written as:

$$dc_2 = 1 - dc_1 = 0.5 - K_{PWM}\varepsilon_f \quad , \quad dc_3 = 1 - dc_4 = 0.5 + K_{PWM}\varepsilon_f \tag{4.12}$$

As a result, the pulse waves applied to the four on/off valves are defined as a linear function of the force control signal ε_f

The controller parameter K_{PWM} allows to modify the closed-loop dynamics and also to ensure the non-saturation of the duty cycles. From (4.11), the following conditions need to be satisfied so that the duty cycles are in the effective range *ERDC*

$$dc_{min} - 0.5 \le K_{PWM}\varepsilon_f \le dc_{max} - 0.5 \quad , \quad -dc_{max} + 0.5 \le K_{PWM}\varepsilon_f \le -dc_{min} + 0.5 \tag{4.13}$$

Concerning the pulse frequency f_{PWM}, its value has to be majored by $1/(T_{open}+T_{close}) \approx 660$Hz (4.6) where T_{open} and T_{close} respectively equal 1.3 ms and 0.2 ms (chapter 3, section V.2.3.2). If f_{PWM} exceeds this value, the linearity is deteriorated because the valves's dynamics cannot follow the variations of the input signal. In practice, f_{PWM} is chosen equal to 100Hz due to the trade-off between the continuity of the flow and the *ERDC* performance (section III.1). Thus from (4.9), the maximum and minimum values of the duty cycles (i.e., dc_{min} and dc_{max}) are respectively equal to 0.13 and 0.98. Hence the *ERDC* can reach 0.85 (4.10), which is large enough to obtain acceptable responses. Applying the value of dc_{min} and dc_{max} in (4.13) yields

$$-0.37 \le K_{PWM}\varepsilon_f \le 0.37 \tag{4.14}$$

This condition plays a key role in the controller parameter (K_{PWM}) tuning.

III.3. PWM-based teleoperation control

The implementation of the PWM control in the 4CH bilateral teleoperation system is shown in Fig. 4.4. This figure is inspired from the diagram of Lawrence in Fig. 2.5 (chapter 2, section III.1).

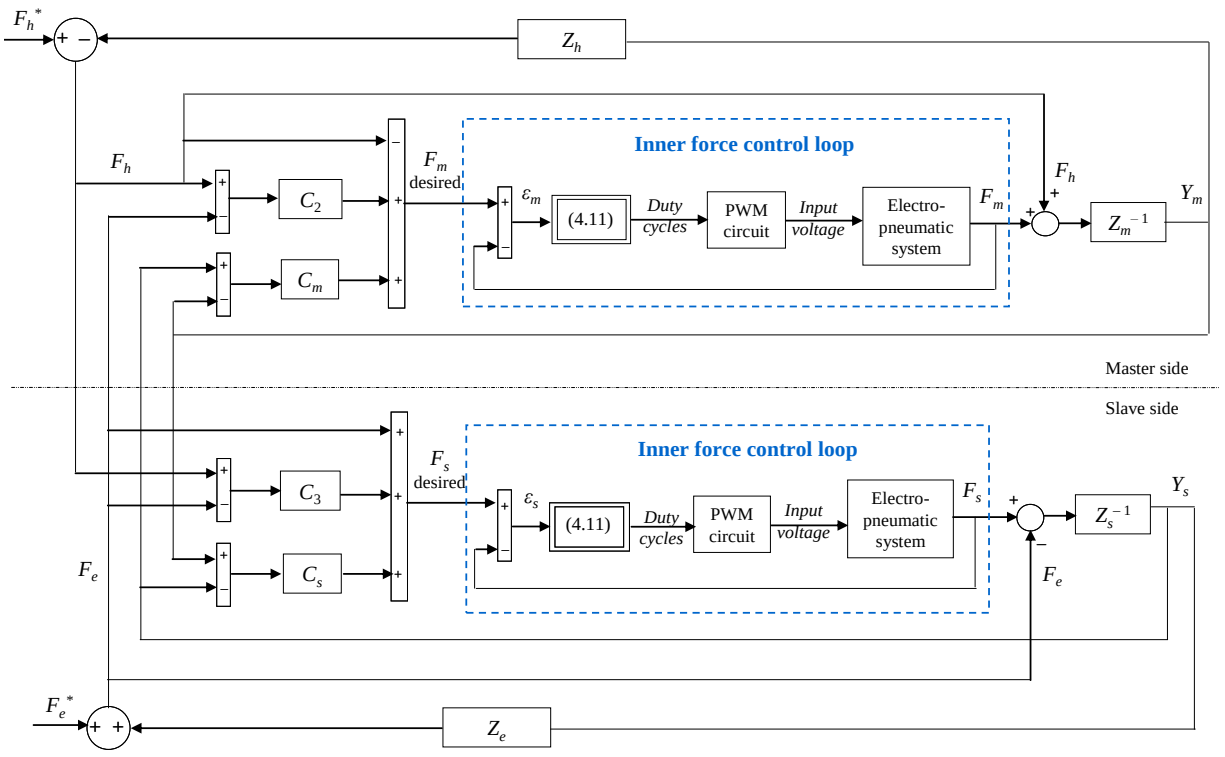

Fig. 4.4. Implementation of the PWM control on the 4CH teleoperation system

In Fig. 4.4, the inner force control loop of Fig. 4.3 is embedded in order to convert the continuous force signals (F_m desired and F_s desired) to the discrete voltage signals for applying to the on/off valves. A complete explanation of such a design, which is similar to the one of hybrid control, will be detailed in section IV.2.1.

IV. Hybrid Control Design

As it can be seen in the previous section, most of the researchers base their work on the traditional PWM method for controlling a pneumatic system with solenoid valves. A main problem with PWM control is the chattering that is caused by the high frequency switching of the valves not only in transients but also in steady state (Nguyen et al. 2007; Le et al. 2010a). The chattering phenomenon can drastically reduce the valve's lifetime and generates noises which could induce disturbances for certain applications.

To overcome the drawbacks of PWM applied to solenoid valves, we investigate a new control method inspired by the *hybrid control* theory, recently developed at Ampere laboratory for asynchronous or synchronous electrical motors control (Retif et al. 2004; Papafotiou et al. 2007; Morel et al. 2008). This approach is used in a switching-based hybrid system, which includes continuous actuators and a discrete controller with a finite number of states. In the case of AC motor drives, contrary to conventional *vector control* such as proportional-integral control in which the inverter model is not taken into account by the controller, hybrid control considers the state of the inverter as a control variable (Lin-Shi et al. 2007). Therefore, it allows obtaining faster torque dynamics than the vector-control algorithms.

The hybrid approach can be extended to various hybrid systems, not only in the electrical case but also in the pneumatic case with on/off solenoid valves (Legrand et al. 2005; Sellier et al. 2006). The originality of our study consists in applying the hybrid algorithm to a bilateral teleoperation system and proving a good transparency could be achieved. For this strategy, a discrete control vector with the same length as the number of possible configurations for the outputs of the solenoid valves is defined. A one-step predictive approach is then developed to determine the best control vector at each sample time such that the reference state in terms of desired forces is tracked (Le et al. 2010c).

Contrary to electrical field, where the switching time of the transistors can be neglected (Morel et al. 2004; Geyer et al. 2008), the main difficulty in our context is that the switching time of the valves is greater than the transistors' one. However, since ten years, the development of new technologies in electro-pneumatic field has allowed to increase significantly the bandwidth of such an on/off component. For instance, one of the fastest solenoid valve proposed by Matrix has a 500Hz bandwidth. This characteristic is by far greater than the ones presented in (Burrows 1972; Legrand et al. 2005; Sellier et al. 2006), where the bandwidth was between 10 Hz and 50 Hz. It clearly appears that such dynamics of new on/off valves can be neglected with respect to the dynamics of the pneumatic actuators.

IV.1. Model-based control design for a single pneumatic manipulator

As it will be seen later, two inner force control loops exist within a pneumatically-driven bilateral teleoperation control system. In the following, we first develop a hybrid control based predictive approach to track the desired force in each inner loop. Then, we incorporate two such hybrid controllers into the four-channel bilateral control architecture and discuss the transparency in terms of position and force tracking of the entire closed-loop haptic teleoperation system.

IV.1.1. Hybrid control principle

Hybrid control uses a hybrid model where the continuous states of a continuous system depend on the configuration of the energy modulator (i.e., the solenoid valves)

$$\dot{\underline{X}}(t) = f\left(\underline{X}(t),\ \underline{u}(t)\right) \tag{4.15}$$

with the state vector $\underline{X} = (x_1, x_2, \ldots, x_m) \in \mathrm{R}^m$ where $x_{i,\ 1\le i\le m}$ is the state variable. Here, f is the dynamic function governing the state-space model of the continuous-time system and $\underline{u}$ is a control vector that has a discrete nature and can correspond to any of the N possible configurations of the energy modular. In other words,

$$\underline{u} \in \left\{\underline{u}_1, \underline{u}_2, \ldots, \underline{u}_N\right\}_{N\ge 2} \tag{4.16}$$

where each vector of the above set represents a unique configuration for the outputs of the solenoid valves in the pneumatic system.

For a small sampling period T, the dynamic model (4.15) can be approximated by a discrete model using the forward-difference method:

$$\underline{X}\left((k+1)T\right) \approx \underline{X}(kT) + f\left(\underline{X}(kT), \underline{u}(kT)\right).T \tag{4.17}$$

The full state $\underline{X}(kT)$ is assumed to be measured at the sample time kT. The state at the sample time $(k+1)T$, denoted by $\underline{X}_j((k+1)T)$, resulting from the energy modulator's j-th configuration, $1 \le j \le N$, can be calculated by (4.17). The N directions $\underline{d}_j$ in the state space are defined as

$$\underline{d}_j = \underline{X}_j\left((k+1)T\right) - \underline{X}(kT) \tag{4.18}$$

For a given reference state $\underline{X}_{ref}$, the hybrid control calculates the N possible directions $\underline{d}_j$. Then, an optimal control among the N configurations is chosen in order to track as close as possible this reference state in the state space.

For the two-dimensional example shown in Fig. 4.5, the desired state (target point) exists in the plane of x_1 and x_2. To track this reference state at each sample time, the hybrid control algorithm proceeds as follows:

- Measurement of the state variables $x_1(kT)$ and $x_2(kT)$;
- Based on the knowledge of the states at time kT, a one-step-ahead prediction of the states at time $(k+1)T$ is carried out thanks to (4.17). Because the control signal $\underline{u}$ belongs to a finite set of possibilities as assumed in (4.16), this step is equivalent to calculation of the N different directions in (4.18); recall that $\underline{d}_j$, $1 \le j \le N$, corresponds to the j-th configuration of the energy modulator ($\underline{d}_1$ to $\underline{d}_5$ in the example in Fig. 4.5). The N possibilities for the state vector at time $(k+1)T$ are called reachable points afterwards;
- Knowing the target point at time kT, select the best configuration among the N possible configurations of the solenoid valves. The chosen configuration is the one that minimizes the Euclidean distance between the different reachable points and the target point. For instance, in the example of Fig. 4.5, the shortest Euclidean distance corresponding to direction $\underline{d}_4$ is chosen and, therefore, the corresponding control $\underline{u}_4$ is applied to the energy modulator.

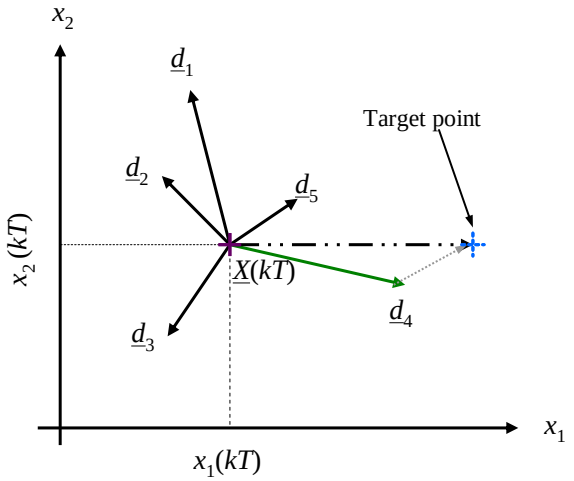

Fig. 4.5. Principle of hybrid control

IV.1.2. Application to a pneumatic system

For the system presented on Fig. 4.1 and the force tracking problem, the pressures in the chambers p and n can be used to define the state vector $\underline{X}(t)=(P_n\ P_p)^T$. At any given time, each valve may show three different input-output behaviors (pressure admission, closed, and pressure exhaust) as shown in (4.3).

Since the cases $U_1 = U_2 = 1$ and $U_3 = U_4 = 1$ have been prohibited to avoid a bypass of the valves, this leads to nine different control vectors $\underline{u}_1$ to $\underline{u}_9$, as shown in Tab. 4.1. Note that the first control configuration in Tab. 4.1 is used to conserve energy and eliminate chattering at steady state.

	$\underline{u}_1$	$\underline{u}_2$	$\underline{u}_3$	$\underline{u}_4$	$\underline{u}_5$	$\underline{u}_6$	$\underline{u}_7$	$\underline{u}_8$	$\underline{u}_9$
U_1	0	1	0	0	0	1	0	0	1
U_2	0	0	1	0	0	0	1	1	0
U_3	0	0	0	1	0	1	0	1	0
U_4	0	0	0	0	1	0	1	0	1
Chamber p	closed	fills	exhausts	closed	closed	fills	exhausts	exhausts	fills
Chamber n	closed	closed	closed	exhausts	fills	exhausts	fills	exhausts	fills

TAB. 4.1. NINE DISCRETE POSSIBLE CONTROL CONFIGURATIONS

As discussed before, knowing the pressures in both chambers at the sample time kT, the objective is to estimate the evolution of the pressures at the next sample time $(k+1)T$ in the chambers p and n for the nine possible control configurations (Tab. 4.1), and then choose the best control configuration for reaching the desired force. Assuming the variations of the pressures during a sampling time are small, the derivatives of the pressures can be discretized similar to (4.17) as

$$\begin{cases} P_p\left((k+1)T\right) \approx \dfrac{d}{dt}\left(P_p(t)\right)\Big|_{t=kT} T + P_p(kT) \\ P_n\left((k+1)T\right) \approx \dfrac{d}{dt}\left(P_n(t)\right)\Big|_{t=kT} T + P_n(kT) \end{cases} \tag{4.19}$$

where the derivatives of the pressures $\frac{dP_p}{dt}$ and $\frac{dP_n}{dt}$ are calculated based on (4.1)–(4.4) and are functions of P_p, P_n, y and $\dot{y}$. At each sample time, P_p, P_n and y are measured by sensors, while $\dot{y}$ is estimated by a numerical derivation of the position measurement y. Thus, for each of the nine control configurations, the algorithm calculates $P_p((k+1)T)$ and $P_n((k+1)T)$ based on (4.19). Consequently, the nine directions $\underline{d}_1$ to $\underline{d}_9$ found from (4.18) define the set of reachable points at time $(k+1)T$ in the state space (See Fig. 4.6).

Because each cylinder has 2 chambers, thus the dimension of the state space is $m = 2$ in a pneumatic manipulator. A geometric interpretation of the hybrid control can be provided in the plane of state variables P_n and P_p. For a given desired force F, the set of target points (i.e. desired states) is defined by a straight line because

$$P_p = \frac{F}{S_p} + \frac{S_n}{S_p} P_n + \left(1 - \frac{S_n}{S_p}\right) P_{atm} \tag{4.20}$$

Knowing the set of target points, the hybrid algorithm selects the optimal configuration that corresponds to the smallest Euclidean distance between the set of the nine reachable points and the set of target points. The choice of the best control configuration has also to take into account that the selected target point is restricted to the domain defined by an upper limit (P_{sa}) and a lower limit (P_{atm}) on the pressures in the two chambers. For example, in Fig. 4.7, the control to reach the desired force F_1 as closely as possible is $\underline{u}_6$. Nevertheless, for the desired force F_2, $\underline{u}_4$ is chosen instead because $\underline{u}_6$ leads to a solution outside the physical limits of the pressures inside the chambers.

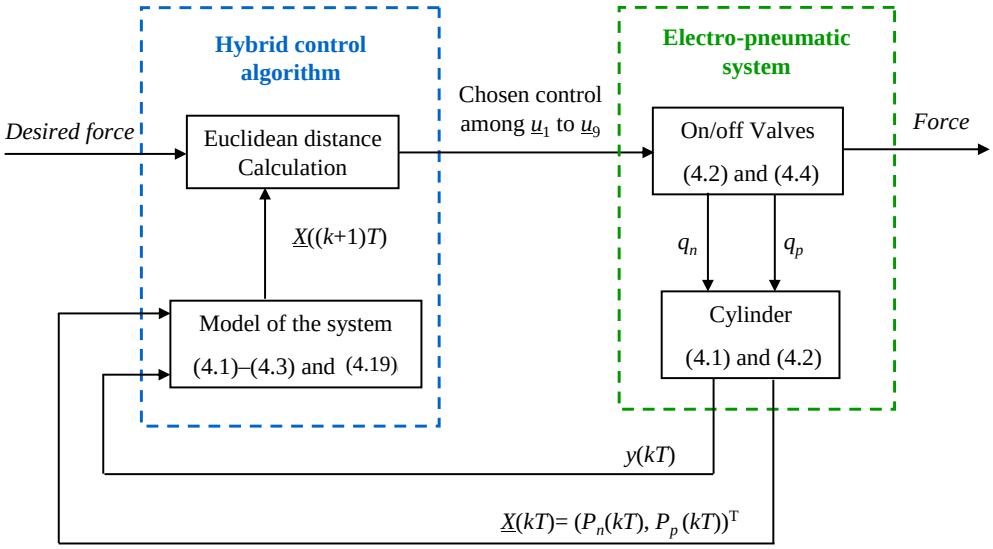

Fig. 4.6. Block diagram of the hybrid control system

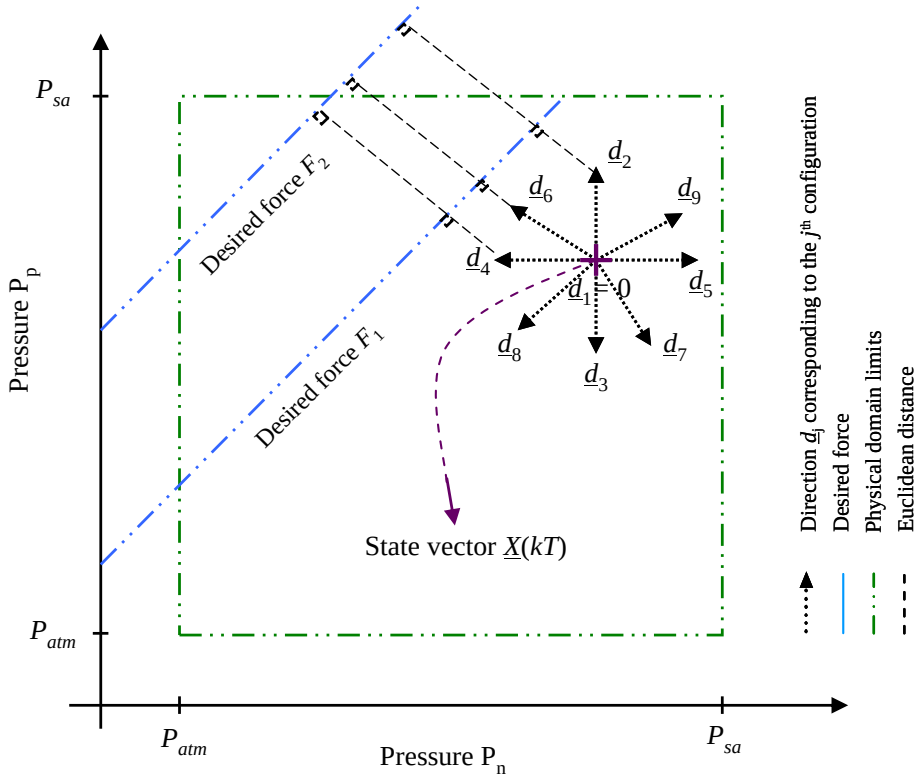

Fig. 4.7. Graphical illustration of the choice of control configuration for given desired forces

IV.1.3. Simulations

Simulations are investigated to validate the proposed control approach. The pneumatic model of a low friction cylinder and the static model of the valves, given by (4.1)–(4.4), are implemented in Matlab-Simulink environment. The model parameters used for the model-based controller are listed in Tab. 4.2.

Parameter	Value	Unit	Description
P_{atm}	10^5	Pa	Atmosphere pressure
P_{sa}	3.10^5	Pa	Supply pressure
r	287	J/kg/K	Perfect gas constant
T_a	293.15	K	Supply temperature
C_{val}	16.10^{-5}	$Nl.mn^{-1}.Pa^{-1}$	Sonic conductance
C_r	0.433		Critical pressure ratio
α	1.2		Polytropic constant
l	0.1	m	Cylinder stroke
S_p	$182.\ 10^{-6}$	m²	Piston area of chamber p
S_n	$182.\ 10^{-6}$	m²	Piston area of chamber n
M	0.2	kg	Load
b	20	N.s/m	Viscosity coefficient
T	2	ms	Sampling time in hybrid control

TAB. 4.2. MODEL AND CONTROLLER PARAMETERS FOR MATLAB IMPLEMENTATION

The force tracking of a square wave is performed in order to assess the hybrid algorithm presented in section IV.1.2. At the beginning, the force is equal to 0 N (see area (0) in Fig. 4.8), the pressures in the chambers p and n are 100 kPa (see area (0) in Fig. 4.9) and the control vector is equal to $\underline{u}_1$ (see time from 0s to 0.5s in Fig. 4.10).

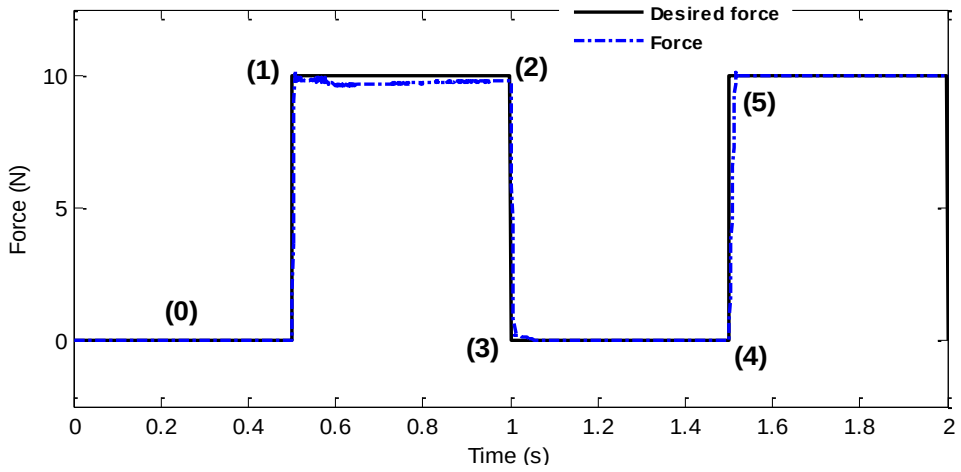

Fig. 4.8. Square wave force tracking

When the desired force reaches 10 N, the hybrid algorithm increases the pressure in the chamber p (see area (1) in Fig. 4.9), by using the control vectors $\underline{u}_2$, $\underline{u}_4$, $\underline{u}_6$ and $\underline{u}_9$ (see the simulation after 0.5s in Fig. 4.10). Afterwards, the control vector becomes again $\underline{u}_1$ in order to maintain constant pressures in the chambers so that the force is close to 10N (see area (2) in Fig. 4.8). When the desired force drops to 0 N, the evolution control vectors are successively $\underline{u}_5$ and $\underline{u}_7$ (see Fig. 4.10), that allows to increase the pressure in the chamber n and to decrease the pressure in the chamber p (see area (3) in Fig. 4.8 and Fig. 4.9). Between areas (3) and (4) the control vector is $\underline{u}_9$, so the valves are fully opened and the pressure in each chamber reaches the supply pressure P_{sa} (see area (4) in Fig. 4.9).

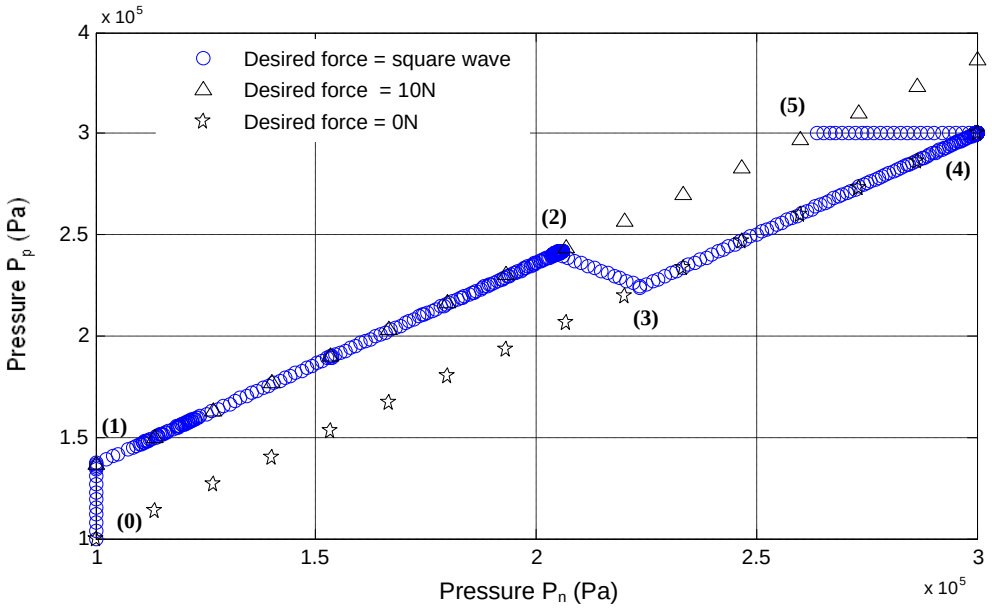

Fig. 4.9. Pressure evolution in the plane (P_n, P_p)

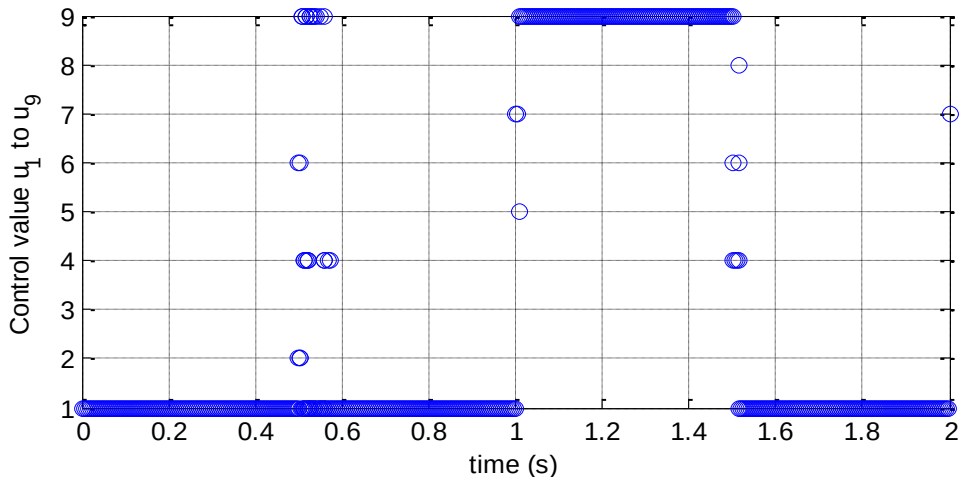

Fig. 4.10. Evolution of the different control modes

As it can be seen in Fig. 4.9, two different control vectors $\underline{u}_1$ (during 0-0.5s) and $\underline{u}_9$ (during 1-1.5s) are used to achieve the same output force (zero value) in steady state. Indeed, the choice of the control vector at time $(k+1)T$ depends only on the conditions at time kT. At the beginning (i.e., $t = 0$), $\underline{u}_1$ applied to the valves results in a zero force. Therefore during the first 0.5s, in order to keep the force at zero value, the algorithm does not need to change the control vector and consequently, $\underline{u}_1$ is always used. At 1s, when the pressures in both chambers are equal (area (3)), either control vectors $\underline{u}_1$ or $\underline{u}_9$ may be used to keep the zero force. The algorithm computes the "Euclidean distance" for these two vectors to find which one is better. In this case, the "Euclidean distance" is smaller in $\underline{u}_9$ case than in $\underline{u}_1$ case, thus the control vector $\underline{u}_9$ is chosen during 1s-1.5s.

IV.1.4. Experiments

IV.1.4.1. Implementation

In this section, experiments are conducted to compare the force tracking performance of the hybrid and the PWM controls. A schematic for the system setup is illustrated in Fig. 4.1. In terms of actuators, the low-friction cylinder (Airpel model M16D100D) has a 16 mm inner diameter, a 100 mm stroke length, and a 5mm rod diameter. The four solenoid valves (Matrix model GNK821213C3KK) used to control the air flow have switching times of approximately 1.3ms (opening time) and 0.2 ms (closing time). With such fast switching times, the on/off valves are appropriated for the purposes of the proposed control. The valves' flow rate characteristics (4.4) used in the control scheme of Fig. 4.3 and Fig. 4.6 come directly from the data sheets of the components. In terms of sensors, a low-friction linear variable differential transformer (LVDT) is connected to each cylinder in order to measure the master's and the slave's linear positions. In addition, each cylinder chamber is equipped with a pressure sensor. The system was supplied with air at an absolute pressure of 300 kPa.

A computer is applied to control the switching solenoid valves to exchange experimental data via a dSPACE controller board (DS1104). The sensor information is fed back to the computer through the ADC block (Analog-to-digital conversion) of the I/O board. The Control Desk application provides a graphical user interface for adjusting dSPACE controller parameters during experiments (see Fig. 4.11).

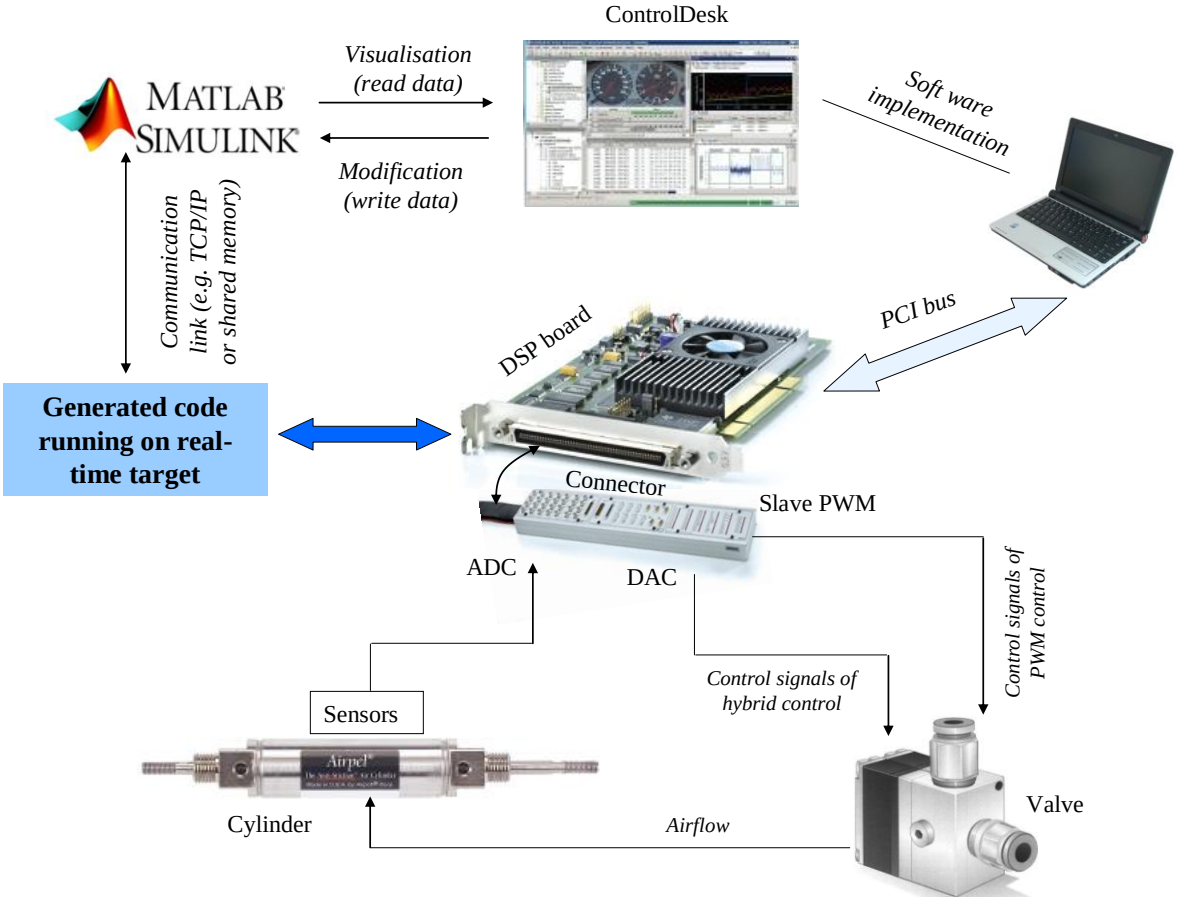

Fig. 4.11. Application of the dSPACE controller board on the experimental pneumatic test-bed

In the hybrid strategy, the models of the electro-pneumatic system are given by (4.1)–(4.4) and the constant parameters used in the tests are listed in Tab. 4.2. The controller output signal is computed in real-time and then transferred through the DAC block (Digital-to-analog conversion) to the solenoid valves (Fig. 4.11). The closed-loop experiment with hybrid algorithm is performed to investigate the control performance of the proposed scheme (Fig. 4.6). The controller is designed with Simulink and written with C programs, running at a sampling rate of 500 Hz. This value has been

chosen according to the open/close bandwidth of the valves and to guarantee acceptable tracking responses.

In the PWM strategy, the pulse waves are generated by "Slave DSP PWM Signal Generator" block in Simulink environment. This block allows to convert the input duty cycles to the output voltages which are then transferred to the fast switching valves. Since the implementation of the model based controller is not necessary, the execution time of DSP controller is faster in the PWM case than in the hybrid case. Note that this point does not influence the tracking performance in the hybrid control because the controller is fast enough to execute the algorithm for each sample time (2 ms).

The performance of the PWM control depends on the switching frequency f_{PWM} and the gain K_{PWM} (defined in section III.2). The choice of f_{PWM} affects the harmonic distortion of the output signal at high switching frequencies and there is a switching frequency above which the output harmonic distortion becomes more visible. As discussed in the section III.2, the switching frequency applied of 100 Hz could be considered as the best tuning found. The proportional controller K_{PWM} is tuned empirically without using any analytical method. An increase of K_{PWM} can improve the force closed-loop behavior. However it could result in a saturation of the valves where the duty cycles can exceed the maximal value dc_{max} or the minimal value dc_{min} (4.13). In practice, the proportional gain K_{PWM} is chosen to be equal to 0.02 in order to achieve good dynamic performances and to satisfy the condition (4.14).

IV.1.4.2. Comparison of PWM and hybrid control

Fig. 4.12 and Fig. 4.13 show the square wave force tracking obtained with a hybrid control and a simple proportional PWM control. The amplitude range of the desired force is ±10N. As it is shown on these figures, the steady state error is respectively about ±1.5N and ±2.5N for the hybrid control and the PWM control. We can see that the predictive aspect of the hybrid control leads to a better accuracy in force tracking than the PWM control because for each sample time, it chooses the best control signals among the nine available control configurations. As illustrated in Fig. 4.14, the state variables P_p and P_n in state space converge quickly to the set of target points, defined by two straight lines corresponding to the desired forces of 10N and – 10N.

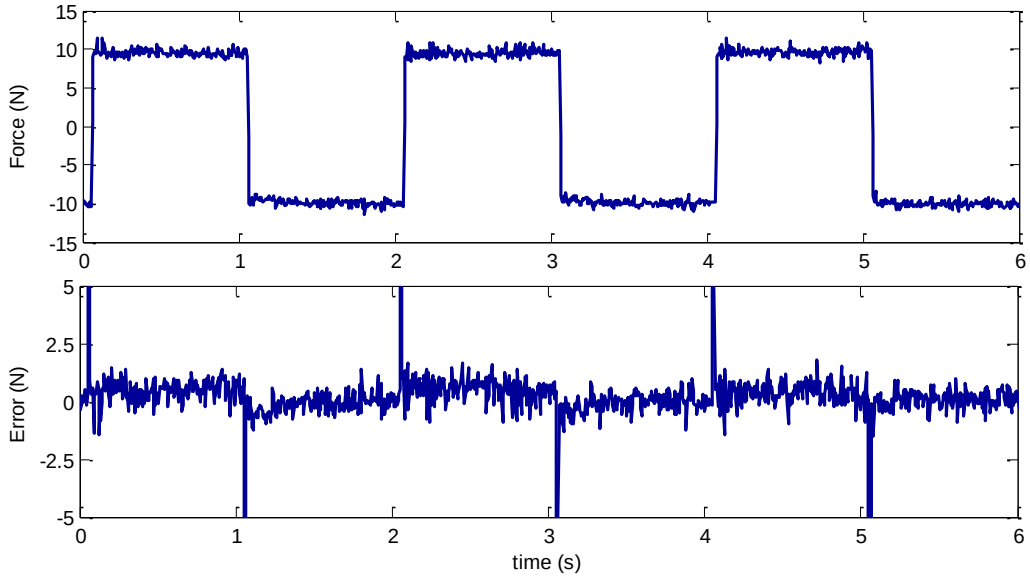

Fig. 4.12. Square wave tracking for the hybrid control

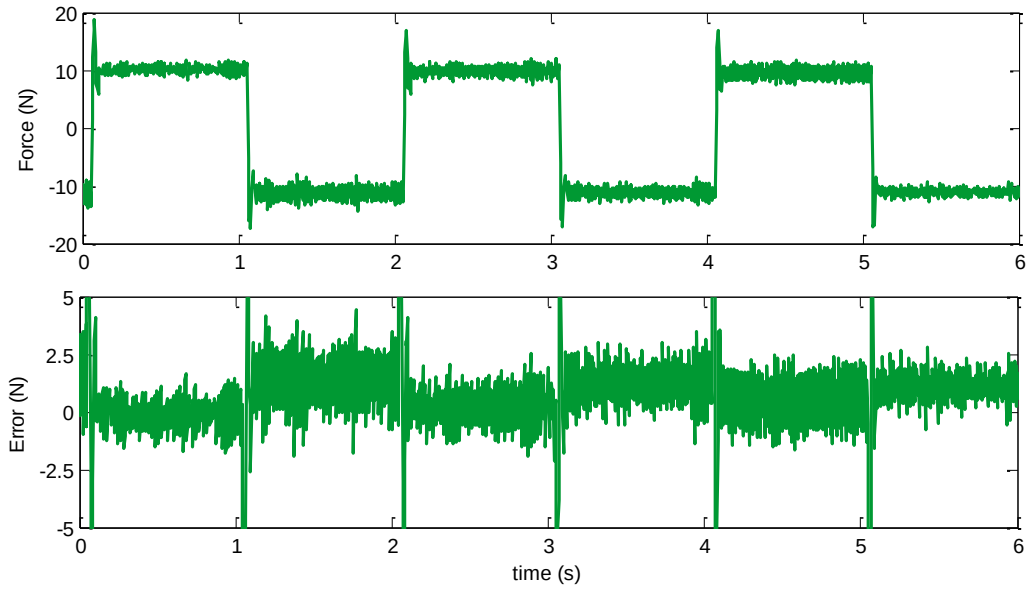

Fig. 4.13. Square wave tracking for the PWM control

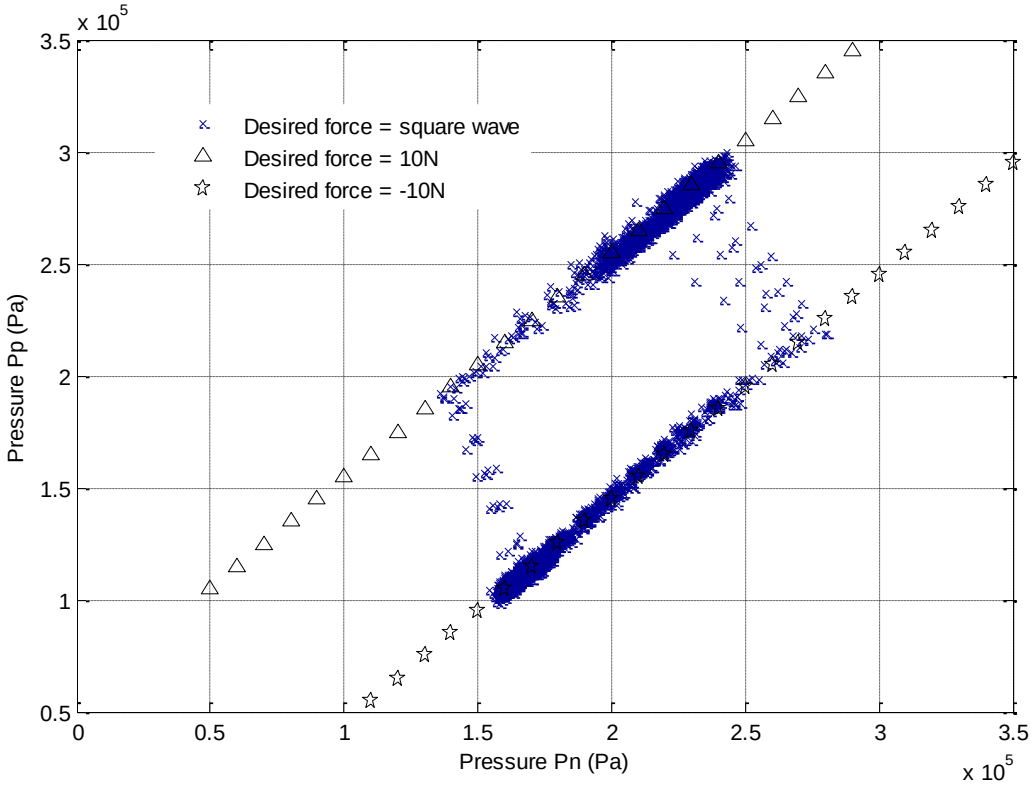

Fig. 4.14. Behavior of the state variables in (P_p, P_n) plan

With the PWM control, when the tracking error is close to zero, the modulation ratio of the input voltage is 50%. That means unnecessary electrical power is used. In order to reduce the chattering phenomenon and to improve the energy consumption in PWM, (Nguyen et al. 2007) defined a "dead band" close to zero, so that if the tracking error is within this region, a third mode $\underline{U}$=[0 0 0 0] allows to switch off all the valves. Thereby a good tracking performance in steady state can be obtained without applying switching pulses to the valves. However, the trade-off between the tracking performance and the energy consumption makes the choice of the "dead band" value quite difficult: with a high "dead band" value, the tracking accuracy can be impaired while with a low value,

the tracking error hardly achieves to the "dead band" zone so saving energy is not efficient. Contrary to the PWM control, the strategy used in the hybrid control allows to guarantee a good tracking performance and also an energy saving without using a "dead band" technique. As it is shown in Fig. 4.15, the system applies the control $\underline{u}_1$ (Tab. 4.1) in steady state to maintain the pressure in the chambers and there is no consumption of power (Al-Dakkan et al. 2003; Ke et al. 2005; Shen & Goldfarb 2007a; Yang et al. 2009).

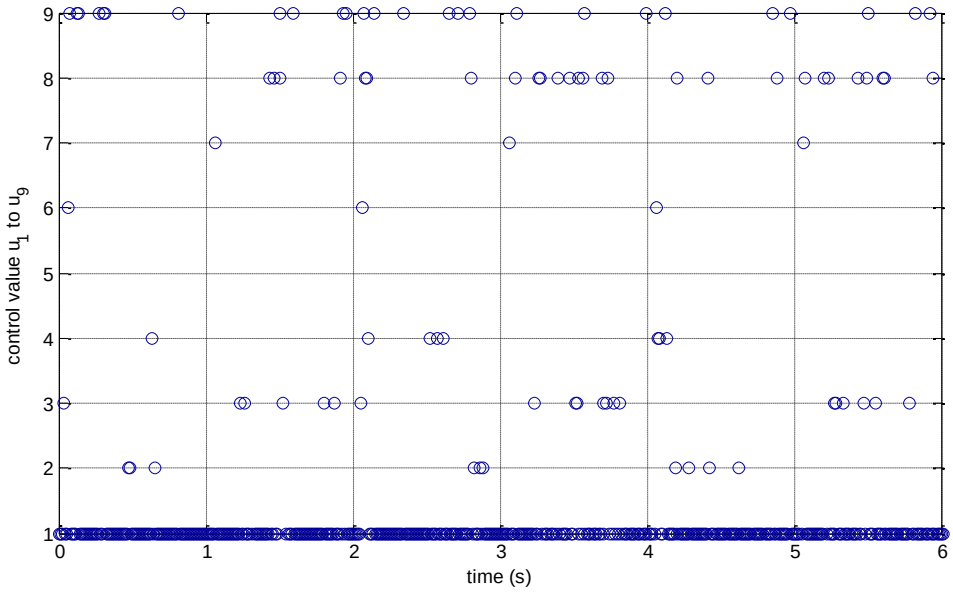

Fig. 4.15. Evolution of the control value in hybrid algorithm

The difference between the two strategies comes from the fact that the hybrid algorithm is based on 9 control modes whereas the PWM algorithm uses only 2 or 3 (if the switch off mode is chosen). This aspect is illustrated on Fig. 4.16 where the pressure in the chamber n for the hybrid control is clearly smoother than the PWM control. Similar results can be observed in the chamber p.

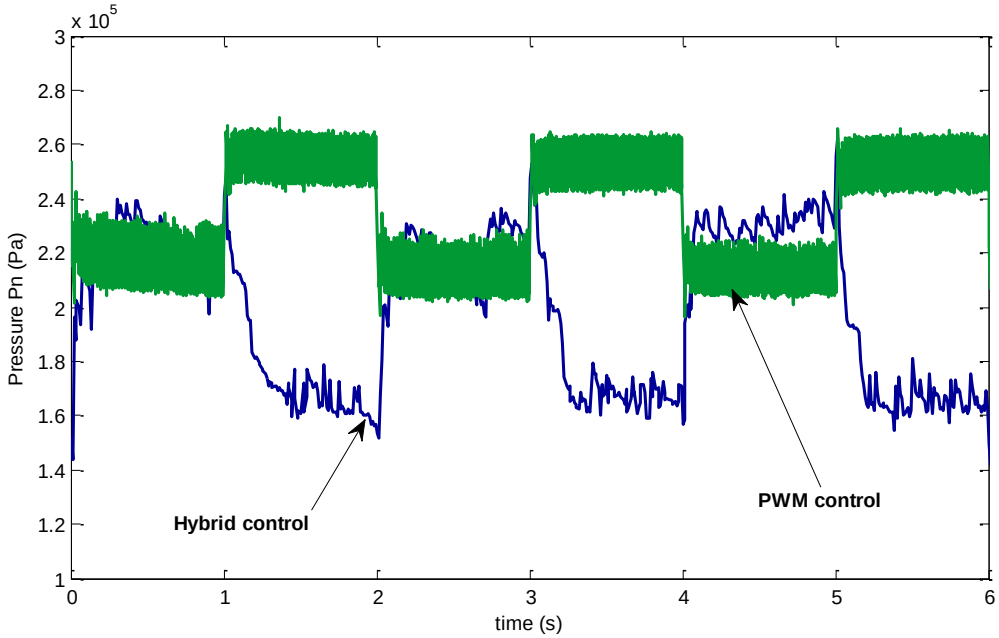

Fig. 4.16. Evolution of the pressures in the chamber n

Based on these results, it is clear that hybrid control is an interesting alternative to save energy and improve the valve's lifetime. Furthermore, the choice of the sampling time is the only tuning parameter in this strategy. The major drawback of this technique is that it requires an accurate model of the process. The estimation of the mass flow rate behavior of the system is an essential stage before applying the control algorithm.

IV.2. Hybrid bilateral control for a pneumatic teleoperation system

In this part, we incorporate the hybrid control algorithm into the four-channel (4CH) bilateral teleoperation architecture (Le et al. 2011c). The reason for this is that the four-channel method is the most general teleoperation control architecture compared to position error based (PEB), direct force reflection (DFR), and is one that can achieve superior transparency (chapter 2, section III). Then, an analysis of the controller parameters is carried out in order to achieve satisfactory performance in terms of teleoperation transparency.

IV.2.1. Implementation of the force inner loop in the 4CH architecture

As discussed in chapter 2 section III.1, the perfect transparent condition is obtained by selecting the controller C_1 through C_6 as

$$C_1 = Z_s + C_s \qquad C_4 = -(Z_m + C_m) \qquad C_6 + 1 = C_2 \qquad C_5 + 1 = C_3 \tag{4.21}$$

With this choice of controllers, it is easy to see, based on Fig. 2.5 (chapter 2), that the master and slave closed-loop equations become:

$$\begin{aligned} C_2(F_h - F_e) &= (Z_m + C_m)(Y_m - Y_s) \\ C_3(F_h - F_e) &= (-Z_s - C_s)(Y_m - Y_s) \end{aligned} \tag{4.22}$$

On the other hand, the master and slave dynamics Z_m and Z_s can generally be modeled by simple mass-spring-damper systems. As it is evident from the previous closed-loop equations (4.22), if the master and slave dynamics include damping terms, they obviously contribute to the closed-loop equations in the same way as the derivative terms of the master and slave PD controllers (i.e., C_m and C_s). Similarly, the spring stiffness terms in the master and slave dynamics can be combined with the proportional terms in C_m and C_s. Therefore, in most of the teleoperation literature, Z_m and Z_s are considered to be pure inertias (Lawrence 1993; Yokokohji & Yoshikawa 1994; Tavakoli et al. 2008).

The control laws described in (4.21) for C_1 and C_4 require acceleration measurements (due to the inertial contributions of the dynamics Z_m and Z_s). If a good transparency is required over a large bandwidth, accurate estimation of inertial parameters based on accelerometers may be justified (Yokokohji & Yoshikawa 1994). Alternatively, it is possible to use differentiators that are robust to noise measurement so that only position sensor is used (Levant 1998; Suzuki et al. 2003; Sidhom et al. 2010). However, at low frequencies, near-transparency can be obtained by ignoring the inertial terms in the expressions for C_1 and C_4 (Salcudean et al. 2000), in which case the original control design (4.21) is modified to

$$C_1 = C_s \qquad C_4 = -C_m \qquad C_6 + 1 = C_2 \qquad C_5 + 1 = C_3 \tag{4.23}$$

According to the choice of controllers in (4.23), based on Fig. 2.5 (chapter 2), the master and slave closed-loop equations become

$$\begin{aligned} C_2(F_h - F_e) &= Z_m Y_m + C_m(Y_m - Y_s) \\ C_3(F_h - F_e) &= Z_s Y_s - C_s(Y_m - Y_s) \end{aligned} \tag{4.24}$$

There is more than one way to choose the controllers in (4.23). Usually, the position controllers are chosen such that $C_m/C_s = Z_m/Z_s$. Since in our experiments the master and the slave robots are identical $Z_m = Z_s = Z$, we take their controllers to be similar as well:

$$C_s = C_m = C_p \qquad C_2 = C_3 = C_f \tag{4.25}$$

where C_p and C_f are the position and force controllers to be determined. Normally, C_p is a PD-type controller and C_f is a scalar gain. With the choice of controllers in (4.25) and based on the closed-loop equations (4.24) and, the position error dynamics becomes

$$(Z + 2C_p)(Y_m - Y_s) = 0 \tag{4.26}$$

indicating that the slave and master positions track each other asymptotically (note that the robot inertia Z and the proportional and derivative gains of the controller C_p are all positive). This fact can also be shown by calculating h_{21} in (2.10) (chapter 2). It is easy to see that for the choice of controllers C_m, C_s, C_2 and C_3 in (4.25) as well as $C_6 = C_2 - 1$ and $C_5 = C_3 - 1$ from (4.23), we get $h_{21} = -1$, which ensures master-slave position tracking in free motion (because $h_{21} = -Y_s / Y_m\big|_{F_e=0}$). Note that (4.26) shows position tracking under both free motion and contact motion.

With perfect position tracking, (4.24) can be rewritten as

$$C_f (F_h - F_e) = ZY_m = ZY_s \tag{4.27}$$

Therefore, force tracking is not perfect for a high magnitude of impedance Z (i.e., for high inertia or high frequencies). As we used the acceleration measurements needed in (4.21), the force tracking error would have converged to zero – a fact evident from (4.22). It is also intuitively clear that absence of knowledge about the manipulator's inertial parameters in the controllers (4.23) can deteriorate the force tracking performance especially over high frequencies. However, for low frequencies, the right-hand side of (4.27) can be negligible, meaning that $F_h - F_e$ converges to zero at a low bandwidth. Worthy of note is that since voluntary motions of the human hand are themselves band-limited, force tracking will be good short of feeling high-frequency phenomena such as the sharp edges or texture of an object. Note that the maximum bandwidth with which the human finger can apply motion or force commands is only 5-10 Hz (Shimoga 1993b) and the maximum bandwidth with which the human finger reacts to tactile stimuli is only 8-10 Hz (Shimoga 1993a).

Good force tracking can also be evaluated by calculating h_{12} in (2.10) (chapter 2). For the choice of controllers C_m, C_s, C_2 and C_3 in (4.25) as well as $C_6 = C_2 - 1$ and $C_5 = C_3 - 1$ from (4.23), we get $h_{12} = 1$, which ensures master-slave force tracking in contact motion (because $h_{12} = F_h / F_e\big|_{Y_m=0}$). Note that (4.27) shows low-frequency force tracking under both free motion and contact motion.

Again, with the choice of controllers C_m, C_s, C_2 and C_3 in (4.25) as well as the conditions $C_6 = C_2 - 1$ and $C_5 = C_3 - 1$ from (4.23), it is possible to see that $h_{11} = Z / C_f$, which is a less-than-ideal value for the free-motion input impedance, and $h_{22} = 0$, which is the ideal value for the locked-motion output admittance. Clearly, the user will feel the free space when the slave is in free motion if the magnitude of Z is low (i.e., for low inertia and/or low frequencies) and/or with a high force feedback gain C_f.

Given the good position and force tracking, the operator indeed feels the environment impedance Z_e without feeling the "tool" impedance (the tool being the master-slave teleoperation system). Thanks to the transparency conditions (4.23) and the simplifying assumption (4.25), the four-channel bilateral teleoperation architecture in Fig. 2.5 with eight controller parameters (C_1 to C_6 , C_m and C_s) has been simplified to only two controllers (C_p and C_f).

After the previous transparency analysis, the pneumatic teleoperation schemes are obtained with hybrid strategy, as illustrated in Fig. 4.17.

A main difference between the original diagram in Fig. 2.5 and the diagram presented in Fig. 4.17 is that the hybrid algorithm for force control of pneumatic manipulators has been incorporated into Fig. 4.17. The teleoperation control signals F_m and F_s correspond to the desired force that is input to the hybrid force control loops shown in Fig. 4.6. With good force tracking obtained with the hybrid control, the behavior of the inner loop becomes equivalent to a unitary transfer function, reducing the block diagram of Fig. 4.6 to the standard block diagram of Fig. 2.5 In this case, the passivity (and thus the closed-loop stability) of the four-channel system is established via analysis of the teleoperation system's scattering matrix, which can be shown to have singular values no greater than unity (Tavakoli et al. 2007a).

In order to simplify the controller parameter calculation, the inner loops in Fig. 4.17 are supposed to be perfect. This assumption will be experimentally verified in the section IV.2.3.2.

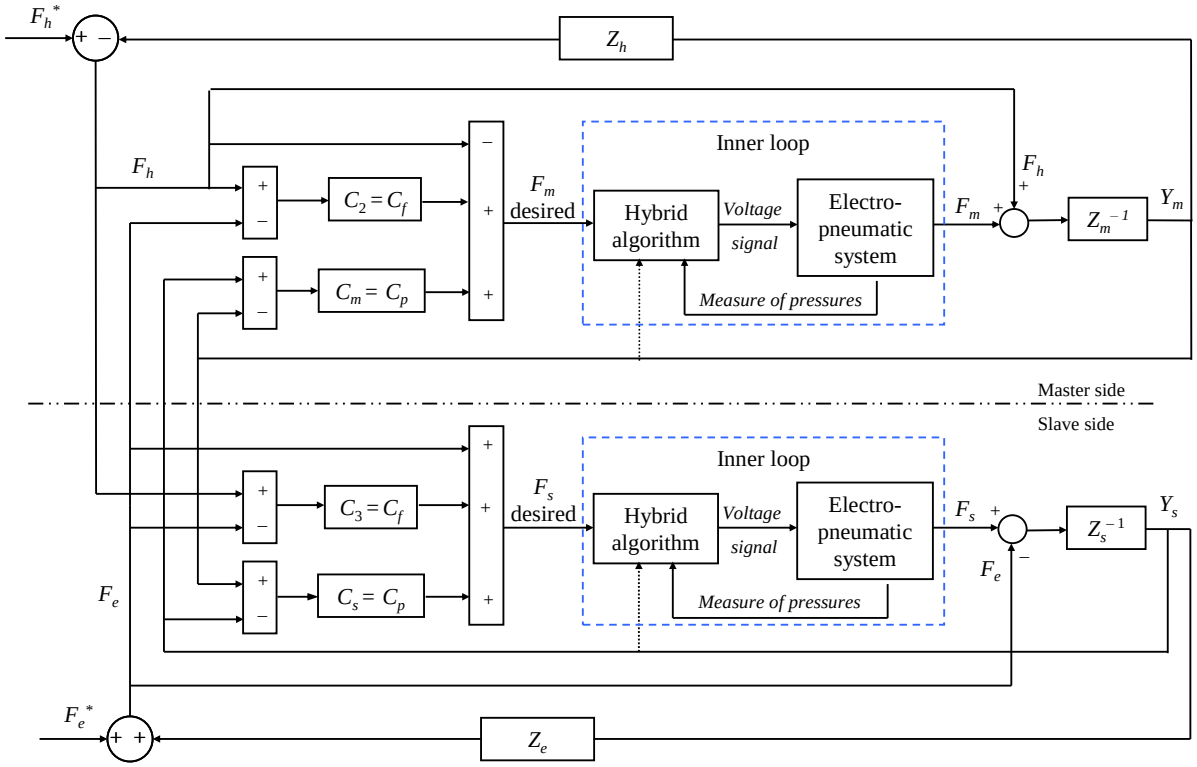

Fig. 4.17. 4CH bilateral teleoperation block diagram with hybrid control

IV.2.2. Simulations

In this section, we verify the efficiency and performance of the hybrid control in a teleoperation system using pneumatic actuators with on/off solenoid valves. The 4CH architecture, presented in section IV.2.1, is used with the hybrid force control described in section IV.1.2. For the sake of simplicity, we neglect the stiction force in (4.2). Hence, the simulations were carried out on a 1-DOF master/slave system whose dynamics are given by

$$\begin{aligned} M\ddot{y}_m + b\dot{y}_m &= f_m + f_h \\ M\ddot{y}_s + b\dot{y}_s &= f_s - f_e \end{aligned} \tag{4.28}$$

where b is the viscous coefficient (N/m/s) and M is the moving load (kg) of both the master and the slave actuators. For the sake of simplicity, the stiction force is supposed to be negligible. The master and slave have been modeled as mass-damper systems with impedances

$$Z_m = Z_s = Z = 0.2s^2 + 50s \tag{4.29}$$

The pneumatic models of the master and slave actuators, given by (4.1)–(4.4), are implemented in Matlab/Simulink. The model and the controller parameters used in simulation are listed in Tab. 4.2. All parameters are considered to be identical for the master and the slave manipulators. For simplicity and in order not to make any specific choice for the human operator's impedance Z_h, in the simulation we model the operator as an exogenous input force. In practice, the human operator with a finite impedance dynamic range improves the stability robustness compared to the case where it is represented as a force input.

The initial values of the position and the velocity are set as $y_m(0) = y_s(0) = 0.05$ and $\dot{y}_m(0) = \dot{y}_s(0) = 0$. The initial pressures in the chambers are supposed to be equal to the atmospheric pressure.

IV.2.2.1. Controller design

The position controller C_p is designed to place the master and the slave closed-loop poles such that a fast response without overshoot is obtained. It is evident that each of the master and the slave robots in free motion has the closed-loop transfer function

$$H_y(s) = \frac{Z^{-1}(s)C_p(s)}{1+Z^{-1}(s)C_p(s)} \tag{4.30}$$

Now, assume that the desired free-motion closed-loop transfer function of the master and the slave $H_y(s)$ is equal to as the following second-order model with fast and critically-damped poles:

$$H_y(s) = \frac{2500}{s^2+100s+2500} \tag{4.31}$$

From (4.30) and (4.31), the position controller C_p is designed as

$$C_p(s) = \frac{H_y(s)}{Z^{-1}(s)\left(1-H_y(s)\right)} = \frac{5s+1250}{0.01s+1} \tag{4.32}$$

The force controller is chosen to be scalar in order to avoid differentiating noisy force signals

$$C_f(s) = K_f \tag{4.33}$$

where K_f is a proportional gain equals to 3. This value is chosen due to the trade-off between the tacking performance and the chattering problem.

IV.2.2.2. Closed-loop performance

The position and force tracking of the master-slave system are investigated in order to assess the transparency of teleoperation. Fig. 4.18 and Fig. 4.19 illustrate the force and position tracking performances when the slave is in contact with soft and hard environments, respectively. The environment is modeled as a spring with 0.5kN/m stiffness for the soft contact case and with 10kN/m stiffness for the hard contact case. Here the human is performing a movement from 0.03 m to 0.07 m on the master robot and, a sinusoidal external force with amplitude 10N and frequency 1Hz is disturbing the slave robot. The solid lines are the responses of the master while the dashed lines are the ones of the slave.

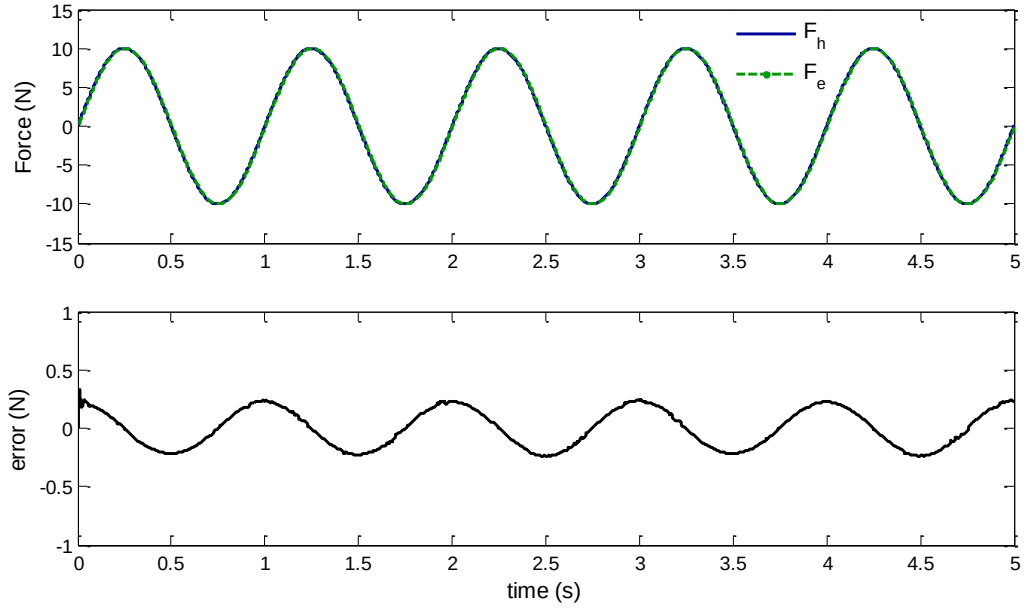

(a). Force tracking

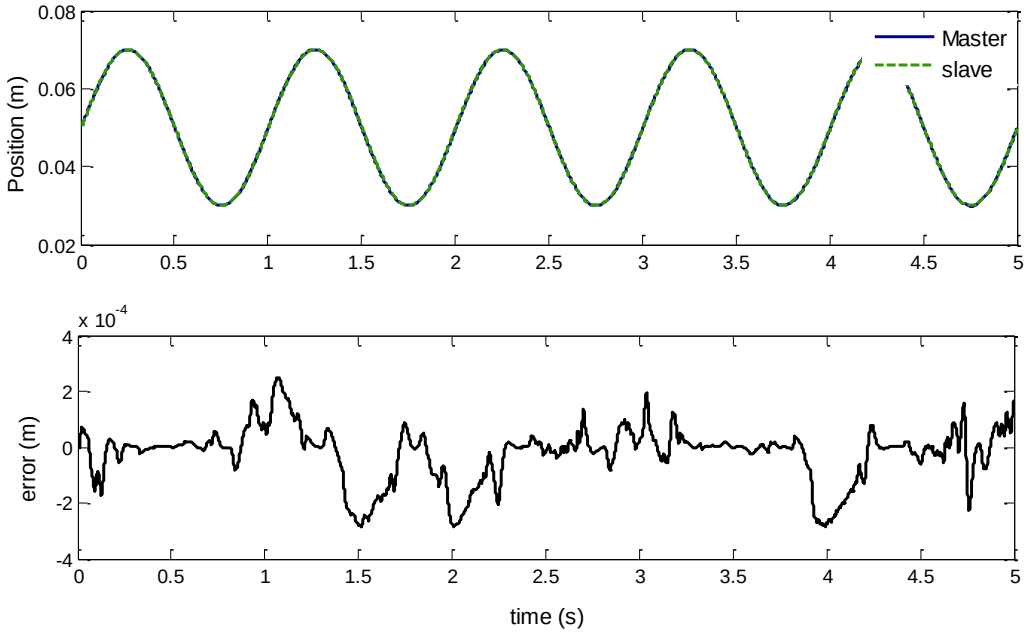

(b). Position tracking

Fig. 4.18. Transparent performance in soft contact

As it is shown in the figures, the force tracking error is about 2% and 6% for the soft contact and the hard contact, respectively. In the soft contact, the system presents a better force tracking performance than in the hard contact. The same remark can be made for the position tracking where the error is respectively about 2% and 15%. As for position tracking, it is only to be expected that under hard contact, the slave cannot penetrate the environment, thus the position tracking error will be larger compared to soft contact. As for force tracking, according to (4.24), larger position tracking errors lead to larger force tracking errors. Therefore, the force tracking error is larger in the hard contact than the soft contact.

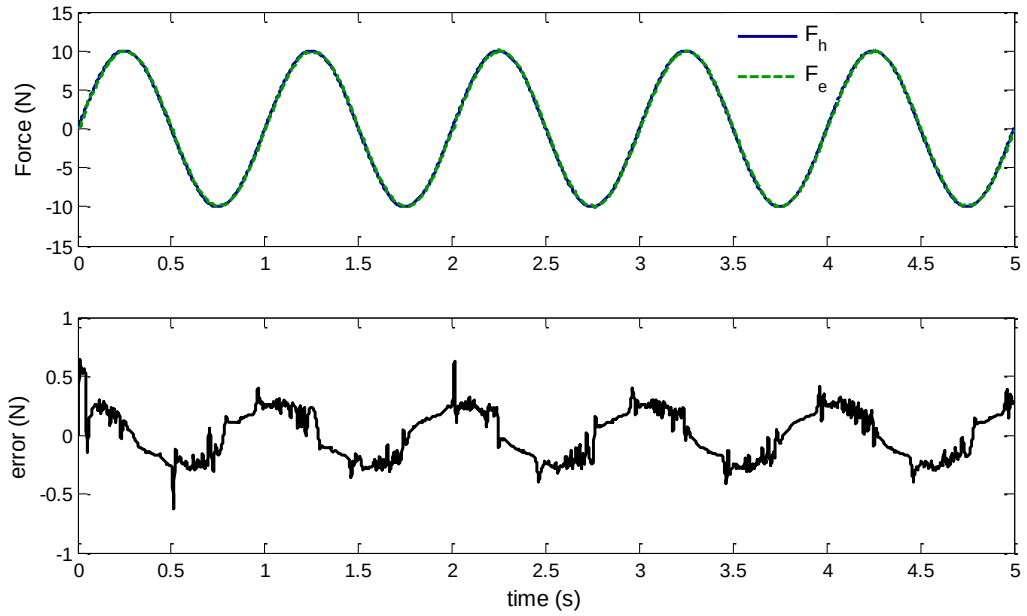

(a). Force tracking

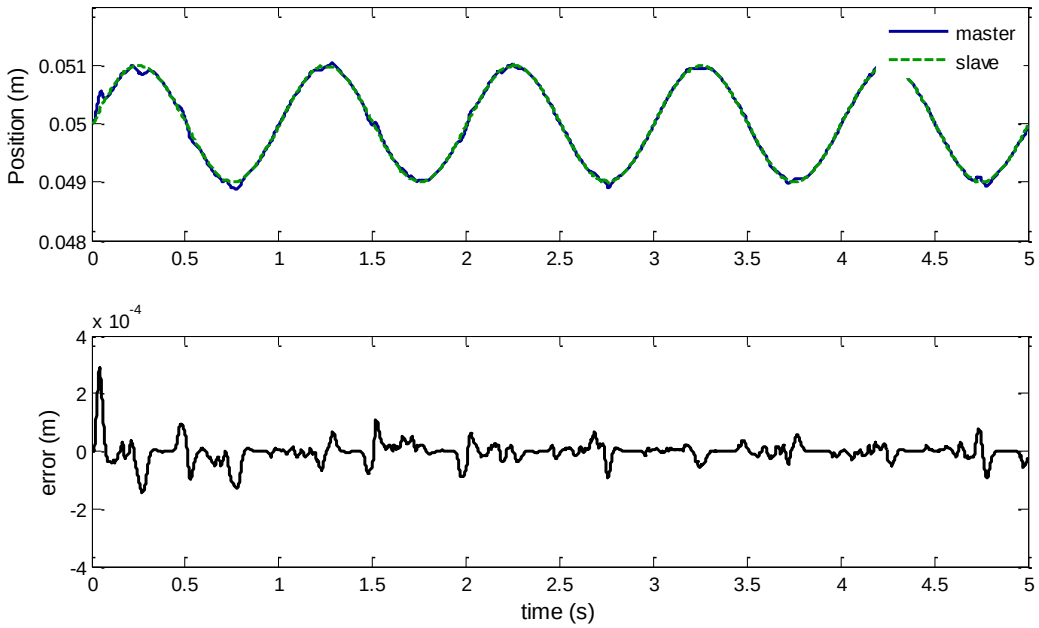

(b). Position tracking

Fig. 4.19. Transparent performance in hard contact

When the slave is in contact with a high-stiffness environment, some small vibrations appear in the interaction force F_e and then affect the displacements Y_m and Y_s (Kuchenbecker & Niemeyer 2006), as simulated in Fig. 4.19. These vibrations may degrade the perception of the operator because he/she will feel them through the master interface in addition to the environment impedance. The high vibrations or oscillations can make the teleoperation system unstable.

In order to study the influence of frequency on the transparency, the system is excited by a 5Hz sine wave instead of the previous 1Hz sine wave. The results of the soft contact case are illustrated in Fig. 4.20.

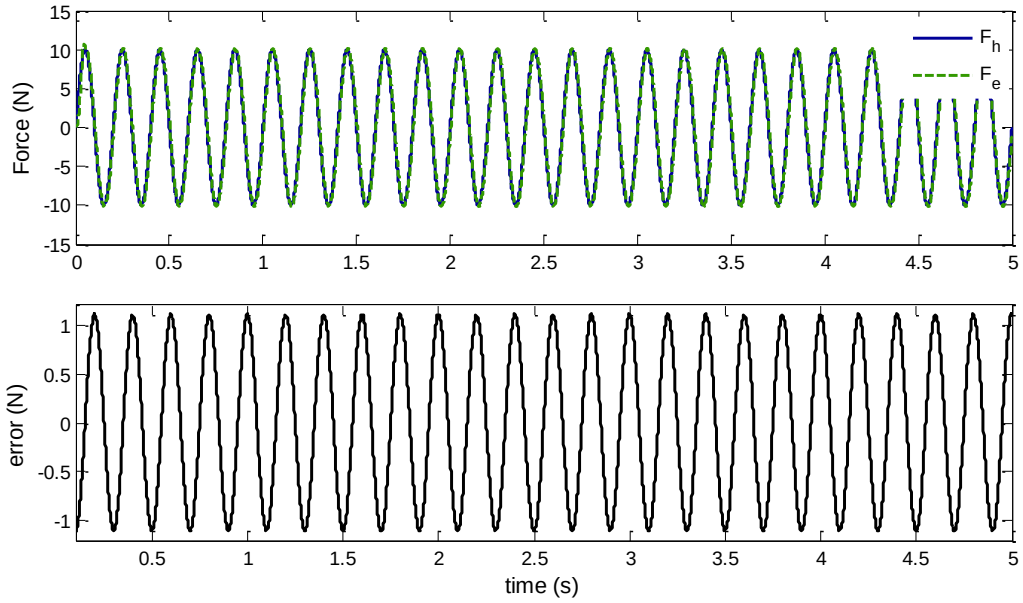

(a). Force tracking

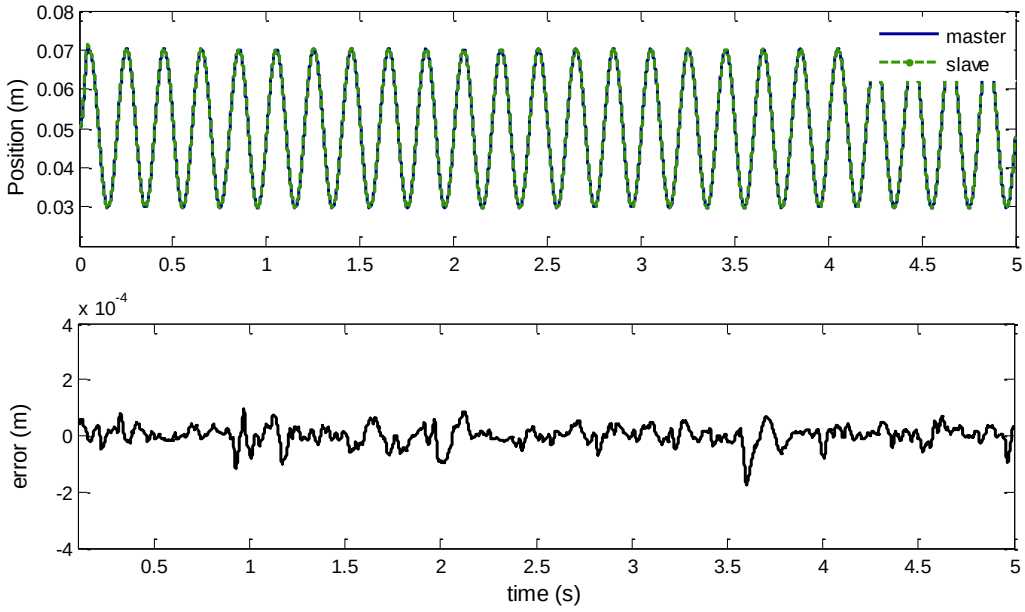

(b). Position tracking

Fig. 4.20. Performance in soft contact at 5Hz sine wave

It can be seen that the same accuracy in position tracking has been obtained in Fig. 4.18 (1Hz input) and Fig. 4.20 (5Hz input). However, the force tracking performance is deteriorated in the 5Hz case compared to the 1Hz case. In fact, the force tracking errors are respectively 12% and 2% for the 5Hz and the 1Hz inputs. This is consistent with (4.27) and shows that modification of the ideal transparent conditions (4.21) to (4.23) can degrade the force tracking performance over high frequencies. Thus, a high accuracy in force tracking is only achieved at a low bandwidth, where the movements of the operator hand are not too fast.

Lastly, in free motion where the slave manipulator is not in contact with the environment, good position tracking is also achieved as shown in Fig. 4.21.

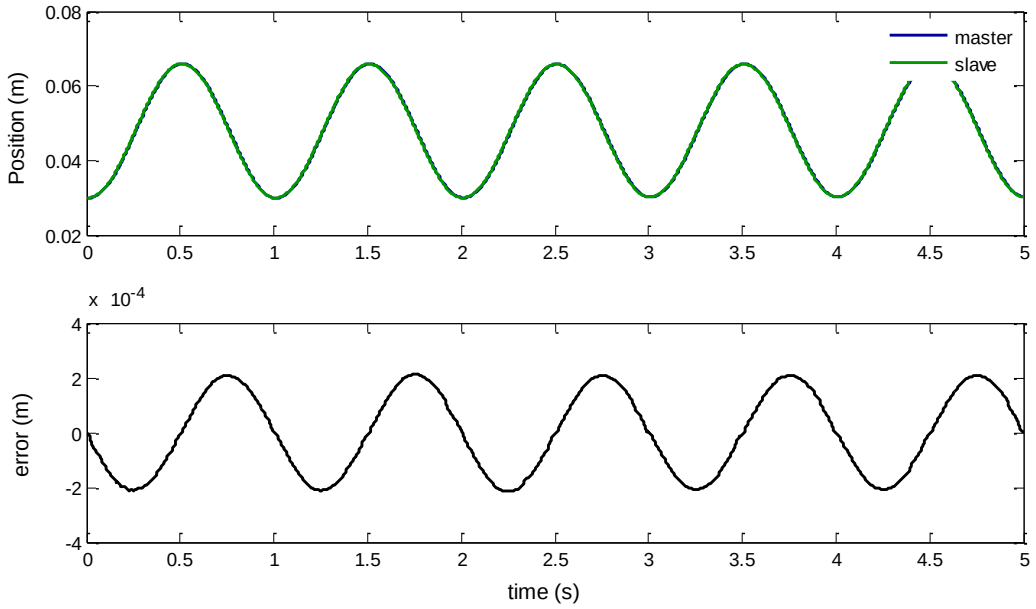

Fig. 4.21. Position tracking in free motion

The following section verifies system performance through experiments.

IV.2.3. Experiments

In this section, experiments with a 1-DOF teleoperation system are reported. As illustrated in Fig. 4.22, the setup consists of two identical pneumatic manipulators (as the master and the slave), the operator's hand and the environment. The description in terms of actuators and sensors of each interface was mentioned in section IV.1.4.1. In addition, each of the end-effectors of the master and the slave manipulators is equipped with a force sensor – this will help to measure the operator's and the environment's forces, respectively. Note that since the distance between the master and slave manipulators is limited to a few meters, their controllers are embedded on one single computer system.

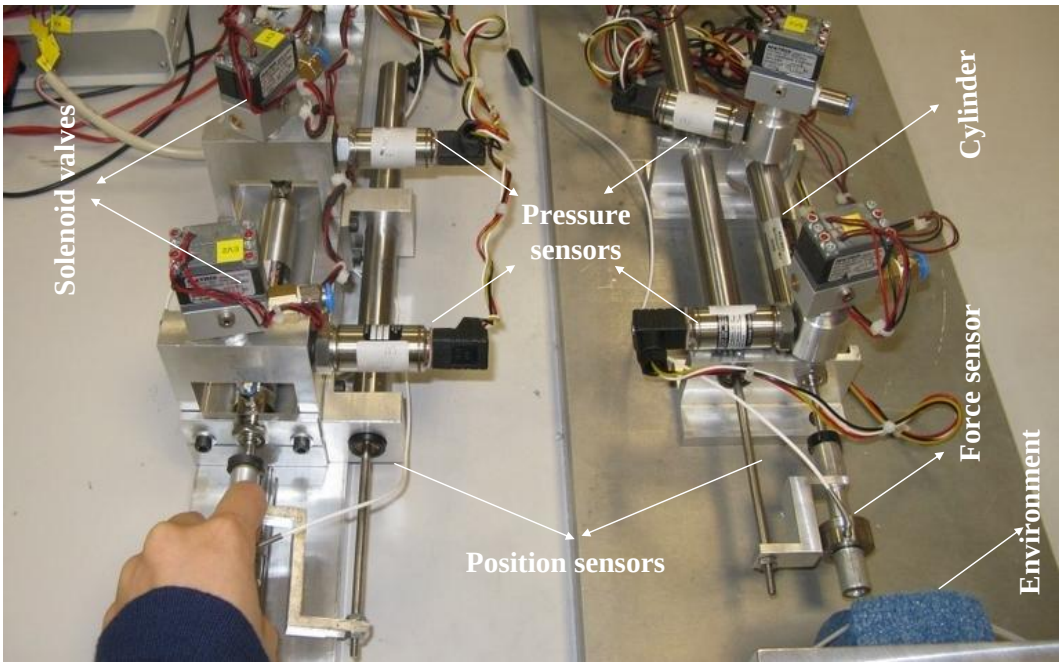

Fig. 4.22. Pneumatic master–slave teleoperation experimental setup

The sampling rate of the controller (500 Hz) is chosen to be higher than the bandwidth above which the human finger cannot distinguish two consecutive force stimuli which is 320 Hz (Shimoga 1993b).

IV.2.3.1. Transparency in the 4CH teleoperation system

Fig. 4.23 shows the force and position tracking responses of the 4CH scheme obtained in the experiments, in which the controller parameters (C_f and C_p) are chosen similar to the simulations.

In the experiments, for the first few seconds, the master is moved back and forth by the user when the slave is in free space. The small but nonzero values for F_e when the slave is in free space are due to the uncompensated mass of the handle-like connector between the slave's force sensor and the slave's end-effector (tip). Similarly, the nonzero values for F_h during slave's free motion are due to the mass of the master's handle, which lies between the force sensor and the operator's hand. Note that the fast movements of the master in the first few seconds do not represent oscillations; rather, they are intentionally created by the operator to examine the system stability and performance in free motion.

Next, the slave makes contact with a rigid environment. The operator pushes against the master handle leading to different levels of the slave/environment contact forces. The controller ensures a good agreement between the operator/master and the slave/environment forces under contact motion.

The fact that the position profiles remain constant during the contact mode is simply because under hard contact the slave cannot penetrate the environment regardless of the operator's force.

Thanks to the good position and force matching at the master and slave sides in free motion and under hard contact, the operator feels the slave/environment interaction.

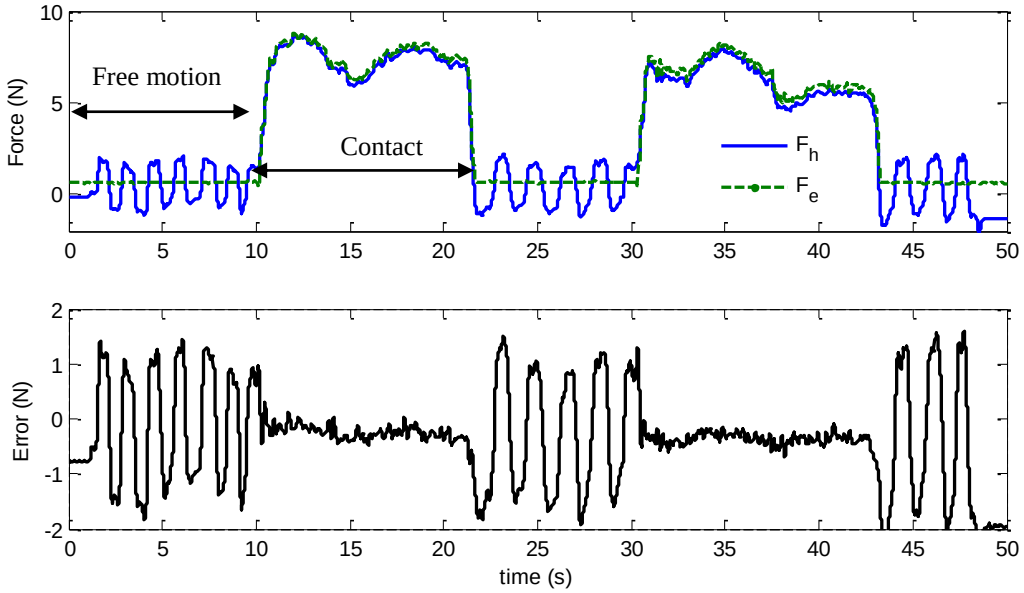

(a). Force tracking

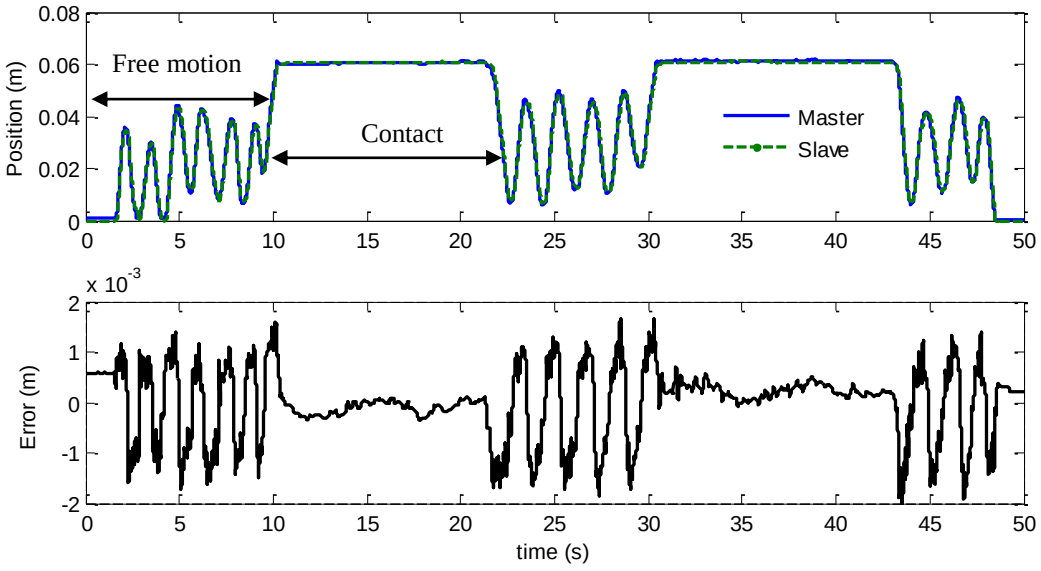

(b). Position tracking

Fig. 4.23. Transparency achieved with the experimental 4CH teleoperation systems based on hybrid control

In this section, in order to evaluate the hybrid algorithm, a comparison between the PWM strategy (section III.3) is carried out. The controller parameters (C_f and C_p) of the PWM case are chosen similar to the ones of the hybrid case. Furthermore, in PWM control, one more parameter need to be tuned, i.e., the proportional gain K_{PWM} (Fig. 4.4). This parameter is selected equal to 0.02 in order to achieve good dynamic performances and to satisfy the condition (4.14).

As it can be seen in Fig. 4.23 and Fig. 4.24 that the hybrid control leads to a better accuracy in force and position tracking than the PWM control because for each sample time, it chooses the best

control among the nine available configurations (section IV.1.2). On the other hand, with only two switching modes (section III.2), it is difficult for the PWM control to rapidly and accurately track the reference. This aspect can be observed on the position tracking where the slave's movement is delayed with respect to the master's movement (see Fig. 4.24 (b)).

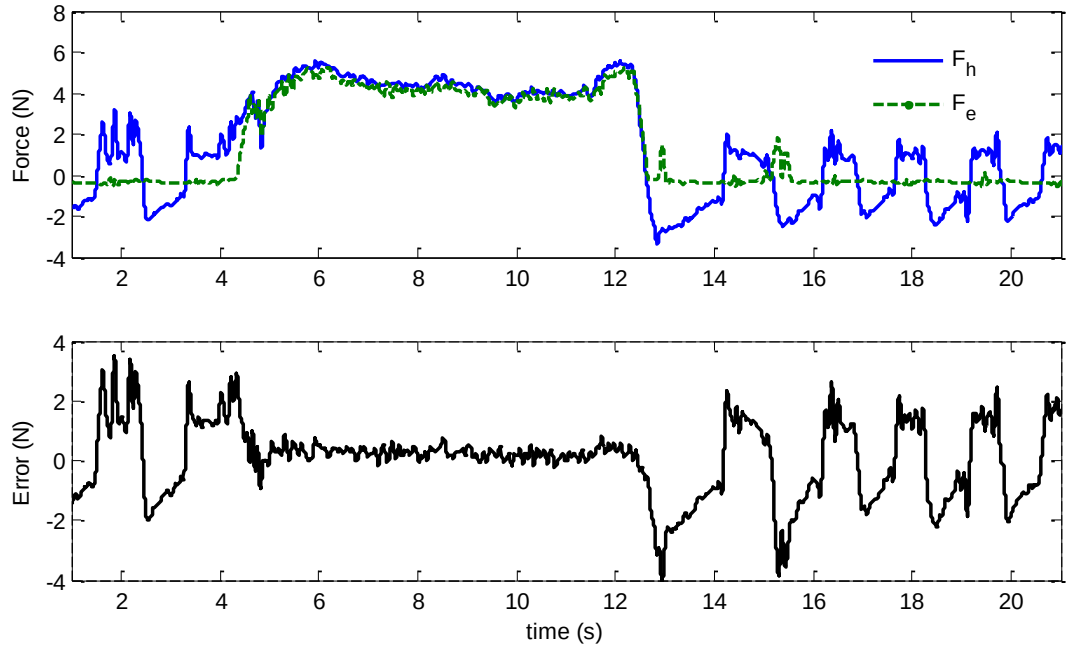

(a). Force tracking

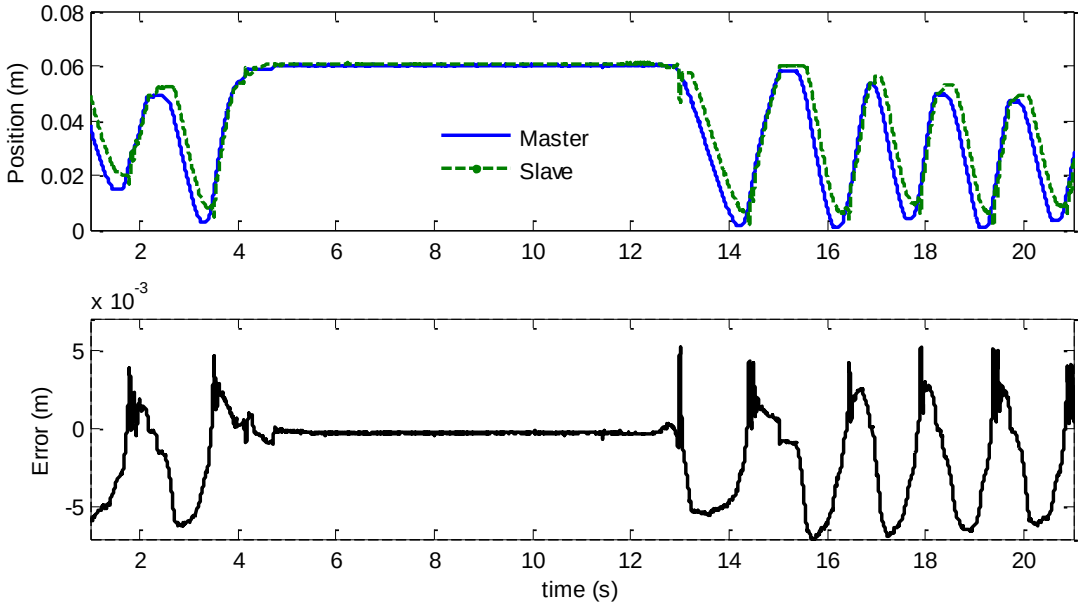

(b). Position tracking

Fig. 4.24. Transparency achieved with the experimental 4CH teleoperation systems based on PWM control

Experimental results indicate that, in addition to high improvements in force and position tracking, the proposed hybrid approach achieves a better behavior in pressure compared to the PWM control. This aspect is illustrated on Fig. 4.25 where the pressures in the chambers of the master actuator for the hybrid control are obviously less oscillating than the PWM control. Similar results are

obtained for the slave actuator. The fact is that in PWM strategy, the valves switch from "charging" to "exhausting", and air flows all the time even after reaching the final reference. However, in the hybrid control, when the system reaches the reference with a desired accuracy, both chambers can be closed to reduce power consumption.

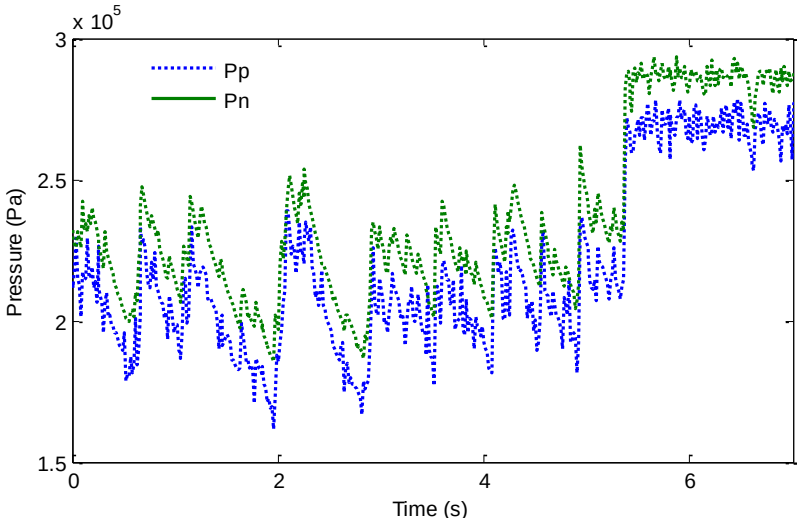

(a). Hybrid control

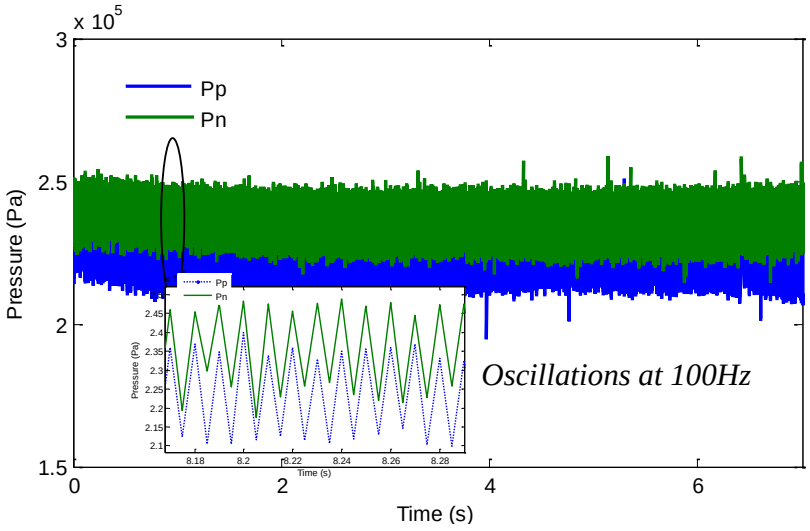

(b). PWM control

Fig. 4.25. Evolution of the pressures P_p and P_n in the experimental 4CH teleoperation systems

To further investigate the teleoperation system transparency, an analysis of the H-matrix parameters in the frequency domain is carried out (chapter 2, section II.6). Since F_e = 0 in the free-motion test data, the frequency responses $h_{11} = F_h / X_m$ and $h_{21} = -X_s / X_m$ can be found by applying the spectral analysis function *spa* of Matlab. Also, by using contact-mode test data, the other two parameters can be obtained as $h_{12} = F_h / F_e - h_{11} X_m / F_e$ and $h_{22} = -X_s / F_e - h_{21} X_m / F_e$ (Tavakoli et al. 2008).

The transparency analysis in frequency domain obtained with the hybrid and the PWM control are shown in Fig. 4.26. As it can be observed, the magnitude of $|h_{21}|$ and $|h_{12}|$ spectra in the hybrid case are close to 0dB, showing excellent tracking in terms of force and position for a wide bandwidth up to 100 rad/s. On the other hand, in the PWM case these parameters are degraded, which is coherent with the time-domain in Fig. 4.24, where the ideal transparency has not achieved. As expected from (2.8)

(chapter 2), low values of the output admittance (h_{22}) in the hybrid and PWM strategies show that the slave's movement in response to external force disturbances quickly converges to zero when the master is locked in motion. With regard to h_{11}, due to the mass of the handle between the force sensor and the operator's hand, over high frequencies the input impedance $h_{11} = F_h / X_m$ is identified less accurately than the other parameters. Nonetheless, low values of h_{11} over low frequencies are evidence of the fact that when the slave is in free space, the user will not experience a force or sticky feel of free-motion movements in the hybrid and PWM cases, which would have been undesirable.

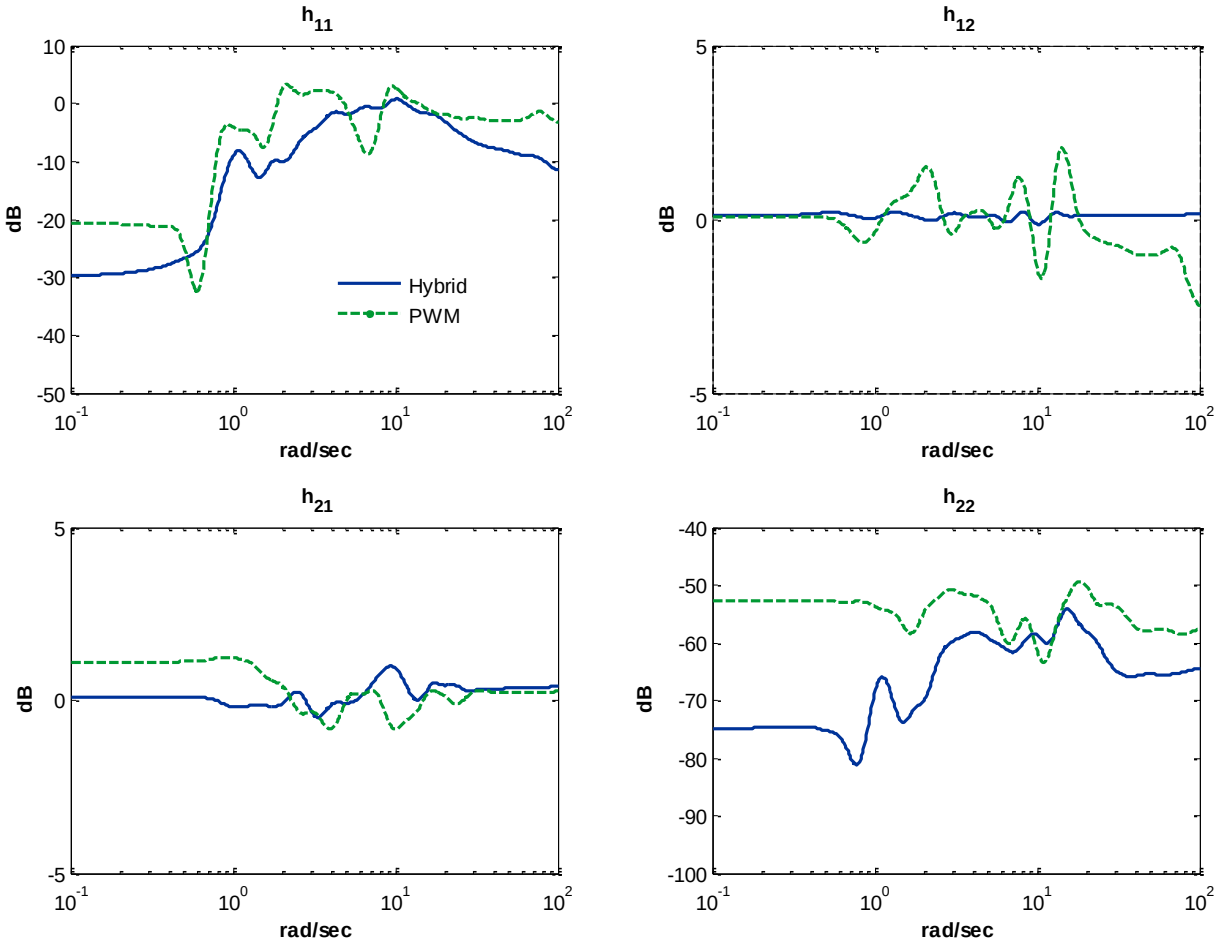

Fig. 4.26. Frequency spectra of the H-matrix parameters of the 4CH scheme:
(Solid) Hybrid control. (Dashed) PWM control.

IV.2.3.2. Inner control loop based on hybrid algorithm

As mentioned in Section IV.2.1, transparency can be achieved in the four-channel teleoperation system in Fig. 4.17 subject to the choice of controllers C_m, C_s, C_2 and C_3 in (4.25) as well as $C_6 = C_2 - 1$ and $C_5 = C_3 - 1$ from (4.23), if the inner force control loop is perfect. This condition involving the inner force control loop is verified in Fig. 4.27, where the force generated by the slave actuator accurately tracks the desired value for the control signal F_s. A similar result can be shown for the master-side inner force control loop.

To better understand the dynamic behavior of the inner force control loop, a spectra analysis is investigated, as illustrated in Fig. 4.28. As it can be seen, the transfer functions of the inner loops approach to the unitary function at low frequencies (less than 2Hz). For faster movements (*e.g.*, at 7Hz), the tracking performance is degraded, but it can be again improved by choosing a smaller sample time (which was not possible in our system due to the switching times of the valves).

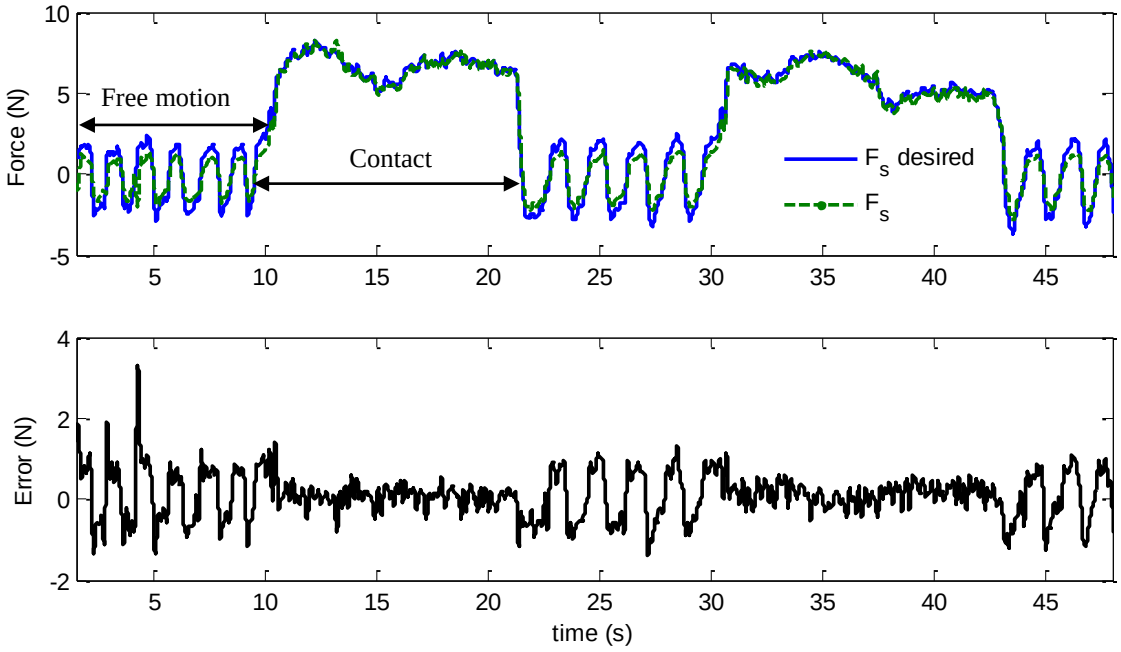

Fig. 4.27. Performance of the inner loop as function of time

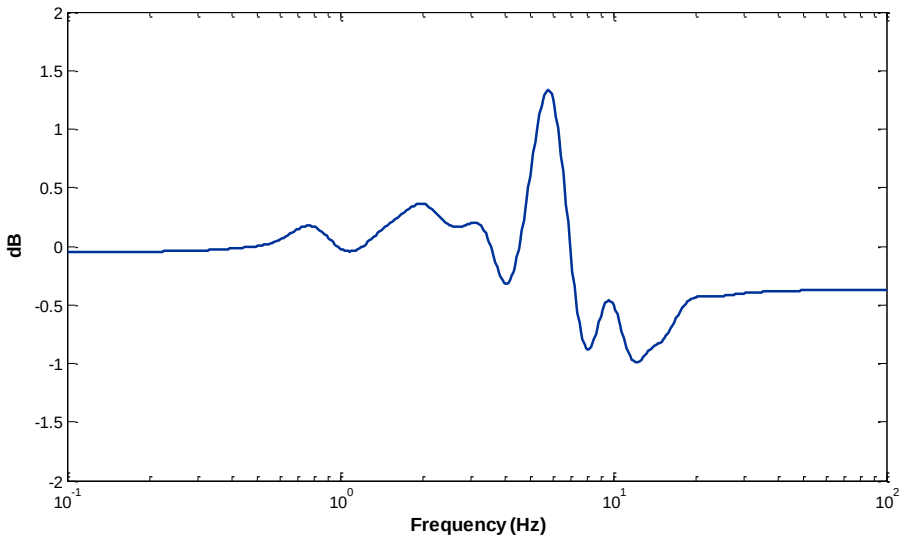

Fig. 4.28. Performance of the inner loop as function of time

The experimental results highlight that good force tracking in the inner loop is obtained within the bandwidth of the human arm movement. In our experimental validation, the arm movements were slow enough to be able to assume that the pressure variation inside each chamber is small – the approximation (4.19) is entirely justified in our experiments. In conclusion, a transparent teleoperation system (whose response is shown in Fig. 4.23) can be obtained through the employed hybrid force control (whose responses are shown in Fig. 4.27).

IV.2.3.3. Hybrid control performance in the 3CH teleoperation system

Fig. 4.29 shows the master and the slave positions and force tracking profiles for the 3CH teleoperation system in which $C_2 = C_6 + 1 = 1$ and $C_3 = C_5 + 1 = 0$. Note that Fig. 4.23 and Fig. 4.29

show similar profiles for the same choice of position controllers (C_m and C_s) but for $C_2 = C_6 + 1 = 3$ and $C_3 = C_5 + 1 = 3$ (4CH system), and $C_2 = C_6 + 1 = 1$ and $C_3 = C_5 + 1 = 0$ (3CH system), respectively.

The results show that the 4CH architecture leads to a better force tracking response compared to the 3CH architecture. As mentioned above, the 3CH case can theoretically achieve perfect transparency similar to the 4CH case. However, in practice, due to the lack of master/operator interaction force measurement, the force tracking performance in the 3CH architecture is somewhat degraded.

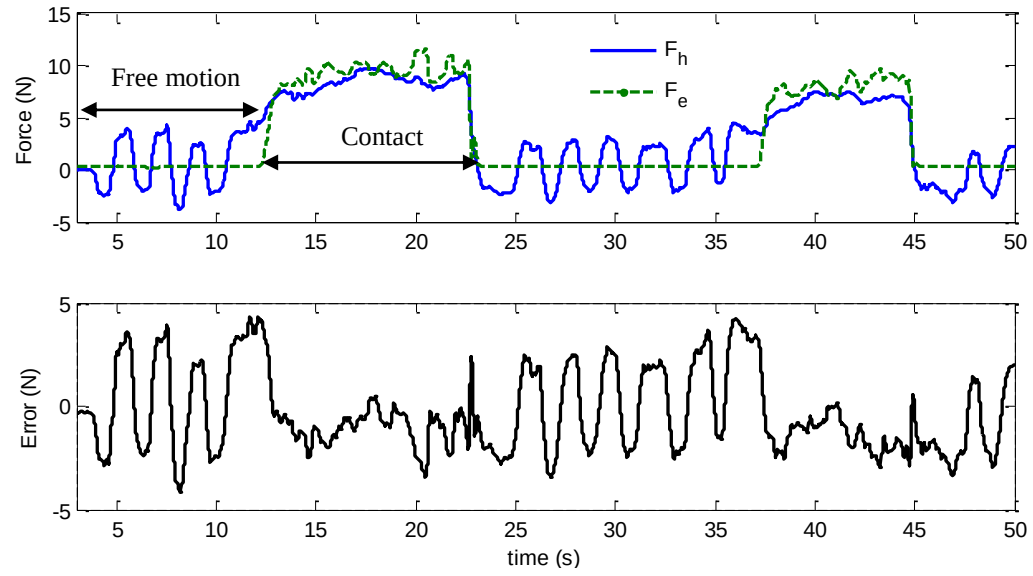

(a). Force tracking

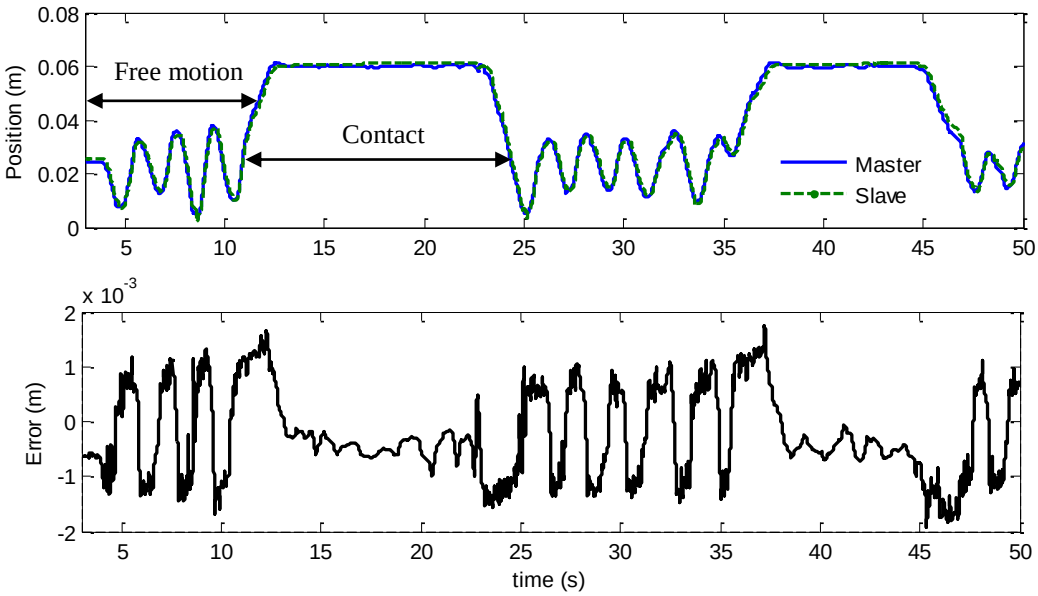

(b). Position tracking

Fig. 4.29. Transparency achieved with the experimental 3CH teleoperation systems based on hybrid control

To resume, we provide in Tab. 4.3 the quantitative assessments of the force and position tracking errors (RMS values with a time period of 50s) of the PWM and hybrid controls in both

contact motion and free motion. Also, operator's opinions are presented in order better evaluate performance of different control approaches.

	Force error (contact motion)	Position error (free motion)	Position error (contact motion)	Human opinions[1]
PWM control (4CH)	0.5 N (8.3 %)	2.9 mm (9.6 %)	0.5 mm (0.9 %)	High chattering in free motion and contact motion. Undesirable acoustic noise (at constant frequency) even in steady state.
Hybrid control (4CH)	0.2 N (3.4 %)	1.1 mm (4.1 %)	0.4 mm (0.7 %)	Acoustic noise (at varying frequency) and chattering still exist but less than the PWM case, especially in free motion. In contact motion, better haptic sensation is obtained.
Hybrid control (3CH)	0.7 N (12 %)	1.2 mm (4.5 %)	0.5 mm (0.9 %)	Similar remarks to the hybrid control with 4CH.

TAB. 4.3. COMPARISON OF PWM AND HYBRID CONTROLS

Concerning the frequency analysis, the magnitude of the H-matrix parameters of the 3CH and the 4CH teleoperation systems are shown in Fig. 4.30.

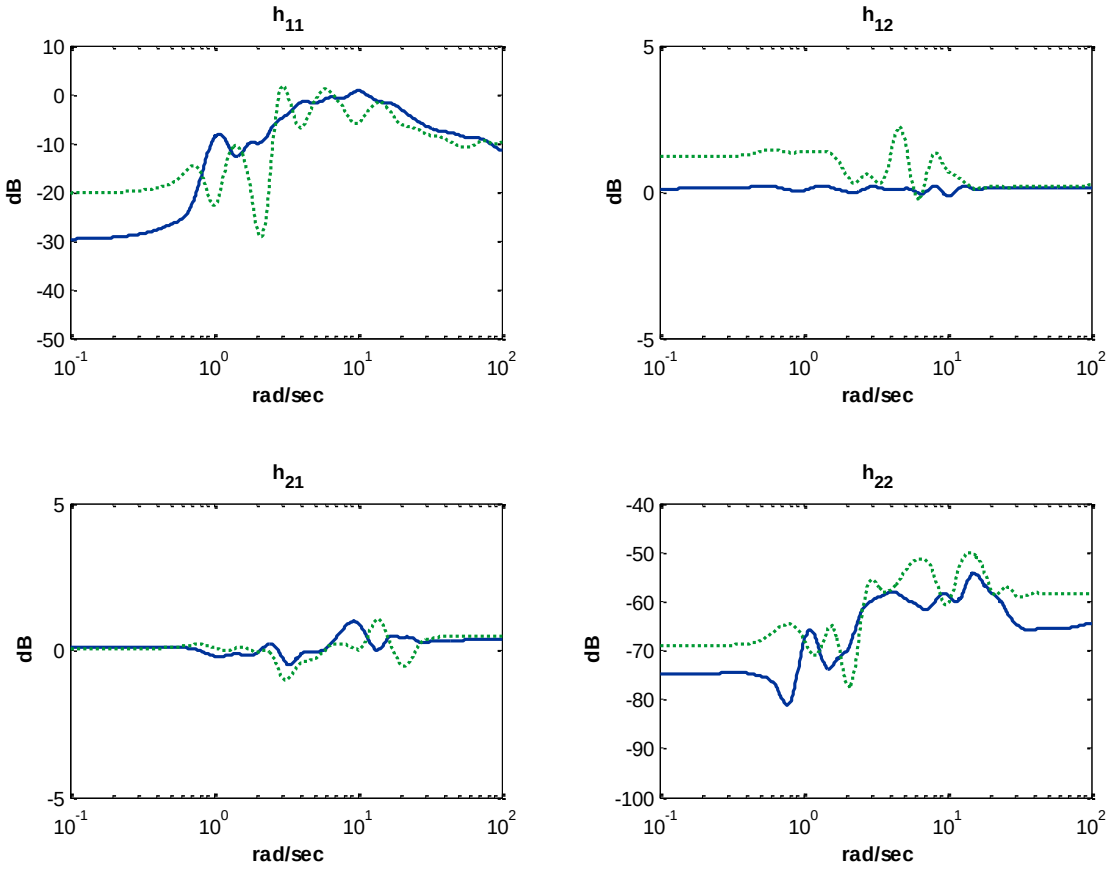

Fig. 4.30. Frequency analysis of the hybrid control with different architectures. (Solid) 4CH. (Dotted) 3CH.

[1] Human opinion is evaluated from three subjects

As it can be seen, $|h_{12}|$ is above the 0 dB level for the 3CH case while it is close to 0 dB in the 4CH case. This is in agreement with the time-domain force profiles in Fig. 4.23 and Fig. 4.29, where force tracking in 3CH architecture is not on par with that in the 4CH case. This, however, does not affect free-space position tracking as illustrated in the $|h_{21}|$ spectra of Fig. 4.30. As it can be observed, for both cases $|h_{21}|$ spectra are close to 0dB, performing good position tracking for frequencies up to 100 rad/s. With regard to h_{11} and h_{22}, similar comments can be obtained as in Fig. 4.26 (section IV.2.3.1).

IV.2.4. Stability discussion

In the thesis, the robustness or stability analysis of the overall hybrid system has not been studied. Since on/off solenoid valves have been used, these analyses would be equivalent to dealing with the robustness and stability of a hybrid system, which entails switching between two models of mass flow rate (4.3), i.e. subsonic and sonic regimes. (Branicky 1997) gives an overview of hybrid systems stability and shows the difficulty of the problem even for a linear system. (Liberzon 2003) suggests some stability methods for linear systems or systems with special structures (triangular, feedback, or two-dimensional systems).

To the best of our knowledge, only a few papers exist on the robustness or stability analysis of nonlinear hybrid systems (Liberzon 2003; Papachristodoulou & Prajna 2009). A recent paper (Papachristodoulou & Prajna 2009) presents a methodology through the algorithmic construction of polynomial and piecewise polynomial Lyapunov-like functions using a convex optimization and in particular the sum of squares decomposition of multivariate polynomials. This strategy provides several improvements compared to previous approaches such as treating in a unified way polynomial switching surfaces and robust stability analysis for nonlinear hybrid systems. However, the method is only applicable to systems whose dynamics are expressed as a polynomial form. It has been seen in (Papachristodoulou & Prajna 2002) that it is possible to transform some non-polynomial systems to the polynomial ones by using a change of variable. In the model considered in our study, this approach could not be applied due to the presence of two nonlinear terms $\frac{1}{V_p(y)}$ and $\frac{1}{V_n(y)}$ in (4.1). We also faced difficulties in finding approximate polynomials in terms of the mass flow rates q_p and q_n that are able to cover the subsonic regime as well as the sonic regime. Last but not least, there are more difficulties in term of applying the stability analysis of the hybrid systems to a teleoperation problem. The reason for this is that teleoperation system stability depends not only on the models of the master and slave manipulators but also on the dynamic behaviors of the human operator and environment, which are unknown, uncertain, nonlinear, and/or time-varying. For instance, (Matsuoka & Howe 2000) has shown that in practice the dynamic parameters of the human operator change in response to the requirements of the task at hand.

To sum up, according to (Liberzon 2003), there is no general theory of switching control that can be applied to all hybrid systems. What has been done in the literature is to provide customized methods for a few particular classes of nonlinear systems. Our system does not belong to any of these classes.

In conclusion, the robustness and stability analyses remain a main concern. This research direction is challenging and nonetheless a priority in our future work.

V. Sliding Control Design

An alternative to the hybrid control of pneumatic systems with on/off valves is to use methods based on sliding mode nonlinear control law. Such a control system utilizes switching operating modes defined directly from the discrete state of the valves, which are based on the current tracking error. More details about the principle of sliding modes can be found in (Utkin 1992; Edwards & Spurgeon 1998).

This section aims at applying a sliding mode control to a two-channel (2CH) bilateral teleoperation architecture with various different schemes, namely position–position, force–force, and force–position. These architectures are chosen due to their implementation simplicity and efficiency. We provide in this study both a tracking performance analysis and a stability analysis for the closed-loop system using a Lyapunov candidate function (chapter 2, section V.1).

Another purpose of our work consists in extending the sliding mode strategy based on the *three-mode control* scheme (subsection V.1) to a *five-mode control scheme* (subsection V.2). This new scheme results in decreased valve-switching activity and, therefore, improves the overall lifetime and reliability of the teleoperation system (Le et al. 2011d).

V.1. Teleoperation based on three-mode control scheme (3MCS)

In order to facilitate the control law design, a switching scheme for the four solenoid valves in Fig. 4.1 is defined so that each of the master and slave robots has the three modes of operation shown in Tab. 4.4 (Le et al. 2011b).

	Mode 1	Mode 2	Mode 3
Chamber p	fills	exhausts	closed
Chamber n	exhausts	fills	closed
Control u	1	-1	0
$\underline{U} = [U_1\ U_2\ U_3\ U_4]$	[1 0 1 0]	[0 1 0 1]	[0 0 0 0]

TAB. 4.4. THREE POSSIBLE CONTROL MODES

In Tab. 4.4, U (the 4th row) is the input voltage vector of the valves, i.e., $U = [U_1\ U_2\ U_3\ U_4]$. Also, u (the 3rd row) is a newly introduced discrete (switching) control input that has three levels to match the three modes of operation. This new input can be chosen either as $u = \text{sign}(s)$ or $u = -\text{sign}(s)$, where s is a *sliding surface* which is a function of tracking error. Whether to choose the switching control u as between sign(s) or as $-\text{sign}(s)$ depends on the definition of s and the open-loop system. As it will be shown later, this choice is crucial to ensure the stability of the teleoperation system.

Note that mode 3 in Tab. 4.4 is used to "de-actuate" the piston and save energy when the tracking error is considered small enough. On the other hand, modes 1 and 2 are used for moving the piston to the right and to the left directions of Fig. 4.1, respectively.

In order to bring the system to the sliding surface $s = 0$ at steady state, which corresponds to a perfect tracking performance, we define a neighbourhood of radius $\varepsilon << 1$ around zero. When $|s|$ is within the interval $[0, \varepsilon]$, mode 3 ($u = 0$) is used to conserve energy and somewhat reduce the chattering. In summary, we get the control law as

$$u = \begin{cases} +/-\text{sign}(s) & \text{if} \quad |s| > \varepsilon \\ 0 & \text{if} \quad |s| \le \varepsilon \end{cases} \tag{4.34}$$

where

$$\text{sign}(x) = \begin{cases} 1 & \text{if} \quad x > 0 \\ 0 & \text{if} \quad x = 0 \\ -1 & \text{if} \quad x < 0 \end{cases} \tag{4.35}$$

V.1.1. Open-loop model of the master and slave devices

Ignoring the stiction force in (4.2), the mechanical dynamics of the master and slave devices can be written as

$$\begin{aligned} M\ddot{y}_m &= S_p P_{p,m} - S_n P_{n,m} - b\dot{y}_m + f_h \\ M\ddot{y}_s &= S_p P_{p,s} - S_n P_{n,s} - b\dot{y}_s - f_e \end{aligned} \tag{4.36}$$

where f_h and f_e are the operator force exerted on the master and the environment force exerted on the slave; y_m and y_s are the master and slave positions.

Differentiating (4.36) and using (4.1) and (4.3), the dynamics of the master and slave manipulators are obtained after some calculations as in (Nguyen et al. 2007)

$$\ddot{y}_m = \begin{cases} \alpha_m + \beta_m^+ + \dot{f}_h/M & \text{for } u_m = 1 \\ \alpha_m - \beta_m^- + \dot{f}_h/M & \text{for } u_m = -1, \\ \alpha_m + \dot{f}_h/M & \text{for } u_m = 0 \end{cases} \qquad \ddot{y}_s = \begin{cases} \alpha_s + \beta_s^+ - \dot{f}_e/M & \text{for } u_s = 1 \\ \alpha_s - \beta_s^- - \dot{f}_e/M & \text{for } u_s = -1 \\ \alpha_s - \dot{f}_e/M & \text{for } u_s = 0 \end{cases} \tag{4.37}$$

where u_m and u_s denote the discrete control input as defined in Tab. 4.4. In the above,

$$\alpha_i = -\frac{b}{M}\ddot{y}_i - \frac{\gamma}{M}\left(\frac{S_p^2 P_{p,i}}{V_p(y_i)} + \frac{S_n^2 P_{n,i}}{V_n(y_i)}\right)\dot{y}_i \tag{4.38}$$

$$\beta_i^+ = \gamma r T_a \left(\frac{S_p}{M}\frac{q(P_{sa}, P_{p,i})}{V_p(y_i)} + \frac{S_n}{M}\frac{q(P_{n,i}, P_{atm})}{V_n(y_i)}\right) \tag{4.39}$$

$$\beta_i^- = \gamma r T_a \left(\frac{S_p}{M}\frac{q(P_{p,i}, P_{atm})}{V_p(y_i)} + \frac{S_n}{M}\frac{q(P_{sa}, P_{n,i})}{V_n(y_i)}\right) \tag{4.40}$$

$i = m$ or s (for master or slave, respectively).

V.1.2. Closed-loop teleoperation system

V.1.2.1. Position-Error-Based (PEB) control system

The pneumatic-actuated PEB teleoperation system with our proposed sliding mode control is shown in Fig. 4.31. In this system, there are two position controllers, one for the master and the other for the slave where each one gets the reference position from the current value of the other (see chapter 2, section III.2.1).

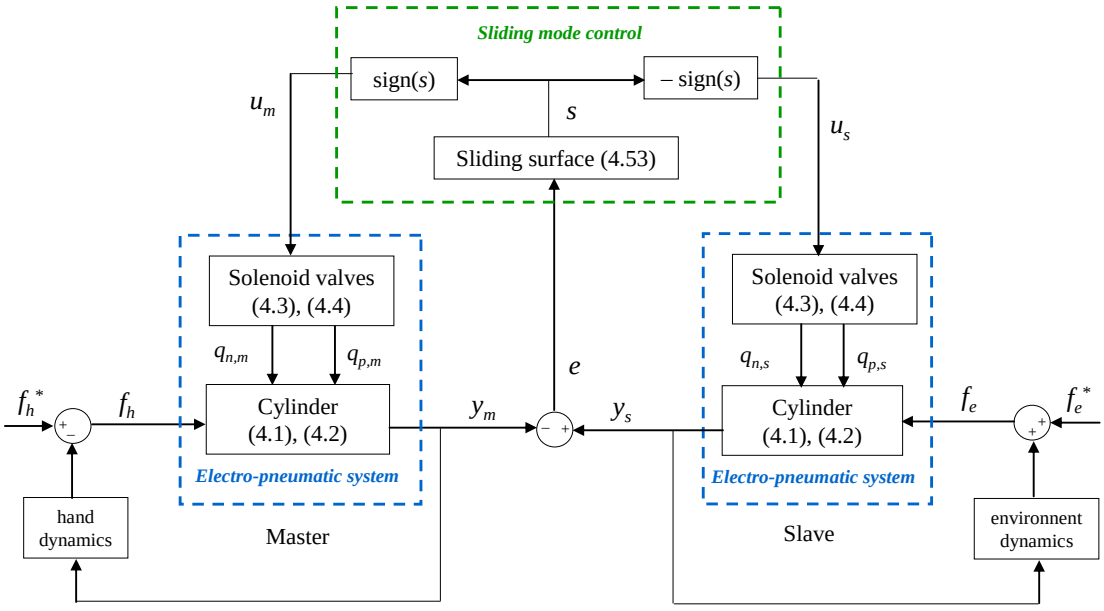

Fig. 4.31. Position-Error-Based approach with sliding mode control

In Fig. 4.31, s is the sliding surface; u_m and u_s are the discrete control signals for the master and the slave manipulators; and $e = y_s - y_m$ is the position tracking error. Also, f_h^* and f_e^* are the operator's and the environment's exogenous input forces, respectively. It is noteworthy that they are independent of the teleoperation system behavior.

In the PEB scheme, the sliding surface s can be defined as

$$s = \ddot{e} + 2\xi\omega\dot{e} + \omega^2 e \tag{4.41}$$

where ξ and ω are constant and positive parameters. The control laws u_m and u_s are defined as $u_s = -u_m = -sign(s)$. In the following, we analyze the position error convergence and the stability of the closed-loop system.

Consider the following Lyapunov candidate function

$$V = \frac{1}{2}s^2 \tag{4.42}$$

The sliding surface $s = 0$ is reached within a finite time if the following condition is satisfied (Slotine et al. 1991; Utkin & Chang 2002)

$$\dot{V} = s\dot{s} < -\eta|s| \tag{4.43}$$

for some constant $\eta > 0$. Thus, from (4.41) and (4.43), we need

$$s(\dddot{e} + 2\xi\omega\ddot{e} + \omega^2\dot{e}) < -\eta|s| \tag{4.44}$$

Case 1: $s > 0$. In this case, (4.44) becomes

$$(\ddot{y}_s - \ddot{y}_m) + 2\xi\omega\ddot{e}^{(4.41)} + \omega^2\dot{e} < -\eta \tag{4.45}$$

Since $s > 0$, thus $u_s = -1$ and $u_m = 1$. Therefore, the open-loop master and slave dynamics in (4.37) become

$$\ddot{y}_m = \alpha_m + \beta_m^+ + \dot{f}_h/M \quad , \quad \ddot{y}_s = \alpha_s - \beta_s^- - \dot{f}_e/M \tag{4.46}$$

Substituting (4.46) in (4.45) leads to the following condition

$$(\alpha_s - \alpha_m) - (\beta_m^+ + \beta_s^-) - (\dot{f}_h + \dot{f}_e)/M + 2\xi\omega\ddot{e} + \omega^2\dot{e} < -\eta \tag{4.47}$$

In other words,

$$\lambda - (\beta_m^+ + \beta_s^-) < -\eta \tag{4.48}$$

where

$$\lambda = \alpha_s - \alpha_m - (\dot{f}_h + \dot{f}_e)/M + 2\xi\omega\ddot{e} + \omega^2\dot{e} \tag{4.49}$$

♦

Case 2 : $s < 0$. In this case, (4.44) becomes

$$(\ddot{y}_s - \ddot{y}_m) + 2\xi\omega\ddot{e} + \omega^2\dot{e} > \eta \tag{4.50}$$

Since $s < 0$, then $u_s = 1$ and $u_m = -1$. Hence, the master and slave dynamics in (4.37) can be expressed as

$$\ddot{y}_m = \alpha_m - \beta_m^- + \dot{f}_h/M \quad , \quad \ddot{y}_s = \alpha_s + \beta_s^+ - \dot{f}_e/M \tag{4.51}$$

Substituting (4.51) in (4.50) yields

$$\lambda + (\beta_m^- + \beta_s^+) > \eta \tag{4.52}$$

where λ is defined in (4.49)

♦

Note that, from (4.39) and (4.40), β_i^+ and β_i^- are positive, and can be as large as desired by choosing a sufficiently large valve orifice C_{val} in (4.4). Thus, to ensure that the conditions (4.48) and (4.52)

(depending on the sign of s) are satisfied, we only need to show that λ is bounded – note that $\eta > 0$ is an arbitrary constant.

To show that λ is bounded, we utilize the dynamic models of the operator and the environment (chapter 2, section II.1 and II.2)

$$\begin{aligned} f_h &= -M_h\ddot{y}_m - B_h\dot{y}_m - K_h y_m + f_h^* \\ f_e &= M_e\ddot{y}_s + B_e\dot{y}_m + K_e y_m + f_e^* \end{aligned} \tag{4.53}$$

where M_h, M_e, B_h, B_e, K_h and K_e are assumed to be positive values corresponding to the mass, damping and stiffness of the operator's hand and the environment, respectively. Substituting (4.53) into the master and slave dynamics (4.36) leads to

$$\begin{aligned} (M + M_h)\ddot{y}_m &= S_p P_{p,m} - S_n P_{n,m} - (b + B_h)\dot{y}_m - K_h y_m + f_h^* \\ (M + M_e)\ddot{y}_s &= S_p P_{p,s} - S_n P_{n,s} - (b + B_e) y_s - K_e y_s - f_e^* \end{aligned} \tag{4.54}$$

To establish the boundedness of λ, we consider the following points:

- Since we are dealing with a physical system, the chamber pressures $P_{p,i}$ and $P_{n,i}$ are supposed to be bounded at all times. In fact, they are lower-bounded by the atmospheric pressure (P_{atm}) and upper-bounded by the supply pressure (P_{sa}).
- The exogenous input forces f_h*, f_e* and their derivatives are supposed to be bounded as they originate from the human operator and the environment, which have limited energy.
- Since the coefficients of position, velocity and acceleration terms in (4.54) (after moving them to the left side of the equations) are positive, and since the pressures, the operator's and the environment's exogenous force f_h* and f_e^* are always bounded, thus each relationship in (4.54) is a second order BIBO stable system. As a result, the positions y_m and y_s are always bounded. In a similar way, (4.54) consists of two first-order stable differential equations in terms of velocities and the other sides of the equations (consisting of positions, pressures and exogenous forces) are bounded, thus the master's and slave's velocities $\dot{y}_m$ and $\dot{y}_s$ are bounded. Hence, again because of (4.54), the accelerations $\ddot{y}_m$ and $\ddot{y}_s$, which are the sums of bounded functions, are also bounded.
- Since the velocities and the accelerations are bounded, from (4.36), knowing that the pressures are bounded, we can infer that the interaction forces f_h and f_e are also bounded at all times.
- $V_p(y_i)$ and $V_n(y_i)$, the chamber volumes of the cylinders, are bounded and non-zero functions.
- The rate of change of pressures $\dot{P}_{p,i}$ and $\dot{P}_{n,i}$ are bounded because each relationship in (4.1) is defined by a mass flow rate a velocity, a pressure and a chamber volume that are all bounded functions.
- Based on the previous points, differentiating (4.54) yields the boundedness of $\dddot{y}_m$ and $\dddot{y}_s$. Consequently, by using the derivative of (4.53) we infer that $\dot{f}_h$ and $\dot{f}_e$ are also bounded at all times.

Eventually, it is found that λ, which is the sum of several bounded functions, is bounded. Therefore, the sliding condition in (4.43) is ensured, which implies that the position tracking error tends to zero (and that the overall system is stable). In fact, according to (4.43), s will be bounded and converges to zero. According to (4.41), which represents a BIBO-stable second-order LTI system, this will ensure the boundedness and convergence to zero of the position tracking error. It is worth noting that a restrictive assumption used in this demonstration is that specific dynamic models of the operator and the environment (4.53) are required.

The main drawback of the PEB method is that it does not guarantee a good transparency in term of force tracking. In order to improve the tracking performance, other schemes are proposed in the next sections.

V.1.2.2. Force-Error-Based (FEB) control system

The FEB system is not commonly used in two-channel bilateral teleoperation since two force sensors are required, which will make the implementation expensive, and since the resulting position

tracking is not good (see chapter 2, section III.2.2). However, compared to the PEB architecture, this architecture can improve the force tracking performance. Fig. 4.32 shows the pneumatic-actuated FEB teleoperation system with a proposed sliding mode control.

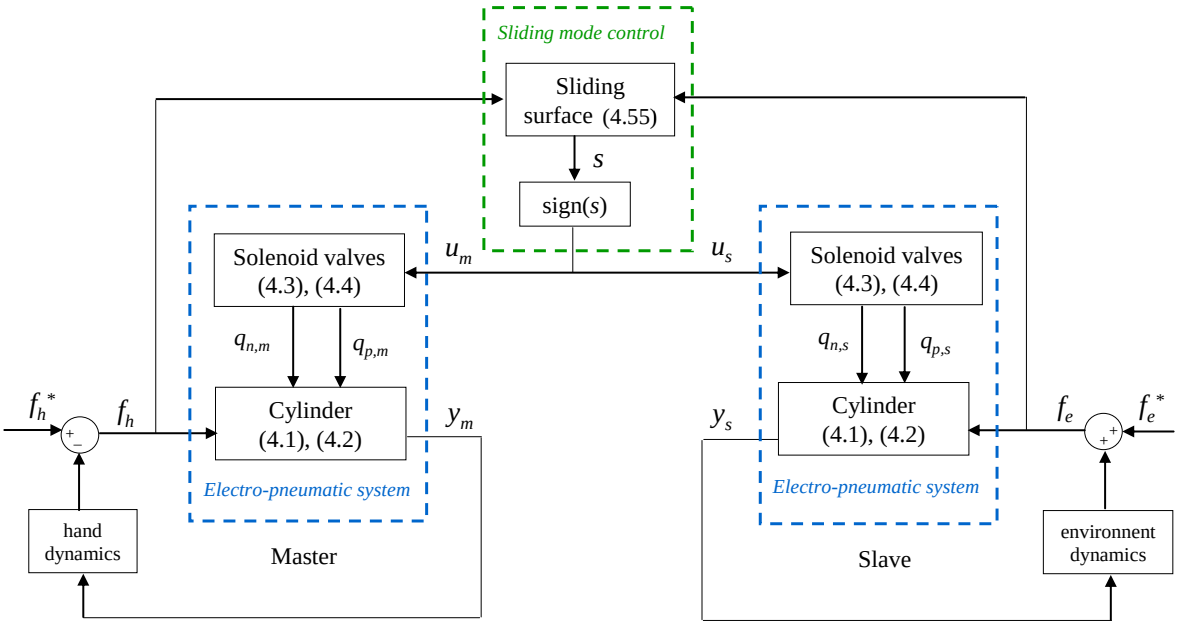

Fig. 4.32. Force-Error-Based approach with sliding mode control

Consider the control law $u_s = u_m = sign(s)$ where the sliding surface is defined as

$$s = f_h - f_e \tag{4.55}$$

Using the Lyapunov function (4.42), we need to show that the sliding condition (4.43) is satisfied.

From the master and slave models (4.37), we calculate $\dot{f}_h$ and $\dot{f}_e$ as

$$\dot{f}_h = \begin{cases} M(\dddot{y}_m - \alpha_m - \beta_m^+) & \text{for } u_m = 1 \\ M(\dddot{y}_m - \alpha_m + \beta_m^-) & \text{for } u_m = -1, \\ M(\dddot{y}_m - \alpha_m) & \text{for } u_m = 0 \end{cases} \quad \dot{f}_e = \begin{cases} M(-\dddot{y}_s + \alpha_m + \beta_s^+) & \text{for } u_s = 1 \\ M(-\dddot{y}_s + \alpha_m - \beta_s^-) & \text{for } u_s = -1 \\ M(-\dddot{y}_s + \alpha_m) & \text{for } u_s = 0 \end{cases} \tag{4.56}$$

Case 1: $s > 0$. In this case $u_m = u_s = 1$. From (4.43), we need

$$\dot{s} = \dot{f}_h - \dot{f}_e = M(\lambda - \beta_m^+ - \beta_s^+) < -\eta \tag{4.57}$$

where

$$\lambda = \dddot{y}_m - \alpha_m + \dddot{y}_s - \alpha_s \tag{4.58}$$

The condition in (4.57) can be verified when λ, defined in (4.58), is bounded. As it was demonstrated above in section V.1.2.1, every signal is bounded, including $\dddot{y}_m$, α_m, $\dddot{y}_s$ and α_s. This implies the boundedness of λ at all times. Thus, by choosing a valve with a large enough orifice, β_m^+ and β_s^+ can be made sufficiently large to satisfy (4.57).

♦

Case 2: $s < 0$. In this case, $u_m = u_s = -1$. We have

$$\dot{s} = \dot{f}_h - \dot{f}_e = M(\lambda + \beta_m^- + \beta_s^-) > \eta \tag{4.59}$$

where λ is defined in (4.58).

Similar to Case 1, the stability of the system can be guaranteed by choosing a large enough value of β_m^- and β_s^-.

♦

Consequently, the force tracking error converges to zero and the overall system is stable. However, the FEB method does not guarantee a good position tracking performance. In order to overcome the PEB and FEB architecture drawbacks, we use the scheme described in the following section.

V.1.2.3. Direct-Force-Reflection (DFR) Control system

As mentioned in chapter 2, section III.2.3, the DFR system has advantages over the position–position and force–force architectures. Compared to the PEB method, improvements in force tracking are achieved due to the measurement of the interaction force between the slave and the environment. Furthermore, its position tracking performance is better than the FEB case thanks to the position information. The pneumatic-actuated DFR teleoperation system with our proposed sliding mode control is illustrated in Fig. 4.33.

In Fig. 4.33, s_m and s_s are the sliding surfaces for the master and slave systems, respectively; $e_m = f_h - f_e$ is the force tracking error calculated for the master controller; and $e_s = y_s - y_m$ is the position tracking error calculated for the slave controller. This architecture involves the transmission of two types of data between the master and the slave: force from the slave to master and position from the master to the slave. Hence, the transparency is improved in terms of force and position tracking, compared to the methods previously presented. This statement will be justified later in our experiment, (cf. section V.1.3).

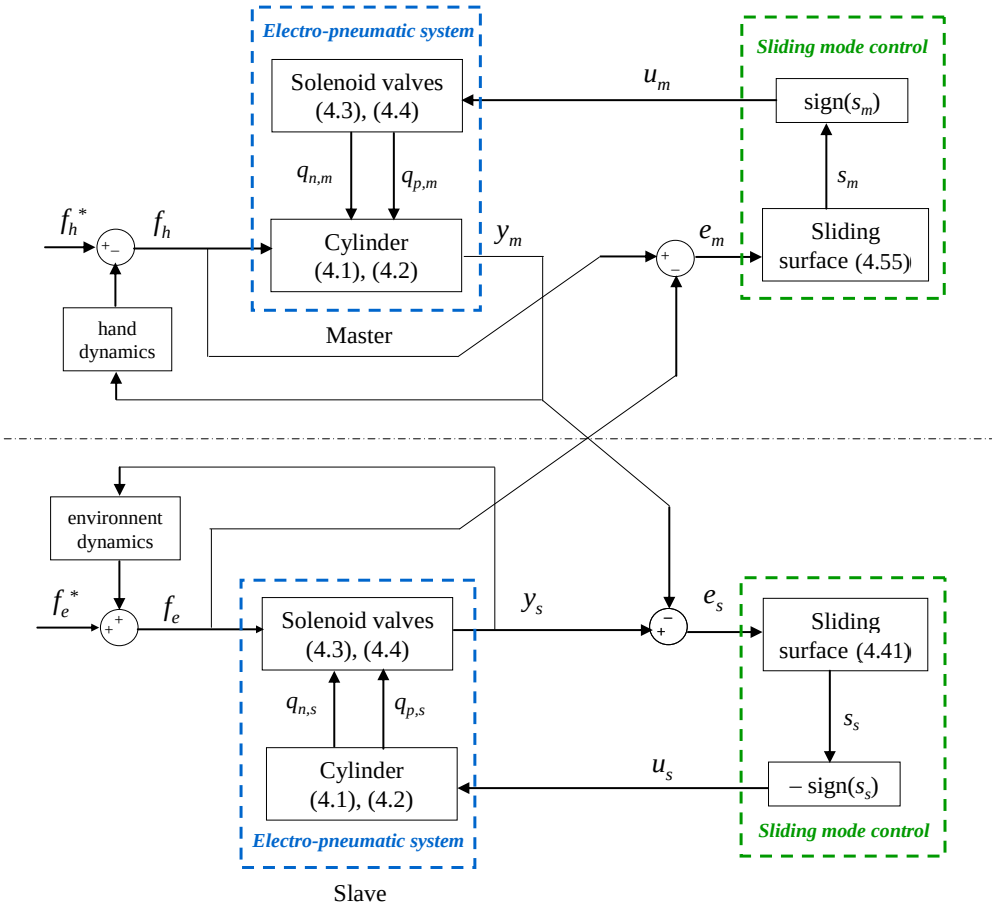

Fig. 4.33. Direct-Force-Reflection approach with sliding mode control

In this section, we use a Lyapunov function to prove the stability of the sliding-mode controlled DFR system. First, we will show the stability of the force-controlled master manipulator. Afterwards, we will show the stability of the position-controlled slave manipulator. However, the stability of the overall system is difficult to show due to the complexities introduced by using different sliding surfaces for the master and for the slave. Indeed, the following proves the stability of each manipulator, but not the stability of the overall teleoperation system.

V.1.2.3.1 Force convergence of the closed-loop master system

Since the desired force for the master robot, i.e., the slave/environment contact force f_e is assumed to be bounded at the beginning, we need to show that f_h converges to f_e in a finite time. The sliding surface s_m and the Lyapunov function V_m are defined as in (4.55) and (4.42), respectively. The controller u_m is chosen to be similar to the FEB system in section III.B.2.

Case 1: $s_m > 0$. In this case, $u_m = 1$. Using the expression of $\dot{f}_h$ in (4.56) and the definition of s_m as in (4.55) we have

$$\dot{s}_m = -\dot{f}_e + M\ddot{y}_m - M\alpha_m - M\beta_m^+ \tag{4.60}$$

To ensure the sliding condition (4.43), we need to show that:

$$-\dot{f}_e + M\ddot{y}_m - M\alpha_m - M\beta_m^+ < -\eta \tag{4.61}$$

Similar to the demonstration in section III.B.1, $\dot{f}_e$, $\ddot{y}_m$ and α_m can be shown to be bounded. Thus, the stability condition (4.61) is satisfied by choosing a large enough value for β_m^+.

♦

Case 2: $s_m < 0$. In this case, $u_m = -1$. From (4.55) and (4.56) we need

$$-\dot{f}_e + M\ddot{y}_m - M\alpha_m + M\beta_m^- > \eta \tag{4.62}$$

Similar to Case 1, it is possible to choose a large enough value of β_m^- in order to ensure the stability of the master manipulator.

♦

Consequently, the sliding surface (the force tracking error) tends to zero, i.e., f_h tends towards f_e.

V.1.2.3.2 Position convergence of the closed-loop salve system

The sliding surface s_s and the Lyapunov function V_s are defined as in (4.41) and (4.42), respectively. The controller u_s is chosen to be similar to the PEB system in section V.1.2.1.

Case 1: $s_s > 0$. In this case, $u_s = -1$. The sliding condition (4.43) is equivalent to

$$(\ddot{y}_s - \ddot{y}_m) + 2\xi\omega\dot{e}_s + \omega^2 e_s < -\eta \tag{4.63}$$

Using the expression of $\ddot{y}_s$ in (4.46) leads to the following condition

$$\alpha_s - \beta_s^- - \dot{f}_e/M - \ddot{y}_m + 2\xi\omega\dot{e}_s + \omega^2 e_s < -\eta \tag{4.64}$$

or

$$\varphi - \beta_s^- < -\eta \tag{4.65}$$

where $\varphi = \alpha_s - \dot{f}_e/M - \ddot{y}_m + 2\xi\omega\dot{e}_s + \omega^2 e_s$

The straightforward reasoning described in section V.1.2.1 allows us to infer that φ is bounded. Therefore, there exists a value of β_s^- such as (4.65) is satisfied.

♦

Case 2: $s_s < 0$. In this case, $u_s = 1$. Thus, we need

$$\alpha_s + \beta_s^+ - \ddot{y}_m - \dot{f}_e/M + 2\xi\omega\dot{e}_s + \omega^2 e_s > \eta \tag{4.66}$$

or

$$\varphi + \beta_s^+ > \eta \tag{4.67}$$

This condition is achieved by choosing a large enough β_s^+.

♦

Note that for both cases, the convergence of the sliding surface (and thus the position tracking errors) to zero is proved, so x_s tends towards x_m.

As it will be confirmed by experiments in the next section, the DFR architecture provides a good transparency in terms of position and force tracking.

V.1.3. Experiments

In this subsection, experiments were performed on a one axis test system. Time domain as well as frequency domain is carried out in order to compare the different architectures of the teleoperation system based on sliding mode control.

V.1.3.1. Experimental setup

The experimental setup of this test bed is similar to the one presented in section IV.1.4.1 for the PWM and hybrid control. The only difference in this case is that a 0.5 kg mass (a joystick) is mounted to the end of the piston rod for each manipulator. The addition of mass load is used to damp the vibrations as well as the oscillations of the acceleration and velocity signals. A photograph of the experimental setup is shown in Fig. 4.34.

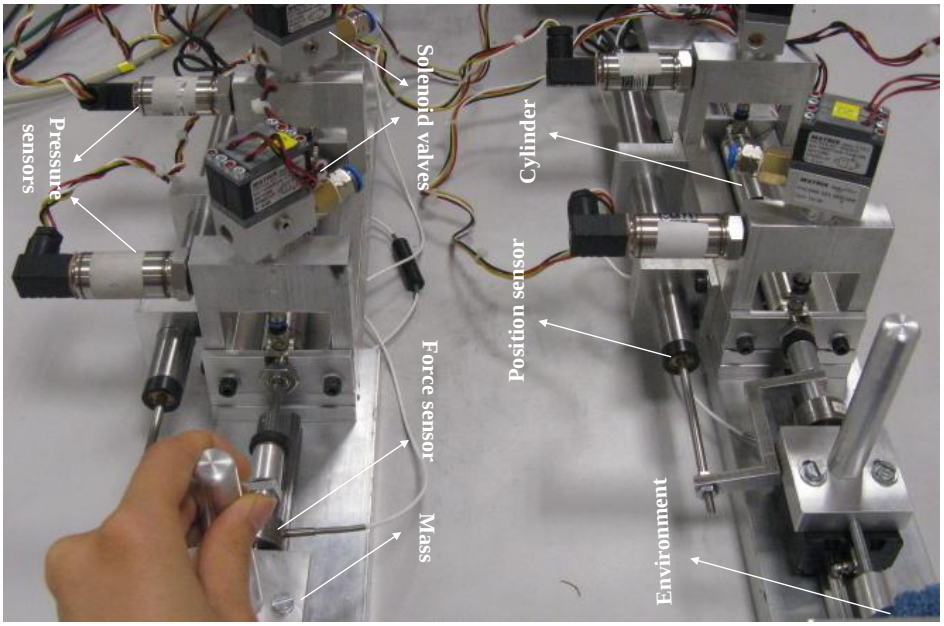

Fig. 4.34. Pneumatic master–slave teleoperation experimental setup

For the PEB and DFR systems, the sliding surface of the position-controlled slave is normalized as

$$s = \frac{\ddot{e}}{\omega^2} + 2\frac{\xi}{\omega}\dot{e} + e \tag{4.68}$$

This is because, in practice, it is easier if the sliding surface for position control is chosen in order to have the same dimension as positions as in (4.68) and not accelerations as in (4.41). The first

derivative of the position error in (4.68) is computed through a backward difference method applied on the position signal followed by a de-noising second-order Butterworth filter with a cut-off frequency of 70Hz. The second derivative is computed in the same way from the filtered first-derivative signal.

There is a trade-off between tracking error and chattering to achieve good performances. In theory, the characteristics of the control system is determined by the poles of the second-order reference model (4.68), which depends on the parameters ω and ξ. It is noteworthy that when ξ and ω^2 in (4.68) increase, the averaged tracking error is better but the chattering increases. It means that the response is around the reference in the transient and steady state but more oscillations can be observed due to the noise of velocity's and acceleration's estimations. This is understandable from the perspective of moving the poles of a second-order transfer function farther to the left of the imaginary axis – faster pole locations result in faster convergence of the tracking error to zero. Since ξ/ω is multiplied by $\dot{e}$ in the sliding surface (4.68), the noise in $\dot{e}$ (corresponding to undesired oscillations and vibrations) will be amplified with a small value of ξ/ω, resulting in increase chattering problem. Similarly, when $1/\omega^2$ is small, the contribution of the noise present in $\ddot{e}$ is amplified in (4.68). To efficiently damp the oscillations and vibrations in $\ddot{e}$, which suffers from differentiation noise, ω is generally not chosen to be too high in practice. For a good trade-off between the position tracking performance and the chattering problem, the parameters ξ = 0.5 and ω = 70 rad/s will be used in our experiment.

Since the coefficient of e in (4.68) equals 1, in the steady state we will have $s = e$. We define the tolerable range (or "threshold") of this error as a neighborhood of radius ε_p. In the experiments, ε_p is chosen equal to 0.5 mm in order to guarantee a good position tracking performance without causing excessive switching of the valves. Concerning the force controller, a force error threshold ε_f needs to be chosen. In practice, we choose ε_f equal to 0.1 N to achieve good force tracking responses.

V.1.3.2. Results and discussions

Fig. 4.35 shows the master and the slave force tracking profiles in free space and in contact motion for the PEB teleoperation system. Similarly,
Fig. 4.36 and Fig. 4.37 illustrate the force and position profiles for the FEB and the DFR systems, respectively.

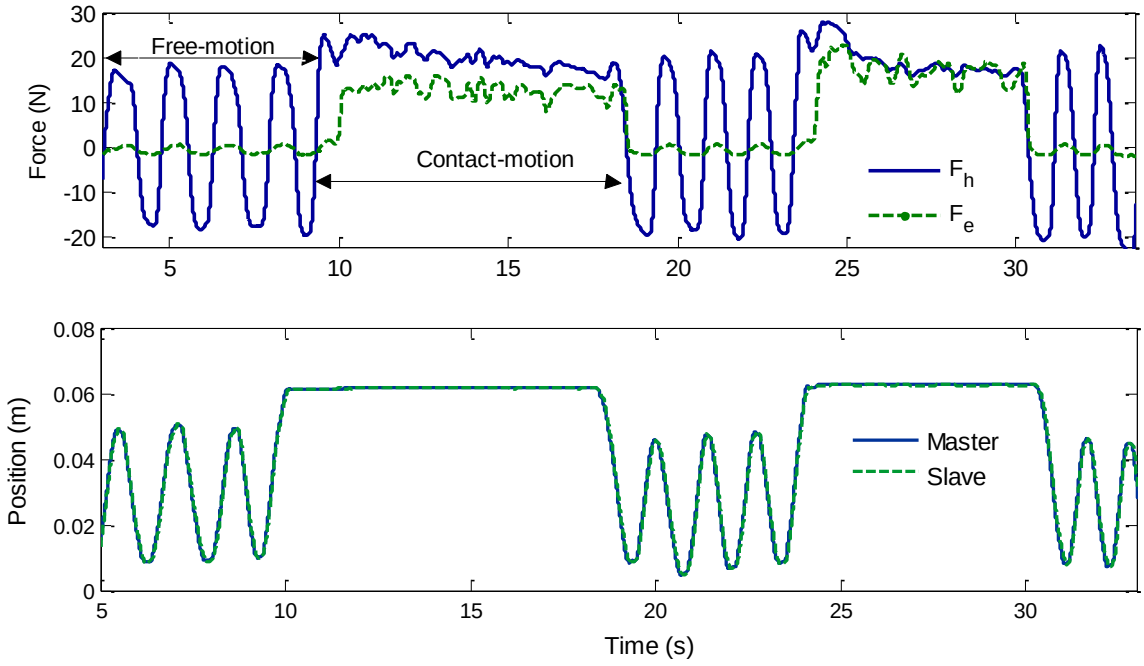

Fig. 4.35. Position and force profiles for the PEB teleoperation system

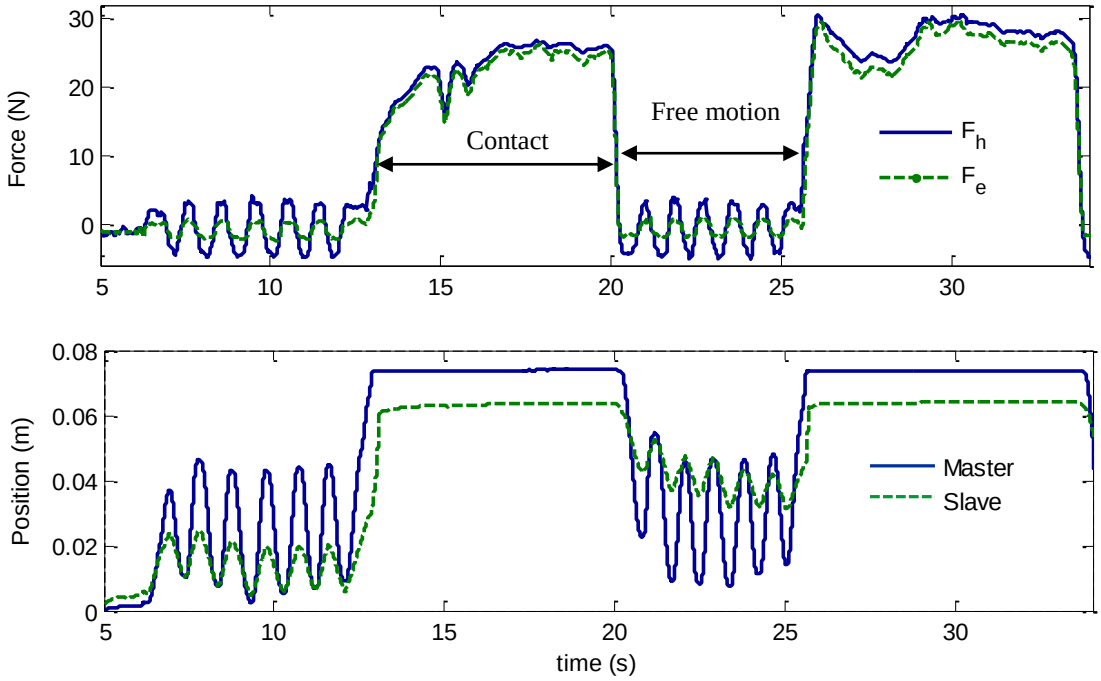

Fig. 4.36. Position and force profiles for the FEB teleoperation system

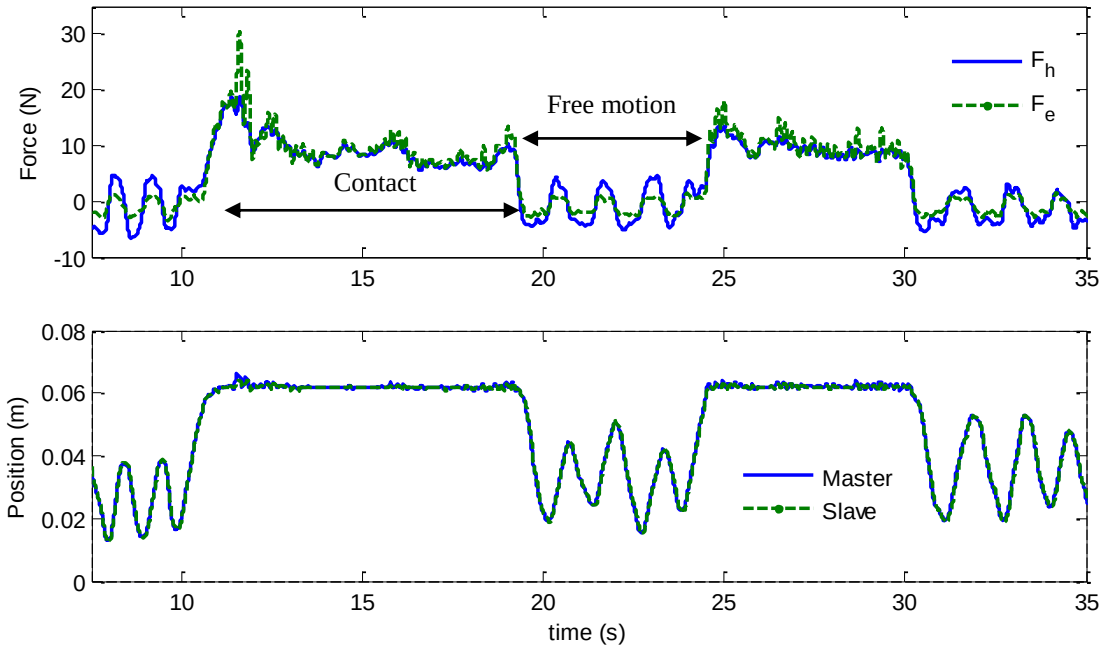

Fig. 4.37. Position and force profiles for the DFR teleoperation system

It is interesting to note that the high values for F_h during slave's free motion are due to the mass of the master's handle, which lies between the force sensor and the system of joystick-and-operator's hand (called moving mass). Furthermore, the interface is not perfect because of friction present between the joystick and the rail. This leads to increase operator's force in free motion if he/she wants to realize the same movement as to the case without friction. Due to the above reasons, the operator force in free motion is naturally high even when no control signal is applied to the system (i.e. all on/off valves exhaust).

As illustrated in Fig. 4.35, the PEB system provides a good position tracking responses. It can be seen that the slave rapidly tracks the master's movement in free space and also in contact mode. However, the force response is not as good because no force sensor is used. On the other hand, the force tracking performance of the FEB system is much better. Since the FEB system uses the measurement of slave/environment contact forces, the feeling of contact motion is highly realistic in our experiments. Therefore, the performance of the teleoperation system is improved significantly by feeding the operator with the slave/environment contact force. Nonetheless, the transparency the position tracking deteriorates in FEB control – as it can be seen in
Fig. 4.36, the slave's movement does not accurately track the master's movement. Note that it is difficult to realize a task with the FEB control where the slave can not impose a position/velocity on the environment. It was mentioned in (Tavakoli et al. 2007a) that in order to have a stiff slave, which is a crucial criterion in haptic system, the slave is necessary under position control. Finally, Fig. 4.35 and
Fig. 4.36 show the tradeoffs between position tracking and force tracking as long as only either both positions or both forces are available for feedback (i.e., PEB and FEB control, respectively).

Interestingly, the DFR system in Fig. 4.37 provides an improvement in terms of position tracking response compared to the FEB system. It also displays a superior force tracking performance compared to the PEB system. This result agrees with the previous theoretical work. However, a drawback of the DFR system is that higher oscillations and vibrations are present in the force and position responses under contact motion. Consequently, when operator's force level increases, the DFR system is less stable than the other cases.

Among the three architectures, the DFR scheme seems to be a better choice to obtain a good transparency. Although the various teleoperation controllers have previously been compared from a performance perspective in the literature (Lau & Wai 2005; Tavakoli et al. 2007b), this is the first study to show that it is possible to achieve stability and satisfactory performance using manipulators actuated by low-cost switching on/off valves.

To better investigate a comparison of the three control architectures, we provide in Tab. 4.5 the operator's opinions as well as the quantitative assessments of the force and position tracking errors (RMS values) in both contact motion and free motion.

	Force (contact motion)	Position (free motion)	Position (contact motion)	Human opinions
PEB system	5.5 N (25.5 %)	1.2 mm (6 %)	0.5 mm (0.8 %)	• In free motion, operators feel a "sticky" force again their movement. Thus, they have to provide higher force level than when they are really in free motion in order to realise the same gesture. • In contact motion, operators feel some chattering and vibration.
FEB system	0.8 N (3.6 %)	5.6 mm (28 %)	5.3 mm (7.1 %)	• In free motion, there is no more "sticky" force as in the PEB control. Operators can realize a movement easier without providing too much force. • In contact motion, less oscillation and vibration are obtained compared to the PEB control
DFR system	1.5 N (7.5 %)	0.8 mm (5.3 %)	0.7 mm (1.1 %)	• In free motion, similar felling is obtained as in the FEB case. • In contact motion, higher oscillations and vibrations occur than the other cases.

TAB. 4.5. COMPARISON OF THREE DIFFERENT CONTROL SCHEMES

It is noteworthy that the performance in terms of position and force tracking of the sliding mode control is less accurate than the one of the hybrid control. Indeed, the 4CH architecture used in the hybrid control lead to superior transparency over the 2CH architecture in the sliding mode control.

V.2. Extension to a five-mode control scheme (5MCS)

In this study, we extend the three-mode control scheme of section V.1 into a five-mode control scheme. The new system has two extra modes, which facilitate appropriate amounts of drive energy for good tracking responses and reduced switching activity (Le et al. 2011c). These two additional modes are defined by connecting only one chamber to the supply while leaving the other chamber locked. Limiting the drive power allows us to make smaller adjustments, improving the tracking accuracy of our controlled system.

V.2.1. Controller mode selection

The different configurations of the 5MCS with four solenoid valves are shown in Tab. 4.6.

	Mode 1	Mode 2	Mode 3	Mode 4	Mode 5
Chamber p	fills	exhausts	closed	fills	closed
Chamber n	exhausts	fills	closed	closed	fills
Control u	1	– 1	0	0.5	– 0.5
$\underline{U} = [U_1\ U_2\ U_3\ U_4]$	[1 0 1 0]	[0 1 0 1]	[0 0 0 0]	[1 0 0 0]	[0 0 0 1]

TAB. 4.6. FIVE POSSIBLE CONTROL MODES

As it can be seen in Tab. 4.6, the first three modes in the 5MCS are inherited from the 3MCS. Modes 4 and 5 are added in the 5MCS in order to offer more control-mode possibilities and to improve the behavior of the system by reducing switching activity of the valves. Mode 4 allows for moving the piston in the same direction as in mode 1 but with a slower dynamics (because in mode 4 the chamber n is closed as opposed to exhausting as in mode 1 – in both cases the chamber p will be filling). Mode 4 may be considered as an intermediate (or average) mode between modes 1 and 3, due to which the control vector u is chosen as 0.5 (Tab. 4.6). On the other hand, mode 5 whose control vector u equals –0.5 is used to move the piston in the other direction and could be regarded as an intermediate level of actuation (and piston acceleration) between modes 2 and 3.

To be able to switch between modes 1 and 4, or modes 2 and 5, a threshold ε_1 is introduced, where ε_1 is greater than the previously-defined neighborhood of radius ε (i.e., $\varepsilon_1 > \varepsilon$). When |s| is within the interval $[\varepsilon, \varepsilon_1]$, either mode 4 or mode 5 ($u = \pm 0.5$) is used to provide slower dynamics compared to modes 1 or 2 ($u = \pm 1$), respectively. When |s| is within the interval $[\varepsilon_1, \infty[$, either mode 1 or mode 2 ($u = \pm 1$) is used to provide fast dynamics, highly accelerating the piston in the direction that minimizes s.

In summary, the new control law for the 5MCS can be given as

$$u = \begin{cases} +/- sign(s) & \text{if} \quad |s| \geq \varepsilon_1 \\ +/- 0.5 sign(s) & \text{if} \quad \varepsilon < |s| < \varepsilon_1 \\ 0 & \text{if} \quad |s| \leq \varepsilon \end{cases} \tag{4.69}$$

where *sign* function is defined in (4.35).

Compared to the 3MCS, the 5MCS requires to adjust one more parameter (i.e., ε_1) and there is no efficient analytical method for pre-tuning it. Note that the choice of ε_1 depends on the value of ε. If ε_1 is too close to ε, the dynamic behavior of the 5MCS becomes similar to the 3MCS. In this case the two additional modes will not offer any additional benefits.

V.2.2. Comparison between the 5MCS and the 3MCS

In order to justify the superior performance of 5MCS over 3MCS, this subsection provides a comparison of the position tracking control between these two schemes, followed by an analysis in time domain as well as in frequency domain for the master-slave teleoperation system implemented on a real-world test bed.

V.2.2.1. Position tracking performance

To facilitate the comparison of the 5MCS and 3MCS performances, all controller parameters are chosen to be similar for both cases, i.e., $\xi = 0.5$, $\omega = 70$ rad/s, $\varepsilon = 0.5$ mm.

Fig. 4.38 shows the position responses obtained by a sine wave input at 0.5 Hz. As it can be seen in Fig. 4.38 (a) and (b), vibrations and oscillation are significantly damped in the 5MCS system. This indicates that switching activity of the valves can be reduced by increasing the number of control levels. Similar remarks are obtained with the trapezoidal input as shown on Fig. 4.39 (a) and (b).

In the 5MCS system, the previously-defined threshold ε_1 is used to switch the valves to the intermediate modes when the dynamic behavior is slow (i.e., $|s| < \varepsilon_1$). In order to assess the influence of this parameter in such a scheme, different values of ε_1 are chosen, i.e., 1 mm and 3 mm, and the results of Fig. 4.38 (b) and (c) are respectively obtained. As it can be seen, when ε_1 is small, the tracking performance is improved, but the solenoid valves seem to chatter more. This aspect can be observed on Fig. 4.39 (b) and (c) with the trapezoidal position profile.

In order to further investigate a comparison between the 5MCS and 3MCS systems as well as the influence of the controller parameter ε_1 to the 5MCS performance, (Hodgson et al. 2011a) proposed a frequency analysis which consists in calculating the *number of switching per second* of four on/off valves and the *root-mean-square (RMS) position tracking error*.

The experiment is run utilizing the sine wave test input for the desired position with frequencies varying from 0.1Hz - 5.0Hz. From the results in Fig. 4.40 (a), we find that for both the 3MCS and 5MCS systems, increasing the input frequency leads to increase RMS tracking error. The inability of the systems to track the reference for high enough frequency input sine waves is due to the fact that such frequencies will require a switching activity that violates the response time of the valves (1.3ms) (Hodgson et al. 2011b). When comparing results from Fig. 4.40 (a) for the 3MCS and 5MCS systems, one can see that there was not a notable improvement or detriment to tracking performance for the 5MCS controller. However, there was a significant decrease in switching activity of the 5MCS case (as has been seen before in Fig. 4.38 (a)-(b) and Fig. 4.39 (a)-(b)).

Fig. 4.40 (b) illustrates the 5MCS behavior with different controller parameters, i.e., $\varepsilon_1 = 3$mm and $\varepsilon_1 = 1$mm. As it has been seen, decreasing controller parameters was found to increase switching activity and decrease the RMS tracking error in the 5MCS system. Similar remark can be found in Fig. 4.38 (c) and Fig. 4.39 (c). Finally, there exists a design trade-off between improved switching performance and tracking accuracy for the 5MCS system depending on the choice of the controller parameters.

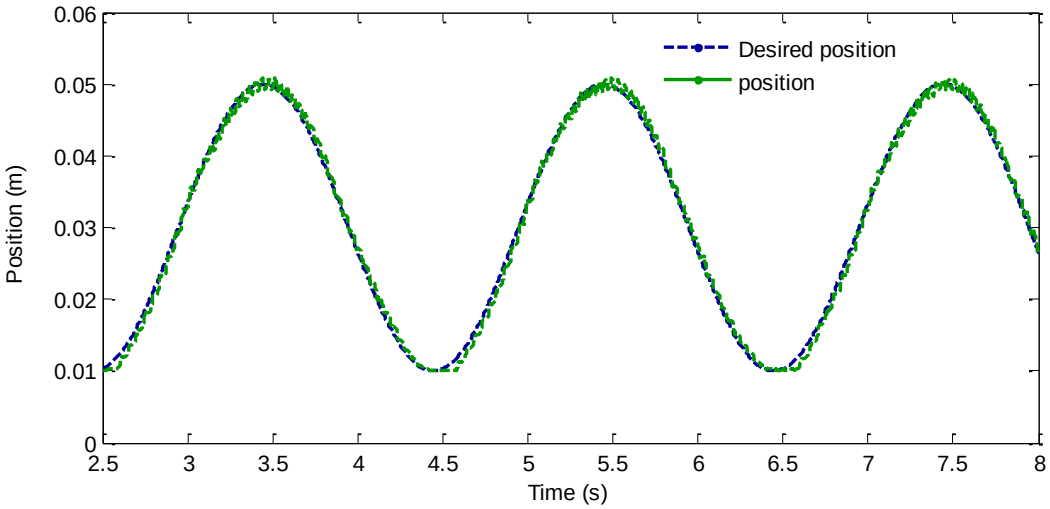

(a). 3MCS: $\xi = 0.5$, $\omega = 70$ rad/s, $\varepsilon = 0.5$ mm

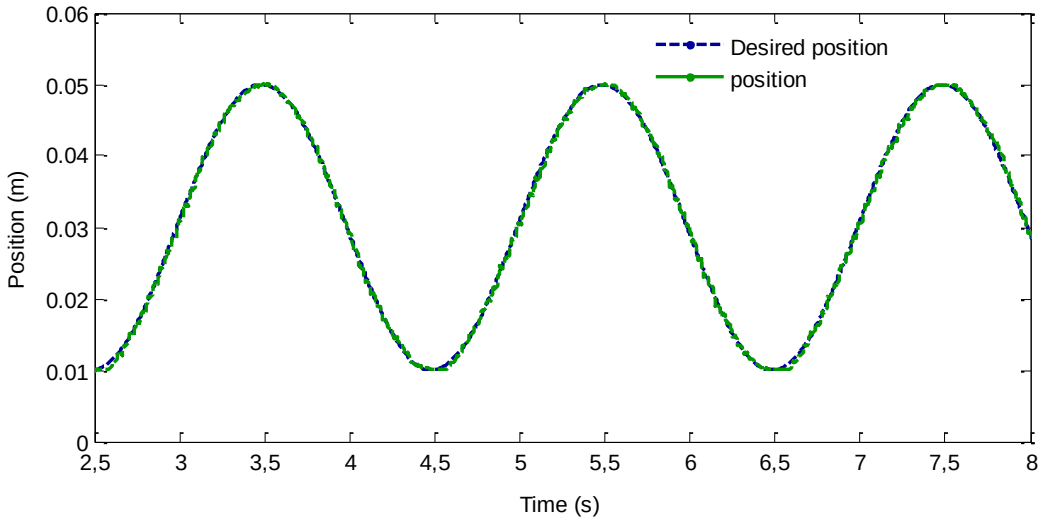

(b). 5MCS: $\xi = 0.5$, $\omega = 70$ rad/s, $\varepsilon = 0.5$ mm, $\varepsilon_1 = 1$ mm

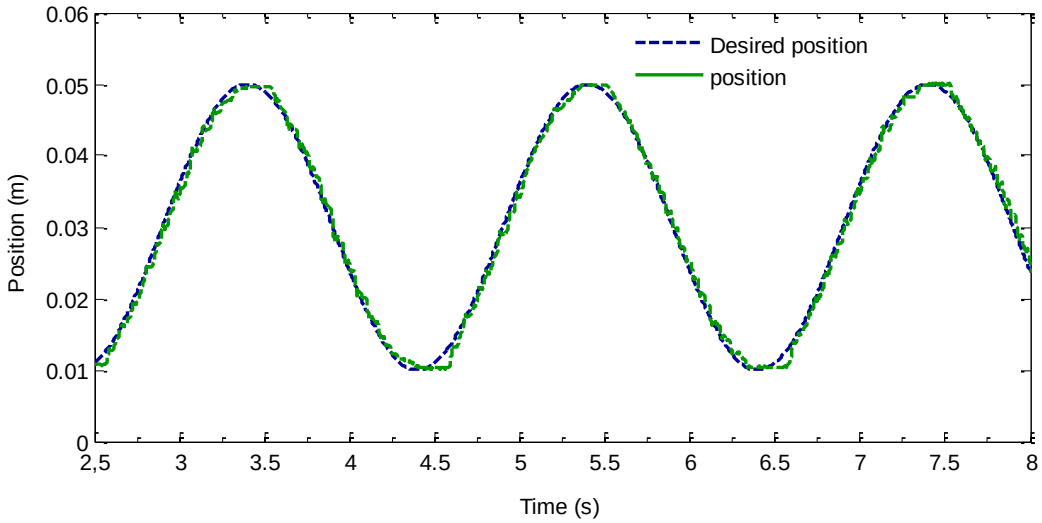

(c). 5MCS: $\xi = 0.5$, $\omega = 70$ rad/s, $\varepsilon = 0.5$ mm, $\varepsilon_1 = 3$ mm

Fig. 4.38. A sine wave position tracking performance based on sliding mode control

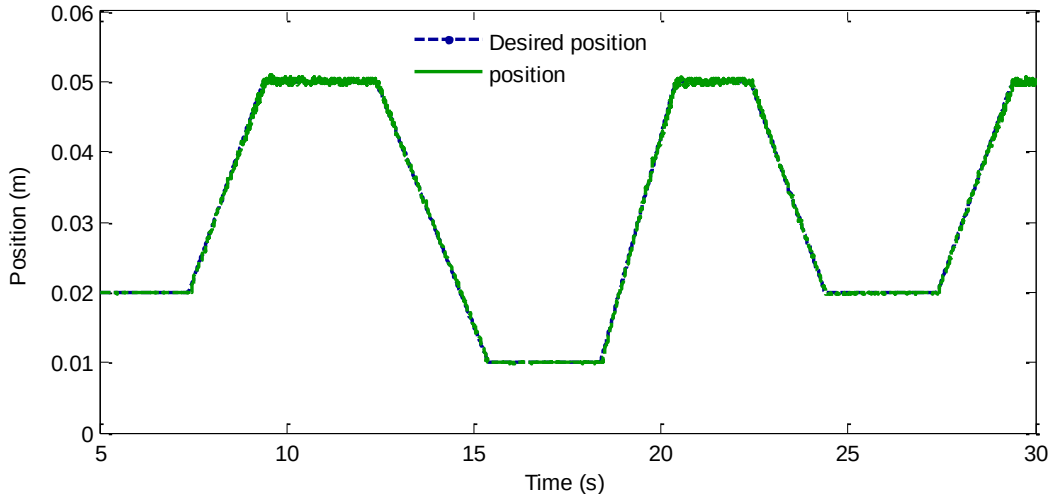

(a). 3MCS: $\xi = 0.5$, $\omega = 70$ rad/s, $\varepsilon = 0.5$ mm

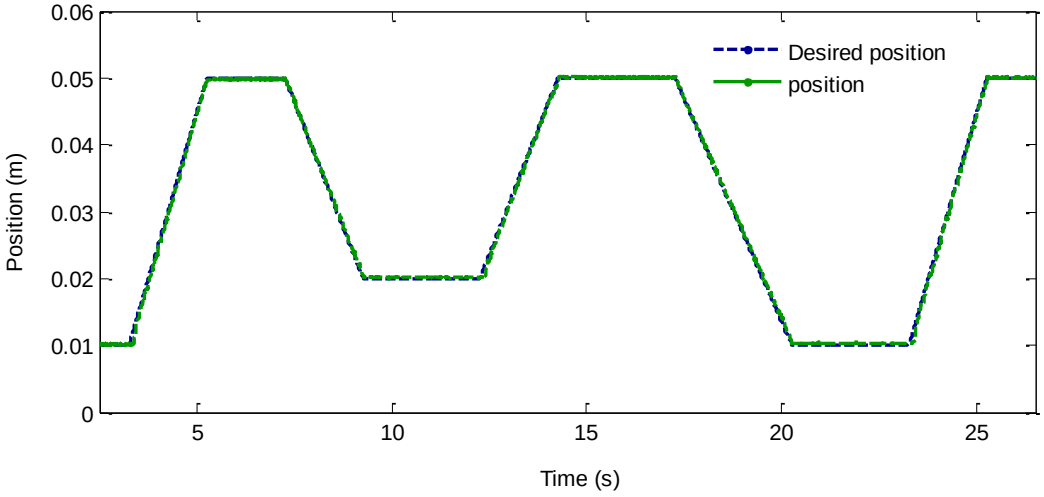

(b). 5MCS: $\xi = 0.5$, $\omega = 70$ rad/s, $\varepsilon = 0.5$ mm, $\varepsilon_1 = 1$ mm

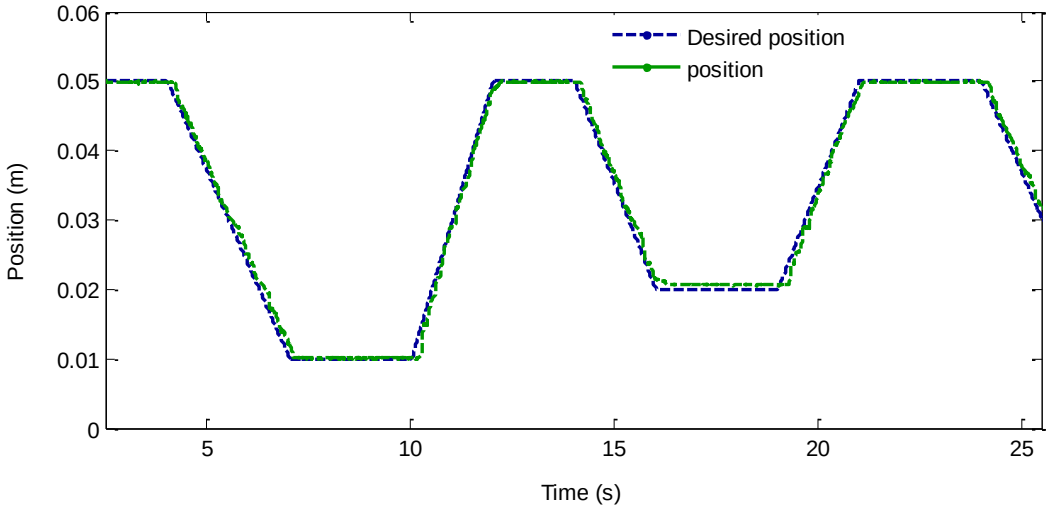

(c). 5MCS: $\xi = 0.5$, $\omega = 70$ rad/s, $\varepsilon = 0.5$ mm, $\varepsilon_1 = 3$ mm

Fig. 4.39. Position responses in the trapeze trajectory based on sliding mode control

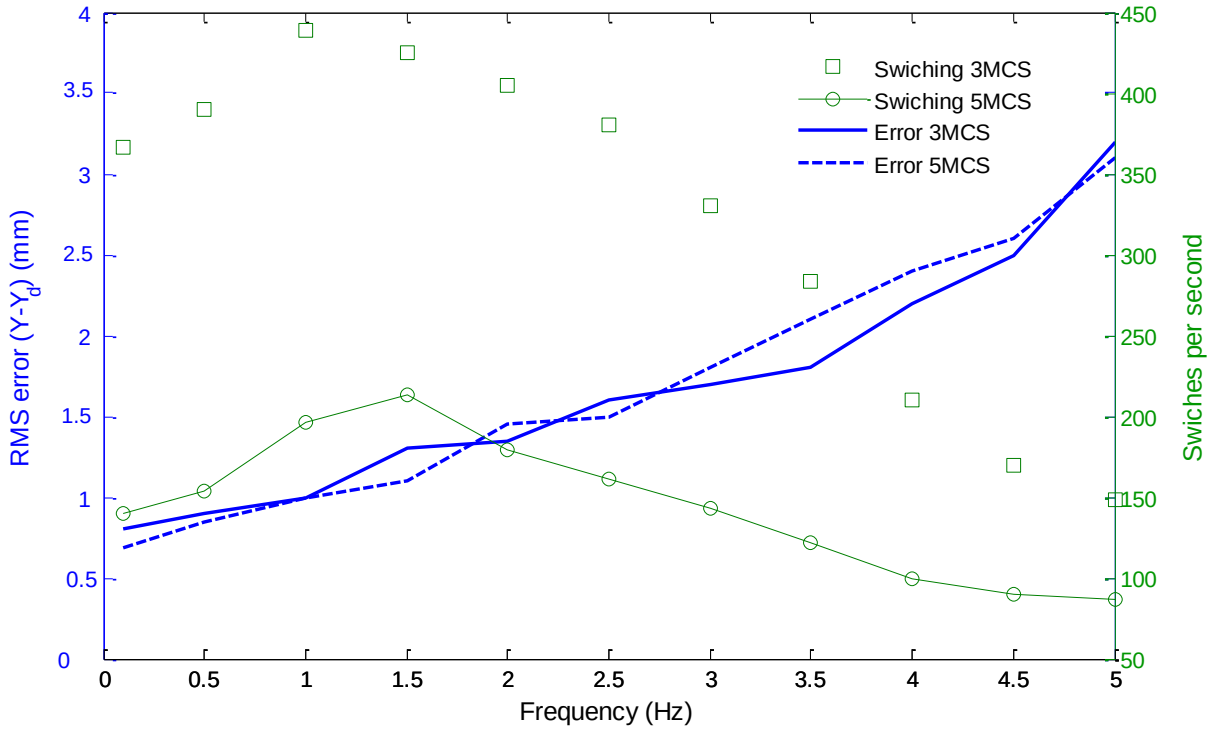

(a). Comparing 3MCS with 5MCS

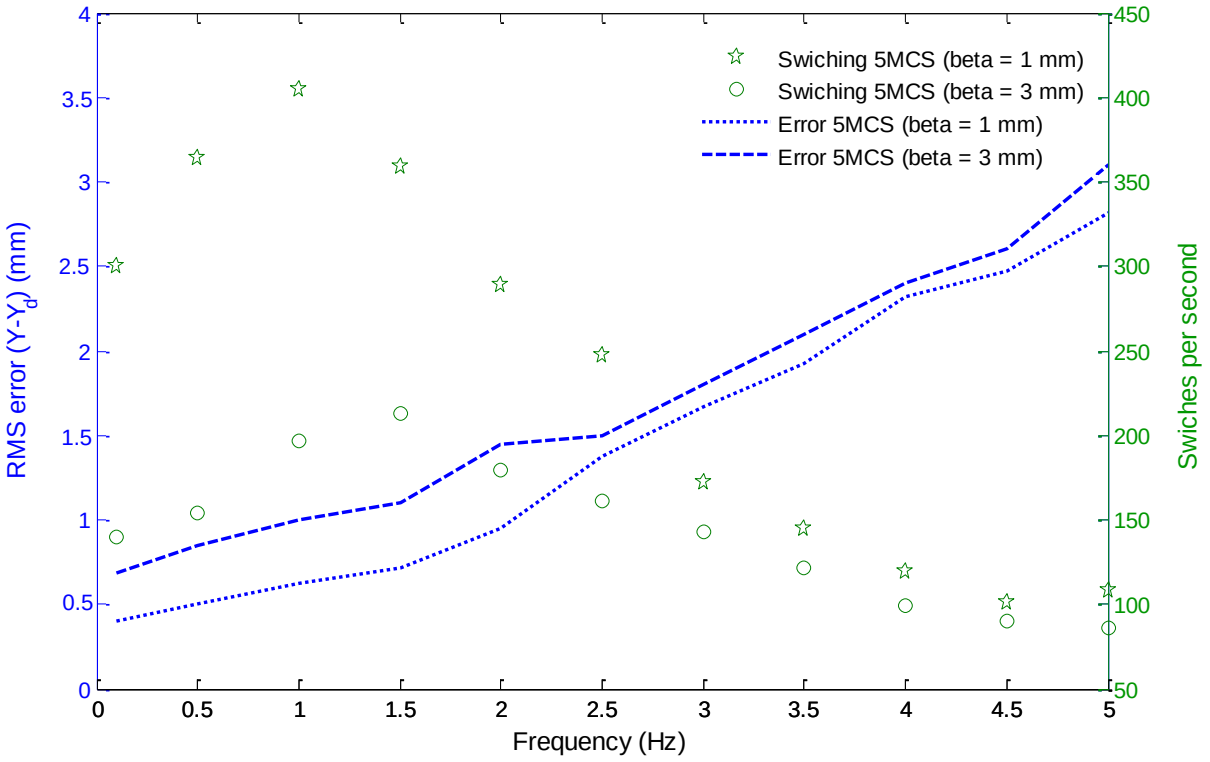

(b). 5MCS comparing (ε_1 = 1 mm) versus (ε_1 = 3 mm)

Fig. 4.40. Frequency analysis of sine-wave experimental results

V.2.2.2. Teleoperation performance

As mentioned previously, the five-switching-mode based on sliding control is obviously an interesting solution to enhance the tracking accuracy and reduce chattering of the valves. Thus in this study, we investigated the use of this approach on the master-slave teleoperation system.

Here, the controller parameters are set up as follow for both systems 5MCS and 3MCS, i.e., ξ = 0.5, ω = 70 rad/s, ε_p = 0.5 mm for the position controller, and ε_f = 0.1 N for the force controller. In addition to the 5MCS, two more parameters need to be tuned, i.e., a position threshold ε_{1p} and a force threshold ε_{1f}. Their values, which were found after many experimental trials to get the best response of the two systems (5MCS and 3MCS), are respectively equal to 1 mm and 0.5 N

Fig. 4.41 shows the master and the slave force and position tracking profiles in the 5MCS teleoperation system. In the PEB and FEB systems, the performance in transparency under 5MCS seems to be similar with that under the 3MCS (compared with Fig. 4.35–Fig. 4.37). On the other hand, under DFR control, less oscillation is observed in the 5MCS case than in the 3MCS case.

To show further benefits of the 5MCS teleoperation, we can take the transparency analysis beyond only studying the force and position responses. Note that the major drawback of solenoid valves is that they tend to switch a lot which both creates noise and non-smooth tracking behavior. Any improvement in this regard is highly important. We will show in the following that the 5MCS teleoperation results in reduced switching activities of the on/off valves while maintaining position and force tracking responses. To do this, a frequency analysis of the control signals (controller outputs) is carried out. For each of the master and slave manipulators there exist four control signals (U_1, U_2, U_3 and U_4), thus eight signals for the overall system. In the following, we only compare the spectra of U_1 of the master side. Similar results can be observed for the other control signals. The frequency responses can be found by using the discrete fast Fourier transform *fft* command in Matlab. The spectral analysis of the control signal U_1 obtained with the 5MCS and the 3MCS are shown in Fig. 4.42.

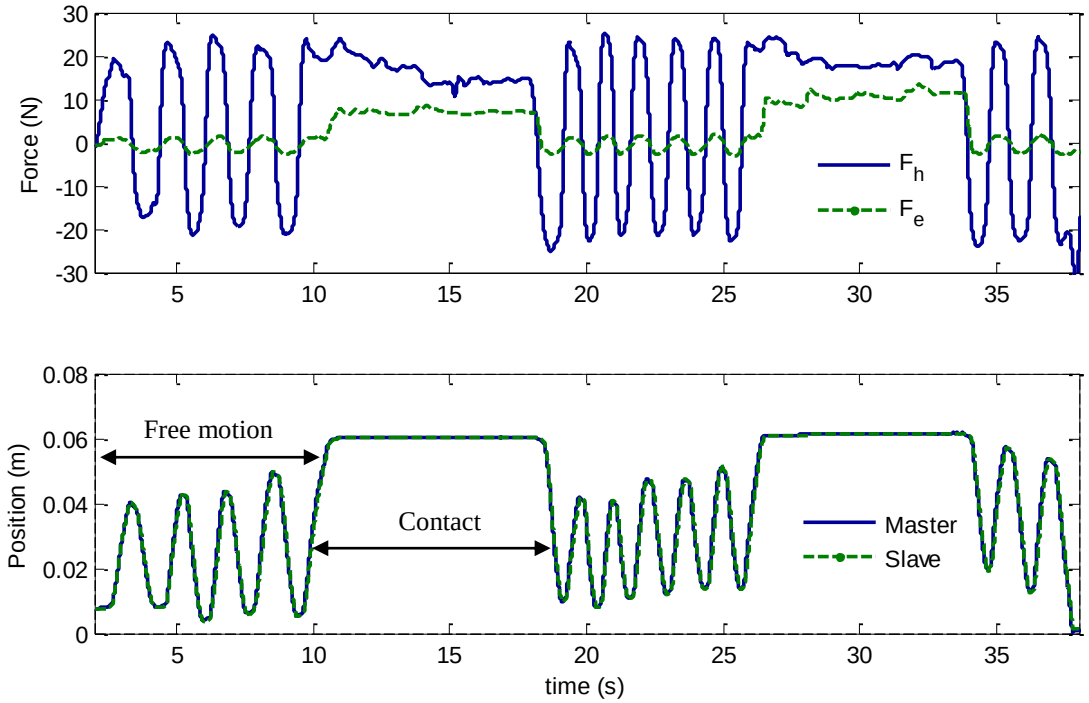

(a). PEB architecture

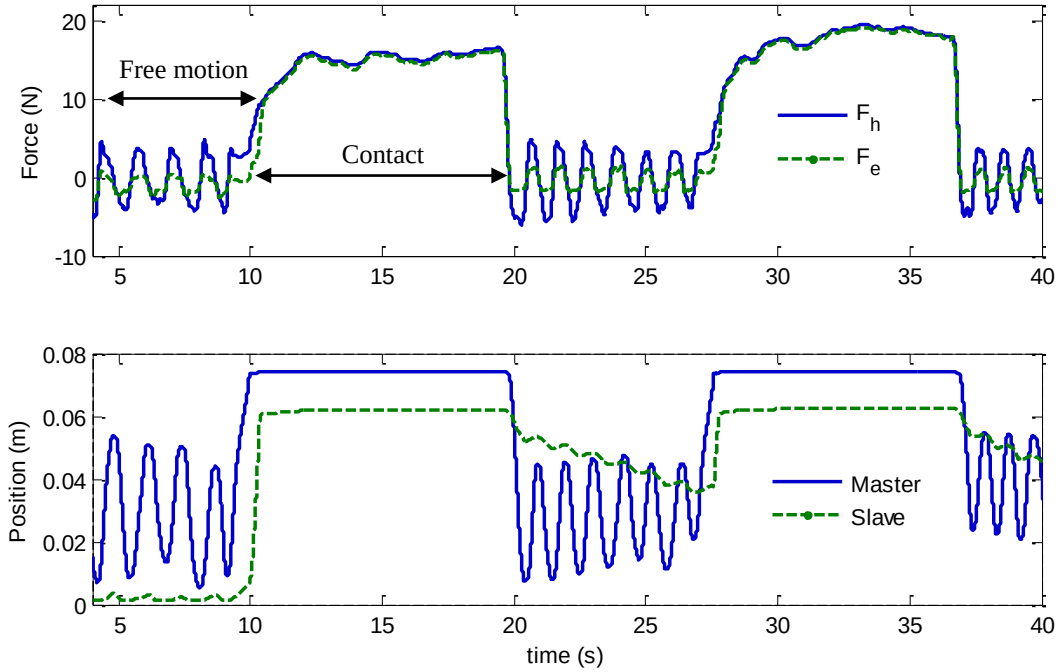

(b). FEB architecture

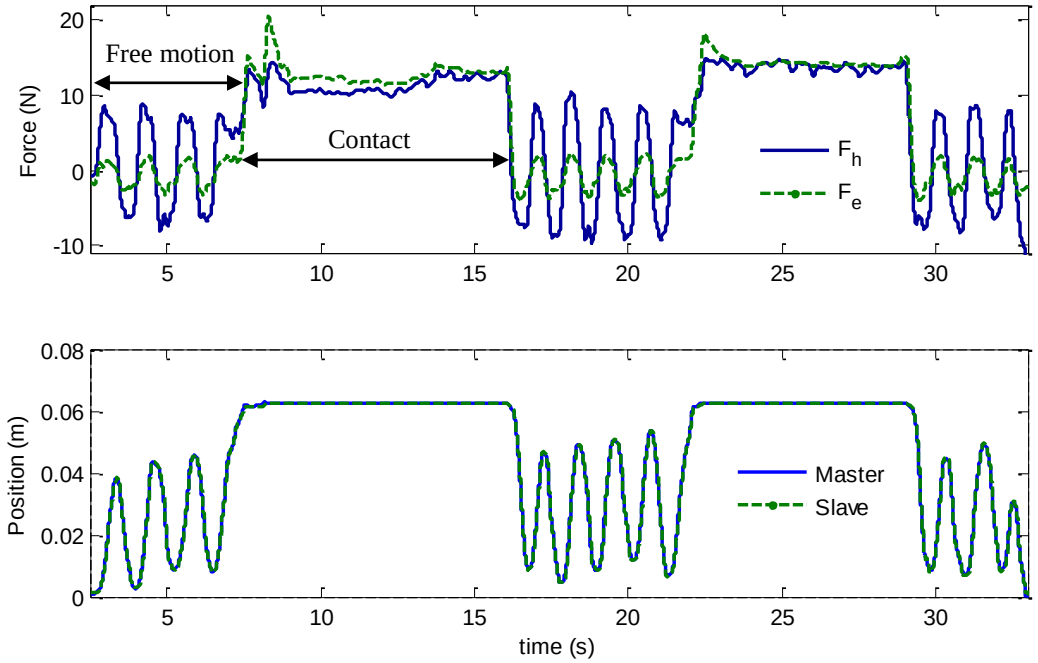

(c). DFR architecture

Fig. 4.41. Transparency of the teleoperation system with 5MCS

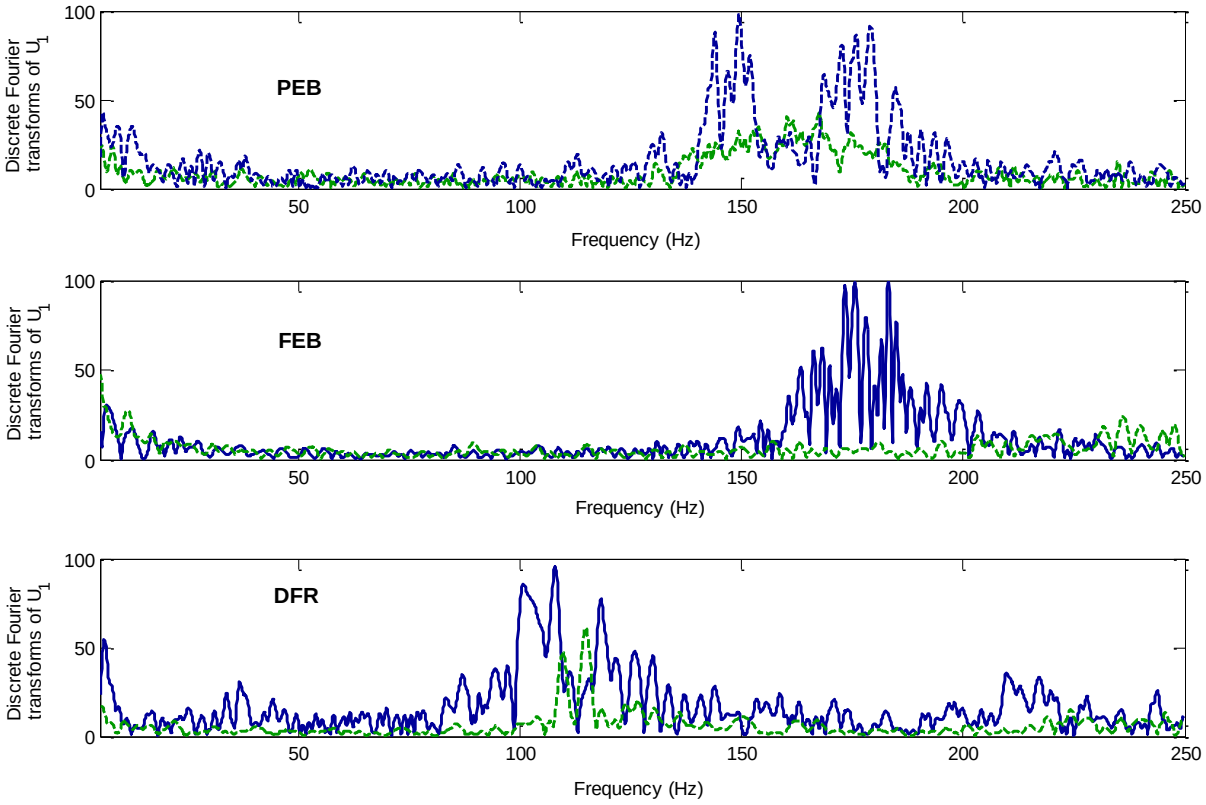

Fig. 4.42. Discrete Fourier transforms of the control signal U_1 for the master manipulator: 3MCS (Solid), 5MCS (Dashed)

As it can be observed, for all three architectures (PEB, FEB and DFR), the magnitude of the Fourier transform of U_1 is lower in the 5MCS case than in the 3MCS case over almost all frequencies, and especially so at high frequencies. This shows that by using two additional modes, the on/off activity of the valves has been reduced, which allows to provide better tracking responses with smoother dynamics and less oscillations, particularly over high frequencies.

Based on these results, it is clear that the 5MCS is an interesting alternative to save energy and improve the valve's lifetime at no cost to teleoperation transparency. An area of possible future development is methods for adjusting the parameters ε_{1p} and ε_{1f} for best performance.

VI. Conclusion

In this chapter, we investigate the use of pneumatic actuators with inexpensive solenoid valves for development of a master-slave teleoperation. To efficiently control the switching on/off valves, three different strategies were proposed, namely pulse width modulation (PWM), hybrid and sliding mode control.

PWM is the most popular method due to its simplicity of implementation and design. A main problem with this method is the chattering phenomenon that is caused by the high frequency switching of the valves at steady state.

To overcome the drawbacks of the PWM, a hybrid control theory is investigated. This technique not only takes into account the nonlinear behavior of the mass flow rate but also the switching control of the valves. In experiments, it was observed that with the four-channel bilateral teleoperation control architecture employing this hybrid control algorithms, satisfactory force and position tracking between the master and the slave is obtained under both free-motion and contact-motion conditions. Furthermore, the results show that an accurate tracking at steady state but also the dynamic behavior of the pressures are better in the case of the hybrid control than the PWM control. It is noteworthy that

stability analysis of the overall hybrid system has not been investigated in our study due to the complexity and difficulty of dealing with highly nonlinear pneumatic actuators and the discrete nature of force control laws. Thus, the robustness and stability analyses will be an interesting research.

The third proposed method is a sliding mode control that allows to perform not only the transparent analysis but also the stability analysis. To evaluate the efficiency of the proposed approach, a comparison of transparency and stability has been investigated between three control architectures (PEB, FEB and DFR) in a two-channel bilateral teleoperation framework. Moreover, in order to improve the dynamic performance and reduce the chattering problem in solenoid valve actuated pneumatic teleoperation systems, a five-mode sliding control scheme has been used, which can be considered as an extension of the three-mode sliding controller. Our study demonstrated that by increasing the number of possible control actions for the valves, we can reduce the valves' switching activities, hence improving the valve's life times.

Finally, the overall results show a feasibility of the different control laws for the pneumatic actuated teleoperation with cheap on/off valves. A major drawback of such components proceeds from the acoustic noise generated by quick switching between two operating positions, i.e. open or closed. Compared to the PWM strategy, the hybrid and the sliding mode controls allow to reduce this noise, but it still exists and can be possibly disturbing for certain applications (e.g., medical area). Therefore, in the following chapter, we investigate the use of proportional servovalves in the pneumatic teleoperation system. A comparison related to the performance between two technologies will be carried out.

Chapter 5
Bilateral Control of a Pneumatic-Actuated Teleoperation System with Proportional Servovalves

Table of contents

I. Introduction

In this chapter, we investigate the use of (jet pipe) proportional servovalves on pneumatic bilateral teleoperation system. Advantages of pneumatic actuators driven by servovalves are well known as quiet, easy compliance control, smooth force and motion, etc. But for their highly nonlinear properties such as compressibility of air, leakages, friction effect and nonlinearity of servovalves, pneumatic actuators are less used in industrial applications than electric motors (Tsai & Huang 2008). Ampere laboratory, with its domain expertise in fluid power since 30 years, have developed and applied several advanced control algorithms on the pneumatic system in order to cope with some of above problems (Det 1991; Sesmat 1996; Brun 1999; Smaoui 2005).

Thanks to the advances in control theory, pneumatic actuators equipped with proportional servovalves have found use in various applications of haptic teleoperation in recent years. For instance, (Tadano & Kawashima 2007) propose a forceps manipulator for a surgical master-slave system, which is able to estimate external forces without using any force sensor. (Durbha & Li 2009) proposed a passive bilateral teleoperation system with human power amplification through pneumatic actuators. The input human force was amplified through the pneumatic teleoperator to provide assistance for the human operator in terms of performing the task (e.g. lifting a heavy object). (Guerriero & Book 2008) controlled the foot positions of two 3-DOF legged slave robots driven by pneumatic actuators. In this system, bilateral teleoperation provided force feedback to the operator through two PHANToM master haptic devices as a function of the foot position error. Pneumatic muscle actuators have been recently used in a teleoperation system (Tondu et al. 2005). They are compact and have high power/weight density, but they are difficult to control and require an accurate experimental characterization.

This chapter is structured as follows. First, the modeling of a pneumatic actuator composed of a cylinder and a proportional servovalve is presented in Section II. Section III describes a bilateral control strategy based on a tangent linearization of the nonlinear pneumatic model. This approach is then implemented in a 1-DOF master-slave robot setup. Stability and transparency analyses of the four-channel (4CH) closed-loop teleoperation system are investigated. In Section IV, we deal with the problem of force sensor-less bilateral teleoperation based on linear observers for hand force and environment force estimations. Experimental results demonstrate high accuracies in terms of position and force tracking in the teleoperation system. Finally, concluding remarks are given in Section V.

II. Model of Pneumatic Actuator and Servovalves

II.1. Theoretical model

A schematic of a 1-DOF pneumatic actuated system is shown in Fig. 5.1. The device consists of a double-acting cylinder, a 4-way double-pilot actuated servovalve, a position sensor, a force sensor and two pressure sensors.

Assuming that air is a perfect gas, the temperature is homogeneous in each chamber and the stiction force is negligible (since the pneumatic actuator used in experiment is frictionless cylinder – Airpel model), the fourth-order control model of the pneumatic actuator can be written as (Brun 1999)

$$\begin{cases} \dfrac{dy}{dt} = \dot{y} \\ \dfrac{d\dot{y}}{dt} = \dfrac{1}{M}(S_p P_p - S_n P_n - b\dot{y} - F_{ext}) \\ \dfrac{dP_p}{dt} = \dfrac{\alpha r T_a}{V_p(y)}\left(q_p(U, P_p) - \dfrac{P_p}{rT_a} S_p \dot{y} \right) \\ \dfrac{dP_n}{dt} = \dfrac{\alpha r T_a}{V_n(y)}\left(q_n(-U, P_n) + \dfrac{P_n}{rT_a} S_n \dot{y} \right) \end{cases} \tag{5.1}$$

where the parameter's definitions in (5.1) is similar to those in (4.1)–(4.2) of chapter 4. Each mass flow rates q_p and q_n of the servovalve were estimated in terms of voltage control and pressure as following (see Appendix 1)

$$q(U,P) = \sum_{i=0}^{3}\sum_{j=0}^{3} a_{ij} U^i P^j \tag{5.2}$$

The value of coefficients a_{ij} can be found in Appendix 1. Equations (5.1) and (5.2) are implemented in Matlab Simulink in order to establish the model of the pneumatic actuator and the servovalve's mass flow rate. In order to test its validity, this model will be compared to the real one in the following subsection.

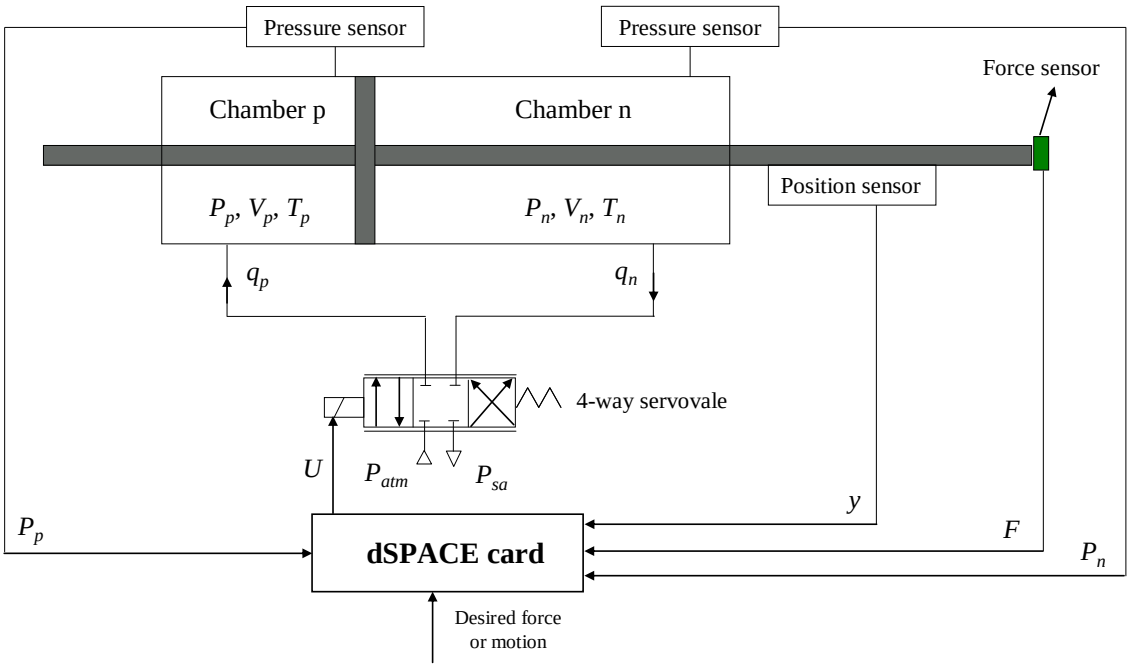

Fig. 5.1. Electro-pneumatic system with 4-way double-pilot operated servovalve

II.2. Comparison of simulation and experimental models

The theoretical model of the servovalve's mass flow rate was justified by an open-loop control presented in Appendix 1. In order to complete a validation of this theoretical work, we provide here the results of the closed-loop position tracking for both simulation and experimental tests. The parameter's values used in simulation can be found in Tab. 4.2.

The experiment and simulation were run by using the sine wave test input for the desired position with three different frequency values, i.e., 0.1Hz (considered as a low frequency), 1 Hz (considered as an average frequency), and 5 Hz (considered as a high frequency). The results in terms of the position tracking and the pressure behavior in the chambers are plotted in Fig. 5.2 – Fig. 5.4.

As it can be seen in Fig. 5.2 (a), high tracking accuracy is achieved with an excited frequency of 0.1 Hz. When the frequency is increased at 1 Hz (cf. Fig. 5.3 (a)), a small phase shift appears in the position response for both simulation and experimental tests. Acceptable tracking performance (i.e., about 10 % of error/amplitude ratio), however, is still achieved. On the other hand, at 5 Hz, the tracking responses are deteriorated, resulting in increase phase shift and distorted position signals, i.e. a loss of sinusoidal form (see Fig. 5.4 (a)).

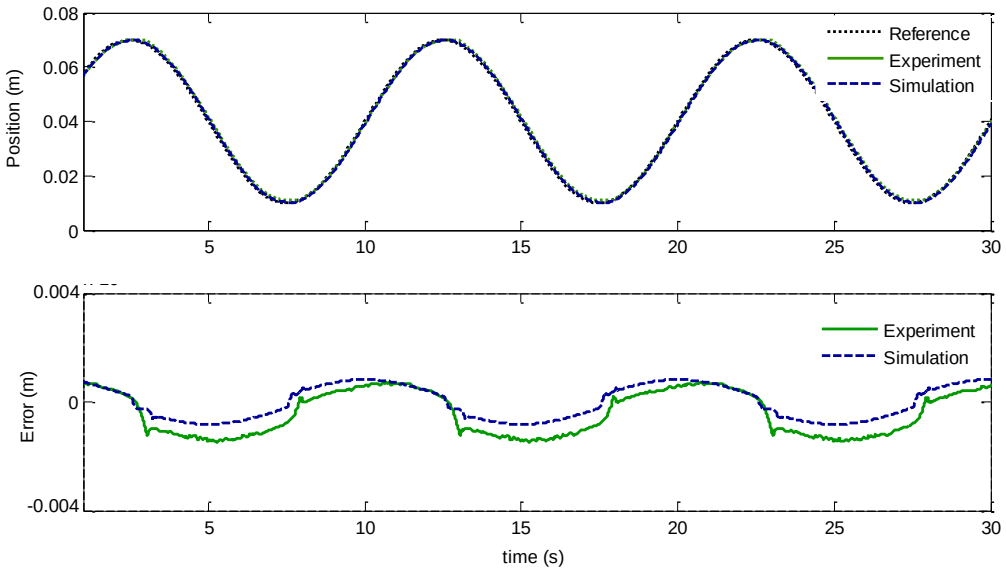

(a). Experimental and simulation position tracking

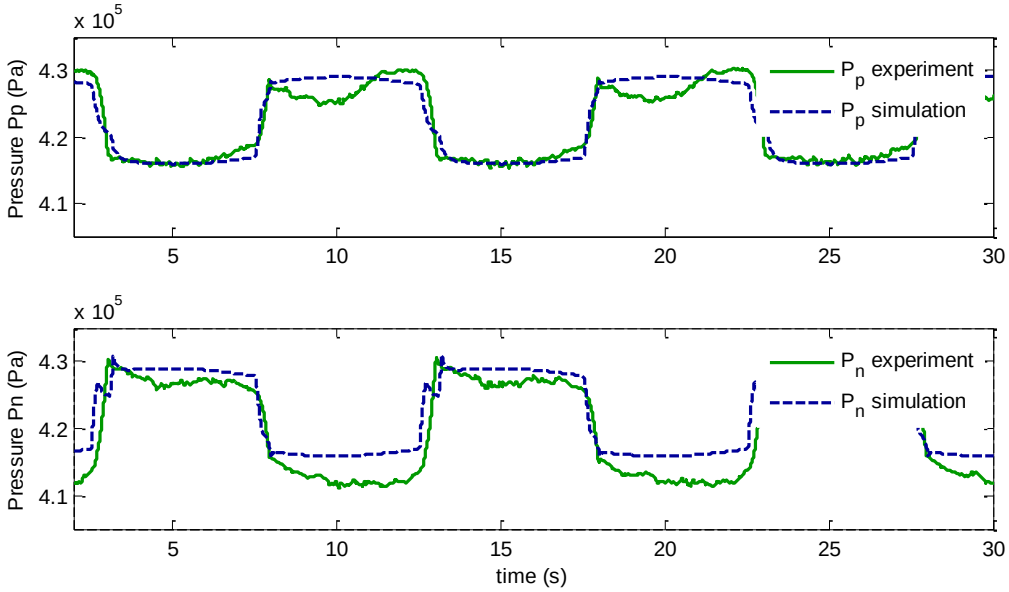

(b). Experimental and simulation pressure behavior

Fig. 5.2. 0.1 Hz sine wave

From the results in Fig. 5.2 (a) – Fig. 5.4 (a), we find that for both the experimental and simulation tests, increasing the input frequency eventually leads to a point where the system is unable

to track the reference. This is due to the fact that a high enough frequency will involve high flow dynamics in which the servovalves cannot generate. Note that the technology of the single-stage jet-pipe valves is usually used for delivering a relatively low mass flow rate (e.g., the 200PN model used in our case is limited at 22 $Nl.mn^{-1}$ with a supply of 600 kPa). In the teleoperation system where the operator hand's movement is generally slow enough (i.e., less than 2 Hz) and where the time delay of the transmission line is negligible, this kind of valve technology may considered to be a suitable solution for our first feasibility study.

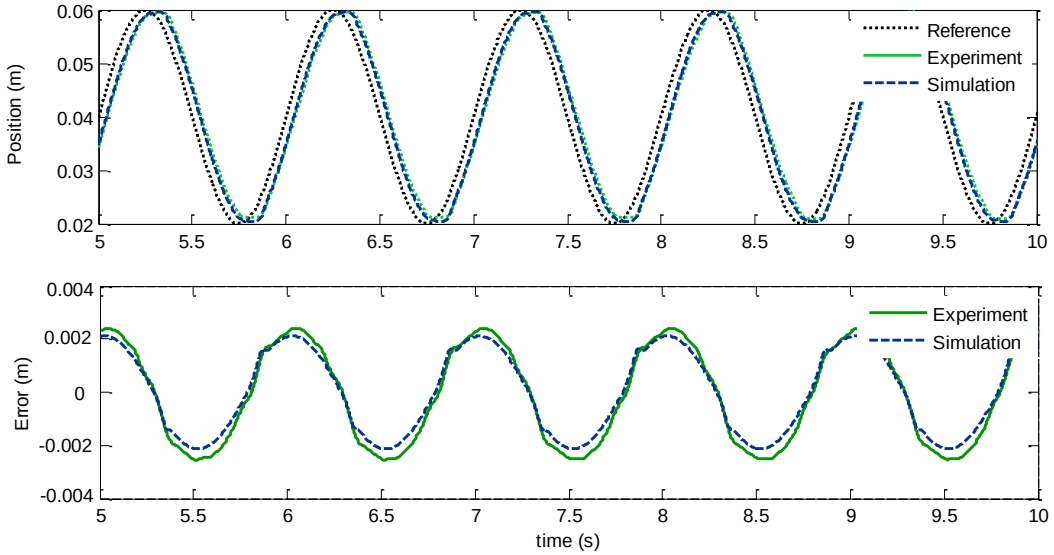

(a). Experimental and simulation position tracking

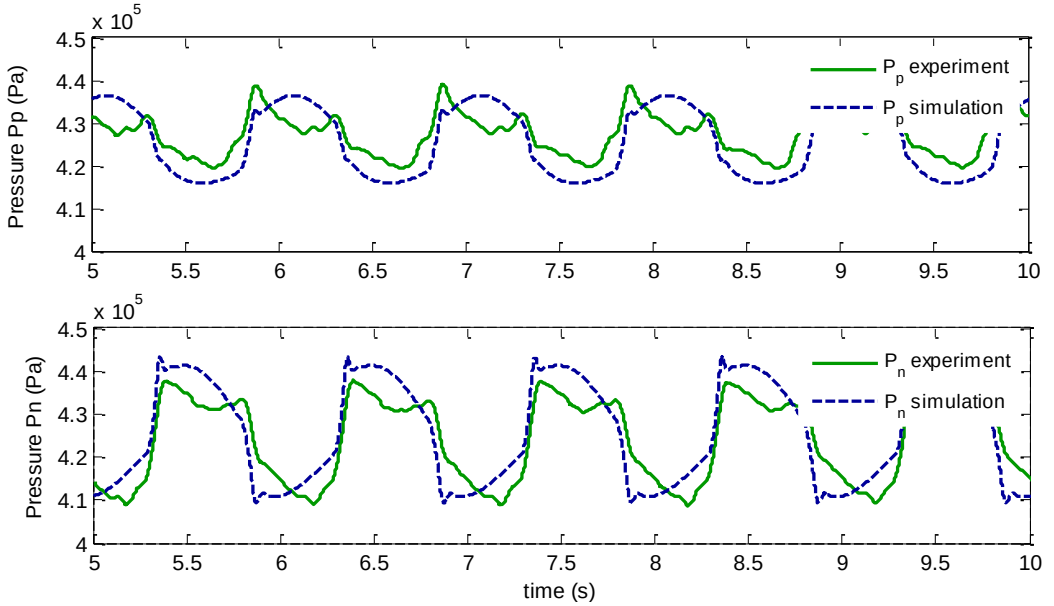

(b). Experimental and simulation pressure behavior

Fig. 5.3. 1 Hz sine wave

Fig. 5.2 (a) – Fig. 5.4 (a) show that the position response in the experiment are consistent with those reported in the simulation. On the other hand, the pressure behaviors are somewhat different between the experiment and the simulation (see Fig. 5.2 (b) – Fig. 5.4 (b)). The fact is that the pressure sensors were not incorporated inside the chambers, which may lead to slightly inaccurate measurements.

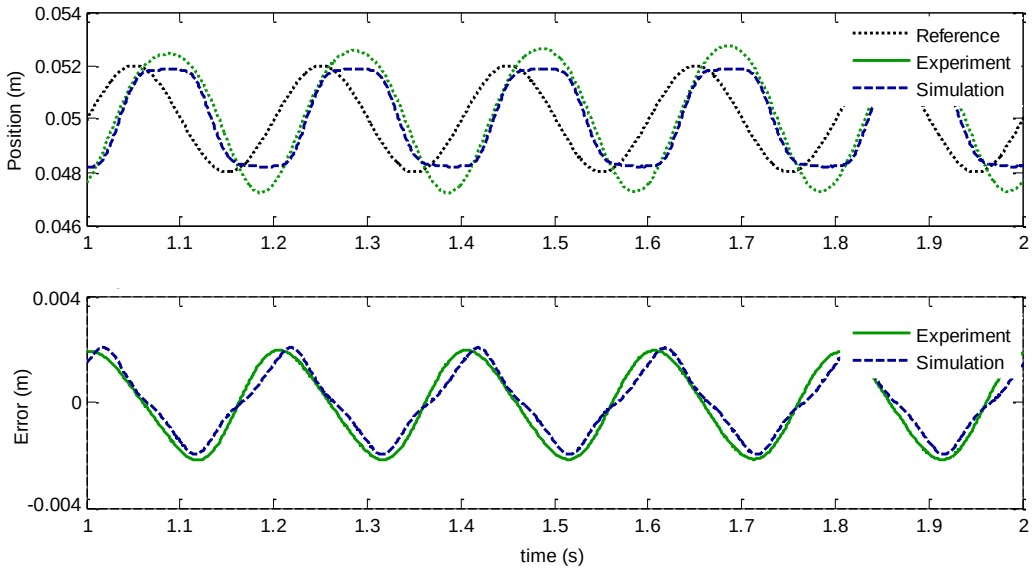

(a). Experimental and simulation position tracking

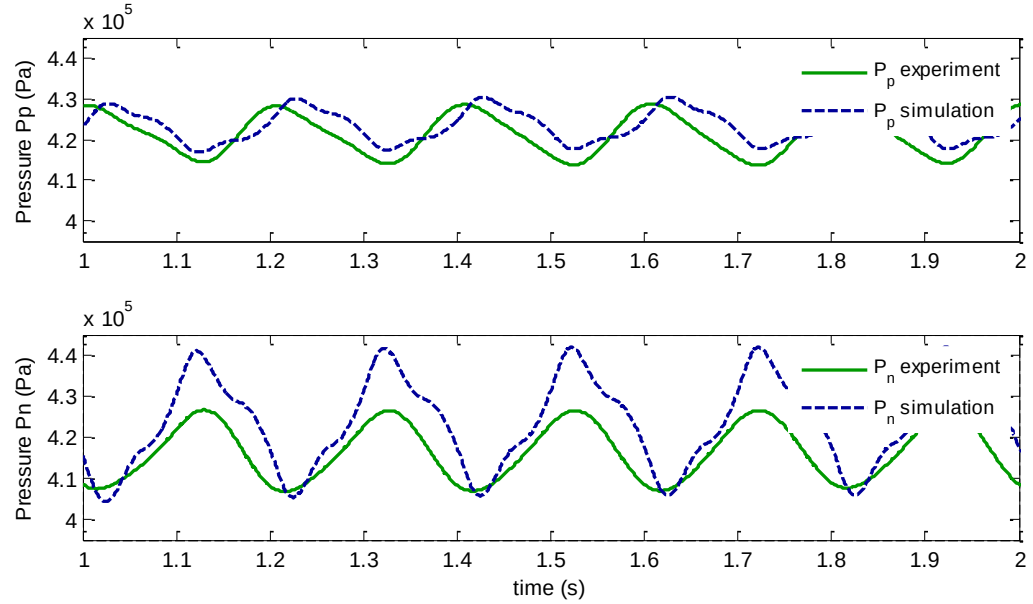

(b). Experimental and simulation pressure behavior

Fig. 5.4. 5 Hz sine wave

Finally, some quantitative descriptions (based on the RMS values) of Fig. 5.2 – Fig. 5.4 are provided in the following table. The results shows that experiment are in agreement with simulation, allowing to validate the theoretical models (5.1) and (5.2).

Frequency	Position tracking error		Error between simulation and experiment		
	Experiment	Simulation	Position y	Pressure P_p	Pressure P_n
0.1 Hz	2.8 %	2.2 %	0.5 %	1.2 %	1.1 %
1 Hz	10.2 %	8.3 %	2 %	4 %	3.3 %
5 Hz	95 %	93 %	2 %	6 %	30 %

TAB. 5.1. CLOSED-LOOP POSITION TRACKING PERFORMANCE VERSUS FREQUENCY

III. Bilateral Control Based Master-Slave Telemanipulator

The aim of this section is to describe a control strategy applied on the four-channel bilateral teleoperation architecture. For an easier design of the 4CH force/position controllers, a linearization of the pneumatic nonlinear system is carried out. An approximate linear model will be used to synthesize the control law implemented in the bilateral teleoperation system.

III.1. Tangent linear model of pneumatic actuator

This subsection is aimed at presenting an application of the tangent linear method to pneumatic actuator (Richard 1990). To do this, an equilibrium point of each actuator has firstly to be determined. A linear model is then obtained by linearizing the nonlinear system around the equilibrium state. Finally, a reduced tangent model is investigated for a simplification of the control analysis in the teleoperation scheme (cf. section III.2).

III.1.1. Equilibrium set

The nonlinear model (5.1) with a single input U is rewritten as following (Brun 1999)

$$\begin{cases} \dot{x} = f(x,U) \\ \dot{z} = h(x) \end{cases} \tag{5.3}$$

where x denotes the state vector defined as $x = (y,\ \dot{y},\ P_p,\ P_n)$ and z denotes the single output.

Considering the equilibrium set

$$\dot{x}^e = f(x^e, U^e) = 0 \tag{5.4}$$

we obtain the following condition

$$\left\{\dot{y}^e,\ \ddot{y}^e,\ \dot{P}_p^e,\ \dot{P}_n^e\right\} = \{0,0,0,0\} \tag{5.5}$$

Substituting (5.5) into (5.1) yields

$$\begin{cases} \dot{y}^e = 0 \\ S_p P_p^e - S_n P_n^e - F_{ext}^e = 0 \\ q_p(U^e, P_p^e) = 0 \\ q_n(-U^e, P_n^e) = 0 \end{cases} \tag{5.6}$$

We need to determine an equilibrium point $\left\{\dot{y}^e = 0,\ P_p^e,\ P_n^e, U^e\right\}$ that satisfied (5.6). The first equation of (5.6) is satisfied when the piston cylinder is locked or move slowly around the equilibrium point. The last two equations signify that the points defined by (U^e, P_p^e) and $(-U^e, P_n^e)$ belong to the experimental characteristics of pressure gain at a zero mass flow rate (see the dashed curve of Fig. 5.5 which is derived from Fig. 3.14 (b), chapter 3). This allows to deduce the force gain characteristics $F_{ext}(U)$, always at a zero flow, where $F_{ext} = S_p P_p - S_n P_n$ (see the solid curve of Fig. 5.5).

Since the pressure gain and the force gain characteristics are monotonic and strictly increasing, for any equilibrium position and for a given external force there is only one equilibrium point given by

$$\left\{y^e,\ \dot{y}^e = 0,\ P_p^e(F_{ext}^e),\ P_n^e(F_{ext}^e), U^e(F_{ext}^e)\right\} \tag{5.7}$$

The dimension of the equilibrium set is the same as the number of state variable of the system (5.1), which is a necessary condition to prove that the tangent linear model is a controllable system (Brun et al. 1999). The last three relationships of (5.6), which can be solved graphically by using Fig.

5.5, allow to obtain three unknown variables P_p^e, P_n^e, and U^e of (5.7) (Sesmat & Scavarda 1998). As illustrated in this figure, the procedure is as follow:

1. A fixed value of the equilibrium external force F_{ext}^e is chosen,
2. A value of the input control U^e at the equilibrium point is obtained thanks to the plot of force gain characteristics,
3. The opposite of U^e can be easily defined,
4. Knowing U^e, the curve of pressure gain enables to infer the value of equilibrium pressure at chamber p (denotes P_p^e),
5. Similarly, the $-U^e$ value allows to determine the equilibrium pressure at chamber n (denotes P_n^e).

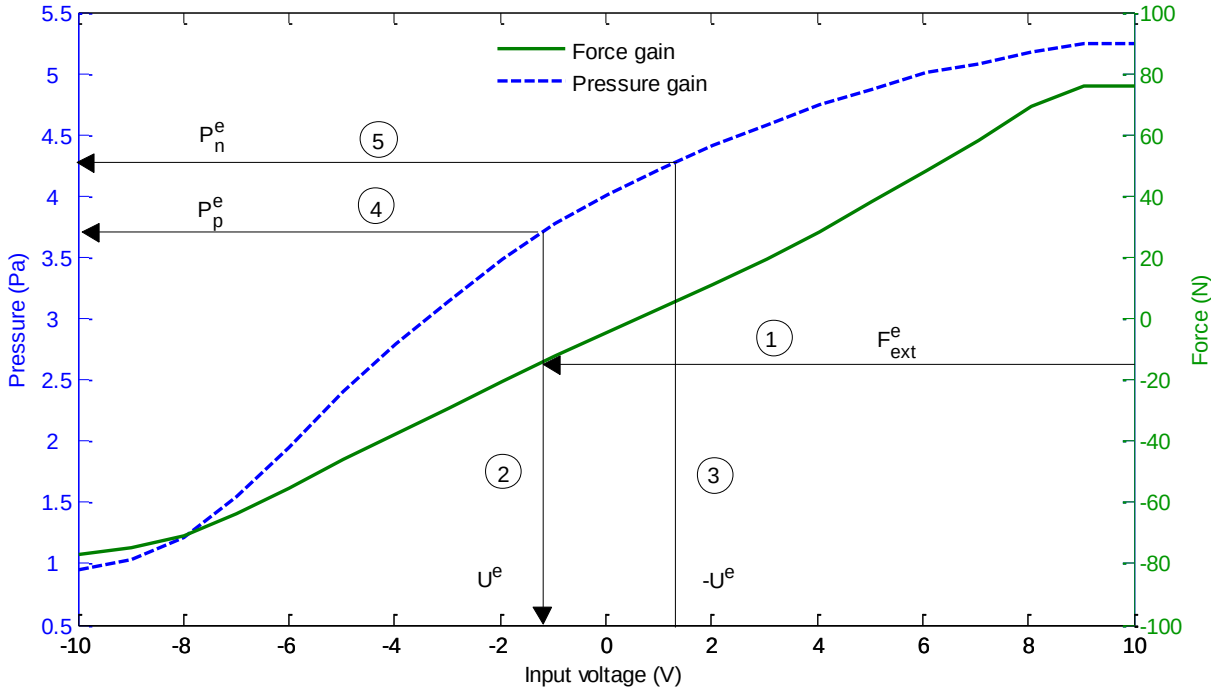

Fig. 5.5. Pressure gain and force gain characteristics at zero mass flow rate

In the teleoperation system, the external force F_{ext} is not fixed and it corresponds to the interaction force between the operator and the master (i.e., $F_h = -F_{ext}$) or the interaction force between the environment and the slave (i.e., $F_e = F_{ext}$). A high variation or high bandwidth of F_h and F_e signals could result in degraded performance of the tangent linear model. However, in our case, since the operator and the environment forces are excited at relatively low frequencies and low amplitude ($\leq$ 20N), a nonlinear pneumatic actuator could be locally approximated as the linear model. In the following, a study on the influence of the static external force to the variation of the equilibrium pressures and the equilibrium control input is carried out.

In our case, we assuming that the force exerted by the operator (or environment) on the master (or slave) manipulator does not exceed 20N. Considering the hand force $F_h = -F_{ext}$ and F_h is within the interval [0 20], the variation of P_p^e and U^e versus F_{ext}^e on the master side is shown in Fig. 5.6 (a). Similar profile on the slave side is illustrated in Fig. 5.6 (b) with $F_e = F_{ext}$. Note that the operating area of the master and slave devices are different due to an opposite sign of the external force applied to each manipulator. Indeed, the hand force F_h has the same direction of the master device's motion whereas the environment force F_e is defined as the contact force pushing on the slave device – opposite the direction of the actuator movement.

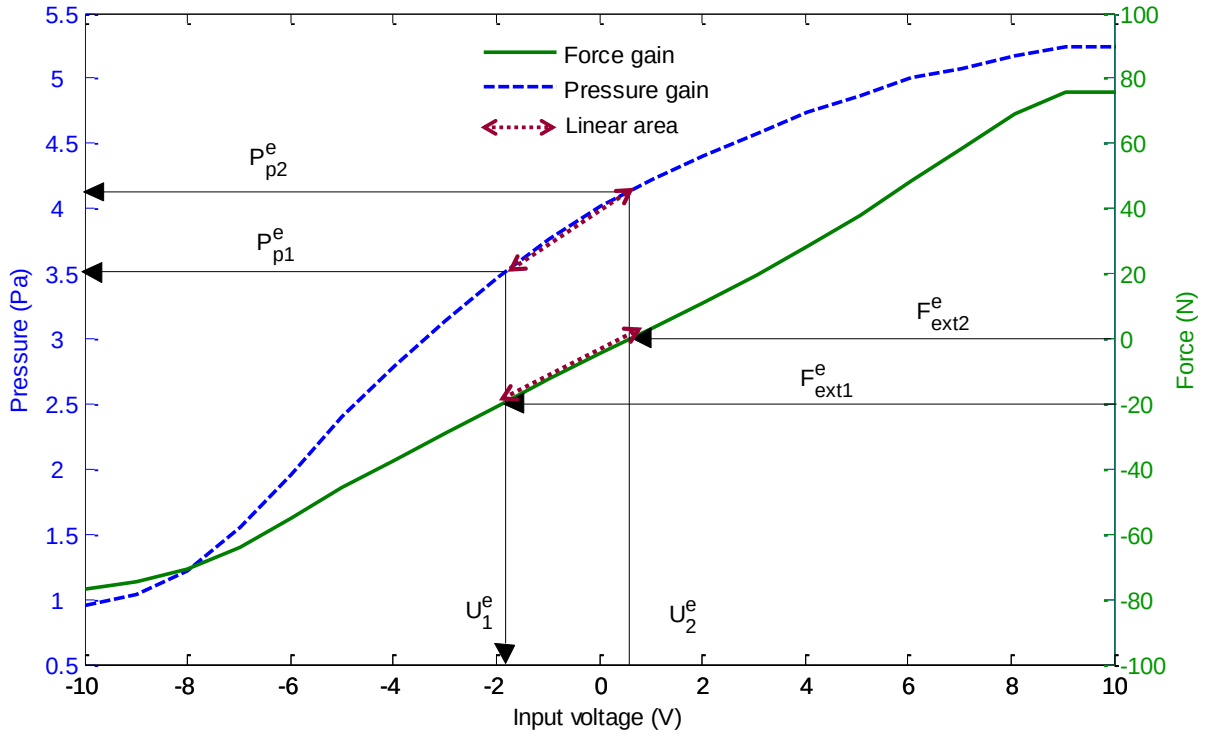

(a). Master side

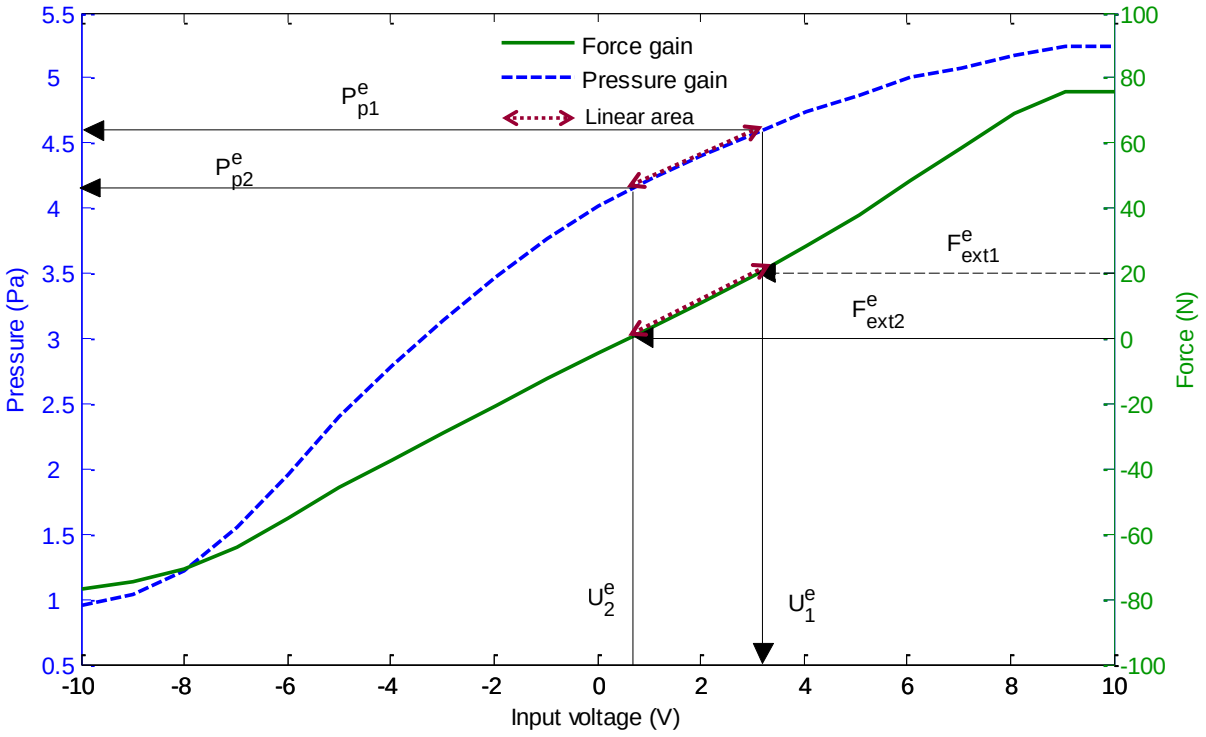

(b). Slave side

Fig. 5.6. Variation of U^e and $P_p{}^e$ versus external force F_{ext}

As it has been seen, the maximum variation of the pressure P_p^e and the input control U^e are less than 15% of their full scale, which is considered to be small enough to ensure that the operating area of the master and slave manipulators is linear (see the dotted curves). Similar result can be observed

for the pressure P_n^e. At the linear area, a slope of the force gain is proportional to that one of the pressure gain. Indeed, the linear relationship between the pressures and the input control lead to

$$P_p = \beta U + \varphi \quad , \quad P_n = -\beta U + \varphi \tag{5.8}$$

which yields

$$F_{ext} = S_p P_p - S_n P_n = (S_n + S_p)\beta U + \varphi(S_p - S_n) \tag{5.9}$$

If the cylinder is symmetric (i.e., $S_p = S_n$), $U^e = 0$ implies $F_{ext} = 0$ and inversely. However, in our case, even when $S_p = S_n$, the relationship $U^e = 0 \Leftrightarrow F_{ext}^e = 0$ is not always true (cf. Fig. 5.6). The fact is that in practice, experimental pressures P_p and P_n are not rigorously similar when the input control equals zero (cf. Fig. 3.14 (b), chapter 3). This effect is probably caused by the non-identical leakages between two orifices of the servovalves when the voltage $U = 0$. Another reason is due to the presence of friction in practice.

III.1.2. Linear model setup

By using the first order development of the Taylor's series around the equilibrium point (5.7), we obtain (Brun 1999)

$$\begin{cases} \dfrac{d\delta P_p}{dt} = \dfrac{\alpha r T_a}{V_p(y^e)}\left(\left.\dfrac{\partial q_p(U^e, P_p)}{\partial P_p}\right|_e \delta P_p + \left.\dfrac{\partial q_p(U, P_p^e)}{\partial U}\right|_e \delta U - \dfrac{P_p^e}{r T_a} S_p \delta \dot{y} \right) \\ \dfrac{d\delta P_n}{dt} = \dfrac{\alpha r T_a}{V_n(y^e)}\left(\left.\dfrac{\partial q_n(U^e, P_n)}{\partial P_n}\right|_e \delta P_n - \left.\dfrac{\partial q_n(-U, P_n^e)}{\partial U}\right|_e \delta U + \dfrac{P_n^e}{r T_a} S_n \delta \dot{y} \right) \\ \dfrac{d\delta \dot{y}}{dt} = \dfrac{S_p}{M}\delta P_p - \dfrac{S_n}{M}\delta P_n - \dfrac{b}{M}\delta \dot{y} \\ \dfrac{d\delta y}{dt} = \delta \dot{y} \end{cases} \tag{5.10}$$

with variation is near the equilibrium set

$$\left\{ \delta P_p = P_p - P_p^e \ , \ \delta P_n = P_n - P_n^e \ , \ \delta \dot{y} = \dot{y} - \dot{y}^e \ , \ \delta y = y - y^e \ , \ \delta U = U - U^e \right\} \tag{5.11}$$

The system of linear equation (5.10) can be rewritten in the matrix form as below

$$\frac{d}{dt}\begin{bmatrix} \delta P_p \\ \delta P_n \\ \delta \dot{y} \\ \delta y \end{bmatrix} = \begin{bmatrix} -\dfrac{1}{\tau_p} & 0 & -\dfrac{\alpha P_p^e S_p}{V_p(y^e)} & 0 \\ 0 & -\dfrac{1}{\tau_n} & \dfrac{\alpha P_n^e S_n}{V_n(y^e)} & 0 \\ \dfrac{S_p}{M} & -\dfrac{S_n}{M} & -\dfrac{b}{M} & 0 \\ 0 & 0 & 1 & 0 \end{bmatrix} \begin{bmatrix} \delta P_p \\ \delta P_n \\ \delta \dot{y} \\ \delta y \end{bmatrix} + \begin{bmatrix} \dfrac{\alpha r T_a}{V_p(y^e)} G_p^e \\ -\dfrac{\alpha r T_a}{V_n(y^e)} G_n^e \\ 0 \\ 0 \end{bmatrix} \delta U \tag{5.12}$$

where the time constants τ_p^e and τ_n^e are given by

$$\tau_p^e = \frac{V_p(y^e)}{\alpha r T_a K_p^e} \quad , \quad \tau_n^e = \frac{V_n(y^e)}{\alpha r T_a K_n^e} \tag{5.13}$$

and the sensibility coefficients of the mass flow rate with respect to the pressure (K_p^e and K_n^e) and the input control (G_p^e and G_n^e) are defined as

$$K_p^e = -\left.\frac{\partial q_p(U^e, P_p)}{\partial P_p}\right|_e \quad , \quad K_n^e = -\left.\frac{\partial q_n(-U^e, P_n)}{\partial P_n}\right|_e \quad , \quad G_p^e = \left.\frac{\partial q_p(U, P_p^e)}{\partial U}\right|_e \quad , \quad G_n^e = \left.\frac{\partial q_n(-U, P_n^e)}{\partial U}\right|_e \tag{5.14}$$

The above coefficients can be determined graphically by Fig. 5.7 which is deducted directly from Fig. 3.17 of chapter 3 (i.e., the mass flow rate characteristics in function of pressure and voltage control). Note that the sensibility coefficients (5.14) are defined so as to be all positive.

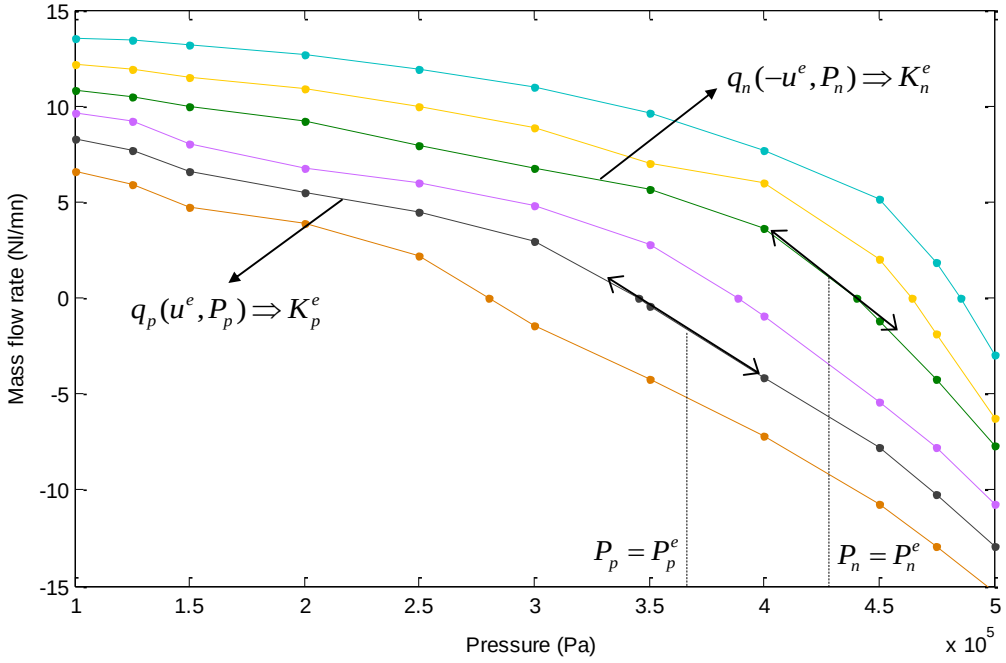

(a) Determination of K_p^e and K_n^e

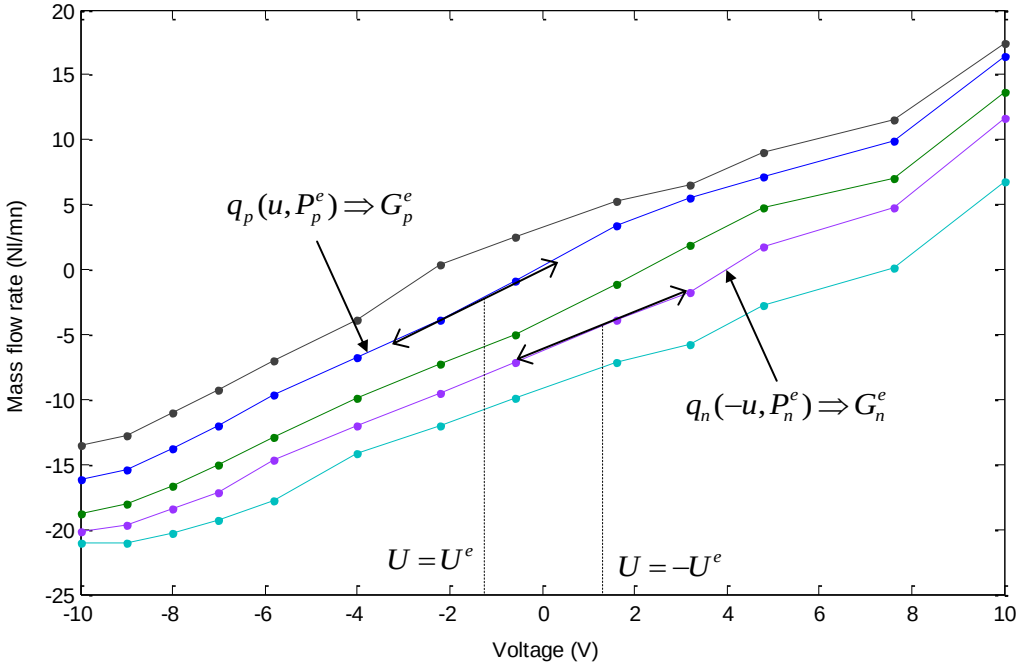

(b) Determination of G_p^e and G_n^e

Fig. 5.7. Mass flow rate characteristics

The model (5.12) can be put under the linear block diagram as shown in Fig. 5.8. The scheme consists of one *parallel structure* corresponding to the pressure's dynamics of the chambers and one *series structure* that allows to link the pneumatic and mechanical parts. Note that in Fig. 5.8 we do not take into account the servovalve dynamics since we consider that it is fast enough with respect to the mechanical dynamics of the pneumatic actuator.

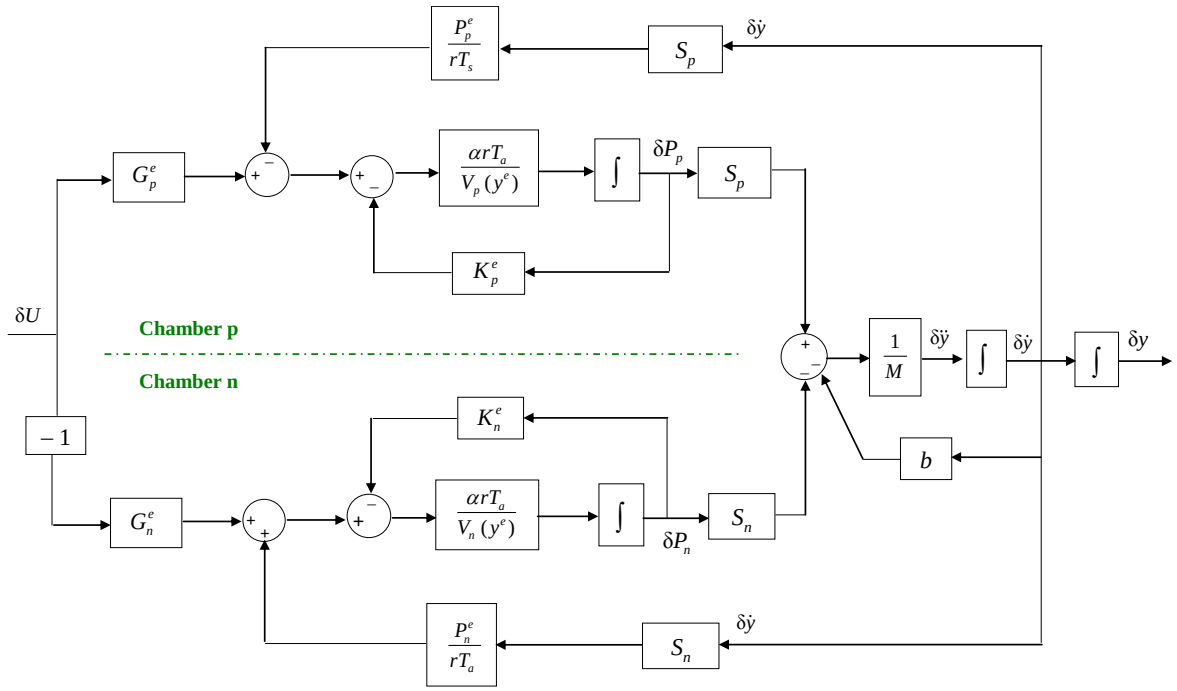

Fig. 5.8. Linear block scheme of 4th order system (5.10)

The following table depicts the characteristics of the master and the slave devices in two cases: when the slave is in free motion and when the slave is in contact with a stiff environment. In both cases the equilibrium position and force of the master and the slave need to be identical to ensure that the transparent teleoperation can be achieved.

Considering the equilibrium position and external force are respectively equal to 0.03 m and 0 N in free-motion case, as well as 0.06 m and 13 N (or – 13 N) in contact-motion case, all constant parameters of the master/slave linear model in Fig. 5.8 can be determined based on the coefficient values provided in Tab. 5.2.

As shown on Tab. 5.2, the constant parameters of the master and slave systems are identical in free motion. On the other hand, in contact motion, their characteristics are slightly different, as a consequence of the opposite sign of the operator's and environment's forces.

From the linear scheme of Fig. 5.8, it is possible to establish the 4th order transfer function between the input voltage and the output position. However, its literal expression is quite complex due to a considerable number of parameters. Therefore, in the following section, we introduce a reduced tangent model which is a simplified version of the 4th order model and we show that both of them have similar behaviors.

Parameter	Value (Free motion)		Value (Contact object)		Unit	Description
	Master	Slave	Master	Slave		
$F_{ext}^{\ e}$	0	0	– 13	13	N	Equilibrium external force
y^e	0.03	0.03	0.06	0.06	m	Equilibrium position
U^e	0.5	0.5	– 1.05	2.2	V	Equilibrium input voltage
$P_p^{\ e}$	$4.1\ 10^5$	$4.1\ 10^5$	$3.8\ 10^5$	$4.4\ 10^5$	Pa	Equilibrium pressure P_p
$P_n^{\ e}$	$3.9\ 10^5$	$3.9\ 10^5$	$4.2\ 10^5$	$3.6\ 10^5$	Pa	Equilibrium pressure P_n
$\tau_p^{\ e}$	0.052	0.052	0.092	0.085	s	Time constant of chamber p
$\tau_n^{\ e}$	0.066	0.066	0.032	0.041	s	Time constant of chamber n
$K_p^{\ e}$	$1.63\ 10^{-9}$	$1.63\ 10^{-9}$	$1.50\ 10^{-9}$	$1.63\ 10^{-9}$	$Kg.s^{-1}.Pa^{-1}$	Sensibility coefficients dq/dP
$K_n^{\ e}$	$1.72\ 10^{-9}$	$1.72\ 10^{-9}$	$1.88\ 10^{-9}$	$1.45\ 10^{-9}$	$Kg.s^{-1}.Pa^{-1}$	Sensibility coefficients dq/dP
$G_p^{\ e}$	$3.04\ 10^{-5}$	$3.04\ 10^{-5}$	$2.83\ 10^{-5}$	$2.89\ 10^{-5}$	$Kg.s^{-1}.V^{-1}$	Sensibility coefficients dq/dU
$G_n^{\ e}$	$2.92\ 10^{-5}$	$2.92\ 10^{-5}$	$3.15\ 10^{-5}$	$3.28\ 10^{-5}$	$Kg.s^{-1}.V^{-1}$	Sensibility coefficients dq/dU

TAB. 5.2. CHARACTERISTICS OF MASTER AND SLAVE DEVICES IN FREE MOTION AND IN CONTACT OBJECT

III.1.3. Reduced tangent linear model

In the case when the cylinder is symmetric (i.e. $S_p = S_n$) and in the absence of the external force (e.g. when the slave is in free motion), the equilibrium pressure of the chambers can be considered to be similar (cf. Tab. 5.2). This lead to an equality of the sensibility coefficients of the mass flow rate with respect to the pressure (i.e., $K_p^e = K_n^e$) and to the input control (i.e., $G_p^e = G_n^e$). As a result, the constants time τ_p^e and τ_n^e have the same value if the volumes of the chambers are supposed to be similar. By combining the state equations associated with the pressures, we can infer the acceleration's dynamics and obtain directly the reduced model of position, velocity and acceleration. According to (Brun et al. 1999), using the acceleration feedback instead of the pressure feedbacks or the differential pressure feedback can be justified by the fact that an external perturbation force quickly influences on the acceleration.

When the slave is in contact with the environment, the external forces exerted to the master and slave devices does not equal to zero. As a result, the characteristics of the chamber p and n are not identical, i.e. $P_p^e \neq P_n^e, K_p^e \neq K_n^e$, and $G_p^e \neq G_n^e$. Furthermore, since the volume chambers are not always assured to be equal, the time constants τ_p^e and τ_n^e can be found different (cf. Tab. 5.2). To obtain a third-order model with position, velocity and acceleration state variables, (Kellal et al. 1986) proposed to replace the time constant of each chamber by an average time constant τ_a^e (called *geometric mean*) as following

$$\frac{1}{\tau_a^e} = \frac{1}{2}\left(\frac{1}{\tau_p^e} + \frac{1}{\tau_n^e}\right) \tag{5.15}$$

Fig. 5.9 shows the evolution of the time constants τ_p^e, τ_n^e and their geometric inverse mean τ_a^e versus the master's and slave's positions in free motion and in contact motion. As it can be seen, different values between τ_p^e and τ_n^e are highlighted when the piston arrives to the extremity.

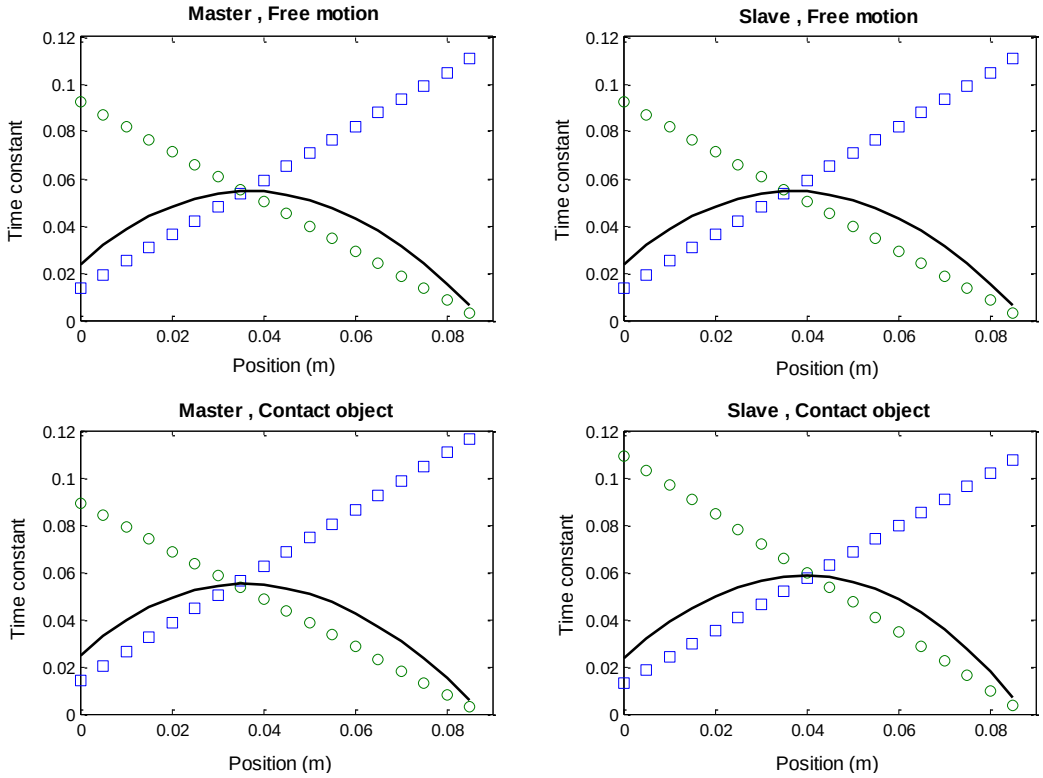

Fig. 5.9. Time constant versus position: τ_p (square), τ_n (circle), τ_a (solid).

Finally, the fourth-order model (5.12) can be simplified by the third-order model as

$$\frac{d}{dt}\begin{bmatrix}\delta y\\ \delta \dot{y}\\ \delta \ddot{y}\end{bmatrix}=\begin{bmatrix}0 & 1 & 0\\ 0 & 0 & 1\\ 0 & -\omega_{cyl}^2-\dfrac{b}{M\tau_a^e} & -\dfrac{1}{\tau_a^e}-\dfrac{b}{M}\end{bmatrix}\begin{bmatrix}\delta y\\ \delta \dot{y}\\ \delta \ddot{y}\end{bmatrix}+\begin{bmatrix}0\\ 0\\ \psi\end{bmatrix}\delta U \tag{5.16}$$

where ψ is the gain and ω_{cyl} is the angular frequency of the cylinder which are defined by

$$\psi=\frac{\alpha r T_a}{M}\left(\frac{S_p G_p^e}{V_p(y^e)}+\frac{S_n G_n^e}{V_n(y^e)}\right) \tag{5.17}$$

$$\omega_{cyl}=\sqrt{\frac{\alpha}{M}\left(\frac{S_p^2 P_p^e}{V_p(y^e)}+\frac{S_n^2 P_n^e}{V_n(y^e)}\right)} \tag{5.18}$$

Fig. 5.10 depicts the linear block diagram of the reduced model (5.16).

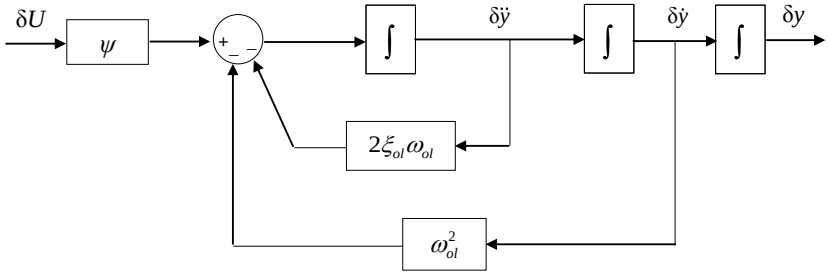

Fig. 5.10. Block scheme of reduced linear model (5.16)

In Fig. 5.10, the open-loop pulsation ω_{ol} is given by

$$\omega_{ol} = \sqrt{\omega_{cyl}^2 + \frac{b}{\tau_a^e M}} \tag{5.19}$$

where ω_{cyl} was defined in (5.18). Thus, the damping coefficient can be written as

$$\xi_{ol} = \frac{1}{2\omega_{ol}}\left(\frac{1}{\tau_a^e} + \frac{b}{M}\right) \tag{5.20}$$

Consequently, the third order transfer function $A(s)$ is established by

$$A(s) = \frac{Y(s)}{U(s)} = \frac{\psi}{s\left(s^2 + 2\xi_{ol}\omega_{ol}s + \omega_{ol}^2\right)} \tag{5.21}$$

The constant parameter's values of the reduced model (Fig. 5.10) is provided in the below table. Note that the open-loop pulsation ω_{ol} is relatively high since the moving mass and the volume chambers are small.

Parameter	Value (Free motion)		Value (Contact object)		Unit	Description
	Master	Slave	Master	Slave		
τ_a^e	0.058	0.058	0.047	0.055	s	Average time constant
ψ	560.5	560.5	667.4	691.2	$m.s^{-3}.V^{-1}$	Gain
ω_{ol}	143.5	143.5	155.8	150.6	$rad.s^{-1}$	Open-loop pulsation
ξ_{ol}	0.93	0.93	0.86	0.89		Damping coefficient

TAB. 5.3. CHARACTERISTICS OF MASTER AND SLAVE REDUCED MODEL

Fig. 5.11 illustrates the frequency responses of the 3rd-order and 4th-order models for the master and slave in free-motion and in contact-motion conditions. For all cases, the behaviors of these two models are perfectly similar, showing an excellent approximation of the reduced system (5.16). By using Matlab, we found that the 4th-order transfer function has four poles, and one zeros which is very close to one of the four poles. As a result, the 4th-order model can be simplified as the 3rd-order model.

Since the master and the slave manipulators are identical and since their variation of force and position between the contact–motion and free-motion modes are small enough, the frequency responses of the (reduced) tangent linear model can be considered to be similar for the four cases (see Fig. 5.11). It is therefore possible to utilize only one model where each parameter τ_a^e, ψ, ω_{ol}, and ξ_{ol} is calculated as an average value of the four values provided in Tab. 5.3. Setting $\tau_a^e = 0.055$ s, $\psi = 620$, $\omega_{ol} = 148$, and $\xi_{ol} = 0.9$ yields

$$A(s) = \frac{620}{s\left(s^2 + 268.2s + 22201\right)} \tag{5.22}$$

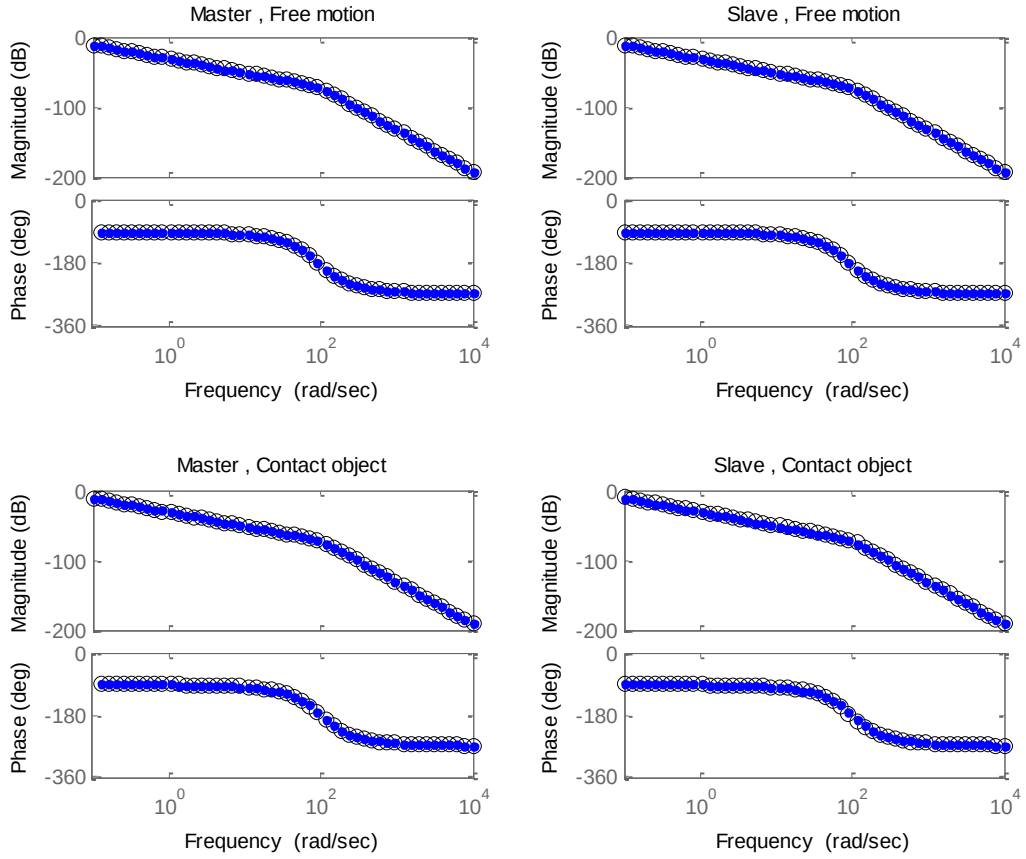

Fig. 5.11. Frequency analysis of the 3rd model (circle) and the 4th model (dotted)

III.2. 4CH teleoperation controller design

The 4CH master-slave teleoperation schemes are obtained with the pneumatic linear model (5.21), as illustrated in Fig. 5.12.

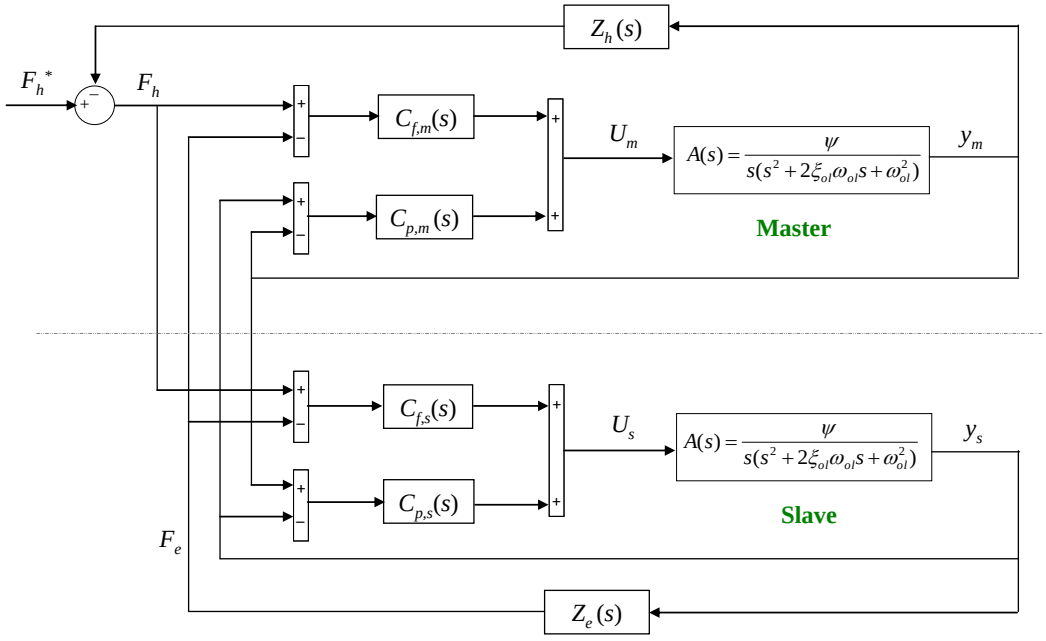

Fig. 5.12. 4CH bilateral teleoperation block diagram with pneumatic linear model

In free motion, since the operator and the environment forces equal zero (i.e., $F_e = F_h = 0$), the master-slave scheme can be simplified as shown on the following figure.

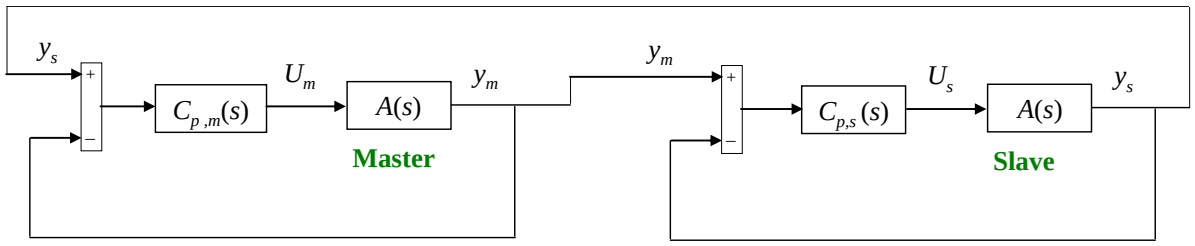

Fig. 5.13. Master and slave schemes in free motion

It has been seen in Fig. 5.13 that each of the master and the slave manipulators in free motion has the closed-loop transfer function

$$H_{y,i}(s) = \frac{A(s)C_{p,i}(s)}{1 + A(s)C_{p,i}(s)} \tag{5.23}$$

where i denotes m (master) or s (slave). For the sake of simplicity, the position controller $C_{p,i}$ of the master and the slave are chosen to be similar and they can be designed as a simple gain as following

$$C_{p,m} = C_{p,s} = K_p \tag{5.24}$$

Substituting (5.21) and (5.24) into (5.23) yields

$$H_{y,i}(s) = \frac{\psi K_p}{s^3 + 2\xi_{ol}\omega_{ol}s^2 + \omega_{ol}^2 s + \psi K_p} \tag{5.25}$$

The stability of the closed-loop transfer function $H_{y,i}$ is determined by its poles or simply the roots of the characteristic equation $D(s) = 0$ where D is the denominator of $H_{y,i}$. For stability, the real part of every pole must be negative. According to the Routh-Hurwitz criterion for the third-order polynomial, i.e., $D(s) = a_3s^3 + a_2s^2 + a_1s + a_0$, all the roots are in the left-half plane if all the coefficients satisfy

$$\begin{cases} a_i > 0, \quad 0 \le i \le 3 \\ a_1 a_2 > a_0 a_3 \end{cases} \tag{5.26}$$

The first relationship in (5.26) is verified since all parameters ω_{ol}, ξ_{ol}, ψ, and K_p are positive. The second relationship is equivalent to

$$2\xi_{ol}\omega_{ol}^3 > \psi K_p \tag{5.27}$$

Thus, a theoretical condition of the gain K_p in which the system is stable is

$$K_p < \frac{2\xi_{ol}\omega_{ol}^3}{\psi} = 9604 \tag{5.28}$$

In practice, the stability condition (5.28) is stricter, i.e. the maximum value of K_p is largely smaller than 4220. The position controller of the master and the slave is experimentally chosen equal to 600 in order to provide a smooth response without overshoot, i.e.,

$$C_{p,m} = C_{p,s} = 600 \tag{5.29}$$

In this case, the free-motion closed-loop transfer function of the master and the slave $H_{y,i}$ has one stable simple pole (i.e., – 222) and two stable imaginary poles (i.e., – 23 ± 40 j).

The force controller is chosen to be scalar as follows

$$C_{f,i}(s) = K_{f,i} \tag{5.30}$$

where $K_{f,m}$ and $K_{f,s}$ are proportional gain respectively equals to 0.5 and 0.1. These values are chosen in order to obtain the best trade-off between the tracking performance and the saturation problem of the control voltage U_m and U_s.

III.3. Experiment and discussions

III.3.1. Experimental setup

The experimental setup of the 1-DOF teleoperation system is similar to the one presented in chapter 4, section IV.1.4.1. The difference in this case is that two servovalves are employed for the control of mass flow rate in place of four solenoid valves. Experiments are conducted under a supply pressure of 520 kPa, which was used for the valve's characterizations (cf. chapter 3, section V.1.2). A photograph of the experimental setup is shown in Fig. 5.14.

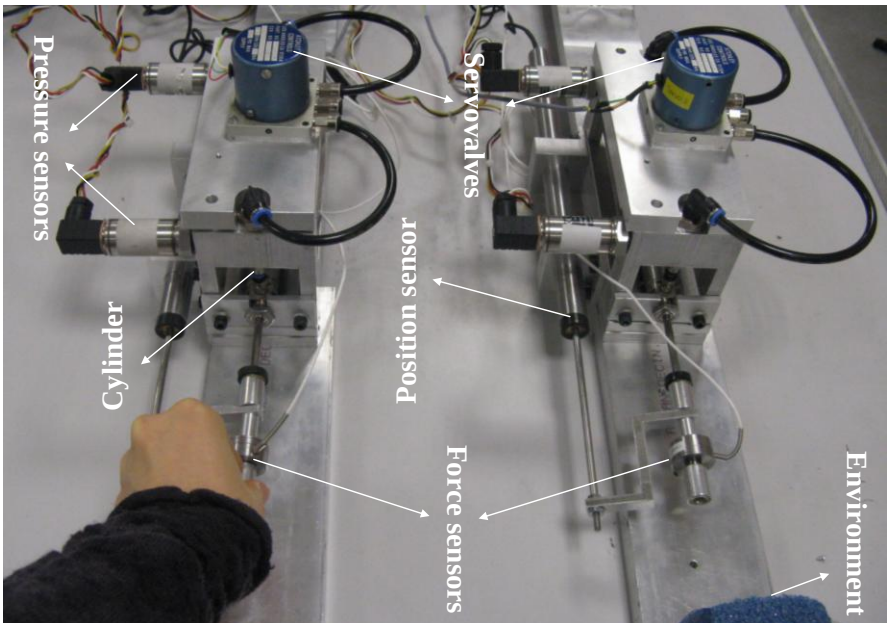

Fig. 5.14. Teleoperation experimental setup using electro-pneumatic servovalves

III.3.2. Experimental results

In this subsection, transparency and stability analyses of the closed-loop teleoperation system are carried out. The proposed linear controller design is experimentally tested on a single-degree-of-freedom pneumatic teleoperation system shown in Fig. 5.14.

III.3.2.1. Transparency analysis

III.3.2.1.1 Time domain

Fig. 5.15 shows the force and position tracking responses of the 4CH scheme experimentaly obtained, in which the controller parameters C_p and C_f are set as (5.29) and (5.30). It can be seen that the proposed control law ensures a good agreement between the operator and the environment forces under hard contact motion. Also, a good performance of the master and the slave positions in free motion is achieved.

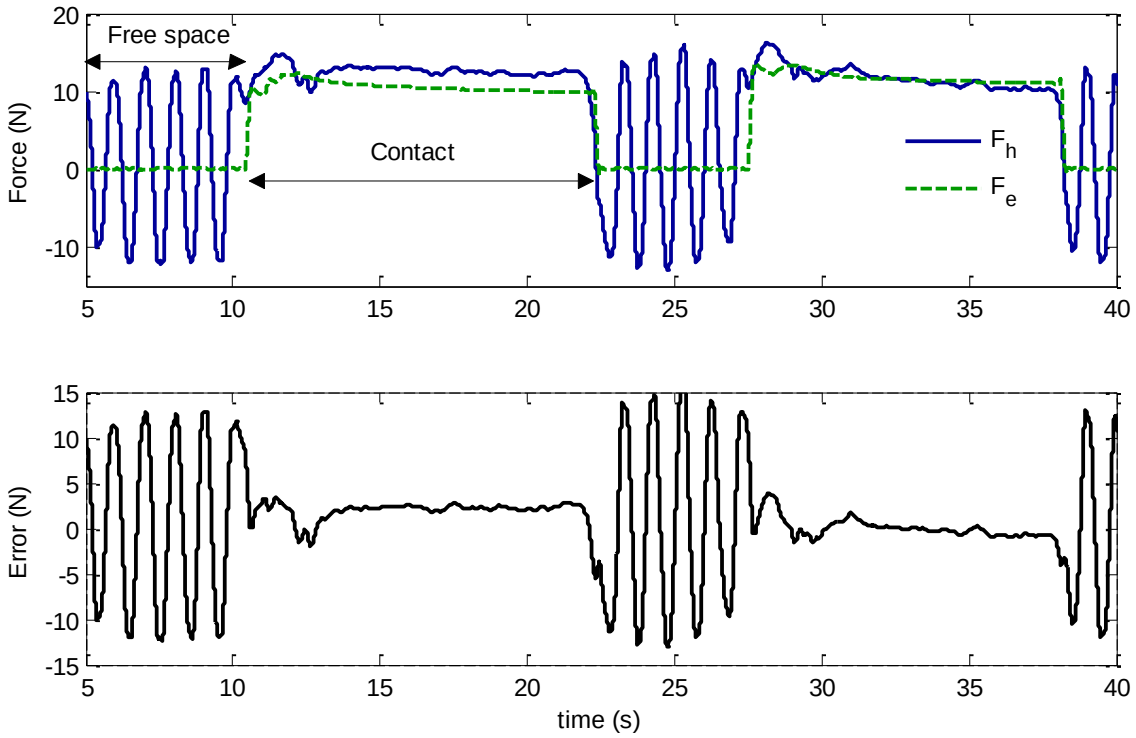

(a). Force tracking

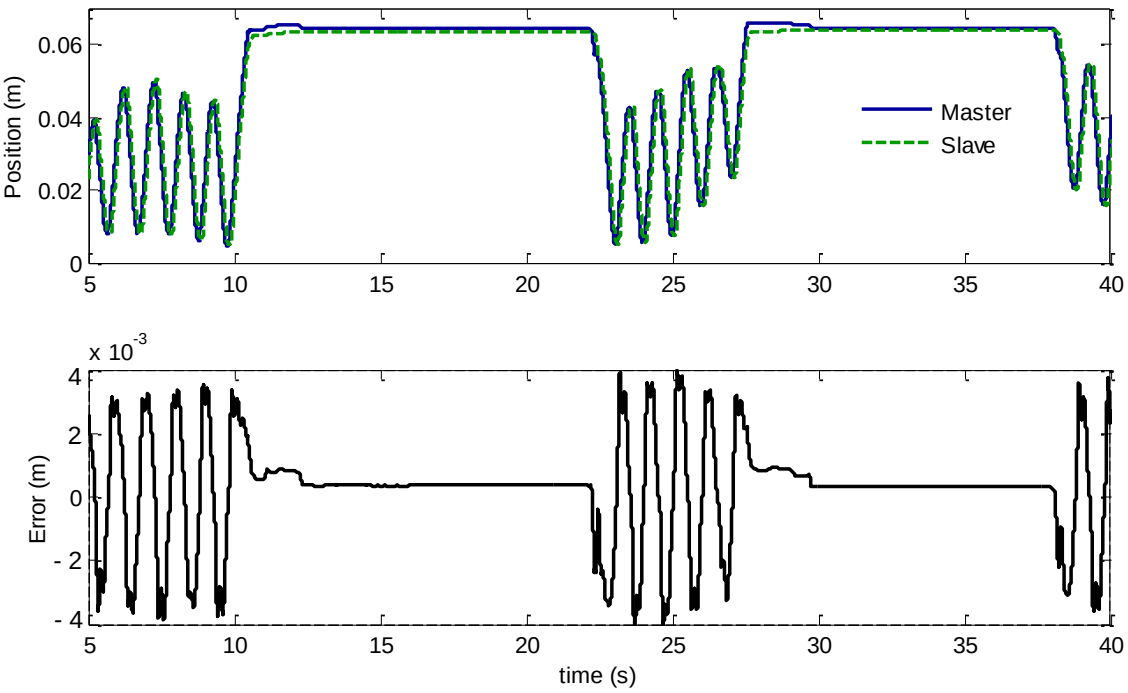

(b). Position tracking

Fig. 5.15. Transparency achieved with experimental 4CH teleoperation systems using servovalves

The nonzero values of F_h even when the slave is in free space, is due to the high leakage of the jet pipe technology employed in the servovalves. Indeed, both chambers of the cylinders are pressurized even when the voltage level is equal to zero (i.e., P_p = 410 kPa and P_n = 425 kPa when U = 0). It can be observed that the pressures P_p and P_n are found slightly different as a consequence of the non-identical leakages between the orifices p and n. This explains the fact that the operator may

feel a constraint force even when the slave is not in contact with the environment. As a result, he/she has to apply a higher force in order to overcome this constraint. This aspect can be seen in Fig. 5.16 where in free motion, the variations of the pressures of the master are more significantly than those at the slave.

As it has been seen, Fig. 5.15 shows a significant change in the force level when the slave robot makes contact with the environment (from free motion to contact motion). During contact motion, the slave's force increases to the level that cannot be overcome by the operator. This means that the operator did not make the slave manipulator apply increasingly higher forces on its environment once the operator's hand received force feedback. The fact that the position profiles remain constant during the contact mode is simply because under hard contact the slave cannot penetrate the environment regardless of the operator's force. The resulting position and force profiles for the master and the slave robots are consistent with those reported in similar papers in the teleoperation control research (Sirouspour et al. 2000; Hashtrudi-Zaad & Salcudean 2002; Lee & Li 2005).

Note that the position range of the master and the slave actuators is inside the interval [0.01, 0.05 m] in free motion, and around the 0.06 m level in contact motion. This allows to validate a choice of the equilibrium position provided in Tab. 5.2. Similar remarks can be observed for the force profile where the equilibrium state in free motion and in contact mode respectively varies around 0 N and 13 N.

Fig. 5.17 depicts the evolution of the voltage control signals U_m and U_s whose level in steady stead (contact mode) of the master and the slave respectively equal –1.1 V and 2.2 V. These experimental values are in agreement with the theoretical work presented in section III.1 (see Tab. 5.2). On the other hand, the experimental pressure levels at steady state for both master and slave actuators as illustrated in Fig. 5.16 are not consistent with those in Tab. 5.2. This is due to the inaccuracy of the pressure measurements since the pressure sensors can not be implemented inside the cylinder chambers (cf. section II.2).

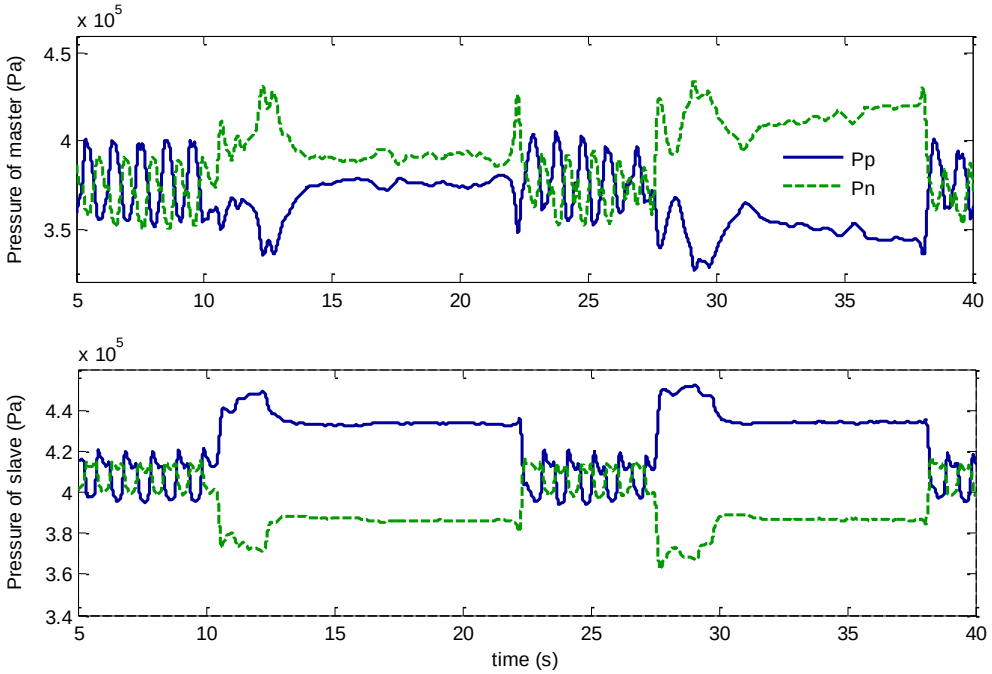

Fig. 5.16. Pressure versus time of the master and slave devices actuated by servovalves

In order to evaluate the servovalve's performance used in the pneumatic teleoperation systems, a comparison of it with the solenoid valve (chapter 4, section IV.2.3.1) is carried out. Among the different control laws based on the on/off valves, the hybrid approach is chosen as it is considered to be the most appropriate for achieving good transparent teleoperation under bilateral 4CH control (see Tab. 4.3, chapter 4). Tab. 5.4 shows the force and position tracking errors (RMS values) in both

contact motion and free motion. The results indicate that both fast switching on/off valves and proportional servovalves allow to obtain acceptable transparency (i.e., tracking error is less than 5 %). However, the motion and the force profiles of the master and slave actuators are smother when using the servovalves. This aspect can be observed on Fig. 5.16 and Fig. 5.18 where the pressures of the master and slave actuators in the servovalves are less oscillating than in the discrete on/off valves.

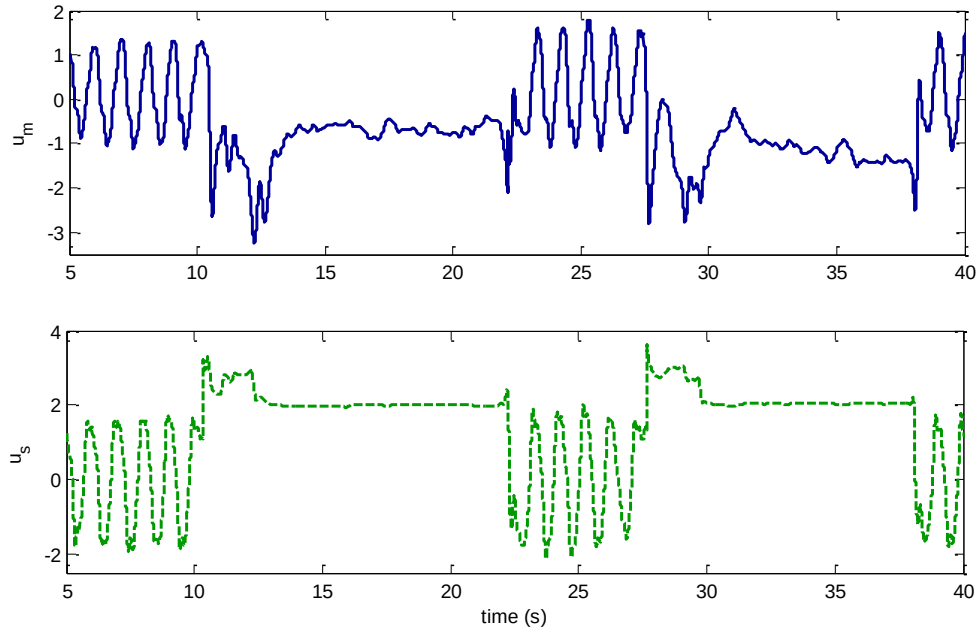

Fig. 5.17. Voltage control signals U_m and U_s

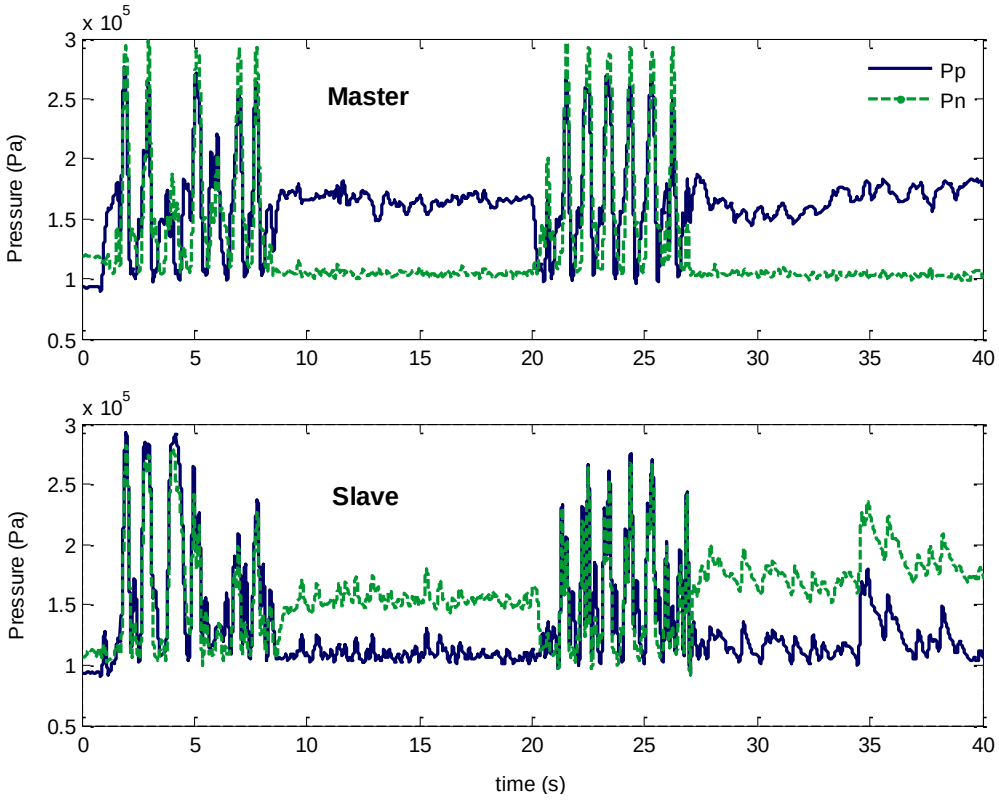

Fig. 5.18. Pressure versus time of the master and slave devices actuated by solenoid valves

To better evaluate the performance of the different valve's technologies, we also provide in Tab. 5.4 some human opinions about the perception quality through the master haptic interface. They all found that the teleoperation system with the servovalves lead to better sensation of contact force because no chattering and vibration are present as with the on/off valves. Another improvement of the servovalves is a significant reduction of the audible noise. It is interesting to note that in our case, performance in terms of tracking errors is better in the on/off valve case than in the servovalve case. Indeed, the servovalves with smaller mass follow rate capability produce some delays in the force and position responses, resulting in higher tracking error. This can be improved by choosing other servovalves with higher follow capability.

	Force (contact motion)	Position (free motion)	Position (contact motion)	Human opinions
On/off valves (4CH)	0.2 N (3.4 %)	1.1 mm (4.1 %)	0.4 mm (0.7 %)	• In free motion, operators feel a little chattering and vibration in motion. • In contact motion, interaction force between slave and environment is well reflected to the operator. However, chattering increases when level of operator's force increase. • Acoustic noise is undesirable.
Servovalves (4CH)	0.8 N (7.3 %)	2.5 mm (9.6 %)	0.5 mm (0.85 %)	• Chattering and undesirable acoustic noise significantly decrease. • Motion is smoother → no ripple neither oscillation in position signals. • In free motion, operators feel "sticky" forces (i.e. due to leakage of servovalve) again them and it makes them difficult to realise the movement. • In contact motion, better perception is obtained.

TAB. 5.4. PERFORMANCE COMPARISON BETWEEN ON/OFF VALVES AND SERVOVALVES

III.3.2.1.2 Frequency domain

To further investigate the teleoperation system transparency based on the four-channel architecture, a frequency analysis of the H-matrix parameters in terms of amplitude and phase-shift is carried out. The free motion and hard contact tests' data in Fig. 5.15 allow to fully identify the teleoperation system's H-matrix elements (h_{11}, h_{12}, h_{21}, h_{22}) as following

1. The transfer functions h_{11} and h_{21} can be determined, according to $h_{11} = F_h / Y_m\big|_{F_e=0}$ and $h_{21} = -Y_s / Y_m\big|_{F_e=0}$, via free-motion test data (F_e = 0).
2. The transfer functions h_{12} and h_{22} ($h_{12} = F_h / F_e\big|_{Y_m=0}$ and $h_{22} = -Y_s / F_e\big|_{Y_m=0}$) may be obtained while the master robot is locked (i.e., y_m = 0) and a force is applied onto the slave end-effector. However, it is difficult to guarantee that the master robot does not move when the measurement of F_h is obtained. Therefore, it is preferable to use the constraint y_s = 0 instead of y_m = 0; in practice, achieving y_s = 0 is easy since it is merely making the slave robot contact a hard surface (Aliaga et al. 2004). Consequently, while h_{11} and h_{21} are found from free-motion experiments, h_{12} and h_{22} can be obtained by using the contact-mode test data and the relationships $F_h / F_e - h_{11} Y_m / F_e$ and $-Y_s / F_e - h_{21} Y_m / F_e$.

The transparency analysis in frequency domain obtained with the tangent linear control is shown in Fig. 5.19. According to chapter 2, section II.6, perfect transparency is achieved if and only if the H-matrix has the following form:

$$H_{\text{ideal}} = \begin{bmatrix} 0 & 1 \\ -1 & 0 \end{bmatrix} \tag{5.31}$$

As it can be observed in Fig. 5.19 (a), the magnitude of $|h_{21}|$ and $|h_{12}|$ spectra are close to 0dB, showing excellent tracking in terms of force and position for a wide bandwidth up to 100 rad/s. As expected from (5.31), low values of the output admittance (h_{22}) show that the slave's movement in response to external force disturbances quickly converges to zero when the master is locked in motion. With regard to h_{11}, due to the mass of the handle between the force sensor and the operator's hand as well as the leakages of the jet pipe servovalves, the input impedance $h_{11} = F_h / X_m$ is identified less accurately than the other parameters, especially over high frequencies.

Fig. 5.19 (b) depicts the phase-shift analysis of the H-parameters, which is an alternative of the amplitude analysis illustrated in Fig. 5.19 (a).

It has been seen that the phase-shift level of the four H-matrix elements is close to zero over low frequencies, resulting in a non-delay position and force tracking between the master and the slave. On the other hand, over high bandwidth, the phase-shift is slightly increased. This effect is in agreement with the results provided in Tab. 5.1, where the delay of the position responses is increased in function of the excited frequency.

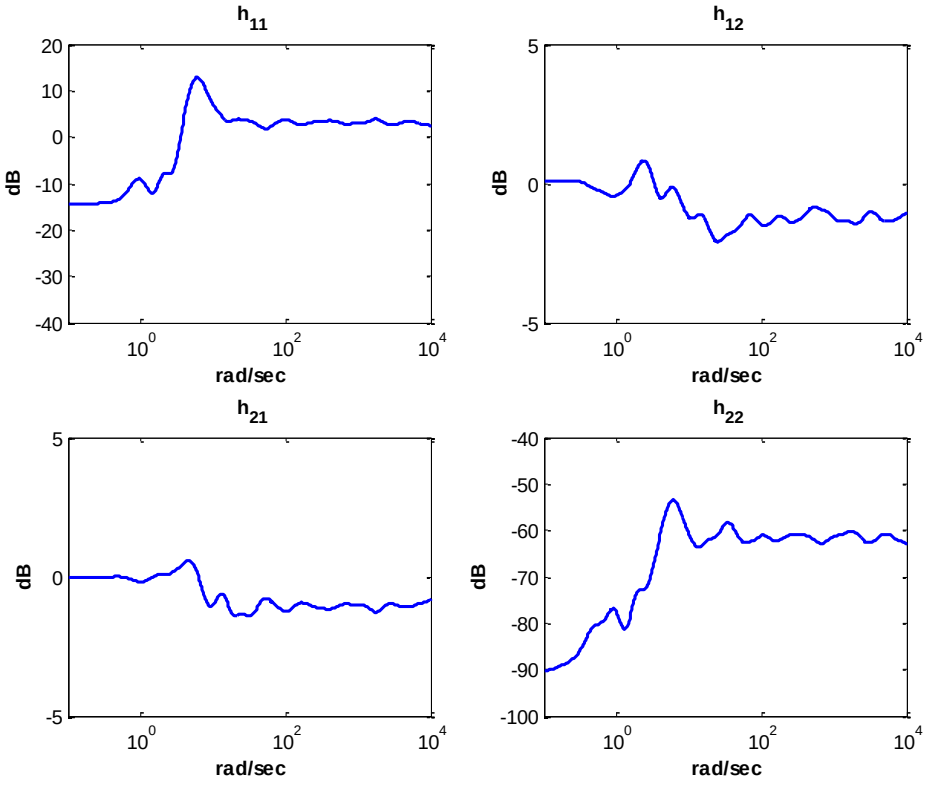

(a). Amplitude

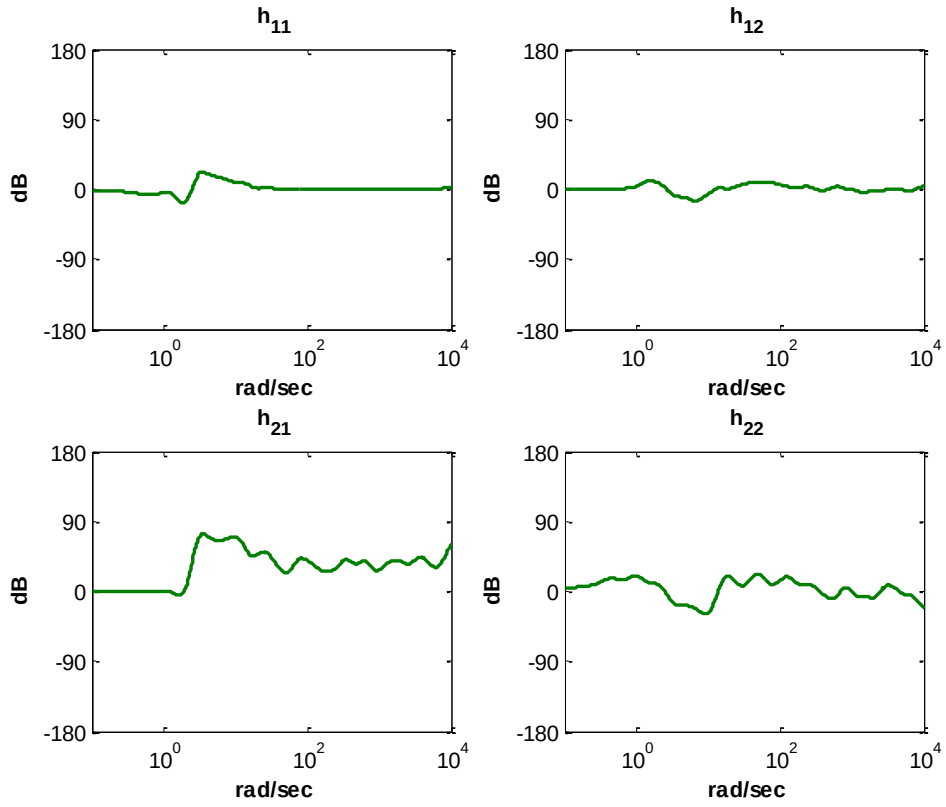

(b). Phase-shift

Fig. 5.19. Frequency analysis of the H-parameters

III.3.2.2. Stability analysis

The necessary and sufficient condition for the absolute stability of the 4CH teleoperation system of Fig. 5.12 under ideal transparency is that all following conditions of the Llewellyn criterion (see chapter 2, section V.2) are fully met.

6. $h'_{11}(s)$ and $h'_{22}(s)$ have no poles in the right half plane;
7. Any poles of $h'_{11}(s)$ and $h'_{22}(s)$ on the imaginary axis are simple with real and positive residue;
8. For $s = j\omega$ and all real values of ω

$$\begin{aligned} &\Re(h'_{11}) \geq 0 \\ &\Re(h'_{22}) \geq 0 \\ &\eta = -\cos\left(\arg(h_{12}h_{21})\right) + 2\frac{\Re(h'_{11})\Re(h'_{22})}{|h_{12}h_{21}|} \quad , \quad \eta \geq 1 \end{aligned} \tag{5.32}$$

where $\Re(.)$ and $|\ .\ |$ are respectively the real and the absolute values, and $h'_{11}(s)$ and $h'_{22}(s)$ are normalized as

$$h'_{11} = h_{11}/s \quad , \quad h'_{22} = h_{22}s$$

Since in our case, the two-port network is feed by the position signals and not the velocity signals, the elements $h'_{11}(s)$ and $h'_{22}(s)$ are used instead of $h_{11}(s)$ and $h_{22}(s)$ as shown in the Llewellyn criterion.

Considering the relationship of the controllers established in chapter 4 section IV.2.1

$$C_1 = C_s = C_p \quad , \quad C_4 = -C_m = -C_p \quad , \quad C_6 + 1 = C_2 = C_f \quad , \quad C_5 + 1 = C_3 = C_f \tag{5.33}$$

and the expressions of the H-matrix parameters in chapter 2 (section III.1, equation (2.10))

$$h_{11} = \left(Z_{ts}Z_{tm} + C_1C_4\right)/D \quad , \quad h_{12} = \left(Z_{ts}C_2 - (1+C_5)C_4\right)/D$$
$$h_{21} = -\left(Z_{tm}C_3 + (1+C_6)C_1\right)/D \quad , \quad h_{22} = -\left(C_2C_3 - (1+C_5)(1+C_6)\right)/D$$

where $Z_{ts} = Z_s + C_s$, $Z_{tm} = Z_m + C_m$, and $D = -C_3C_4 + Z_{ts}(1 + C_6)$ with $D \neq 0$.
The equations of the H-matrix elements can be simplified to

$$h_{11} = Z/C_f \ , \ h_{12} = 1 \ , \ h_{21} = -1 \ , \ h_{22} = 0 \tag{5.34}$$

where $Z = Z_s = Z_m = Ms^2 + bs$ and C_f is a scalar. As a result, we have

$$h'_{11} = (Ms + b)/C_f \ , \ h_{12} = 1 \ , \ h_{21} = -1 \ , \ h'_{22} = 0 \tag{5.35}$$

From (5.35), it can be easily demonstrated that all Llewellyn conditions are satisfied. As a result, the 4CH teleoperation system is absolutely stable.

It is interesting to notice that when ideal transparency is achieved (5.33), the equality of the three last equations in (5.32) occurs. This means that the perfectly transparent system is marginally absolutely stable. As a result, to have a higher stability robustness, perfect transparency has to be compromised. This is one of illustrations of the classical trade-off between stability and performance. Another explanation is that, in bilateral teleoperation, it has been proved that a profitable manner for increasing system transparency is to reflect back to the operator information about the force applied to the environment. On the other hand, it results that the force reflection gain, i.e. the gain which gives the operator the feeling of the interaction, may destabilize the systems (Melchiorri 2003). As a matter of fact, in traditional force reflection teleoperation, where force reflection is obtained by a direct feedback of the measured force signal, in order to have stability the force reflection, this gain should be maintained relatively low. This is, however, often not sufficient for a significant force feedback, which results in degraded transparent teleoperation.

The third expression of the Llewellyn criterion can be verified by using the experimental data as shown in Fig. 5.20. Good results have been achieved within a bandwidth up to 10^4 rad/s.

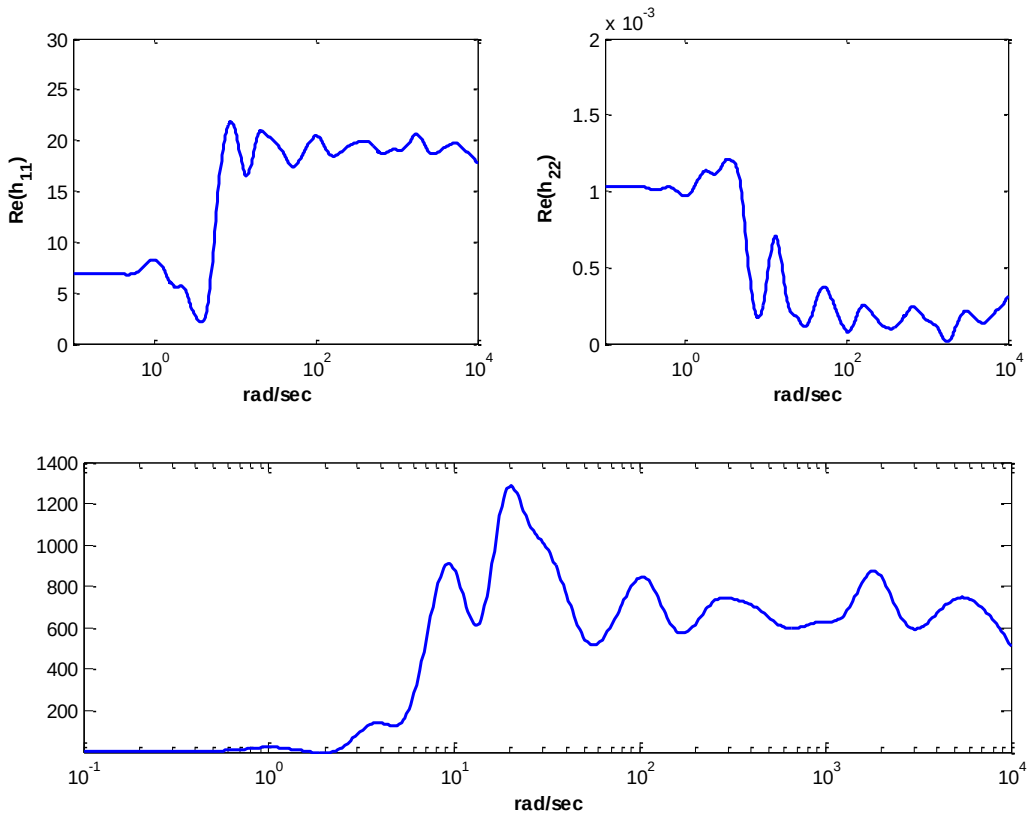

Fig. 5.20. Stability analysis of the linear teleoperation system based on Llewellyn's criterion.

IV. Bilateral Control Based on Force Observer

It is well-known that haptic teleoperation systems exploit information regarding the external forces (Lawrence 1993; Yokokohji & Yoshikawa 1994; Hokayem & Spong 2006). For instance, implementation of transparent bilateral teleoperation controllers require operator and environment contact forces to be measured and transmitted to slave and master manipulators, respectively. In some teleoperation applications, when force sensors are expensive, cumbersome and susceptible to overload, *hand observer* (HOB) as well as *environment observer* (EOB) becomes a good alternative for force estimation. Nonetheless, as mentioned in chapter 3, section IV.2, a main drawback of the force observers is that they are generally designed based on the exact knowledge of the master-slave dynamics and kinematics, which are sometimes difficult to determine.

Generally, in the HOB and EOB schemes, operator/master and slave/environment contact forces are dynamically observed by using position and velocity information as well as torque/force control signals. (Huang & Tzeng 1989) proposed a stable observable model-based state to estimate the contact force in a force control scheme. (Lee et al. 1993) employed a joint torque disturbance observer, knowing robot dynamics model parameters, to estimate the external reaction force and to achieve high accuracy in robot trajectory tracking. (Hacksel & Salcudean 1994) proposed a simplified dynamics state observer to predict contact forces with an accurate dynamics model as well as joint measured angles and applied actuator torques. Although robot dynamic equations were required, (Eom et al. 1998) assumed that precise knowledge of the manipulator or haptic interface model is difficult to identify. Therefore, they proposed a steepest descent optimization method that adjusts inaccurate dynamic parameters to improve force estimation performance.

In this section, we deal with the problem of bilateral teleoperation in force-sensor-less device setups. To do this, we develop and implement in the four-channel bilateral teleoperation system an algorithm for force estimation, which is based on the linear Nicosia's observer (Nicosia & Tomei 1990). Such kind of observer has been chosen due to its simplified implementation where no velocity measurements are required. Finally, discussion on the transparency in terms of position and force tracking of the entire closed-loop haptic teleoperation system is carried out.

IV.1. Implementation of the HOB and EOB schemes

Before developing the observers, an observability analysis of the pneumatic system needs to be investigated. For more details, the reader can refer to (Richard 1990).

Since the master and slave devices respectively interact with the operator and environment, their dynamics dependent on the external forces f_h and f_e as given by following

$$\begin{aligned} M\ddot{y}_m &= S_p P_{p,m} - S_n P_{n,m} - b\dot{y}_m + f_h \\ M\ddot{y}_s &= S_p P_{p,s} - S_n P_{n,s} - b\dot{y}_s - f_e \end{aligned} \tag{5.36}$$

Choosing the state variables $x_{1m} = y_m$ and $x_{2m} = \dot{y}_m$ for the master controller, and $x_{1s} = y_s$ and $x_{2s} = \dot{y}_s$ for the slave controller, we have

$$\begin{cases} \dot{x}_{1m} = x_{2m} \\ \dot{x}_{2m} = M^{-1}(f_{m\Delta P} + f_h - bx_{2m}) \end{cases} \tag{5.37}$$

$$\begin{cases} \dot{x}_{1s} = x_{2s} \\ \dot{x}_{2s} = M^{-1}(f_{s\Delta P} - f_e - bx_{2s}) \end{cases} \tag{5.38}$$

where $f_{m\Delta P} = S_p P_{p,m} - S_n P_{n,m}$ and $f_{s\Delta P} = S_p P_{p,s} - S_n P_{n,s}$.

An estimation of the hand force f_h (HOB) based on the Nicosia's observer can be achieved as following

$$\text{(HOB):}\quad \begin{cases} \dot{\hat{x}}_{1m} = \hat{x}_{2m} + k_{2m} e_m \\ \dot{\hat{x}}_{2m} = M^{-1}(f_{m\Delta P} + k_{1m} e_m - b x_{2m}) \\ e_m = x_{1m} - \hat{x}_{1m} \end{cases} \tag{5.39}$$

where k_{1m} and k_{2m} are positive constant.
Similarly, the controller for environment-force estimation (EOB) should be written as

$$\text{(EOB):}\quad \begin{cases} \dot{\hat{x}}_{1s} = \hat{x}_{2s} + k_{2s} e_s \\ \dot{\hat{x}}_{2s} = M^{-1}(f_{s\Delta P} - k_{1s} e_s - b x_{2s}) \\ e_s = x_{1s} - \hat{x}_{1s} \end{cases} \tag{5.40}$$

where k_{1s} and k_{2s} are positive constant.

From the second derivative of the third expression in (5.39), we obtain

$$\ddot{e}_m = \ddot{x}_{1m} - \ddot{\hat{x}}_{1m} \tag{5.41}$$

Substituting (5.37) and (5.39) into (5.41) yields

$$\begin{aligned} \ddot{e}_m &= \dot{x}_{2m} - \dot{\hat{x}}_{2m} - k_{2m}\dot{e}_m \\ &= M^{-1}(f_{m\Delta P} + f_h - b x_{2m}) - M^{-1}(f_{m\Delta P} + k_{1m} e_m - b x_{2m}) - k_{2m}\dot{e}_m \\ &= M^{-1} f_h - M^{-1} k_{1m} e_m - k_{2m}\dot{e}_m \end{aligned} \tag{5.42}$$

It can be shown that the hand observer is asymptotically stable and its second-order error equation is

$$M\ddot{e}_m + M k_{2m}\dot{e}_m + k_{1m} e_m = f_h \tag{5.43}$$

In the same way, from (5.38) and (5.40), a relationship between the environment force f_e and the motion of the slave manipulator can be given by

$$M\ddot{e}_s + M k_{2s}\dot{e}_s + k_{1s} e_s = -f_e \tag{5.44}$$

In steady state (e.g., in a hard contact), $\ddot{e}_m = \dot{e}_m = 0$ and $\ddot{e}_s = \dot{e}_s = 0$. Therefore, the hand force and the environment force are respectively estimated at low frequencies as

$$\bar{f}_h = k_{1m} e_m \tag{5.45}$$

$$\bar{f}_e = k_{1s} e_s \tag{5.46}$$

Generally, the gains k_{1m} and k_{1s} are usually chosen relatively high in order to improve the force-estimation performance. This technique is called *high gain linear observer* and was proposed by (Nicosia et al. 1990). When k_{1m} and k_{1s} are high enough, the velocity terms bx_{2m} and bx_{2s} of the second expressions in (5.39) and (5.40) may be negligible compared to the observed forces $k_{1m}e_m$ and $k_{1s}e_s$. As a result, the controllers HOB and EOB can be simplified as

$$\text{(HOB):}\quad \begin{cases} \dot{\hat{x}}_{1m} = \hat{x}_{2m} + k_{2m} e_m \\ \dot{\hat{x}}_{2m} = M^{-1}(f_{m\Delta P} - k_{1m} e_m) \\ e_m = x_{1m} - \hat{x}_{1m} \end{cases} \tag{5.47}$$

$$\text{(EOB):}\quad \begin{cases} \dot{\hat{x}}_{1s} = \hat{x}_{2s} + k_{2s} e_s \\ \dot{\hat{x}}_{2s} = M^{-1}(f_{s\Delta P} - k_{1s} e_s) \\ e_s = x_{1s} - \hat{x}_{1s} \end{cases} \tag{5.48}$$

This allows to remove the velocity measurements and therefore, only position and pressure information are required to design the observers (5.47) and (5.48) (see Fig. 5.21).

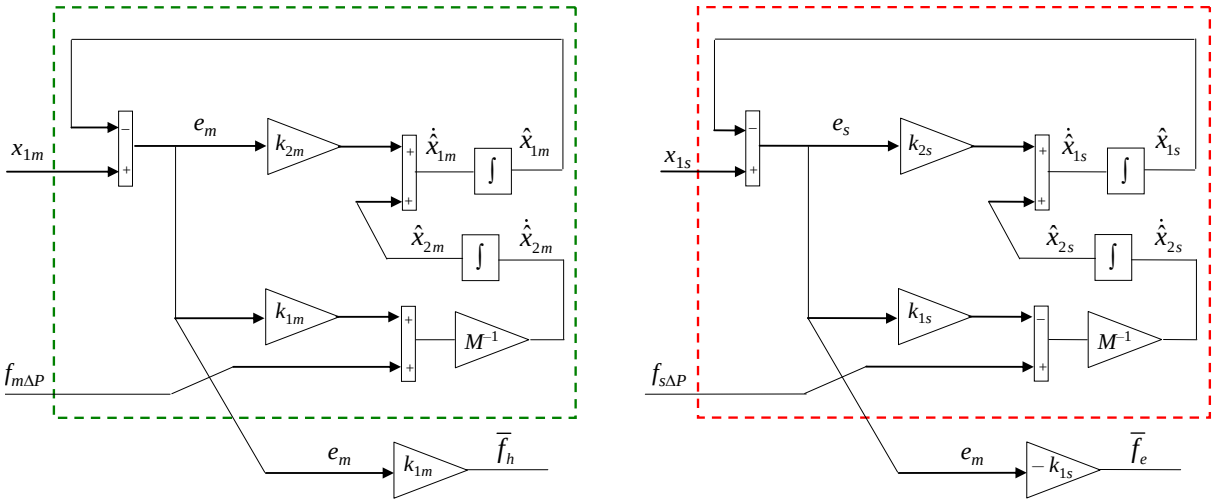

(a). Observer HOB (5.47) (b). Observer EOB (5.48)

Fig. 5.21. HOB and EOB schemes based on the Nicosia's observer

The implementation of the observers HOB and EOB in the 4CH teleoperation architecture of Fig. 5.12 is illustrated in Fig. 5.22. The "bilateral control" block depicted in Fig. 5.22 consists of the position and the force controller parameters (i.e., $C_{p,i}$ and $C_{f,i}$) whose expression can be found in (5.29) and (5.30), respectively.

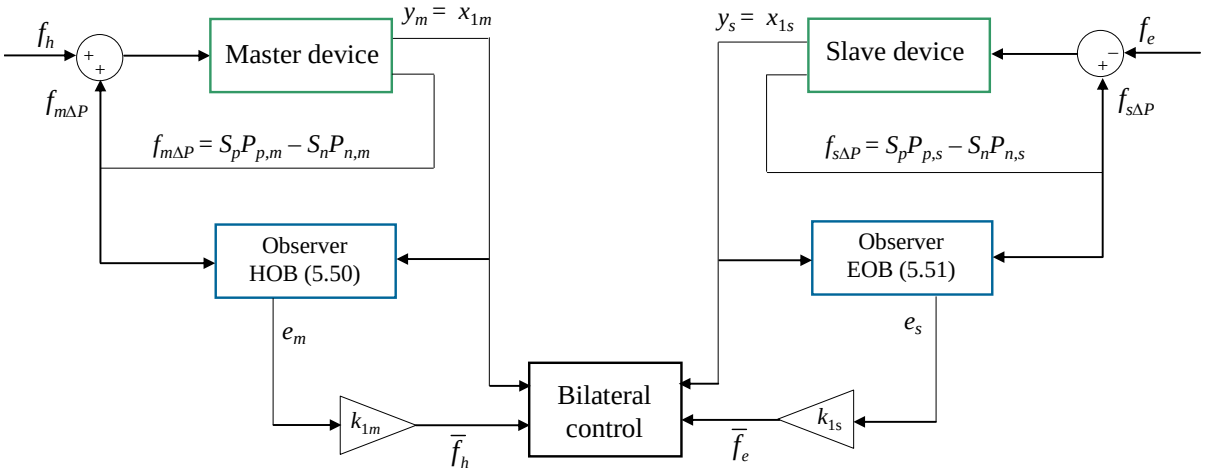

Fig. 5.22. Observer for estimating externally applied forces of teleoperation system

Using the observer's error dynamics (5.43) and (5.44), the gains k_{1m}, $k_{2m} = 2\sqrt{k_{1m}/M}$, k_{1s}, and $k_{2s} = 2\sqrt{k_{1s}/M}$ are empirically chosen such as the master and slave observers have very fast critically damped poles at (– 2000, – 2000) and (– 300, – 300), respectively. It is noteworthy that the controller gains of the HOB are not similar to that ones of the EOB due to the difference of the hand's dynamics

and environment's dynamics. Consequently, the value of the controller gains are shown as on the below table.

k_{1m}	k_{2m}	k_{1s}	k_{2s}
$8\ 10^5$	$4\ 10^3$	$18\ 10^3$	$6\ 10^2$

TAB. 5.5. VALUE OF GAINS

IV.2. Experiment results

The experimental setup of this test bed is similar to the one presented in section III.3.1. The only difference in this case is that observers are used in place of force sensors for an estimation of the hand force f_h and the environment force f_e. The force sensors are still, however, mounted at the master's and slave's end-effectors in order to compare the actual force measurements and the observed forces.

Fig. 5.23 depicts the master and the slave force and position tracking profiles in free space and in contact motion for the 4CH teleoperation system. Note that the force signals of Fig. 5.23 (b) are built from the observers HOB and EOB of Fig. 5.21. As it can be seen, good position and force matching at the master and slave sides ensure that the operator accurately feels the slave/environment interaction. Such a good transparency was made possible thanks to the choice of the controller performance C_p and C_f in the four-channel bilateral teleoperation.

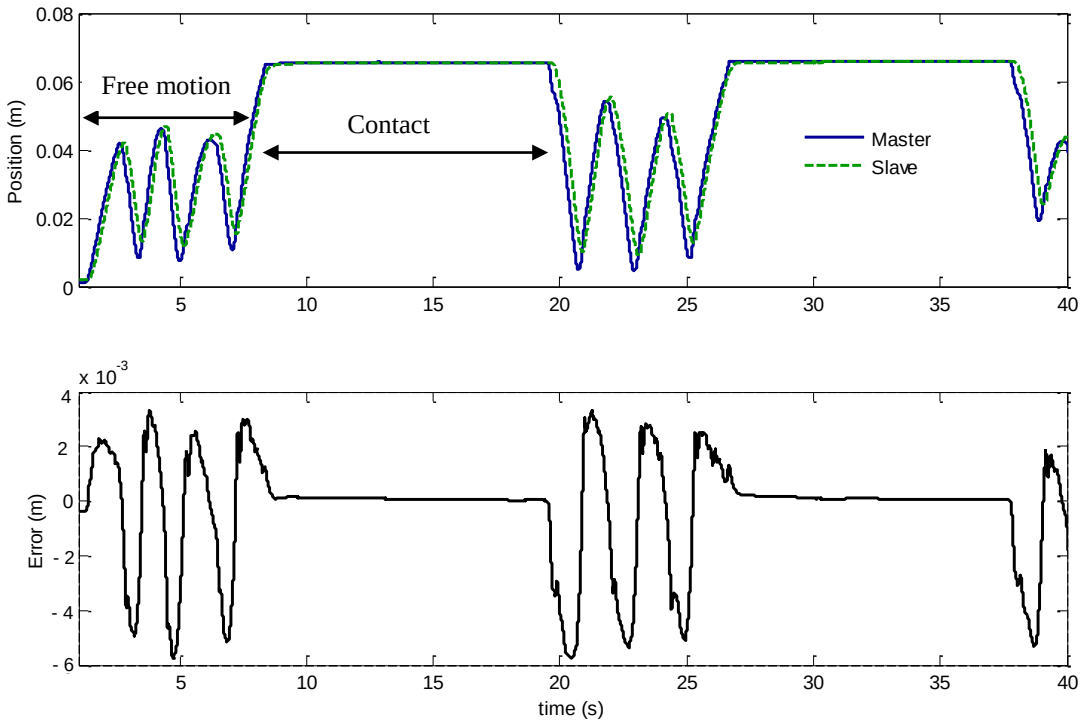

(a). Position tracking performance

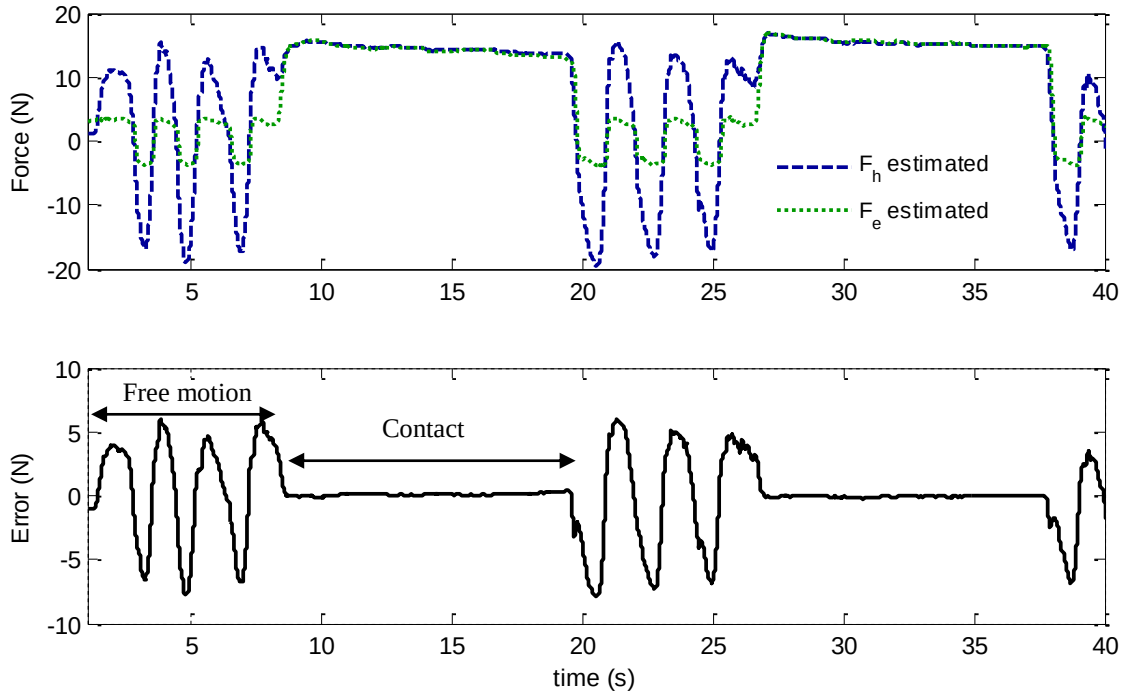

(b). Hand and environment estimation forces

Fig. 5.23. Position and force responses of the 4CH teleoperation system

Fig. 5.24 shows a comparison between the force sensor measurement and the force observation of the operator's hand and the environment. It can be seen that the EOB system displays a superior force estimation performance compared to the HOB. This can partially be attributed to the fact that in the contact mode, the human hand's dynamics is relatively high with respect to the observer's dynamics (5.43). It means that over high frequencies, the hand force observation (5.45) is less accurate, resulting in degraded human haptic perception. Contrary to the operator, the environment does not introduce any exogenous force to the system, i.e. $f_e^* = 0$ and $f_h^* \neq 0$. As a result, its dynamics is considered to be slower than the human's one. This leads to an easier and more accurate estimation of the EOB observer with respect to the HOB. Moreover, as discussed previously (section III.3.2.1), due to the high leakage problem of the jet pipe servovalves, the input force level of the operator f_h becomes higher in order to overcome the constraint caused by the leakage. Consequently, there is an increase error of the hand observation.

The force observation can be enhanced by improving the performance of the servovalve such as decreasing the leakages or increasing the mass flow rate. Indeed, smaller leakages lead to smaller input hand force level thus smaller observation errors. Besides, higher mass flow rate results in faster observer dynamics, especially in transient where the movement and the force vary quickly.

It is clear that the servovalves used in experiment are not the most appropriate for achieving high performance in force estimation but they allow us to validate the feasibility of the control law in the force-sensorless teleoperation system.

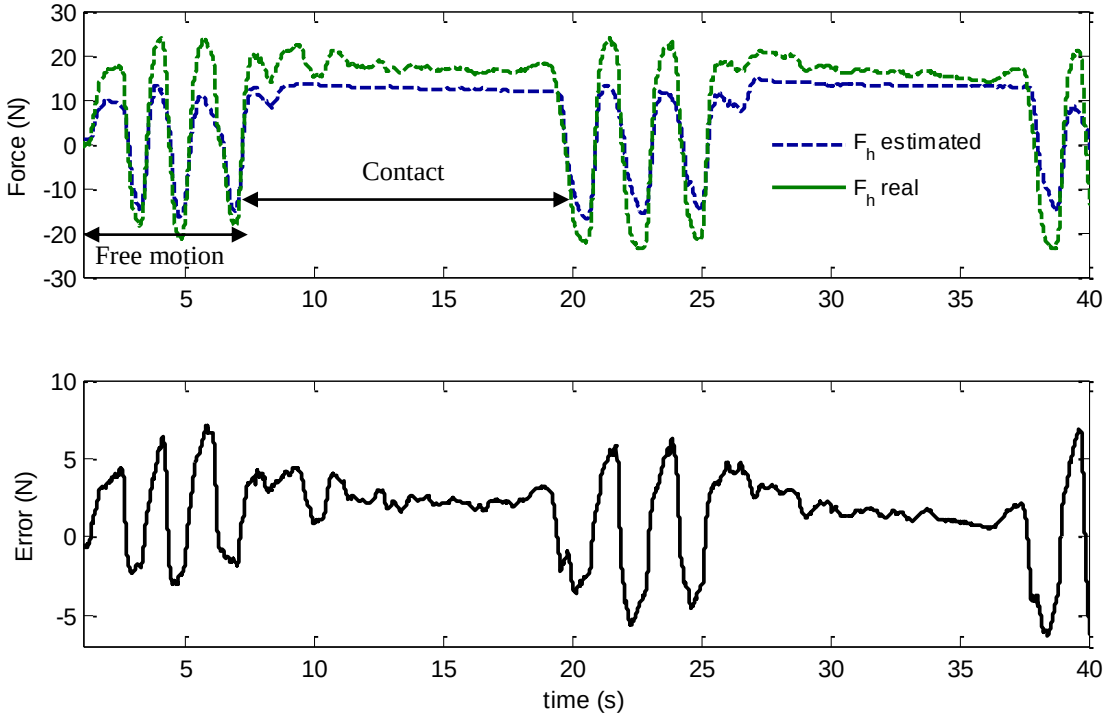

(a). HOB controller

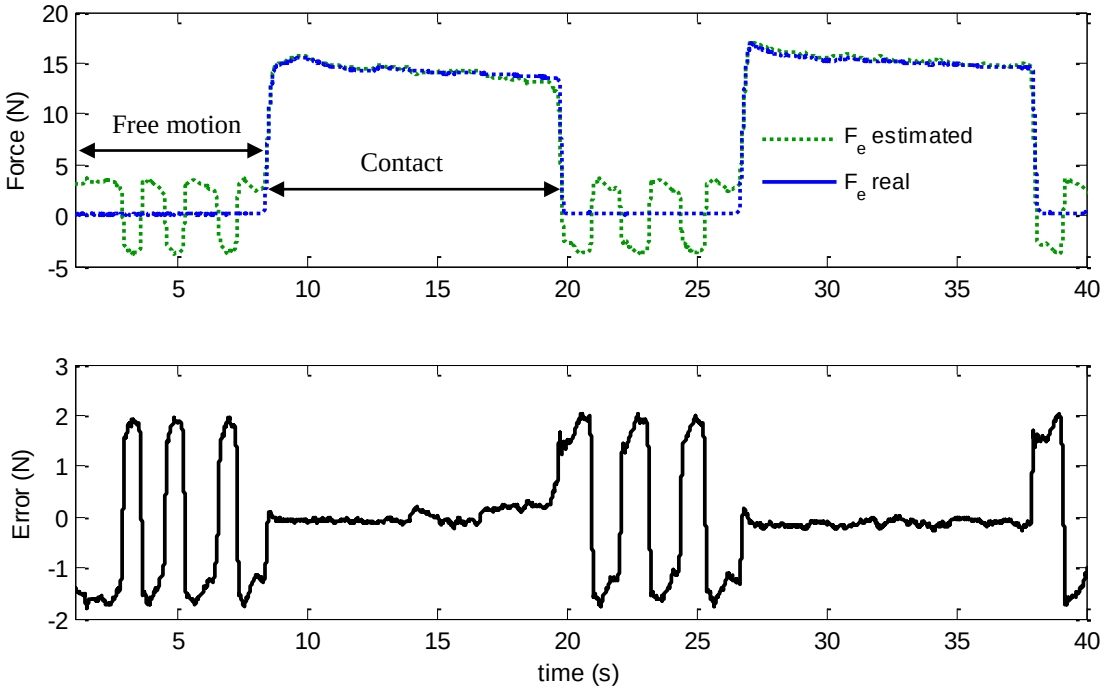

(b). EOB controller

Fig. 5.24. Force response performance of observer-based-controllers.

V. Conclusion

In this chapter, pneumatic actuators with proportional servovalves were chosen for feasibility study of a master-slave teleoperation system. For an easier design of the bilateral force/position

controllers, a linearization of the pneumatic nonlinear system was carried out. The control approach based on a reduced tangent model was implemented and validated in a 1-DOF master-slave robot setup. Thanks to the linearized pneumatic model, stability and transparency analyses of the four-channel closed-loop teleoperation system were easily investigated.

In experiments, it was observed that with the four-channel bilateral teleoperation architecture employing the linear control approach, acceptable force and position tracking between the master and the slave was obtained under both free-motion and contact-motion conditions. The results show that the tracking performance is less accurate in the servovalve case than in the solenoid valve case. However, the use of the proportional servovalves allows a better dynamics in pressures. This leads to an enhancement of the haptic teleoperation performance as well as the human's perception. Moreover, the use of servovalves allows to reduce significantly the acoustic noise compared to the on/off valves.

In bilateral teleoperation control, to reduce the dynamic influence of the device within the feedback given to the human, most master devices are lightweight to have low inertia or specific kinematic structures to compensate their own weight. As a result, normally no force sensor is integrated into the master device (e.g., the Phamtom of SensAble). Concerning the slave device, in some applications (e.g., surgery), the use of force sensor at the end of the instrument manipulator (e.g., forceps) can make the sterilization process difficult. Therefore, another aspect of our work consists in using observers for an estimation of both operator and environment forces. Experimental results show that acceptable teleoperation transparency based on a simple Nicosia observer and a linear control approach can be achieved. Furthermore, good agreement between the observed force and measured force of the environment was obtained. On the other hand, the hand force estimation is degraded but it can be again improved by using other servovalves that have higher flow capability and less leakage. Finally, the overall results demonstrated a feasibility to deal with the force-sensorless teleoperation setups equipped pneumatic actuators and proportional servovalves. While the proposed force observer in this chapter is based on the measurement of two pressure sensors, an aspect of future work is to extend the method by using only one pressure sensor in order to reduce the cost of overall system.

Conclusions and Perspectives

I. Contributions

A main objective of our work is to investigate the control of electro-pneumatic actuators in a haptic teleoperation system. For this, a 1-DOF experimental setup, which consists of two identical master and slave manipulators, has been designed and built at the Ampere Laboratory. In the following, we provide a resume of our contributions in the course of this thesis. Perspective and future works will be conducted at the end of the chapter.

After giving a general overview of haptic device (i.e. haptic-rendering algorithms, human-sensing capabilities, and design requirements), **chapter 1** presents a comparison of different actuation haptic technologies. It has been seen that electrical motors are the choice of most commercially available haptic interfaces as they are simple and capable of providing high bandwidth at relatively low cost and maintenance. Nonetheless, they can exhibit some level of torque ripple, backlash and high inertia. On the other hand, pneumatic actuators, which are able to drive higher mass-to-force ratio and simplify compliance control, can be an interesting solution for some haptic applications. However, they suffer from common drawbacks including friction and limited bandwidth. Also, from a control perspective, controlling a pneumatic actuator is a challenge because the system dynamics are highly nonlinear. In this study, pneumatic actuators are utilized for our future development in order to carried out a first feasibility study and propose an alternative to electric motors.

Bilateral master-slave teleoperation is considered to be one of the most promising application areas in robotics field. However, a major shortcoming of the present generation of teleoperation system is the lack of haptic feedback, i.e., the operator is not able to feel what he/she is touching while performing a task. Establishing the haptic sensation in the teleoperation system has attracted attention of many researchers during the last twenty years, since it presents interesting theoretical challenges and is crucial in many applications (e.g., minimally-invasive surgery). In order for readers to better understand the principle of bilateral master-slave systems, **chapter 2** provides some basic concepts of the haptic teleoperation such as linear modeling of different blocks (i.e., operator, environment, controller, master, and slave), and comparison of different control architectures based on some performance criteria. These criteria can also be used for the proper tuning of the parameters characteristic of each scheme, on the basis of the overall design specifications (e.g. stability, transparency, bandwidth, tracking performances, etc.)

After defining specifications of the 1-DOF pneumatic system, **chapter 3** is dedicated to the selections as well as the characteristics of different components such as actuators, sensors, and valves.

As any actuators, the pneumatic cylinders have some drawbacks, in particular friction effect which may lead to deteriorated performance of haptic interface. In order to minimize this disadvantage, a low-friction cylinder was selected.

Besides the actuation, sensing is also an essential part as regard to the performance of haptic control. This chapter therefore presents features of three types of sensors (i.e. position, force and pressure). These sensors were chosen to have high bandwidth and high accuracy, and also to satisfy the previously-defined specifications. Generally, only position and force measurements are sufficient to achieve ideally transparent bilateral teleoperation system. However, the use of pressure sensors in pneumatic systems allows improving the control performance and offering a possibility to remove the force sensors which are relatively expensive and complex to implement.

The final part of this chapter aims at providing a description of different valve technologies, i.e. servovalves and on/off solenoid valves. Generally, the solenoid valves performance is not on par with

that in the servovalves due to the discrete-input nature of the system. Nonetheless, thanks to the development of high-performance materials, fast electronic components and enhanced mechanical design, the solenoid valves now are faster and more accurate than the former valves. Actually, when the dynamics of the on/off valves is high enough, their discrete mass flow rate can be considered continuous, allowing them to achieve acceptable performance. As a result, a solution of fast switching on/off valve is chosen in this study. Finally, in order to control efficiently the servovalves and solenoid valves, a study characteristics of each technology was carried out, which is considered to be an essential stage in pneumatic control.

Chapter 4 deals with the nonlinear pneumatic teleoperation system under discrete control caused by solenoid valves and showed that acceptable tracking performance could be achieved with such a system. While traditional bilateral control (i.e., 4-channel, 3-channel, and 2-channel architectures) has been used mostly for linear/linearized teleoperation systems in the literature, we have extended the use of it to a fully nonlinear teleoperation system. Notably, the nonlinear characteristics of a pneumatics actuator are heightened when it uses on/off solenoid valves instead of proportional servovalves (which would also result in nonlinear dynamics). To efficiently control the switching on/off valves, different strategies were proposed, i.e., pulse width modulation (PWM), hybrid algorithm, and sliding mode control.

PWM is the most common method for controlling discrete systems thanks to its simple design. Chattering phenomenon caused by high frequency switching of the valves (in steady state as well as in transient) is considered to be a major drawback of the PWM in the case of pneumatic system.

Another control strategy was therefore investigated, i.e. a hybrid algorithm, in order to overcome the downsides of the PWM. This control approach were implemented and validated on a 1-DOF master-slave experimental setup. It was observed that with the four-channel bilateral teleoperation architecture employing the hybrid control algorithms, satisfactory transparency is obtained under both free-motion and contact-motion conditions. Moreover, experimental results indicate that, in addition to high improvements in force and position tracking, the proposed hybrid approach achieves smoother pressure dynamics compared to the PWM control. Consequently, this allows to reduce the chattering and enhance the transparent teleoperation.

An alternative to the hybrid strategy of a pneumatic actuator with on/off valves is to use methods based on sliding mode control law. To evaluate the efficiency of the proposed approach, transparent and stability analyses have been investigated on three control architectures (Position-Error-Based, Force-Error-Based and Direct-Force-Reflection systems) in a two-channel bilateral teleoperation framework. The drawbacks of the PEB and FEB schemes in terms of less-than-ideal force or position tracking performance were analytically and experimentally demonstrated. Also, the DFR control scheme was shown to be improved transparent as both force and position sensors are used. Finally, we propose an enhanced sliding mode control for the master-slave teleoperation systems. While the on/off valve pneumatic actuators have previously been modeled as having three discrete operating modes, an extension to five discrete control levels helps to improve the actuator dynamic performance and reduce the switching activities of the valves. It has been seen in experiment that by using two additional modes, the chattering has been reduced, which allows to provide better tracking responses with smoother dynamics and less oscillations, particularly over high frequencies. Based on these results, it is clear that the five-mode scheme is an interesting alternative to save energy and improve the valve's lifetime at no cost to teleoperation transparency.

It has been demonstrated in chapter 4 that highly transparent teleoperation could be achieved with pneumatic actuators and inexpensive on/off valves. However, a major drawback of such components proceeds from the audible noise generated by the high switching frequencies of the valves. Furthermore, in order to compare the performance of two valve technologies (i.e., on/off valves and proportional servovalves), **chapter 5** investigates the use of (jet pipe) servovalves on pneumatic bilateral teleoperation system.

In our case, the variation of the state variables (i.e., pressures, velocity, and acceleration of the master/slave actuator) and the external forces (i.e., operator and environment forces) are considered to be small. Therefore, it is possible to linearize the nonlinear pneumatic model by applying the first order development of the Taylor's series. To do this, an equilibrium point was graphically determined

using the servovalve's characteristics provided in chapter 3. For an easier manipulation, a reduced tangent model (3^{rd}-order) of pneumatic actuator inferred from the full linear model (4^{th}-order) was investigated. It has been demonstrated that the behaviors of these two transfer functions are perfectly similar, showing an excellent approximation of the 3^{rd}-order model. Based on the reduced tangent model, the parameter controllers implemented on the four-channel teleoperation scheme were easily designed. To validate the proposed control approach, stability and transparent analyses of the closed-loop teleoperation system were carried out and satisfactory results have been achieved.

It has been shown that both valve technologies (servovalves and solenoid valves) lead to acceptable transparency in teleoperation but the servovalves provide better pressure behavior than the on/off valves. This results in smother force signals and improved haptic sensation when employing teleoperation system with the servovalves.

In bilateral master-slave control, force sensors are often omitted to save cost and to reduce weight/volume of manipulators. Therefore, we introduced here the use of observer for a four-channel teleoperation architecture in force-sensorless setups. Experimental results showed a feasibility of the control law which is based on a simple linear Nicosia observer.

To resume, the contribution of our research leads to an investigation of different control laws for pneumatic actuated bilateral teleoperation system. Despite of control challenge when dealing with highly nonlinear pneumatic actuator as well as discrete control law, good transparent teleoperation has been achieved with inexpensive on/off valves. However, contrary to the servovalve, some drawbacks of the solenoid valve technology such as chattering phenomenon and high audible noise still has limited their applications in haptic field so far. Accordingly, it would be desirable to provide a better control design of the solenoid valves while also reducing the pneumatic system noise and chattering, caused by discrete operation of the valves.

II. Future Works

In the following, we provide different directions for future work such as improvement of the current control limits and extension the control law to more complex and dexterous devices (i.e., multi-DOF robots). Another perspective of this work is to deal with several problems existed in haptic teleoperation system such as communication time delay, variant environment, and safety of human-robot interaction.

- Controller design

It has been seen in chapter 4 that highlight transparent teleoperation was achieved with pneumatic actuated on/off valves based on hybrid control. However, neither robustness nor stability analysis of overall hybrid system has been investigated in our study due to the complexity of dealing with highly nonlinear pneumatic actuators and the discrete nature of control laws. Another difficulty is that teleoperation stability depends not only on the models of the master and slave manipulators but also on the dynamic behaviors of the human operator and environment, which are unknown, uncertain, nonlinear, and/or time-varying. Consequently, robustness and stability analysis in hybrid teleoperation system is an interesting problem to be investigated. While the proposed hybrid control in this thesis is based on a one-step-ahead prediction of pressures in the pneumatic chambers, an aspect of future work is to extend the control law to involve a multi-step prediction in order to improve the tracking performance.

Contrary to the hybrid strategy, the sliding mode control allows to perform both transparent and stability analyses. However, only two-channel control architecture was investigated to evaluate the efficiency of the proposed approach. Although the DFR system takes advantage of both PEB and FEB architectures in terms of position and force tracking, it is not usually suitable for teleoperation applications with very hard (wall) contact or requiring high bandwidth. As a result, another aspect of

this work is to incorporate the sliding mode control in more complex bilateral architectures (e.g., three or four-channel schemes) in order to improve the teleoperation performance.

In chapter 5, a tangent linear method was proposed for a control of the pneumatic teleoperation system driven by proportional servovalve. This approach is, however, only applicable to relatively slow-dynamic systems whose state variables vary slightly around the equilibrium set. Another limit of the control strategy is the high sensibility of disturbance (e.g., external force) that may deteriorate the performance of some teleoperation applications, especially when the environment's characteristics is variant (e.g., human organ). In this case, different force levels of the operator are required to adapt the environment change, leading to several solutions of the equilibrium points and the approximate linear models. As a result, the controller algorithm, which requires switching between the different models, becomes complex and inaccurate. In order obtain better performance in higher bandwidth and variant-environment teleoperation system, other control strategies need to be considered in future work.

- Extension to multi-DOF robots

In this thesis, the analysis and control of the bilateral teleoperation have been only elaborated for a 1-DOF master-slave setup in order to validate the first feasibility study. Future perspectives of our work will focus on an extension to a direct-drive, multi-DOFs haptic teleoperation system.

Generally, to build a multi-DOF robot, several stages are required such as architecture definition (e.g., serial/parallel/hybrid architecture), mechanical design, kinematic analysis (calculations of inverse and forward kinematics), etc. The architecture performances should be analyzed and the mechanism should be optimized in order to satisfy a number of criteria related to dexterity, force capability, workspace, singularity, weight, size, etc. One of differences to design a multi-DOF device instead of a 1-DOF is that solving algebraically the direct and/or inverse kinematic problem can be cumbersome and sometime impossible. Moreover, the highly non-linear dynamics and kinematics of the multi-DOF manipulator vary significantly over its workspace, leading to complex controller design. In order to reduce the control analysis to the single-DOF model, it is sometime possible to decouple multiple degrees of freedom so that each one can be analyzed separately. A main drawback of this method is that the control law is only locally valid at each degree of freedom.

Finally, achieving a high performance of a multi-DOF haptic teleoperation system is challenging and nonetheless a priority in our future works.

- Haptic teleoperation challenges

In parallel with the development of the multi-DOF robots, other future research directions can be investigated to improve the teleoperation performance.

Firstly, communication time delay is one of main concerns in teleoperation since the operation site is usually located far from the remote environment. In the presence of time delays, the stability and transparency of a bilateral teleoperation system are severely affected. Various time delay compensation methods have been developed and testified in real-world teleoperation systems but most of them utilize electric actuator technology (Anderson & Spong 1989; Hokayem & Spong 2006; Aziminejad et al. 2008). Implementation of these methods on pneumatic master-slave setup with a presence of time delays is clearly an interesting investigation for future works.

Secondly, one of the major current problems when designing a controller for haptic teleoperation systems is the enormous change in the environmental properties. For instance, during a typical operation in the human body, the slave end-effector comes in touch with both stiff materials (when grasping a needle or touching a bone) and soft tissues, sometimes even with nothing during free motion. Therefore, the master-slave controller should be robust against abrupt changes in the remote environment. As mentioned above, in our case, the tangent linear method is not suitable for a control of teleoperation with variant environment. Thus, it would be motivating to study other control laws that enable to fulfill, in a better way, the haptic teleoperation requirements.

Last but not least, design and control of mechanical compliance on master-slave system would be one of the most important techniques in insuring human safety when interacting with robots. However, this aspect has not been much investigated in teleoperation literature so far due to the complexities of bilateral control and communication time delay.

As a control system actuated by motors for the purpose of safety, an impedance control system was proposed (Tachi & Sakaki 1991). However, safety against collisions with obstacles in an unpredictable environment is difficult to insure in this system, partially due to a small power-to-mass ratio of the electric actuator.

The pneumatic actuator's safety is intrinsic because of its being passive compliant (i.e., compressibility of air and high back-drivability). This leads to an avoidance motion when a collision occurs, which is an important function for human-robot interaction. In addition, the pneumatic servo system can give an easier way to deal with the design and control of mechanical compliance since its compliance can be tuned by just changing the pressures.

Finally, compliance control approaches for pneumatic actuators such as those in (Kosaki & Sano 2006; Shen & Goldfarb 2007b; Vanderborght et al. 2008) have not been implemented in teleoperation systems yet. This represents an alternative research path to be investigated.

To resume, the development of a bilateral teleoperation system, including several stages such as mechanical conception, material selection and controller design, depends on the task requirements as well as the application area. Currently, the minimally-invasive surgery (MIS) is considered to be one of the most promising applications of teleoperation with force feedback. The advantages of such a system are large because many obstacles of conventional MIS surgery are overcome (Rosen et al. 1999). To do this, a number of issues have to be investigated, e.g. compensation of surgeons' tremor, scale movements or/and forces, improved haptic sensation, etc. This aspect is considered to be a final goal of our research.

List of Publications

Referred international journals (Accepted)

M.Q. Le, M.T. Pham, R. Moreau, J.P. Simon, and T. Redarce, "Force Tracking of Pneumatic Servo Systems using on/off Solenoid Valves based on a Greedy Control Scheme", *ASME Journal of Dynamic Systems, Measurement and Control*, n°. 5, vol. 133, 2011, in press.

S. Hodgson, **M.Q. Le**, M. Tavakoli, and M.T. Pham, "Improved Tracking and Switching Performance of an Electro-Pneumatic Positioning System", *Journal of IFAC (International Federation of Automatic Control), Mechatronics, Elsevier*, Accepted paper, 2011.

Referred international journals (in Revision)

M.Q. Le, M.T. Pham, M. Tavakoli, R. Moreau, J.P. Simon, and T. Redarce, "Bilateral Control of a Nonlinear Pneumatic Teleoperation System with Solenoid Valves", *IEEE Transactions on Control Systems Technology*, Minor revision, Re-submitted in September 2011.

M.Q. Le, M.T. Pham, M. Tavakoli, R. Moreau, and T. Redarce, "Sliding-Mode Bilateral Teleoperation Control Design for Master-Slave Pneumatic Servo Systems", *Journal Control Engineering Practice, Elsevier*, Major revision, Re-submitted in July 2011.

Referred international conferences with proceeding (Accepted)

M.Q. Le, M.T. Pham, R. Moreau, and T. Redarce, "Comparison of a PWM and a Hybrid Force Control for a Pneumatic Actuator Using On/off Solenoid Valves", *IEEE/ASME International Conference on Advanced Intelligent Mechatronics (AIM)*, Montreal, p. 1146–1151, July 2010.

M.Q. Le, M.T. Pham, R. Moreau, and T. Redarce, "Transparency of a pneumatic teleoperation system using on/off solenoid valves", *IEEE International Symposium on Robot and Human Interactive (RoMan)*, Viareggio, p. 15–20, September 2010.

M.Q. Le, M.T. Pham, M. Tavakoli, and R. Moreau, "Development of a hybrid control for a pneumatic teleoperation system using on/off solenoid valves", *IEEE International Conference on Intelligent Robots and Systems (IROS)*, Taipei, p. 5818–5823, October 2010.

M.Q. Le, M.T. Pham, M. Tavakoli, and R. Moreau, "Sliding Mode Control of a Pneumatic Haptic Teleoperation system with on/off solenoid valves", *IEEE International Conference on Robotics and Automation (ICRA)*, Shanghai, p. 874–879, 2011.

M.Q. Le, M.T. Pham, M. Tavakoli, and R. Moreau, "An Enhanced Sliding-Mode Control for a Pneumatic-Actuated Teleoperation System", *IEEE International Conference on Intelligent Robots and Systems (IROS)*, San Francisco, 659-664, 2011.

S. Hodgson, **M.Q. Le**, M. Tavakoli, and M.T. Pham, "Improved Sliding Mode Control of Nonlinear Discrete-Input Pneumatic Actuators", *IEEE International Conference on Intelligent Robots and Systems (IROS)*, San Francisco, 738-743, 2011.

Referred National conferences (Poster session)

M.Q. Le, M.T. Pham, R. Moreau, and T. Redarce, "Pneumatic teleoperation system based on hybrid control with on/off solenoid valves," *Journées des Jeunes Chercheurs en Robotiques (JJCR)*, Paris, 8 November 2010.

References

Adams, R. J., & Hannaford, B. Stable haptic interaction with virtual environments. *IEEE Transactions on Robotics and Automation*,1999, **15**, 465–474.

Adelstein, B. D., & Rosen, M. J. Design and implementation of a force reflecting manipulandum for manual control research. *ASME Dynamic Systems and Control Division*, 1992, **42**, 1–12.

Ahn, K., & Yokota, S. Intelligent switching control of pneumatic actuator using on/off solenoid valves. *Mechatronics*, 2005 **15**, 683–702.

Al-Dakkan, K. A., Goldfarb, M., & Barth, E. J. 2003 June Nashville . Energy saving control for pneumatic servo systems. *IEEE/ASME International Conference on Advanced Intelligent Mechatronics (AIM)*, 2003 **1**, 284–289.

Aliaga, I., Rubio, A., & Sanchez, E. Experimental quantitative comparison of different control architectures for master-slave teleoperation. *IEEE Transactions on Control Systems Technology*, 2004, **12**, 2–11.

Allin, S., Matsuoka, Y., & Klatzky, R. 2002 March Orlando. Measuring just noticeable differences for haptic force feedback: implications for rehabilitation. *10th Symposium on Haptic Interfaces for Virtual Environment and Teleoperator Systems*, 2002, 299–305.

Andersen, B. W. *The analysis and design of pneumatic systems.* Wiley New York, 1967, p.302.

Anderson, R. J., & Spong, M. W. Bilateral control of teleoperators with time delay. *IEEE Transactions on Automatic Control*, 1989, **34**, 494–501.

An, K. N., Askew, L. J., & Chao, E. Y. Biomechanics and functional assessment of upper extremities. *Trends in Ergonomics/Human Factors III, Elsevier Science Publishers*, 1986, **16**, 573–580.

Auricchio, F., Taylor, R. L., & Lubliner, J. Shape-memory alloys: macromodelling and numerical simulations of the superelastic behavior. *Computer Methods in Applied Mechanics and Engineering*, 1997 **146**, 281–312.

Aziminejad, A., Tavakoli, M., Patel, R. V., & Moallem, M. Transparent Time-Delayed Bilateral Teleoperation Using Wave Variables. *IEEE Transactions on Control Systems Technology*, 2008 **16**, 548–555.

Bar-Cohen, Y., & Breazeal, C. L. *Biologically inspired intelligent robots.* SPIE Press, 2003, p.405.

Barth, E. J., Zhang, J., & Goldfarb, M. 2002 May Anchorage. Sliding mode approach to PWM-controlled pneumatic systems. *American Control Conference*, 2002, 2362–2367.

Barth, E. J., Zhang, J., & Goldfarb, M. Control design for relative stability in a PWM-controlled pneumatic system. *Journal of Dynamic Systems, Measurement, and Control*, 2003, **125**, 504–508.

Bejczy, A., & Salisbury, K. Kinematic coupling between operator and remotemanipulator. *Advances in Computer Technology*, 1980, **1**, 197–211.

Bejczy, A. K. Sensors, Controls, and Man-Machine Interface for Advanced Teleoperation. *Science*, 1980 **208**, 1327–1335.

Ben-Dov, D., & Salcudean, S. E. A force-controlled pneumatic actuator. *IEEE Transactions on Robotics and Automation (ICRA)*, 1995 **11**, 906–911.

Bergamasco, M., Allotta, B., Bosio, L., Ferretti, L., Parrini, G., Prisco, G. M., Salsedo, F., & Sartini, G. 1994 May Piza. An arm exoskeleton system for teleoperation and virtual environments applications. *IEEE International Conference on Robotics and Automation*, 1994, **2**, 1449–1454.

Birglen, L., Gosselin, C., Pouliot, N., Monsarrat, B., & Laliberte, T. SHaDe, a new 3-DOF haptic device. *IEEE Transactions on Robotics and Automation*, 2002 **18**, 166–175.

Blackburn, R. *Shearer, Fluid Power Control.* John Wiley and Sons, Inc, 1960, p.705.

Bobrow, J. E., & McDonell, B. W. Modeling, identification, and control of a pneumatically actuated, force controllable robot. *IEEE Transactions on Robotics and Automation (ICRA)*,1998, **14**, 732–742.

Bouzit, M., Richard, P., & Coiffet, P. LRP dextrous hand master control system. *Technical Report, Laboratoire de Robotique de Paris*, 1993, p. 21.

Branicky, M. S. 1997 December San Diego. Stability of hybrid systems: State of the art. *IEEE Conference on Decision and Control*, 1997, **1**, 120–125.

Brooks, F. P., Ouh-Young, M., Batter, J. J., & Jerome Kilpatrick, P. 1990 August New York. Project GROPE: Haptic displays for scientific visualization. *Conference on Computer graphics and interactive techniques*, 1990, 177–185.

Brooks, T. L. 2002 August Lanham. Telerobotic response requirements. *Proceedings of IEEE International Conference on Systems, Man and Cybernetics*, 2002 113–120.

Brun, X., Belgharbi, M., Sesmat, S., Thomasset, D., & Scavarda, S. Control of an electropneumatic actuator: comparison between some linear and non-linear control laws. *Journal of Systems and Control Engineering*, 1999, **213**, 387–406.

Brun, X. Commandes linéaires et non linéaires en électropneumatique. Méthodologies et applications. INSA de Lyon, 1999, p.200.

Burdea, G. C., & Akay, M. *Force and touch feedback for virtual reality.* John Wiley & Sons New York, 1996, p. 360.

Burdea, G., & Coiffet, P. Virtual Reality Technology. *Presence: Teleoperators and Virtual Environments*,2003, **12**, 663-664.

Burrows, C. R. *Fluid power servomechanisms.* Van Nostrand Reinhold Co, 1972, p. 237.

Buttolo, P., Braathen, P., & Hannaford, B. Sliding control of force reflecting teleoperation: Preliminary studies. *Presence*, **3**, 1994, 158–172.

Caldwell, D. G., & Gosney, C. 2002 May, Salford. Enhanced tactile feedback (tele-taction) using a multi-functional sensory system. *IEEE International Conference on Robotics and Automation*, 2002, 955–960.

Caldwell, D. G., Andersen, U., Bowler, C. J., & Wardle, A. J. A high power/weight dexterous manipulator using « Sensory Glove » based motion control and tactile feedback. *Transactions of the Institute of Measurement and Control*, 1995, **17**, 234–241.

Chopra, N., Spong, M. W., Ortega, R., & Barabanov, N. E. Position and Force Tracking in Bilateral Teleoperation. *Advances in Communication Control Networks*,2005, **305**, 410–413.

Chotiprayanakul, P., & Liu, D. K. 2009 June Zuhai. Workspace mapping and force control for small haptic device based robot teleoperation. *International Conference on Information and Automation (ICIA'09)*, 2009, 1613–1618.

Chou, C. P., & Hannaford, B. Measurement and modeling of McKibben pneumatic artificial muscles. *IEEE Transactions on Robotics and Automation*,2002, **12**, 90–102.

Christiansson, G. A. V., & Helm, F. C. T. The Low-Stiffness Teleoperator Slave — a Trade-off between Stability and Performance. *International Journal of Robotics Research*,2007, **26**, 287–299.

Christiansson, G. A. V. 2007. Introduction to Analysis and Control in Haptic Teleoperation, Delft University of Technology 2007, p.56.

Clark, F. J., & Horch, K. W. Kinesthesia. *Handbook of perception and human performance*, 1986, **1**, 13–1.

Clover, C. L., Luecke, G. R., Troy, J. J., & McNeely, W. A. 1997 April Albuquerque. Dynamic simulation of virtual mechanisms with haptic feedback using industrial robotics equipment. *IEEE International Conference on Robotics and Automation*, 1997, **1**, 724–730 vol.1.

Conti, F., & Khatib, O. 2005 March Stanford. Spanning large workspaces using small haptic devices. *Eurohaptics Conference and Symposium on Haptic Interfaces for Virtual Environment and Teleoperator Systems*, 2005, 183–188.

Conti, F., Khatib, O., & Baur, C. 2007 March Tsukaba. A hybrid actuation approach for haptic devices. *Conference and Symposium on Haptic Interfaces for Virtual Environment and Teleoperator Systems*, 2007, 367–372.

Corradini, A., Mehta, M., Bernsen, N. O., & Charfuelan, M. 2005 May Madrid. Animating an interactive conversational character for an educational game system. *International Conference on Intelligent User Interfaces*, 2005, 183–190.

Daniel, R. W., & McAree, P. R. Fundamental Limits of Performance for Force Reflecting Teleoperation. *International Journal of Robotics Research*, 1998, **17**, 811–830.

Det, F. Modélisation en bond graphs simulation et commande d'une pince à souder électropneumatique. INSA de Lyon, 1991, p.278.

DiFranco, D. E., Beauregard, G. L., & Srinivasan, M. A. 1997 June Miami. The effect of auditory cues on the haptic perception of stiffness in virtual environments. *Proceedings of the ASME Dynamic Systems and Control Division*, 1997, **61**, 17–22.

Diolaiti, N., & Melchiorri, C. 2002 November Ottawa. Teleoperation of a mobile robot through haptic feedback. *IEEE International Workshop on Haptic Virtual Environments and Their Applications*, 2002, 67–72.

Dongjun Lee, Martinez-Palafox, O., & Spong, M. W. 2006 October Beijing. Bilateral teleoperation of a wheeled mobile robot over delayed communication network. *IEEE International Conference on Robotics and Automation (ICRA)*, 2006, 3298–3303.

Durbha, V., & Li, P. Y. 2009 March San Fransico. Passive bilateral tele-operation and human power amplification with pneumatic actuators. *Proceedings of ASME Dynamic Systems and Control Conference, California, USA*, 2009, 1–8.

Durfee, W. K., Hendrix, C. M., Cheng, P., & Varughese, G. 1997 April, Bologna. Influence of haptic and visual displays on the estimation of virtual environment stiffness. *Proceedings of the ASME Dynamic Systems and Control Division*, 1997, 139–145.

Edwards, C., & Spurgeon, S. K. *Sliding mode control: theory and applications.* CRC, 1998, P. 237.

Ehmann, S. A., Gregory, A. D., & Lin, M. C. A touch-enabled system for multi-resolution modeling and 3D painting. *Journal of Visualization and Computer Animation*, 2001 **12**, 145–157.

Eom, K. S., Suh, I. H., Chung, W. K., & Oh, S. R. 1998 May Leuven. Disturbance observer based force control of robot manipulator without force sensor. *IEEE International Conference on Robotics and Automation*, 1998, **4**, 3012–3017.

Falvo, M., Superfine, R., Washburn, S., Finch, M., Taylor, R., Chi, V. L., & Brooks Jr, F. P. The nanomanipulator: A teleoperator for manipulating materials at the nanometer scale. *Proceedings International Symposium on the Science and Technology of Atomically Engineered Materials, World Scientific Publishing, Singapore*, 1995, 579–586.

Feygin, D., Keehner, M., & Tendick, R. 2002 March Orlando. Haptic guidance: Experimental evaluation of a haptic training method for a perceptual motor skill. *Proceedings Symposium on Haptic Interfaces for Virtual Environment and Teleoperator Systems*, 2002, 40–47.

Fischer, P., Daniel, R., & Siva, K. V. 1990 May Cincinnati. Specification and design of input devices for teleoperation. *IEEE International Conference on Robotics and Automation*, 1990, **1**, 540–545.

Fite, K. B., Speich, J. E., & Goldfarb, M. 2001. Transparency and stability robustness in two-channel bilateral telemanipulation. *Journal of Dynamic Systems, Measurement, and Control*, **123**, 400–407.

Formaglio, A., Prattichizzo, D., Barbagli, F., & Giannitrapani, A. Dynamic performance of mobile haptic interfaces. *IEEE Transactions on Robotics*,2008, **24**, 559–575.

Fourati, H., & Maalej, T. 2006. *Modélisation de la chaîne d'actionnement d'une tête souple de coloscope.* Projet de fin d'étude, Laboratoire Ampère, INSA de Lyon, France, 62p.

Franklin, G. F., Powell, J. D., Emami-Naeini, A., & Powell, J. D. *Feedback control of dynamic systems.* Addison-Wesley Reading, 1994, p. 910.

Funda, J., & Paul, R. P. 1991 October Honolulu. A Symbolic Teleoperator Interface For Time-delayed Underwater Robot Manipulation. *Ocean Technologies and Opportunities in the Pacific*, 1991, 1526–1533.

Gasca, M., & Sauer, T. Polynomial interpolation in several variables. *Advances in Computational Mathematics*, 2000, **12**, 377–410.

Gentile, A., Giannoccaro, N. I., & Reina, G. 2002 December Bongkok. Experimental tests on position control of a pneumatic actuator using on/off solenoid valves. *IEEE International Conference on Industrial Technology, Thailand*, 2002, **11**, 555–559.

Geyer, T., Papafotiou, G., & Morari, M. Hybrid Model Predictive Control of the Step-Down DC–DC Converter. *IEEE Transactions on Control Systems Technology*, 2008, **16**, 1112–1124.

Goertz, R. C. Fundamentals of General Purpose Remote Manipulators. *Nucleonics (U.S.)*, 1952, **10**, 36–42.

Goldstein, S. R., & Richardson, H. A differential pulse-width modulated pneumatic servo utilizing floating flapper disc switching valves. *ASME Transactions, J Basic Enga Series C*, 1968, 143.

Guerriero, B., & Book, W. 2008 October Ann Arbor. Haptic Feedback Applied to Pneumatic Walking. *ASME Dynamic Systems and Control Conference*, 2008, 591–597.

Gupta, A., & O'Malley, M. K. Design of a haptic arm exoskeleton for training and rehabilitation. *IEEE/ASME Transactions on Mechatronics*, 2006, **11**, 280–289.

Hacksel, P. J., & Salcudean, S. E. 1994 May San Diego. Estimation of environment forces and rigid-body velocities using observers. *IEEE International Conference on Robotics and Automation*, 1994, 931–936.

Handlykken, M., & Turner, T. 1980 December Albuquerque . Control system analysis and synthesis for a six degree-of-freedom universal force-reflecting hand controller. *IEEE International Conference on Decision and Control*, 1980, **19**, 1197–1205.

Hannaford, B. A design framework for teleoperators with kinesthetic feedback. *IEEE transactions on Robotics and Automation*, 1989, **5**, 426–434.

Hannaford, B., & Anderson, R. 1988 April Philadelphia. Experimental and simulation studies of hard contact in force reflecting teleoperation. *IEEE International Conference on Robotics and Automation*, 1988, **1**, 584–589.

Han, Y. M., & Choi, S. B. Force-feedback control of a spherical haptic device featuring an electrorheological fluid. *Smart Materials and Structures*, 2006, **15**, 1438–1446.

Hashtrudi-Zaad, K., & Salcudean, S. E. Analysis of control architectures for teleoperation systems with impedance/admittance master and slave manipulators. *The International Journal of Robotics Research*, 2001, **20**, 419–445.

Hashtrudi-Zaad, K., & Salcudean, S. E. Transparency in time-delayed systems and the effect of local force feedback for transparent teleoperation. *IEEE Transactions on Robotics and Automation*, 2002, **18**, 108–114.

Haykin, S. S. *Active network theory.* Addison-Wesley, 1970, p.556.

Hayward, V., & Armstrong, B. 2000 October New-York. A new computational model of friction applied to haptic rendering. *Experimental Robotics VI*, 2002, 403–412.

Hayward, V., Astley, O. R., Cruz-Hernandez, M., Grant, D., & Robles-De-La-Torre, G. Haptic interfaces and devices. *Sensor Review*, 2004, **24**, 16–29.

Henri, P. D., Hollerbach, J. M., & Nahvi, A. An analytical and experimental investigation of a jet pipe controlled electropneumatic actuator. *IEEE Transactions on Robotics and Automation*, 2002, **14**, 601–611.

Hodgson, S., Le, M. Q., Tavakoli, M., & Pham, M. T. 2011 September San Fransico. Sliding-Mode Control of Nonlinear Discrete-Input Pneumatic Actuators. *IEEE International Conference on Intelligent Robots and Systems (IROS)*, 2011, 738-743.

Hodgson, S., Le, M. Q., Tavakoli, M., & Pham, M. T. Improved Tracking and Switching Performance of an Electro-Pneumatic Positioning System. *Mechatronics, Elsevier*, Accepted paper, 2011.

Hogan, N. 1989 May Scottsdale. Controlling impedance at the man/machine interface. *IEEE International Conference on Robotics and Automation*, 1989, 1626–1631.

Hokayem, P. F., & Spong, M. W. Bilateral teleoperation: An historical survey. *Automatica*, 2006, **42**, 2035–2057.

Hollis, R. L., Salcudean, S. E., & Allan, A. P. A six-degree-of-freedom magnetically levitated variable compliance fine-motion wrist: design, modeling, and control. *IEEE Transactions on Robotics and Automation*, 1991, **7**, 320–332.

Huang, H. P., & Tzeng, W. L. 1989 December Tampa. Robotic force control by using estimated contact force. *IEEE Conference on Decision and Control*,1989, **3**, 2158–2163.

Hu, Z., Salcudean, S. E., & Loewen, P. D. 1995 March Changsha City. Robust controller design for teleoperation systems. *IEEE International Conference on Systems, Man and Cybernetics*, 1995, **3**, 2127–2132.

Imaida, T., Yokokohji, Y., Doi, T., Oda, M., & Yoshikawa, T. Ground-space bilateral teleoperation of ETS-VII robot arm by direct bilateral coupling under 7-s time delay condition. *IEEE Transactions on Robotics and Automation*, 2004, **20**, 499–511.

Ishii, M., & Sato, M. A 3D spatial interface device using tensed strings. *Presence*, 1994, **3**, 81–86.

Iwata, H. 1993 September Seattle. Pen-based haptic virtual environment. *IEEE Virtual Reality Annual International Symposium*, 1993, 287–292.

Iwata, H. 1990 June Tampa. Artificial reality with force-feedback: development of desktop virtual space with compact master manipulator. *Proceedings of the 17th annual Conference on Computer Graphics and Interactive Techniques*, 1990, 165–170.

Jacobsen, S. C., Iversen, E. K., Knutti, D. F., Johnson, R. T., & Biggers, K. B. Design of the Utah. *IEEE Transactions on Robotics and Automation*, 1986, **3**, 96–102.

Jian Wang, & Shuxiang Guo. 2007 May Beijing. Development of a Precision Parallel Micro-mechanism for Nano Tele-operation. *IEEE/ICME International Conference on Complex Medical Engineering*, 2007, 56–61.

Jiang, H. J., Qin, Y., Du, S. S., Yu, Z. Y., & Choudhury, S. 1998 October San Francisco. DSP based implementation of a digitally-controlled single phase PWM inverter for UPS. *20th International Conference on Telecommunications Energy (INTELEC)*, 1998, 221–224.

Jones, L. A., Hunter, I. W., & Irwin, R. J. Differential thresholds for limb movement measured using adaptive techniques. *Perception & Psychophysics*, 1992, **52**, 529–535.

Jones, L. A., & Hunter, I. W. A perceptual analysis of stiffness. *Experimental Brain Research*, 1990, **79**, 150–156.

Kazerooni, H., Tsay, T.-I., & Hollerbach, K. A controller design framework for telerobotic systems. *IEEE Transactions on Control Systems Technology*, 1993, **1**, 50–62.

Kellal, A., Scavarda, S., & Fontaine, J. G. 1986. Electropneumatic servodrive for a robot. *International Symposium on Industrial Robots*, 1986, 117-128.

Kella, A. Contribution à l'étude des asservissements électropneumatiques. Application à la réalisation d'un asservissement numérique d'un axe de robot. INSA de Lyon, 1987, p.173.

Ke, J., Wang, J., Jia, N., Yang, L., & Wu, Q. H. 2005 August Toronto. Energy efficiency analysis and optimal control of servo pneumatic cylinders. *IEEE Conference on Control Applications*, 2005, 541–546.

Kirat, R. Modélisation et commande en position d'un vérin pneumatique controlé par un ensemble de quatre électrovannes pilotées en modulationde largeur différentielle. INSA de Lyon, 1992, p.183.

Klomp, F. M. Haptic feedback control designs in teleoperation systems for minimal invasive surgery DCT Report No. 2004.117.

Klomp, F. M. 2006. Haptic Control for Dummies: An introduction and analysis. Eindhoven University of Technology, Department of Mechanical Engineering, Control Systems Technology Group.

Kosaki, T., & Sano, M. 2006 October Beijing. A Compliance Controller for a Pneumatic Actuator With Observer-Based Friction Compensation. *IMACS Multiconference on Computational Engineering in Systems Applications*, 2006, **2**, 1144–1148.

Kuchenbecker, K. J., & Niemeyer, G. Induced master motion in force-reflecting teleoperation. *Journal of Dynamic Systems, Measurement, and Control*, 2006, **128**, 800–810.

Lau, H. Y. K., & Wai, L. C. C. Implementation of position-force and position-position teleoperator controllers with cable-driven mechanisms. *Robotics and Computer-Integrated Manufacturing*,2005, **21**, 145–152.

Lawn, C. A., & Hannaford, B. 1993 May Atlanta. Performance testing of passive communication and control in teleoperation with time delay. *IEEE International Conference on Robotics and Automation*, 1993, 776–783.

Lawrence, D. A. Optimizing dynamic transparency in teleoperator architectures. *Guidance and control 1992*, 353–365.

Lawrence, D. A. Stability and transparency in bilateral teleoperation. *IEEE Transactions on Robotics and Automation*, 1993, **9**, 624–637.

Lee, C. Y., Chan, S. P., & Mital, D. P. A joint torque disturbance observer for robotic assembly. *Proceedings of the 36th Midwest Symposium on Circuits and Systems*, 1993, **2**, 1439–1442.

Lee, D., & Li, P. Y. Passive bilateral control and tool dynamics rendering for nonlinear mechanical teleoperators. *IEEE Transactions on Robotics*,2005, **21**, 936–951.

Lee, S., & Lee, H. S. Modeling, design, and evaluation of advanced teleoperator control systems with short time delay. *IEEE Transactions on Robotics and Automation*,1993 **9**, 607–623.

Legrand, X., Retif, J. M., Smaoui, M., Brun, X., Thomasset, D., & Lin-Shi, X. F. 2005. Hybrid control with on/off electropnaumatic standard valve for tracking positioning. *Procceding Bath Workshop Power Transmiss and Motion Control*, 45–58.

Le, M. Q., Pham, M. T., Moreau, R., & Redarce, T. 2010 September Viareggio . Transparency of a pneumatic teleoperation system using on/off solenoid valves. *IEEE International Conference on Robot and Human Communication (ROMAN), Italy*, 15–20.

Le, M. Q., Pham, M. T., Moreau, R., & Redarce, T. 2010 Juily Montreal. Comparison of a PWM and a Hybrid Force Control for a Pneumatic Actuator Using On/off Solenoid Valves. *IEEE/ASME International Conference on Advanced Intelligent Mechatronics (AIM), Canada*, 2010, 1146–1151.

Le, M. Q., Pham, M. T., Moreau, R., Simon, J. P., & Redarce, T. Force Tracking of Pneumatic Servo Systems using on/off Solenoid Valves based on a Greedy Control Scheme. *ASME Journal of Dynamic Systems, Measurement, and Control*, 2011, **133**, Accepted paper.

Le, M. Q., Pham, M. T., Tavakoli, M., & Moreau, R. 2010 October Taipei. Development of a hybrid control for a pneumatic teleoperation system using on/off solenoid valves. *IEEE International Conference on Intelligent Robots and Systems (IROS), Taiwan*, 2010, 5818–5823.

Le, M. Q., Pham, M. T., Tavakoli, M., & Moreau, R. 2011 May Shanghai. Sliding Mode Control of a Pneumatic Haptic Teleoperation System with on/off Solenoid Valves. *IEEE International Conference on Robotics and Automation (ICRA)*, 2011, 874–879.

Le, M. Q., Pham, M. T., Tavakoli, M., & Moreau, R. 2011 September San Fransico. An Enhanced Sliding-Mode Control for a Pneumatic-ActuatedTeleoperation System. *IEEE International Conference on Intelligent Robots and Systems (IROS)*, 2011, 659-664.

Le, M. Q., Pham, M. T., Tavakoli, M., Moreau, R., Simon, J. P., & Redarce, T. Bilateral Control of a Nonlinear Pneumatic Teleoperation System with Solenoid Valves. *IEEE Transactions on Control Systems Technology*, Re-submitted paper, 2011.

Le, M. Q., Pham, M. T., Tavakoli, M., Moreau, R., Simon, J. P., & Redarce, T. 2011e. Sliding-Mode Bilateral Teleoperation Control Design for Master-Slave Pneumatic Servo Systems. *Control Engineering Practice*, Revised paper, 2011.

Levant, A. Robust exact differentiation via sliding mode technique. *Automatica*, 1998, **34**, 379–384.

Liberzon, D. *Switching in systems and control.* Springer, 2003, p.243.

Lin-Shi, X., Morel, F., Llor, A. M., Allard, B., & Rétif, J. M. Implementation of hybrid control for motor drives. *IEEE Transactions on Industrial Electronics*, 2007, **54**, 1946–1952.

Lindemann, R., & Tesar, D. Construction and demonstration of a 9-string 6 DOF force reflecting joystick for telerobotics. *Proceedings of the NASA Conference on Space Telerobotics*, 1989, **4**, 55–63.

Liu, C., & Bar-Cohen, Y. 1999 March Newport Beach. Scaling laws of microactuators and potential applications of electroactive polymers in MEMS. *Proceedings of SPIE's 6th Annual International Symposium on Smart Structures and Materials*, 1999, **1**, 1–5.

Liu, G. R., & Gu, Y. T. A point interpolation method for two-dimensional solids. *International Journal for Numerical Methods in Engineering*, 2001, **50**, 937–951.

Love, L. J., & Book, W. J. Force reflecting teleoperation with adaptive impedance control. *IEEE Transactions on Systems, Man, and Cybernetics*, 2004, **34**, 159–165.

Mahvash, M., & Hayward, V. High-fidelity passive force-reflecting virtual environments. *IEEE Transactions on Robotics*, 2005, **21**, 38–46.

Mannetje, J. J. Pneumatic servo design method improves system bandwidth twenty-fold. *Control Engineering*, 1981, **28**, 79–83.

Massie, T. H., & Salisbury, J. K. The phantom haptic interface: A device for probing virtual objects. *Proceedings of the ASME International Mechanical Engineering Congress and Exposition*, 1994, **1**, 295–302.

Matsuoka, Y., & Howe, R. D. Hand impedance change during learning of a novel contact task. *World Congress on Medical Physics and Biomedical Engineering 2000*,

McCloy, D. 1968. Discharge characteristics of servo valve orifices. *Fluid International Conference*, 1968, 43–50.

McLaughlin, M., Rizzo, A., Jung, Y., Peng, W., Yeh, S., & Zhu, W. 2005. Haptics-enhanced virtual environments for stroke rehabilitation. *Conference on Advances in the Internet, Processing, Systems and Interdisciplinary Research*,

McNeely, W. A., Puterbaugh, K. D., & Troy, J. J. 1999. Six degree-of-freedom haptic rendering using voxel sampling. *Conference on Computer graphics and interactive techniques*, 1999, 401–408.

Melchiorri, C. 2003. Robotic telemanipulation systems: An overview on control aspects. *7th IFAC Symposium on Robot control*, 2003, 1–10.

Mitsuishi, M., Watanabe, T., Nakanishi, H., Hori, T., Watanabe, H., & Kramer, B. 1995 August Pittsburgh. A tele-micro-surgery system across the Internet with a fixed viewpoint/operation-point. *IEEE/RSJ International Conference on Intelligent Robots and System*, 1995, 178–185.

Morel, F., Lin-Shi, X., Retif, J. M., & Allard, B. A predictive current control applied to a permanent magnet synchronous machine, comparison with a classical direct torque control. *Electric Power Systems Research*, 2008, **78**, 1437–1447.

Morel, F., Retif, J. M., Lin-Shi, X., & Llor, A. M. 2004 December. Fixed switching frequency hybrid control for a permanent magnet synchronous machine. *IEEE International Conference on Industrial Technology (ICIT)*, 2004, 127–131.

Morita, Y. S., Shimizu, M., & Kagawa, T. 1985. An Analysis of Pneumatic PWM and its Application to a Manipulator. *Proc. of International Symposium of Fluid Control and Measurement*, 1985, 3–8.

Neilson, P. D., & Neilson, M. D. An overview of adaptive model theory: solving the problems of redundancy, resources, and nonlinear interactions in human movement control. *Journal of Neural Engineering*, 2005, **2**, 279–312.

Nguyen, T., Leavitt, J., Jabbari, F., & Bobrow, J. E. Accurate sliding-mode control of pneumatic systems using low-cost solenoid valves. *IEEE/ASME Transactions on mechatronics*, 2007, **12**, 216–219.

Nicosia, S., & Tomei, P. Robot control by using only joint position measurements. *IEEE Transactions on Automatic Control*,1990, **35**, 1058–1061.

Nicosia, S., Tornambe, A., & Valigi, P. 1990 December Honolulu. Experimental results in state estimation of industrial robots. *IEEE Conference on Decision and Control*, 1990, **1**, 360-365.

Noritsugu, T. 1985. Pulse-width modulated feedback force control of a pneumatically powered robot hand. *Proceedings of International Symposium of Fluid Control and Measurement*, 1985, 47–52.

Noritsugu, T. Development of PWN mode electro-pneumatic servomechanism. II: Position control of a pneumatic cylinder. *Journal of Fluid Control*, 1987, **17**, 7–31.

Olaby, O. Robotique pour l'apprentissage de gestes médicaux. Mise en œuvre de séquences d'accouchement automatisées.INSA de Lyon, 2006, p.203.

Onal, C. D., & Sitti, M. A Scaled Bilateral Control System for Experimental One-dimensional Teleoperated Nanomanipulation. *International Journal of Robotics Research*, 2009, **28**, 484–497.

Ostoja-Starzewski, M., & Skibniewski, M. A master-slave manipulator for excavation and construction tasks. *Robotics and Autonomous Systems*, 1989 **4**, 333–337.

Oura, M., Kobayashi, Y., Okamoto, J., & Fujie, M. G. 2006 February Pisa. Development of MRI compatible versatile manipulator for minimally invasive surgery. *IEEE/RAS-EMBS International Conference on Biomedical Robotics and Biomechatronics*, 2006, 176–181.

O'Malley, M. K., & Goldfarb, M. The effect of virtual surface stiffness on the haptic perception of detail. *IEEE/ASME Transactions on Mechatronics*, 2004, **9**, 448–454.

O'Malley, M. K., Gupta, A., Gen, M., & Li, Y. Shared Control in Haptic Systems for Performance Enhancement and Training. *ASME Journal of Dynamic Systems, Measurement, and Control*, 2006, **128**, 75–85.

Papachristodoulou, A., & Prajna, S. 2002 December Las Vegas. On the construction of Lyapunov functions using the sum of squares decomposition. *IEEE Conference on Decision and Control*, Vol 3 pp. 3482–3487. IEEE.

Papachristodoulou, A., & Prajna, S. Robust stability analysis of nonlinear hybrid systems. *IEEE Transactions on Automatic Control*, 2009, **54**, 1035–1041.

Papafotiou, G., Geyer, T., & Morari, M. A hybrid model predictive control approach to the direct torque control problem of induction motors. *International Journal of Robust and Nonlinear Control*, 2007, **17**, 1572–1589.

Paul, A. K., Mishra, J. E., & Radke, M. G. Reduced order sliding mode control for pneumatic actuator. *IEEE transactions on control systems technology*, 1994, **2**, 271–276.

Pawluk, D. T., & Ellis, R. E. 1991. Dynamics identification and control of a teleoperational system. *Proceedings of the IEEE International Conferenceon Robotics and Automation*, 1991, 1901–1906.

Pop, O., Chindris, G., & Dulf, A. 2004 May Orlando. Using DSP technology for true sine PWM generators for power inverters. *27th International Spring Seminar on Electronics Technology*,2004 **1**, 141– 146.

Prelle, C. Contribution au contrôle de la compliance d'un bras de robot à actionnement électropneumatique. INSA de Lyon, 1997, p.132.

Ren, Y., Lai-Yuen, S. K., & Lee, Y. S. Virtual prototyping and manufacturing planning by using tri-dexel models and haptic force feedback. *Virtual and Physical Prototyping*, 2006, **1**, 3–18.

Retif, J. M., Lin-Shi, X., Llor, A. M., & Morand, F. 2004 June. New hybrid direct-torque control for a winding rotor synchronous machine. *IEEE 35th Annual Power Electronics Specialists Conference*, 2004, **1**, 1438–1442.

Richard, E. 1990. De la commande linéaire et non linéaire en position des sytème électropneumatiques. INSA de Lyon, 1990, p.123.

Richert, D., Macnab, C. J. B., & Moreau, J. K. 2010 July Montreal. Force-Force Bilateral Haptic Control Using Adaptive Backstepping with Tuning Functions. *IEEE/ASME International Conference on Advanced Intelligent Mechatronics (AIM), Canada*, 2010, 341–346.

Riviere, C. N., Ang, W. T., & Khosla, P. K. Toward active tremor canceling in handheld microsurgical instruments. *IEEE Transactions on Robotics and Automation*, 2003, **19**, 793–800.

Rosen, J., Hannaford, B., MacFarlane, M. P., & Sinanan, M. N. Force controlled and teleoperated endoscopic grasper for minimally invasive surgery-experimental performance evaluation. *IEEE Transactions on Biomedical Engineering*, 1999, **46**, 1212–1221.

Rovan, J., & Hayward, V. Typology of tactile sounds and their synthesis in gesture-driven computer music performance. *Trends in Gestural Control of Music*, 2000, 297–320.

Salcudean, S., & Vlaar, T. On the emulation of stiff walls and static friction with amagnetically levitated input/output device. *Journal of Dynamic Systems, Measurement, and Control*, 1997, **119**, 127–132.

Salcudean, S. E., Hashtrudi-Zaad, K., Tafazoli, S., DiMaio, S. P., & Reboulet, C. Bilateral matched impedance teleoperation with application to excavator control. *IEEE Control Systems Magazine*, 1999, **19**, 29–37.

Salcudean, S. E., Zhu, M., Zhu, W.-H., & Hashtrudi-Zaad, K. Transparent Bilateral Teleoperation under Position and Rate Control. *International Journal of Robotics Research*, 2000, **19**, 1185–1202.

Salisbury, K., Conti, F., & Barbagli, F. Haptic rendering: Introductory concepts. *IEEE on Computer Graphics and Applications*, 2004, **24**, 24–32.

Schmidt, H., Hesse, S., Bernhardt, R., & Kr\üger, J. HapticWalker—a novel haptic foot device. *ACM Transactions on Applied Perception (TAP)*, 2005, **2**, 166–180.

Sellier, A., Brun, X., Sesmat, S., Retif, J., Lin-Shi, X., Thomasset, D., & Smaoui, M. Hybrid force control with on/off electropneumatic standard distributors. *International Journal of Fluid Power*, 2006, **7**, 51.

Sesmat, S., & Scavarda, S. 1998. Study of the behaviour of an electro pneumatic positioning system near the equilibrium state. *Proceedings of the International Fluid Colloquium*, 1998, **2**, 321–334.

Sesmat, S. Modélisation, simulation et commande d'une servovalve electropnaumatique. INSA de Lyon, 1996, p.307.

Shearer, J. L. Study of Pneumatic Processes in the Continuous Control of Motion with Compressed Air, Parts I and II. *ASME Transactions*, 1956, **78**, 233–249.

Shen, X., Zhang, J., Barth, E. J., & Goldfarb, M. 2004 July Boston. Nonlinear averaging applied to the control of pulse width modulated (PWM) pneumatic systems. *American Control Conference*, 2004, **5**, 4444–4448.

Shen, X., & Goldfarb, M. Energy Saving in Pneumatic Servo Control Utilizing Interchamber Cross-Flow. *Journal of Dynamic Systems, Measurement, and Control*, 2007, **129**, 303–310.

Shen, X., & Goldfarb, M. Simultaneous Force and Stiffness Control of a Pneumatic Actuator. *Journal of Dynamic Systems, Measurement, and Control*, 2007, **129**, 425–434.

Shen, X., Zhang, J., Barth, E. J., & Goldfarb, M. Nonlinear Model-Based Control of Pulse Width Modulated Pneumatic Servo Systems. *Journal of Dynamic Systems, Measurement, and Control*, 2006, **128**, 663–669.

Shimoga, K. B. 1992 October New-York. Finger force and touch feedback issues in dexterous telemanipulation. *Proceedings of NASA-CIRSSE International Conference on Intelligent Robotic Systems for Space Exploration*, 1992, 159–178.

Shimoga, K. B. 1993a. A survey of perceptual feedback issues in dexterous telemanipulation: Part II. Finger touch feedback. *Proceedings in IEEE Virtual Reality Annual International Symposium*, 271–279.

Shimoga, K. B. 1993 September Boston. A survey of perceptual feedback issues in dexterous telemanipulation: Part I. Finger force feedback. *Proceedings in IEEE Virtual Reality Annual International Symposium*, 1993, 263–270.

Sidhom, L., Pham, M. T., Thevenoux, F., & Gautier, M. 2010 July Montreal. Identification of a robot manipulator based on an adaptive higher order sliding modes differentiator. *IEEE/ASME International Conference on Advanced Intelligent Mechatronics*, 2010, 1093–1098.

Sirouspour, M. R., DiMaio, S. P., Salcudean, S. E., Abolmaesumi, P., & Jones, C. 2000 April San Fransico. Haptic interface control-design issues and experiments with a planar device. *IEEE International Conference on Robotics and Automation (ICRA)*, 2000, **1**, 789–794.

Sledd, A., & O'Malley, M. 2006 March Dallas. Performance Enhancement of a Haptic Arm Exoskeleton. *International Symposium on Haptic Interfaces for Virtual Environment and Teleoperator Systems*, 2006, 375–381.

Slotine, J. J. E., Li, W., & others. *Applied nonlinear control.* Prentice Hall Englewood Cliffs, NJ, 1991, P. 471.

Smaoui, M. Commandes non linéaires robustes mono et multidimensionnelles de dispositifs électropneumatiques. INSA de Lyon, 2004, p.195.

Smith, R. C. *Smart material systems: model development.* SIAM, 2005, p. 501.

Son, H. I., & Lee, D. Y. 2008 August Vancouver. Enhancement of kinesthetic perception for microsurgical teleoperation using impedance-shaping. *30th Annual International Conference of the IEEE Engineering in Medicine and Biology Society (EMBS)*, 2008, 1939–1942.

Srinivasan, M. A., & LaMotte, R. H. Tactual discrimination of softness. *Journal of Neurophysiology*, 1995, **73**, 88–101.

Staab, H., Sonnenburg, A., & Hieger, C. 2007. The DOHELIX-Muscle: A Novel Technical Muscle for Bionic Robots and Actuating Drive Applications. *IEEE International Conference on Automation Science and Engineering (CASE)*, 306–311.

Stadler, W. *Analytical robotics and mechatronics.* McGraw-Hill, Inc. New York, NY, USA, 1995, p. 576.

Stewart, D. A platform with six degrees of freedom. *Proceedings of the Institution of Mechanical Engineers*, 1965, **180**, 371–386.

Stramigioli, S., van der Schaft, A., Maschke, B., & Melchiorri, C. Geometric scattering in robotic telemanipulation. *IEEE Transactions on Robotics and Automation*, 2002, **18**, 588–596.

Strassberg, Y., Goldenberg, A. A., & Mills, J. K. 1992 May Nice. A new control scheme for bilateral teleoperating systems: Lyapunov stability analysis. *IEEE International Conference on Robotics and Automation*, 1992, **1**, 837–842.

Suzuki, S., Furuta, K., & Shiratori, S. Adaptive Impact Shot Control by Pendulum-like Juggling System. *JSME International Journal Series C*, 2003, **46**, 973–981.

Tachi, S., & Sakaki, T. Impedance controlled master-slave manipulation system. Part 1. Basic concept and application to the system with a time delay. *Advanced robotics*, 1991, **6**, 483–503.

Tadano, K., & Kawashima, K. 2007 April Roma. Development of a master slave system with force sensing using pneumatic servo system for laparoscopic surgery. *IEEE International Conference on Robotics and Automation*, 2007, **18**, 947–952.

Taft, C. K., & Harned, T. J. Electro-Fluid Four-Way On-Off Pneumatic Valve. *Journal of Dynamic Systems, Measurement, and Control*, 1980, **102**, 174–179.

Taghizadeh, M., Ghaffari, A., & Najafi, F. Modeling and identification of a solenoid valve for PWM control applications. *Comptes Rendus Mecanique*, 2009, **337**, 131–140.

Taghizadeh, M., Najafi, F., & Ghaffari, A. Increased tracking ability of pulse width modulation-driven pneumatic servo systems via a modified pneumatic circuit. *Electrical Engineering*, 2009, **91**, 79–87.

Taghizadeh, M., Ghaffari, A., & Najafi, F. Improving dynamic performances of PWM-driven servo-pneumatic systems via a novel pneumatic circuit. *ISA Transactions*, 2009, **48**, 512–518.

Takaiwa, M., & Noritsugu, T. 2003 September Taipei. Development of force displaying device using pneumatic parallel manipulator and application to palpation motion. *IEEE International Conference on Robotics and Automation*, 2003, **3**, 4098–4103.

Tan, H. Z., Durlach, N. I., Beauregard, G. L., & Srinivasan, M. A. Manual discrimination of compliance using active pinch grasp: The roles of force and work cues. *Perception and Psychophysics*, 1995, **57**, 495–510.

Tan, H. Z., Durlach, N. I., Rabinowitz, W. M., & Reed, C. M. Tactual performance with motional stimulation of the index finger. *The Journal of the Acoustical Society of America*, 1994, **95**, 2986–2986.

Tan, H. Z., Srinivasan, M. A., Eberman, B., & Cheng, B. Human factors for the design of force-reflecting haptic interfaces. *ASME Dynamic Systems and Control*, 1994, **55**, 353–359.

Tao, R., & Roy, G. D. *Electrorheological fluids: mechanisms, properties, technology, and applications.* World Scientific London, 1994, p.600.

Tavakoli, M., Aziminejad, A., Patel, R. V., & Moallem, M. High-fidelity bilateral teleoperation systems and the effect of multimodal haptics. *IEEE Transactions on Systems, Man, and Cybernetics, Part B*, 2007, **37**, 1512–1528.

Tavakoli, M., Aziminejad, A., Patel, R. V., & Moallem, M. 2007 July New York. Enhanced Transparency in Haptics-Based Master-Slave Systems. *American Control Conference (ACC '07)*, 2007, 1455–1460.

Tavakoli, M., Patel, R. V., & Moallem, M. *Haptics for Teleoperated Surgical Robotic Systems.* World Scientific, 2008, p.180.

Thomann, G. 2003. Contribution à la chirurgie minimalement invasive : conception d'un coloscope intelligent. INSA de Lyon, 2003, p.214.

Tondu, B., Boitier, V., & Lopez, P. 1995 October San Antonio. Naturally compliant robot-arms actuated by McKibben artificial muscles. *IEEE International Conference on Systems, Man, and Cybernetics*, 1995, **3**, 2635–2640.

Tondu, B., Ippolito, S., Guiochet, J., & Daidie, A. A Seven-degrees-of-freedom Robot-arm Driven by Pneumatic Artificial Muscles for Humanoid Robots. *The International Journal of Robotics Research*, 2005, **24**, 257–274.

Topçu, E. E., Yüksel, I., & KamIs, Z. Development of electro-pneumatic fast switching valve and investigation of its characteristics. *Mechatronics*, 2006, **16**, 365–378.

Tsagarakis, N., Caldwell, D. G., & Medrano-Cerda, G. A. 1999 September Pisa. A 7 DOF pneumatic muscle actuator (pMA) powered exoskeleton. *IEEE International Workshop on Robot and Human Interaction (ROMAN)*, 1999, 327–333.

Tsai, Y. C., & Huang, A. C. Multiple-surface sliding controller design for pneumatic servo systems. *Mechatronics*,2008, **18**, 506–512.

Utkin, V., & Chang, H. C. Sliding mode control on electro-mechanical systems. *Mathematical Problems in Engineering*, 2002 **8**, 451–473.

Utkin, V. I. *Sliding modes in control and optimization.* Springer-Verlag Berlin, 1992, p.286.

Vanderborght, B., Verrelst, B., Ham, R., Michaël, D., Beyl, P., & Lefeber, D. Development of a compliance controller to reduce energy consumption for bipedal robots. *Autonomous Robots*, 2008, **24**, 419–434.

Vertut, J., & Coiffet, P. *Teleoperations and robotics: evolution and development.* Prentice-Hall, Inc. Upper Saddle River, NJ, USA, 1986, p.216.

Walairacht, S., Yamada, K., Hasegawa, S., Koike, Y., & Sato, M. 4 + 4 Fingers Manipulating Virtual Objects in Mixed-Reality Environment. *Presence: Teleoperators and Virtual Environments*, 2002, **11**, 134–143.

Wang, W., & Yuan, K. 2004 April Boston. Teleoperated manipulator for leak detection of sealed radioactive sources. *IEEE International Conference on Robotics and Automation*, 2004, 1682–1687.

Wiker, S., Hershkowitz, E., & Zik, J. Teleoperator comfort and psychometric stability: Criteria for limiting master-controller forces of operation and feedback during telemanipulation. *Proceedings of NASA Conference on Space Telerobotics*, 1989, **1**, 99–107.

Williams II, R. L. Cable-suspended haptic interface. *International Journal of Virtual Reality*, 1998, **3**, 13–21.

Winter, S. H., & Bouzit, M. Use of magnetorheological fluid in a force feedback glove. *IEEE Transactions on Neural Systems and Rehabilitation Engineering*, 2007, **15**, 2–8.

Yang, A., Pu, J., Wong, C. B., & Moore, P. By-pass valve control to improve energy efficiency of pneumatic drive system. *Control Engineering Practice*, 2009, **17**, 623–628.

Ye, N., Scavarda, S., Betemps, M., & Jutard, A. Models of a pneumatic PWM solenoid valve for engineering applications. *Journal of Dynamic Systems, Measurement, and Control*, 1992, **114**, 680–688.

Yokokohji, Y., & Yoshikawa, T. Bilateral control of master-slave manipulators for ideal kinesthetic coupling-formulation and experiment. *IEEE Transactions on Robotics and Automation*, 1994, **10**, 605–620.

Yoshida, S., Kurumisawa, J., Noma, H., Tetsutani, N., & Hosaka, K. 2004. Sumi-nagashi: creation of new style media art with haptic digital colors. *ACM International Conference on Multimedia*, 636–643.

Yoshikawa, T., & Ichinoo, Y. 2003 July Kobe. Impedance identification of human fingers using virtual task environment. *IEEE/ASME International Conference on Advanced Intelligent Mechatronics (AIM)*, 2003, **2**, 759–764.

Yu, N., Hollnagel, C., Blickenstorfer, A., Kollias, S. S., & Riener, R. Comparison of MRI-compatible mechatronic systems with hydrodynamic and pneumatic actuation. *IEEE/ASME Transactions on Mechatronics*, 2008, **13**, 268–277.

Zhu, W. H., & Salcudean, S. E. Stability guaranteed teleoperation: An adaptive motion/force control approach. *IEEE Transactions on Automatic Control*, 2000, **45**, 1951–1969.

List of Figures

Chapter 1

Chapter 2

Chapter 3

Chapter 4

Chapter 5

List of Tables

Chapter 1

Chapter 3

Chapter 4

Chapter 5

Appendix 1
Polynomial interpolation method

In this part, we estimate a theoretical model of the servovalve's mass flow rate in term of the pressure and the control voltage. To do this, a polynomial interpolation method (Fourati & Maalej 2006) is employed by using the experimental data of Fig. 3.16 (b).

Assuming that the mass flow rate has the following polynomial model:

$$q_{est} = \sum_{i=0}^{n}\sum_{j=0}^{m} a_{ij} U^i P^j \tag{A.1}$$

where U is the voltage polynomial (i.e., N×1 matrix), P is the pressure polynomial (i.e., 1×M matrix), N and M are respectively the number of the measured points of U and P, q_{est} is the estimated mass flow rate (i.e., N×M matrix), a_{ij} is the coefficients of the polynomial q_{est}, n and m are respectively the degrees of U and P.

The N×M absolute-error matrix, which defined by the difference between the measured and the estimated mass flow rates (i.e. q and q_{est}), can be expressed as

$$\Delta_a = q - q_{est} \tag{A.2}$$

Considering the maximum value (scalar) of the matrix Δ_a defined as

$$\varepsilon_a = \max\left(\max\left|\Delta_a\right|\right) \tag{A.3}$$

Note that the polynomial method is not aimed at minimizing the estimated error ε_a. Indeed, ε_a reach its minimum only if the degree of q_{est} tends to infinity, which is thus not realistic. Our objective here is to find acceptable values of n and m to obtain a small enough estimation error. In this case, the degrees n and m are limited to six since the servovalve is rarely modeled as a function of order greater than six.

Fig. A.1 shows a matrix of ε_a whose value depends on n and m. It can be seen that when n and m vary from 1 to 3, a considerable reduction of the mass-flow-rate error is obtained, i.e., from 5.973 to 1.658 Nl/mn. On the other hand, when n and m are within the interval [3, 6], the error decreases slightly, i.e., from 1.658 to 1.485 Nl/mn.

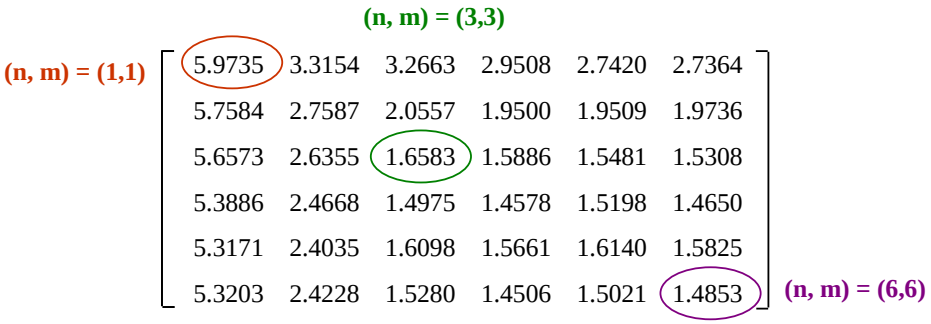

Fig. A.1. Matrix ε_a versus (n, m)

Fig. A.1 can be obtained graphically by Fig. A.2 (a). It seems that ε_a remains constant in the zone where both degrees are greater than or equal to three. Finally, the third iteration (n, m) = (3,3) has

been selected because an increase of the polynomial degrees doesn't affect any significant decrease on the estimation error.

The coefficients a_{ij} of the polynomial q_{est} which corresponds to the chosen degrees are:

$a_{ij,\ 0 \le i,j \le 3}$ = [0.1753 0.0119 0.0026 0.0000 –0.2498 0.0938 –0.0203 0.0011 0.0497 –0.0285 0.0083 –0.0005 –0.0052 0.0023 – 0.0009 0.0001].

After having found the degrees of U and P as well as the coefficients a_{ij}, we can calculate the relative estimation error Δ_r of the mass flow rate as

$$\Delta_r = \frac{q - q_{est}}{q} \tag{A.4}$$

Fig. A.2 (b) shows the variation of Δ_r according to the pressure and the voltage. It can be seen that the relative error is negligible for almost all coordinates (except for three peaks), allowing to validate our model.

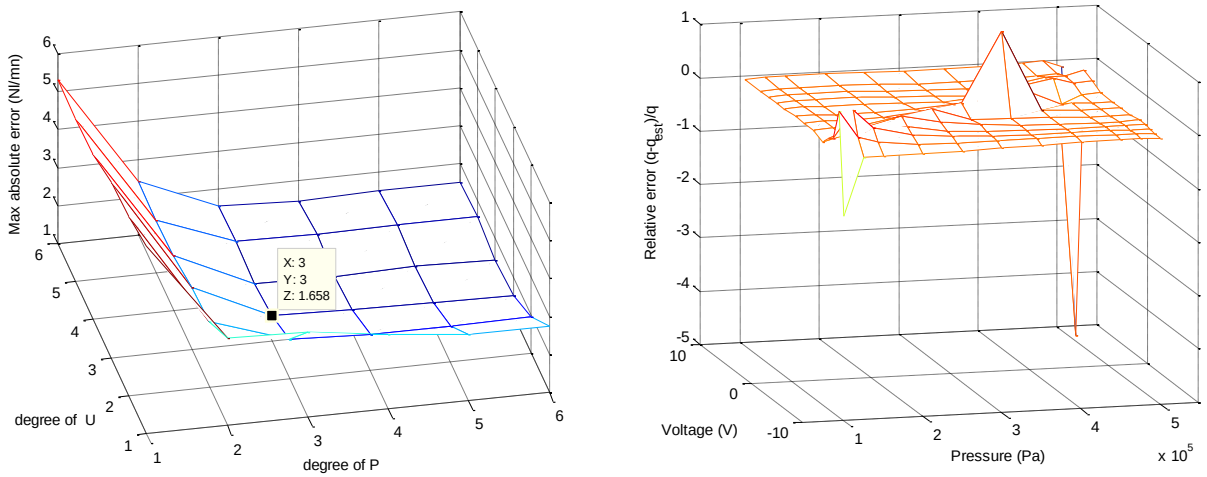

(a) Absolute error versus degrees of U and P

(b) Relative error versus voltage and pressure

Fig. A.2. Evolution of the estimated mass-flow-rate error (Fourati & Maalej 2006)

Fig. A.3 shows the measured mass flow rate of the jet-pipe servovalve together with the estimated mass flow rate in function of the control voltage and the pressure. As indicated in this figure, good agreement is obtained between the experimental and theoretical curves. Finally, these results allow to approve the validity of the model (A.1).

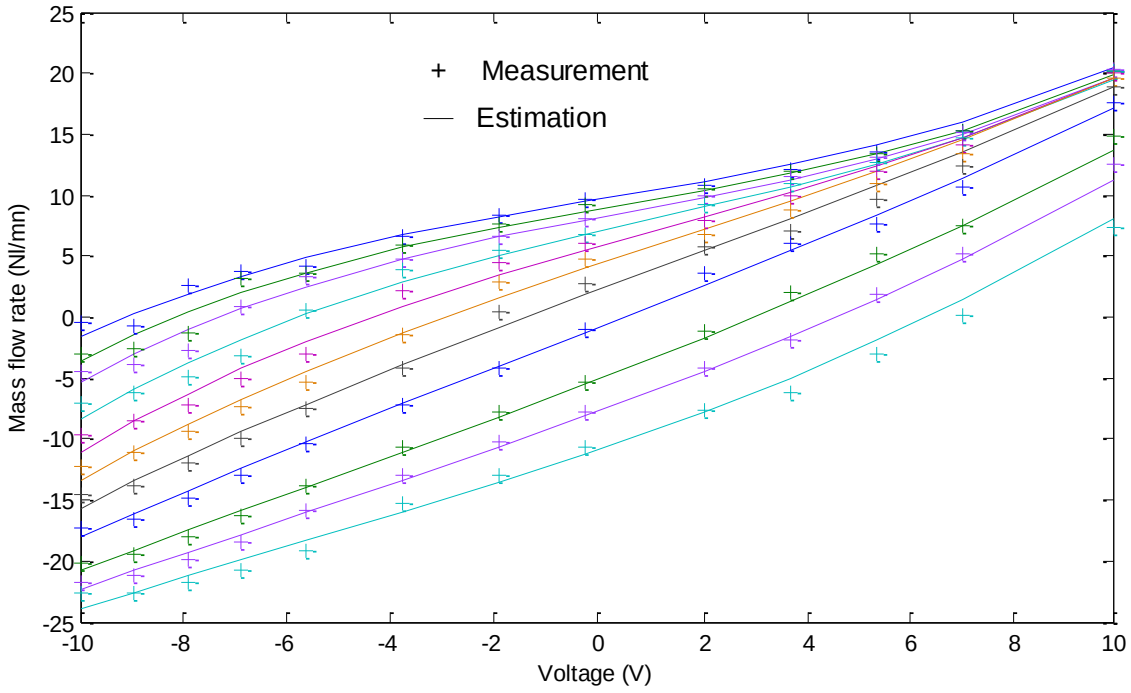

(a) Versus control voltage

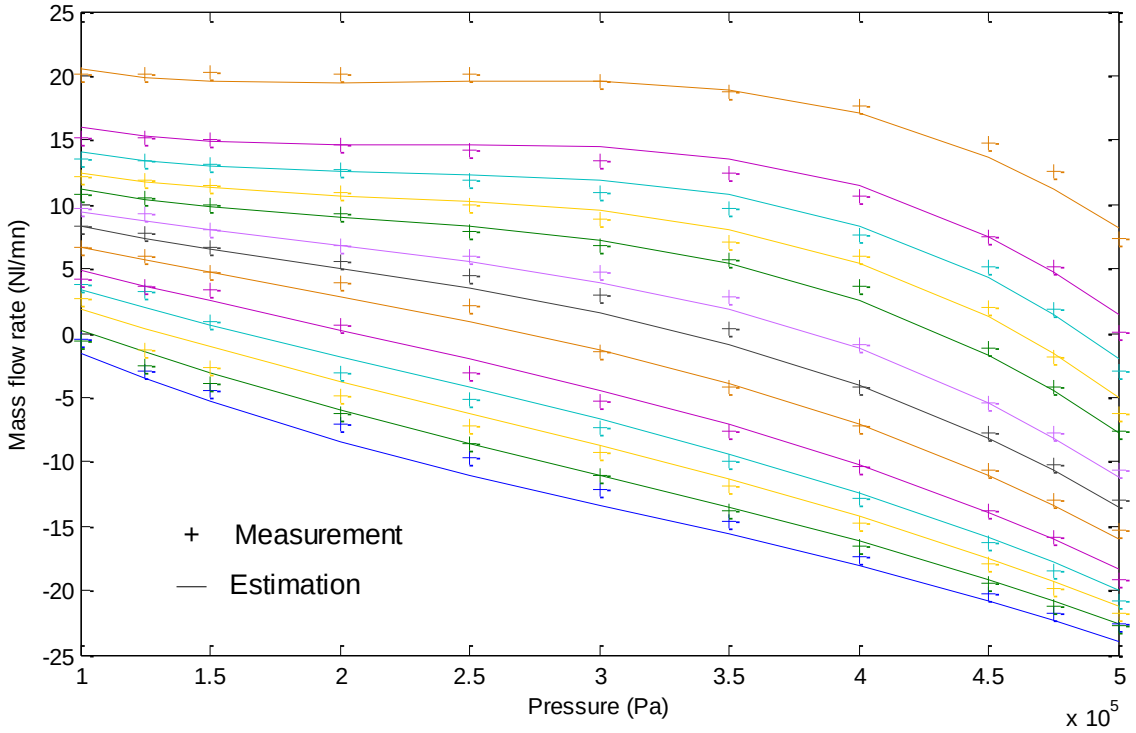

(b) Versus pressure

Fig. A.3. Experimental and estimated mass-flow-rate (Fourati & Maalej 2006)

Appendix 2
How PWM works

I. Principle

Pulse-width modulation (PWM) is a method of transmitting information on a series of pulses. The data transmission is encoded on the width of these pulses to control the amount of power that is sent to a load. In other words, PWM is a modulation technique for generating variable width pulses to represent the amplitude of an input analog signal. PWM is widely used in power delivery, voltage regulation, amplification and audio effects.

PWM allows to reduce the total power delivered to a load without resulting in loss, which normally occurs when a power source is limited by a resistive element. The underlying principle in the whole process is that the average power delivered is directly proportional to the modulation duty cycle. If the modulation rate is high, it is possible to smooth out the pulse train with passive electronic filters. The basic concept of PWM is illustrated in Fig. A.4.

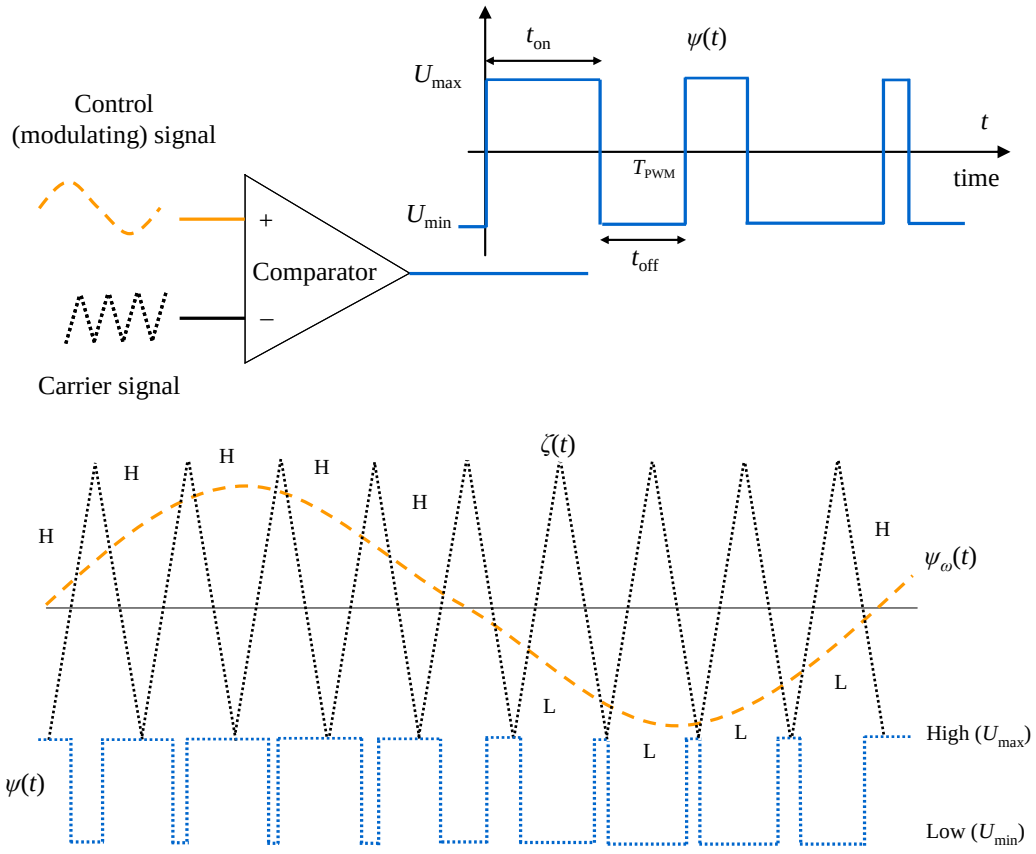

Fig. A.4. The basic concepts of PWM

By using a sinusoid ψ_ω as an *input signal* (the dashed wave), it is possible to produce an *output waveform* ψ (the solid wave) whose average voltage varies sinusoidally in a manner suitable for driving continuous actuators. The states of the output waveform are controlled by *a comparator*, a

device that allows to compare the input voltage to a *carrier signal* ζ (the dotted wave) and turns switches "on" or "off" depending on the result of the comparison. Indeed, output ψ stays high as long as the control signal is greater than the carrier signal, otherwise it stays on the low state.

Consequently, a simple comparator with a triangle or sawtooth carrier wave (easily generated using a simple oscillator) can turn a sinusoidal input into a pulse-width modulated output, resulting in the variation of the average value of the waveform. Generally, the greater the input signal is, the wider the resulting pulses become.

In Fig. A.4, $\psi(t)$ denotes the output waveform with a low value $U_{\min}$ and a high value $U_{\max}$; TPWM is the pulse period of the triangle wave $\zeta(t)$; t_{on} is the pulse width or on-time; and t_{off} is the off-time. The PWM waveform has a constant frequency (fPWM = 1/TPWM) and a variable pulse width. The sum of the on-time and off-time is a constant ($t_{on} + t_{off} = T$PWM), but the ratio of the on-time over the pulse period is a variable defined as the duty cycle dc ($dc = t_{on} / T$PWM).

The average value $\bar{\psi}$ of the waveform $\psi(t)$ is given by:

$$\bar{\psi} = \frac{1}{T_{\text{PWM}}} \int_0^{T_{\text{PWM}}} \psi(t)dt \tag{A.5}$$

As the value of $\psi(t)$ is $U_{\max}$ for $0 < t < t_{on}$ and $U_{\min}$ for $t_{on} < t < T$PWM, the above expression becomes:

$$\begin{aligned} \bar{\psi} &= \frac{1}{T_{\text{PWM}}} \int_0^{t_{on}} U_{\max} dt + \frac{1}{T_{\text{PWM}}} \int_{t_{on}}^{T_{\text{PWM}}} U_{\min} dt \\ &= \frac{t_{on}}{T_{\text{PWM}}} U_{\max} + (1 - \frac{t_{on}}{T_{\text{PWM}}}) U_{\min} \end{aligned} \tag{A.6}$$

With $U_{\max} = -U_{\min} = U$ where $U > 0$, and $t_{on} = dc.T_{\text{PWM}}$, the latter expression of (A.6) is simplified as:

$$\bar{\psi} = (2dc - 1)U / 2 \tag{A.7}$$

It is obvious that the average value of the pulse waveform $\bar{\psi}$ depends directly on the duty cycle dc. By imposing the value of dc as

$$dc = 0.5 + \eta \psi_{\omega}(t) / U \tag{A.8}$$

where η is a positive gain which allows to ensure that the duty cycle dc is in the interval [0, 1]. Indeed, the following condition needs to be satisfied:

$$-0.5 \le \eta \psi_{\omega}(t) / U \le 0.5 \tag{A.9}$$

Thus the amplitude of the signal $\eta\ \psi_{\omega} U$ has not to be grater than 0.5.

Substituting (A.8) in (A.7) yields

$$\bar{\psi} = \eta \psi_{\omega}(t) \tag{A.10}$$

Consequently, the average value of the pulse-wave output is directly proportional to the input signal.

In order to simplify a study of the PWM control in the pneumatic system, a classical example of the PWM method for the full-bridge single-phase inverter is carried out. Indeed, the operating principle of the pneumatic system with four solenoid valves is similar to the electrical system controlled by four switches. The only difference between these two systems is the switching time.

II. Full-bridge single-phase inverter based on PWM control

The full-bridge PWM single-phase inverter is widely used in uninterruptable power supplies, wind and solar power DC-AC interfacing, stand-alone voltage regulators in distributed power systems, and many other applications. The main goal of its control system is to achieve a fast dynamic AC voltage and frequency regulation during transients.

PWM control is considered to be one of the most powerful techniques that offers a simple method for digitally-controlled inverters (Jiang et al. 1998). With the availability of low cost high

performance DSP (Digital Signal Processor) chips characterized by the execution of most instructions in one instruction cycle, complicated control algorithms can be executed with fast speed and high sampling rate (Pop et al. 2004). The basic circuit diagram of the PWM controlled single-phase inverter is shown in Fig. A.5.

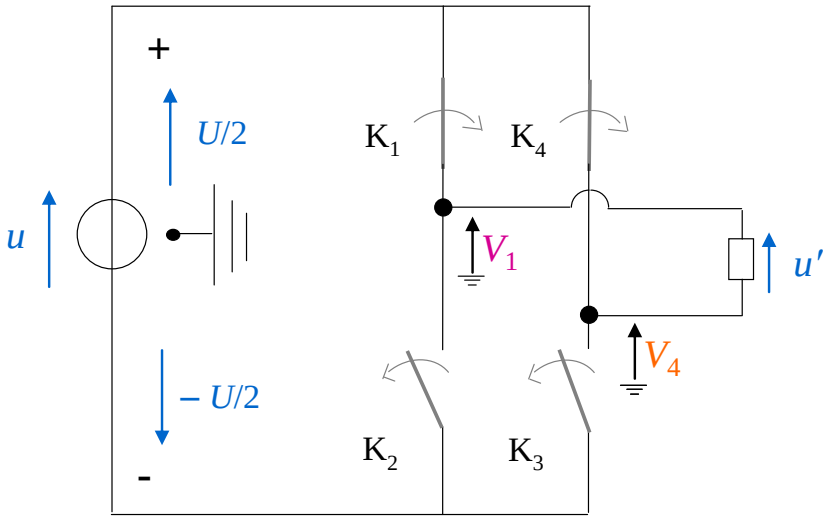

Fig. A.5. Full-bridge PWM single-phase converter

In this figure, the output voltage u' has the value

$$u' = V_1 - V_4 \tag{A.11}$$

By rapidly commuting from one value to the other, the potential V_1 and V_4 can take, as average, any value between $-U/2$ and $U/2$. Since $-U/2 \le \bar{V}_1, \bar{V}_4 \le U/2$, we can assign to $\bar{u}'$ (average value of u') a value between $-U$ and U.

There exist two possible configurations of the PWM controlled single-phase inverter in which the output voltage u' is not null (see Tab. A.1).

	K_1	K_2	K_3	K_4	u'
$V_1 = U/2$, $V_4 = -U/2$	On	Off	On	Off	U
$V_1 = -U/2$, $V_4 = U/2$	Off	On	Off	On	$-U$

TAB. A.1. SWITCHING SCHEME OF PWM CONTROLLED INVERTER

Consider f_ω as the desired image of u', we choose the image signals (i.e., $V_{1\omega}$ and $V_{4\omega}$) of V_1 and V_4 as (see Fig. A.6):

$$V_{1\omega} = -V_{4\omega} = f_\omega / 2 \tag{A.12}$$

From (A.8), we chose the duty cycles of V_1 and V_4 as:

$$dc_1 = 0.5 + \eta f_\omega(t)/U \quad , \quad dc_4 = 0.5 - \eta f_\omega(t)/U \tag{A.13}$$

Similar to how it was demonstrated in section I, the average value of V_1 and V_4 can be written as:

$$\bar{V}_1 = -\bar{V}_4 = \eta f_\omega(t)/2 \tag{A.14}$$

This leads to the following expression:

$$\bar{u}' = \bar{V}_1 - \bar{V}_4 = \eta f_\omega(t) \tag{A.15}$$

Thus the average value of u' is proportional to its desired image f_ω. By getting $f_\omega = U_0 \sin(\omega t)$, we have

$$\bar{u}' = \eta U_0 \sin(\omega t) \tag{A.16}$$

Finally, the width of the output waveform u' as well as its average voltage varies sinusoidally as similar to the input signal form.

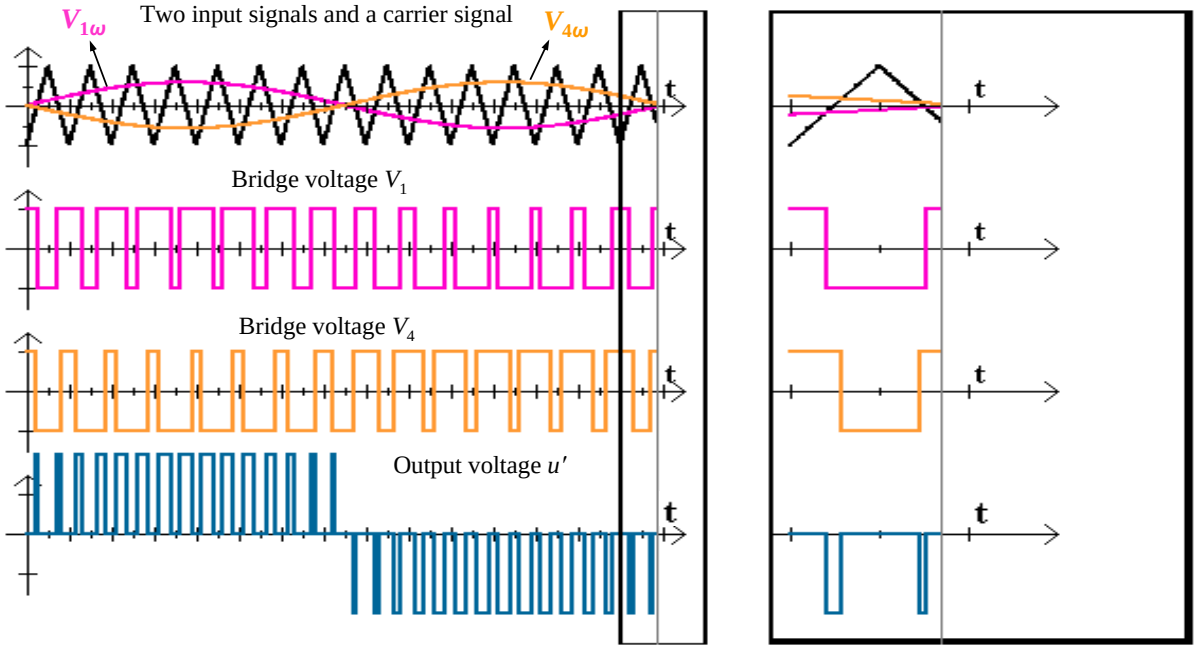

Fig. A.6. PWM output with a sinusoidal input voltage.